Dissertation

submitted to the

Combined Faculties of the Natural Sciences and Mathematics
of the Ruperto-Carola University of Heidelberg, Germany

for the degree of

Doctor of Natural Sciences

Put forward by

Thomas Hugle

born in: Oberndorf a.N.
Oral examination: 8 July 2020

Low-Scale New Physics in Dark Sectors

1st Referee: Prof. Dr. Dr. h.c. Manfred Lindner
2nd Referee: Prof. Dr. Björn Malte Schäfer

Abstract

Low-Scale New Physics in Dark Sectors
In this thesis we investigate two particular examples of phenomena that require introducing new physics beyond the standard model, namely the baryon asymmetry of the universe and dark matter. As the corresponding newly introduced fields or particles have eluded detection so far, they are usually associated with so-called dark sectors. Our focus throughout this work is on low-scale realizations of mechanisms explaining these phenomena, with low scale either referring to a comparison to the standard scenarios of the mechanisms, or the mass scales of the fields or particles involved. One well-established mechanism to explain the baryon asymmetry of the universe is leptogenesis. We study the possibility to realize low-scale leptogenesis in both the scotogenic and the singlet scalar assisted model by employing analytical and semi-analytical methods, with a focus on understanding the important ingredients. Our parameter scans show that we are able to recreate the baryon asymmetry in the universe via leptogenesis for right-handed neutrino masses of as low as $\sim 10\,\text{TeV}$ in the scotogenic model, while for singlet scalar assisted leptogenesis we can even reach scales below 1 TeV. Importantly, both of these results are achieved without a strong degeneracy of right-handed neutrino masses. In our study of dark matter, we first analyze and compare the LHC signatures of two benchmark models given by the two Higgs doublet model with an additional scalar or pseudoscalar. To do so, we study their $t\bar{t}$, mono-Z and mono-h signatures and derive limits from current experimental searches at the LHC. Furthermore, we also look at the reach of the mono-Z channel for future LHC upgrades and comment on the possibility to distinguish between the two models in case of a signal detection. Finally, we analyze a possibility to explain dark matter without using the standard particle dark matter picture via (pseudo)scalar and vector dark matter from non-minimal curvature couplings. With the misalignment and stochastic scenario, we investigate two different options how the dark matter could be created during the period of inflation. In the misalignment scenario we find that the parameter space substantially opens up due to the non-minimal coupling, whereas in the stochastic scenario any non-minimal coupling is tightly constrained for the mechanism to work while not violating isocurvature constraints. We conclude this thesis with a recapitulation of our main results and an outlook to further research.

Zusammenfassung

Neue Physik in Dunklen Sektoren an Niedrigen Skalen
In dieser Dissertation widmen wir uns zwei Beispielen von Phänomenen die Physik jenseits des Standardmodells benötigen, nämlich der Baryonen Asymmetrie des Universums und dunkler Materie. Da die zugehörigen neu eingeführten Felder und Teilchen bisher nicht detektiert werden konnten, werden sie als Teil sogenannter dunkler Sektoren angesehen. Für diese Arbeit fokussieren wir uns auf niederskalige Versionen der Mechanismen die diese Phänomene erklären können. Dabei drückt der Begriff niederskalig entweder einen Vergleich zum Standardszenario des Mechanismus aus oder bezieht sich auf die Größe der involvierten Massenskala. Eine etablierte Möglichkeit die Baryonen Asymmetrie im Universum zu erklären ist Leptogenese und wir untersuchen die Möglichkeit eine niederskalige Variante hiervon im Scotogenen Modell und im Modell mit einem zusätzlichen skalaren Singulett zu realisieren. Dabei arbeiten wir sowohl mit analytischen als auch semi-analytischen Methoden um ein Verständnis der zentralen Mechanismen von Leptogenese in beiden Modellen zu erhalten. Die durchgeführten Untersuchungen der Parameterräume zeigen, dass es möglich ist mittels Leptogenese die Baryonen Asymmetrie im Universum zu erklären mit rechtshändigen Neutrinomassen von nur $\sim 10\,\text{TeV}$ im Scotogenen Modell und sogar unter $1\,\text{TeV}$ im Modell mit einem zusätzlichen skalaren Singulett. Dabei ist es wichtig festzuhalten, dass für keines dieser Ergebnisse eine starke Degeneriertheit der rechtshändigen Neutrinomassen angenommen werden musste. Für unsere Untersuchung von dunkler Materie analysieren und vergleichen wir zunächst die LHC Signaturen von zwei Referenzmodellen - Modelle mit zwei Higgs Dubletten und entweder einem weiteren Skalar oder einem weiteren Pseudoskalar. Wir untersuchen die Signaturen ihrer $t\bar{t}$, mono-Z und mono-h Kanäle und leiten daraus Einschränkungen ab mit Hilfe der aktuellen experimentellen Suchen am LHC. Des Weiteren schauen wir uns den Einfluss von zukünftigen Aufrüstungen des LHCs im mono-Z Kanal an, als auch die Möglichkeit die beiden Modelle anhand ihrer Signaturen zu unterscheiden falls ein Signal gefunden wird. Als letztes untersuchen wir die Möglichkeit dunkle Materie nicht im üblichen teilchenphysikalischen Rahmen zu erklären, sondern mittels nicht-minimaler Kopplungen von (Pseudo)Skalar- oder Vektorfeldern an die Gravitation. Dabei analysieren wir sowohl das Fehlausrichtungs- als auch das Stochastische-Szenario, welche die Erschaffung der dunklen Materie während der Phase der Inflation erklären können. Im Fehlausrichtungs-Szenario zeigt sich, dass der Teil des Parameterraums durch die nicht-minimale Kopplung deutlich größer wird der die korrekte Menge an dunkler Materie vorhersagen kann und gleichzeitig die Einschränkungen durch die Nichtbeobachtung unkorrelierter Dichteschwankungen nicht verletzt. Im Gegensatz dazu ist im Stochastischen Szenario aufgrund der selben Restriktionen eine nicht-minimale Kopplung an die Gravitation stark eingeschränkt. Abschließend heben wir nochmals die wichtigsten Erkenntnisse dieser Arbeit hervor und geben einen Ausblick auf mögliche zukünftig interessante Forschungsgebiete.

Contents

Chapter 1

Introduction

Nullius in verba
(Take nobody's word for it)
- Motto of the Royal Society [1]

The field of astroparticle physics nowadays rests mainly on two pillars. On the one hand, there is the standard model of particle physics (SM) with its $SU(3) \times SU(2) \times U(1)$ gauge structure, providing a very precise description of sub-atomic interactions of particles. On the other hand, we have the standard model of cosmology (ΛCDM), accurately describing the evolution of the universe since the Big Bang and being closely intertwined with the description of gravity by means of general relativity (GR). Although both theories work extraordinarily well in their respective contexts, like for example for measurements at the Large Hadron Collider (LHC) [2, 3] or of the cosmic microwave background (CMB) [4], they lack explanations for several well-observed phenomena. Among the most outstanding of these phenomena are arguably dark matter (DM) [4, 5], dark energy (DE) [6, 7] and the matter–anti-matter–asymmetry or baryon asymmetry of the universe (BAU) [8–10]. While the ΛCDM provides an effective description of DM and DE in terms of their influence on the evolution of the universe, it does not (and is not meant to) address the question what the fundamental constituents of these two phenomena are. At the same time these problems are also not addressed in the SM, as there are no fundamental fields that can constitute DM and DE. Thus, our understanding of the microscopic appears to be incomplete. For the BAU the general picture is similar: like for DM and DE, the ΛCDM only covers its effect but not its origin, and even though the SM is in general able to explain a matter–anti-matter–asymmetry, the size of the BAU is much larger than could be explained by it [11].

Besides these unexplained experimental observations, there is also the underlying problem that the SM, describing three of the four fundamental forces[1], and GR, providing a description of gravity as the fourth force, are within the standard framework completely separated. This issue is usually addressed by theories of quantum-gravity. However, already from an effective point of view, combining the SM and GR can have far reaching consequences by potentially introducing couplings between fields and gravity.

[1] The three forces described by the SM are of course the strong, weak and electromagnetic force.

As the SM aims at explaining the fundamental interactions of all particles, it needs to be extended by new fields and interactions to accommodate for effects like DM or the generation of the BAU. Searches for these new fields and interactions have been ongoing since the shortcomings of the SM have first become obvious, be it through more and more precise measurements of the known contents of the SM, at for example the LHC [2, 3], or searches for the unknown, in experiments like XENON [12, 13]. It is from these experiments that we know that any potential new field may at most interact weakly with the SM to not have already left a trace in the measurements. Thus, the new physics we are searching for is "dark" to our current experiments and therefore often referred to as being part of a "dark sector". Furthermore, the term also nicely fits as an umbrella term for candidates of DM or DE, where the "dark" in their names again refers to their elusiveness.

With these new fields or particles, there is likely also a new mass or energy scale introduced into the SM, which by itself only contains the vacuum expectation value (vev) of the SM Higgs field as a scale that has a value of the order of $\sim 200\,\text{GeV}$. Either directly, by an explicit (effective) mass parameter or vev, or indirectly, by the size of a coupling that can, for example by a Higgs mechanism, be linked to a mass parameter. A natural comparison for these new scales is their relation to the SM Higgs vev as the only scale present in the SM, thereby splitting the new physics scenarios into high and low scale ones. Besides this in a sense absolute scale of new physics, it is also possible to compare different new physics scenarios among themselves and sort them in this way into high and low scale ones. This relative comparison is most often done for phenomena that allow for several explanations at vastly different scales. In both cases, low-scale new physics is particularly interesting because it is either in experimental reach in terms of the necessary energy to access these scales, or at least easier reachable. However, even low-scale new physics can be difficult to access experimentally due to the possibly high precision that might be necessary to find potentially tiny couplings.

These general considerations lay the groundwork for this thesis, in which we investigate new physics scenarios that aim at explaining the BAU or DM at (relative or absolute) low scales. To do so, we will work our way from the largest scales of new physics considered in this thesis of above 10 TeV, down to the smallest scales in the sub-eV regime. In Ch. 2 and Ch. 3 we discuss two different new physics scenarios that make it possible to explain the BAU via low-scale leptogenesis. Although the idea to create a baryon asymmetry via a lepton asymmetry, called leptogenesis, has been well studied, the standard leptogenesis scenario requires very high scales that are far out of reach for experiments. Therefore, it would be of interest to find a version of leptogenesis that works at low scales so that it can potentially be verified "by an appeal to facts determined by experiment" as described by the Royal Society in the explanation of their motto *Nullius in verba* [1]. In Ch. 2, we will do so by studying low-scale leptogenesis in the scotogenic neutrino mass model, which provides besides a radiative mechanism to explain the small (active) neutrino masses also a potential DM candidate. Our study of the scotogenic model will include both the scenario of two as well as three right-handed neutrinos (RHNs) and focus on exact analytical results whenever possible. Afterwards in Ch. 3, we study in the same spirit singlet scalar assisted leptogenesis, for which we will develop a semi-analytical understanding. While both of these models are at low scales for leptogenesis scenarios, they are still above the scale of the SM, by introducing new mass scales of at least $\sim 10\,\text{TeV}$ for the scotogenic model and of the order of $\sim 1\,\text{TeV}$ (or above) for the singlet scalar model. After our investigation of

the BAU, we will switch to looking at models dedicated to DM and continue by slightly decreasing the energy scale of interest to $\sim$500 GeV in Ch. 4. At and around this scale, we will compare the LHC signatures of two benchmark models, given by the two Higgs doublet model (2HDM) with an additional scalar (2HDM+S) and the 2HDM with an additional pseudoscalar (2HDM+PS). In Ch. 5, we will then look at possible non-minimal gravitational couplings of scalar and vector fields with very low mass scales in the sub eV, how they might constitute DM and in which way these models are accessible by experiments, before finally concluding in Ch. 6.

Chapter 2

Leptogenesis in the Scotogenic Model

One of the problems of the SM is that it can not account for the observed excess of baryons over anti-baryons in the universe [11], which is usually referred to as the BAU. Therefore, the observation of the BAU "provides ... one of the few observational proofs of physics beyond the SM" [11] (BSM physics). This asymmetry is usually captured by the baryon-to-photon ratio $\eta_B^{\text{obs}} \approx 6.1 \cdot 10^{-10}$ [8–10], representing the ratio of the excess number density of baryons to the one of photons, and can be precisely determined from CMB and big bang nucleosythesis (BBN) data [10]. But before jumping right into how the baryon-to-photon ratio can be explained via leptogenesis in the scotogenic model, let us first have a brief look at how and why leptogenesis became of general interest to study. We remark that the results presented in this chapter are based on work published as Ref. [14], especially from Sec. 2.2 onward.

2.1 The Baryon Asymmetry and Leptogenesis

Historically, the journey to understand the BAU started with major discoveries in cosmology like the expansion of the universe [15] and the detection of the CMB [16, 17], together with the development of the big bang model [18, 19]. Thanks to these discoveries, it was understood that the universe was hot in its early stages [20, 21] and therefore annihilation and pair creation processes that control the abundance of particles and anti-particles must have been in equilibrium. However, this equilibrium implies that both matter and anti-matter were abundant in the early universe and the asymmetry we now observe is the leftover after most of the matter and anti-matter annihilated into radiation, when the universe got too cold for pair creation to keep the balance.

With the discoveries of charge conjugation (C) violation and charge and parity conjugation (CP) violation [22, 23], the possibility opened up that the universe was not initially in an asymmetric state but dynamically ended up in one, driven by C and CP violating processes. This dynamic generation of the BAU is called baryogenesis, as it could explain the origin of the (leftover) baryons in the universe we observe today.

In general, the necessary conditions for baryogenesis, or a non-zero baryon-to-photon

ratio, when starting from a symmetric universe, are given by the Sakharov conditions [24]:

- B violation
- C and CP violation
- deviation from thermal equilibrium

where B stands for baryon number, which is the number of baryons minus the number of anti-baryons in the universe. These conditions to create the BAU can be intuitively understood. First, without B violation, a universe that started out with $B = 0$ is not able to generate any baryon asymmetry ($B \neq 0$), so especially not the BAU. Second, without C and CP violation, any asymmetry created by a process would be canceled by the C or CP conjugated process creating the same amount of asymmetry but with the opposite sign. Third, for a process in thermal equilibrium, the rate of the process is by definition identical to the rate of its inverse, thus making it impossible for any process to generate a baryon asymmetry.

Among the different possibilities to realize baryogenesis in BSM models, leptogenesis [25] is a very attractive option, since it allows (in its standard formulation) for a simultaneous explanation of the BAU and the small neutrino masses. The name is derived from the fact that in leptogenesis the asymmetry is first created in the lepton sector through CP violating decays of new heavy leptons, before it gets converted into a baryon asymmetry by means of $SU(2)$-sphalerons that naturally occur in the SM. For the explanation of the small neutrino masses, standard leptogenesis employs the type-I seesaw mechanism [26–30], including at least one heavy RHN for each non-zero (light) active neutrino mass. In this way, the RHNs can create the lepton asymmetry through their possibly CP violating decays as well as serving as the heavy partners to the active neutrinos to explain their small masses.

One important drawback of standard leptogenesis is that to create a sufficient baryon asymmetry the RHNs have to be very heavy, with necessary RHN masses above approximately 10^9 GeV [31–34]. Even though this scale can be lowered by up to three orders of magnitude down to 10^6 GeV by using flavor effects [35–38], it is still far out of reach for any direct tests at colliders. Furthermore, introducing a new very large scale into the theory via the RHN sector leads to significant loop corrections to the Higgs mass parameter of the SM, requiring a fine-tuning of the parameters of the model which one might refer to as a hierarchy problem [39, 40]. Finally, if there exist lepton number violating processes at low energies, high-scale leptogenesis may be ruled out altogether because the processes can potentially wash out any created lepton asymmetry necessary for leptogenesis [41–43]. Therefore, as described in Ch. 1, it is of interest to find a low-scale version of leptogenesis that can be realized at scales accessible by future colliders and other experiments or, at least, to gain an understanding of which conditions force leptogenesis to take place at high scales. This will be our guiding question in both this chapter on leptogenesis in the scotogenic model as well as in the following chapter on singlet scalar assisted leptogenesis.

To achieve leptogenesis at low scales, there exist popular approaches like resonant leptogenesis [44, 45] and the Akhmedov-Rubakov-Smirnov mechanism of RHN oscillations [46]. However, both of these approaches require a (more or less strong) degeneracy in the RHN mass spectrum, which is an additional assumption we do not want to rely on.

Therefore, we will focus on hierarchical RHN mass spectra for our analysis, keeping in mind that in general assuming some degeneracy of the RHN masses makes it easier to realize leptogenesis.

2.2 The Scotogenic Model

The scotogenic model of radiative neutrino masses [47] is arguably the simplest model of neutrino masses generated by quantum corrections, being a minimal extension of the SM in which the neutrino masses arise from one-loop (radiative) Feynman diagrams. In addition to these naturally small neutrino masses due to the loop suppression, the model also links their generation to the physics of DM by providing two viable dark matter candidates (a fermionic or a bosonic one, depending on the mass spectrum) that are involved in the radiative loop[1].

Explicitly, the SM is extended by a second Higgs-doublet η and at least two RHNs N_i that constitute a "dark sector". All of these new particles transform odd under an exact $\mathbb{Z}_2$ symmetry, which serves a twofold purpose. The $\mathbb{Z}_2$ symmetry stabilizes the lightest $\mathbb{Z}_2$-odd particle, making it a viable DM candidate if it is electrically neutral, and also prevents the new doublet η from getting a vev, thereby ensuring that the neutrino masses are zero at tree level. This leaves us with an important choice, namely whether we want the lightest RHN N_1 [48–50] or the lightest neutral component of the scalar doublet η [51–59] to be DM, as in principle both is possible. If N_1 is the DM, the relic density depends on the Yukawa couplings related to N_1, while in the case of η DM the relevant couplings will appear in the scalar and gauge interactions. Analyzing the option of N_1 being the DM, one finds that for the scenario to work one needs large Yukawa couplings, which in turn leads to an efficient washout of the lepton asymmetry [48, 60]. Thus, leptogenesis and the correct DM relic density can not be realized simultaneously if a hierarchical mass spectrum of the RHNs is assumed. Moreover, the necessary large Yukawa couplings can easily lead to a violation of the bounds on lepton flavor violation [61–63]. Therefore, we assume the DM to be part of the scalar doublet η and we will see that in this case both leptogenesis and the correct DM relic density can be realized simultaneously.

In terms of the Lagrangian of the model, the interactions of the new fields are described by

$$\mathcal{L}_{N,\eta} = -h_{\alpha i}\,\overline{\ell_L^\alpha}\,\tilde{\eta}\,N_i + \frac{1}{2}M_i\overline{N_i}(N^c)_i + \text{h.c.}\,, \tag{2.1}$$

with the Yukawa couplings $h_{\alpha i}$, the SM lepton doublets $\ell_L^\alpha \equiv (\nu_L^\alpha, \alpha_L)^T$ $(\alpha = e, \mu, \tau)$, the conjugate new scalar doublet $\tilde{\eta} \equiv i\sigma_2\eta^*$ and the Majorana masses M_i of the RHNs N_i. As discussed in Sec. 2.1, we will assume a hierarchical mass spectrum that is of the form

$$M_{i+1} \gtrsim 3\,M_i\,, \qquad\qquad M_1 \gg m_\eta\,, \tag{2.2}$$

where m_η represents the masses of the particles in the new scalar doublet before electroweak symmetry breaking. The first term of the interaction Lagrangian, Eq. (2.1), also shows

[1] From this link between neutrino mass generation and dark matter physics the model also got its name as the word *scotos* is Greek and means "dark".

that a vev ($\langle\eta\rangle \neq 0$) would break the $\mathbb{Z}_2$ symmetry, as stated above. This means that, in contrast to the standard type-I seesaw scenario, there is no Dirac mass term generated due to electroweak symmetry breaking. The scalar sector of the model includes the SM Higgs doublet H as well as the inert doublet η and is described by the potential

$$\begin{aligned} V(H,\eta) = \mu^2 H^\dagger H + m_\eta^2 \eta^\dagger \eta + \frac{\lambda_1}{2}(H^\dagger H)^2 + \frac{\lambda_2}{2}(\eta^\dagger \eta)^2 \\ + \lambda_3 (H^\dagger H)(\eta^\dagger \eta) + \lambda_4 (H^\dagger \eta)(\eta^\dagger H) \\ + \frac{\lambda_5}{2}\left[(H^\dagger \eta)(H^\dagger \eta) + (\eta^\dagger H)(\eta^\dagger H)\right], \end{aligned} \tag{2.3}$$

where all λ_i can be chosen as real valued without loss of generality. For λ_5 this is the case after a possible phase has been absorbed by a field redefinition and the reality of all λ_i implies that the potential is CP conserving.

After electroweak symmetry breaking, the physical scalar states are given by $H = (0, (v+h)/\sqrt{2})^T$ and $\eta = (\eta^+, (\eta_R + i\eta_I)/\sqrt{2})^T$ with their corresponding masses

$$\begin{aligned} m_h^2 &= \lambda_1 v^2 \,, \\ m_{\eta^\pm}^2 &= m_\eta^2 + \frac{v^2}{2}\lambda_3 \,, \\ m_{\eta_R}^2 &= m_\eta^2 + \frac{v^2}{2}(\lambda_3 + \lambda_4 + \lambda_5) \,, \\ m_{\eta_I}^2 &= m_\eta^2 + \frac{v^2}{2}(\lambda_3 + \lambda_4 - \lambda_5) \,, \end{aligned} \tag{2.4}$$

where the SM Higgs doublet vev $v = 246\,\text{GeV}$ appears. As we want the DM to belong to the new scalar doublet η, we have to ensure that one of its neutral components is the lightest state. This can be done by assuming $\lambda_4 \pm \lambda_5 < 0$ and $\lambda_5 > 0$, since under this assumption both the real scalar η_R and the real pseudoscalar η_I are lighter than the charged scalar $\eta^\pm$. Together with our assumption on the mass hierarchy in Eq. (2.2), this guarantees that η_I is the lightest new state and therefore the DM candidate. This constellation of η DM in the scotogenic model has been well studied and it has been found that for the mass range [51–59]

$$534\,\text{GeV} \leq m_{\eta_I} \lesssim 20\,\text{TeV} \,, \tag{2.5}$$

the correct relic abundance can be achieved, while all constraints are evaded by adjusting the scalar couplings accordingly. As for our analysis of leptogenesis the only relevant scalar coupling turns out to be λ_5, whereas the relic density and the other constraints depend on combinations of the scalar couplings [51–59], we can keep the full parametric freedom for λ_5 by always adjusting the other scalar couplings such that their combined value does not change.

With the fields and couplings as defined above, the mass matrix of the active neutrinos

can be determined to be [60, 64][2]

$$(\mathcal{M}_\nu)_{\alpha\beta} = \sum_i \frac{M_i h^*_{\alpha i} h^*_{\beta i}}{32\pi^2} \left[\frac{m^2_{\eta_R}}{m^2_{\eta_R} - M_i^2} \ln\left(\frac{m^2_{\eta_R}}{M_i^2}\right) - \frac{m^2_{\eta_I}}{m^2_{\eta_I} - M_i^2} \ln\left(\frac{m^2_{\eta_I}}{M_i^2}\right) \right] . \tag{2.6}$$

From Eq. (2.4), we can see that $m^2_{\eta_R} - m^2_{\eta_I} = v^2\lambda_5$ and thus we have $m^2_{\eta_R} = m^2_{\eta_I}$ in the limit of $\lambda_5 \to 0$. This in turn means that the active neutrino masses, as given by Eq. (2.6), vanish and a global $U(1)$ lepton number symmetry emerges. Therefore, small values of λ_5 are technically natural in the sense of 't Hooft [65].

Moreover, it is convenient to introduce an adapted Casas-Ibarra (CI) parametrization [66] for the Yukawa matrix h. To do so, we rewrite Eq. (2.6) in matrix form as

$$\mathcal{M}_\nu = h^* \Lambda^{-1} h^\dagger \, , \tag{2.7}$$

where we introduced the diagonal matrix Λ with entries

$$\Lambda_i \coloneqq \frac{2\pi^2}{\lambda_5} \, \xi_i \, \frac{2M_i}{v^2} \tag{2.8}$$

and

$$\xi_i \coloneqq \left(\frac{1}{8} \frac{M_i^2}{m^2_{\eta_R} - m^2_{\eta_I}} \left[\frac{m^2_{\eta_R}}{m^2_{\eta_R} - M_i^2} \ln\left(\frac{m^2_{\eta_R}}{M_i^2}\right) - \frac{m^2_{\eta_I}}{m^2_{\eta_I} - M_i^2} \ln\left(\frac{m^2_{\eta_I}}{M_i^2}\right) \right] \right)^{-1} . \tag{2.9}$$

This definition is especially handy, since the parameters ξ_i are of order one in most of the parameter space of interest. Furthermore, for a better comparability of our results to the standard type-I seesaw case, we split the definition of Λ_i (cf. Eq. (2.8)) into the part that appears also in the type-I seesaw, $2M_i/v^2$, and a part which is characteristic of the scotogenic model, $(2\pi^2/\lambda_5)\,\xi_i$. Following the notation of [66], we can use the Pontecorvo-Maki-Nakagawa-Sakata (PMNS) leptonic mixing matrix U [67, 68] to diagonalize the in general complex symmetric mass matrix $\mathcal{M}_\nu$ via $D_{\mathcal{M}_\nu} = U \mathcal{M}_\nu U^T$. In this way, the Yukawa couplings can be rewritten as[3]

$$h_{\alpha i} = \left(U \, D_{\sqrt{\mathcal{M}_\nu}} \, R^\dagger \, D_{\sqrt{\Lambda}} \right)_{\alpha i} , \tag{2.10}$$

where the arbitrary complex matrix R satisfies $RR^T = 1$. Therefore, with the help of the CI parametrization, we can split the Yukawa couplings into experimentally measured quantities like the PMNS matrix U, parameters related to the low mass scale of active neutrinos represented by $\mathcal{M}_\nu$, the parametric freedom included in R and the high energy quantities encoded in Λ. Moreover, by using this parametrization, we also automatically ensure to always be compatible with the measured data on active neutrinos.

The scotogenic model has been intensively studied in the literature and it was quickly

[2] Whether or not there appears a complex conjugation with the Yukawa couplings depends on which part of the Lagrangian, Eq. (2.1), is used to define the Yukawa couplings and which is "hidden" in the hermitian conjugate (h.c.) part. Sometimes this change of definition is also reflected by using the variable y for the Yukawa couplings instead of h.

[3] In the notation of [66], the matrix $D_{\sqrt{\Lambda}}$ refers to the diagonal matrix with entries $\sqrt{\Lambda_i}$.

realized that, in addition to an explanation of SM neutrino masses and DM, the model can also be used to explain the BAU via leptogenesis [60]. This led to more detailed studies of leptogenesis in the scotogenic model as for example presented in [69–73]. However, some of these studies (cf. [69–71]) focus on particular parameter points for which they perform a numerical analysis, thereby only covering a small part of the available parameter space. Others restrict themselves to the case of two RHNs (cf. [72]), which suppresses some interesting phenomenology, as we will see in our analysis. In addition, [69–72] use a resonant enhancement of the CP asymmetry, which we want to avoid as detailed in Sec. 2.1. The analysis of [73] has a more general perspective on two Higgs doublet models and provides a couple of analytical estimates, but does not numerically solve the corresponding set of Boltzmann equations or provide fully analytical expressions. For a more comprehensive study of the existing literature on radiative neutrino mass models in general and the scotogenic model in particular, see [74].

To extend the knowledge gained by the previous studies, the aim of our analysis is to gain an analytical understanding of leptogenesis in the scotogenic model and to flesh out the interplay between different parameters necessary to achieve a sufficiently large baryon asymmetry. Whenever needed, we will extend the analytical analysis with numerical simulations, so that the full parameter space is accessible.

2.3 Ingredients for Leptogenesis

With the scotogenic model now at hand, we can detail how leptogenesis can work in principle and how it fulfills the Sakharov conditions that are necessary for any kind of baryogenesis, as laid out in Sec. 2.1.

In the thermal bath of the early universe, there are inverse decays ($\eta+\ell \to N_1$) and decays ($N_1 \to \eta + \ell$) of RHNs, cf. Eq. (2.1), that create and destroy those particles, resulting in a thermal equilibrium in which the particles are Maxwell-Boltzmann distributed (cf. App. A and Eq. (A.2)). The process of inverse decays is specific to finite temperature quantum field theories (QFTs) (thermal baths) and can not happen in the standard zero temperature QFT, since the phase space would be zero at zero temperature. As the universe cools over time, at some point the energy in the thermal bath is not high enough any more to create a sufficient amount of RHNs to keep the equilibrium, leading to the RHNs dropping out of thermal equilibrium. This happens around $M_1 \approx T$, when the thermal energy ($\approx T$) in the leptons and scalars becomes smaller than the rest mass M_1 of the RHN. From then on, the decay of the RHNs will be the dominant process, which can be C and CP violating, by decaying dominantly into leptons instead of anti-leptons. Any such generated L (or $B-L$) asymmetry will be automatically converted to a baryon asymmetry by the $SU(2)$-sphalerons[4] present in the SM and which are B violating. Therefore, all Sakharov conditions are fulfilled.

To facilitate an analytical treatment and to get the parameter relations as clear as possible, we restrict our analysis to the most important physical effects. They are the decay and inverse decay of the lightest RHN N_1 in combination with the corresponding $\Delta L = 2$ washout processes, which are the processes that change the lepton number L

[4] Sphalerons are non-perturbative processes in the SM that conserve $B-L$ but violate $B+L$ and are related to the non-trivial vacuum structure of the SM, cf. e.g. [75] for details.

by two units and thereby washout (decrease) the generated baryon asymmetry. The contributions of decays and inverse decays of N_2 and N_3 to the final baryon asymmetry are negligible as we will see, due to strong washout effects mediated by either the N_1 or the N_2 and N_3 themselves. This also holds true for any initial $B-L$ asymmetry, so that the model is insensitive to this initial condition. Note that we refer to the $B-L$ asymmetry here, because $B-L$ is conserved in the SM, whereas B is not. Additionally, there is a one-to-one correspondence between the $B-L$ and the B asymmetry, which makes $B-L$ a very useful quantity for calculational purposes. Focusing on the above mentioned processes means that we neglect possible corrections from $\Delta L = 1$ scatterings [76, 77], thermal corrections [33, 78], flavor effects [79, 80] and quantum kinetic effects [81, 82].

Let us gather now all the relations necessary to describe leptogenesis in the scotogenic model, with our notation and conventions being based on [34, 80]. As a simplification of our analysis, we can revert to [34] for some of the analytical relations, since the underlying Boltzmann equations for our model turn out to be identical (cf. Sec. 2.5.2). Like for standard leptogenesis, where the role of the second Higgs doublet η is covered by the SM Higgs doublet, one important distinction is between the weak and strong washout regime, so how strongly the processes that create the $B-L$ asymmetry destroy it again through their inverse counterparts. These different regimes can be characterized by the value of the decay parameter that specifies the strength of the washout and is given by

$$K_1 \coloneqq \frac{\Gamma_1}{H(z_1=1)}\,, \tag{2.11}$$

where typically one distinguishes between the weak washout regime for $K_1 \lesssim 1$ and the strong washout regime for $K_1 \gtrsim 4$, with a transition region in between (cf. [34]). Here, Γ_1 is the decay width of N_1, H is the Hubble parameter and $z_1 \coloneqq M_1/T$, with photon bath temperature T, is a convenient measure of time. Since the RHNs drop out of thermal equilibrium around $M_1 \approx T$, as mentioned above, the most important time for leptogenesis is normally around $z_1 \approx 1$. For masses above the electroweak scale, $M_1 > v = 246\,\mathrm{GeV}$, leptogenesis thus occurs during radiation domination. During this cosmological era, the Hubble parameter can be expressed as, cf. Eq. (A.10),

$$H = \sqrt{\frac{8\pi^3 g_*}{90}}\frac{T^2}{M_{\mathrm{Pl}}} = H(z_1=1)\frac{1}{z_1^2}\,. \tag{2.12}$$

By calculating the decays $N_i \to \ell_L^\alpha \eta$ and $N_i \to \overline{\ell_L^\alpha}\eta^*$, see Fig. 2.1 for relevant Feynman diagrams, we find for the CP asymmetry parameter ε

$$\begin{aligned}\varepsilon_{i\alpha} = \frac{1}{8\pi (h^\dagger h)_{ii}} \sum_{j\neq i} \Bigg[& f\left(\frac{M_j^2}{M_i^2}, \frac{m_\eta^2}{M_i^2}\right) \mathrm{Im}\Big[h_{\alpha i}^* h_{\alpha j} (h^\dagger h)_{ij}\Big] \\ & - \frac{M_i^2}{M_j^2 - M_i^2}\left(1 - \frac{m_\eta^2}{M_i^2}\right)^2 \mathrm{Im}[h_{\alpha i}^* h_{\alpha j} H_{ij}] \Bigg]\,,\end{aligned} \tag{2.13}$$

which is linked to the generated lepton asymmetry as it describes the decay of the RHNs. Here, the function f stems from the interference of the tree-level diagram with the one-loop

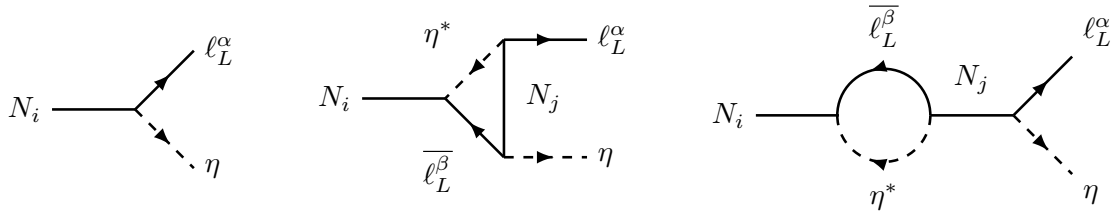

Figure 2.1.: Feynman diagrams for the decay $N_i \to l_L^\alpha \eta$ that lead to a CP asymmetry in the scotogenic model, with the tree-level diagram to the left, vertex correction in the middle and self-energy contribution to the right.

vertex correction and is given by

$$f(r_{ji}, \eta_i) \coloneqq \sqrt{r_{ji}}\left[1 + \frac{(1 - 2\eta_i + r_{ji})}{(1-\eta_i)^2} \ln\left(\frac{r_{ji} - \eta_i^2}{1 - 2\eta_i + r_{ji}}\right)\right], \tag{2.14}$$

with $r_{ji} \coloneqq M_j^2/M_i^2$ and $\eta_i \coloneqq m_\eta^2/M_i^2$. In the limit of $m_\eta = 0$ this reduces to the well-known result [83]

$$f(r_{ji}, 0) = \sqrt{r_{ji}}\left[1 + (1 + r_{ji}) \ln\left(\frac{r_{ji}}{r_{ji}+1}\right)\right]. \tag{2.15}$$

In the same way, the self-energy contributions are found to be

$$H_{ij} \coloneqq (h^\dagger h)_{ij} \frac{M_j}{M_i} + (h^\dagger h)_{ij}^* . \tag{2.16}$$

The expressions simplify when flavor effects are neglected, since in this case it is possible to sum over the final state flavor α, which makes the second term of H_{ij} drop out in the expression for $\varepsilon_{i\alpha}$ as it does not lead to an imaginary part (cf. Eq. (2.13)). The more compact expression for the CP asymmetry parameter then reads

$$\varepsilon_i = \frac{1}{8\pi (h^\dagger h)_{ii}} \sum_{j \neq i} \mathrm{Im}\left[(h^\dagger h)_{ij}^2\right] \frac{1}{\sqrt{r_{ji}}} F(r_{ji}, \eta_i) , \tag{2.17}$$

where we defined

$$F(r_{ji}, \eta_i) \coloneqq \sqrt{r_{ji}}\left[f(r_{ji}, \eta_i) - \frac{\sqrt{r_{ji}}}{r_{ji} - 1}(1 - \eta_i)^2\right]. \tag{2.18}$$

Note that for a hierarchical mass spectrum as in our case ($r_{ji}, \eta_i \ll 1$), $F(\cdot)$ can be well approximated by $F(r_{ji}, \eta_i) \approx -3/2$. Additionally, for the decay width Γ_1, which is relevant for the decay parameter K_1, we find

$$\Gamma_1 = \frac{M_1}{8\pi}\left(h^\dagger h\right)_{11} (1 - \eta_1)^2 . \tag{2.19}$$

As can be seen from the above expressions, the expression $h^\dagger h$ is important for leptoge-

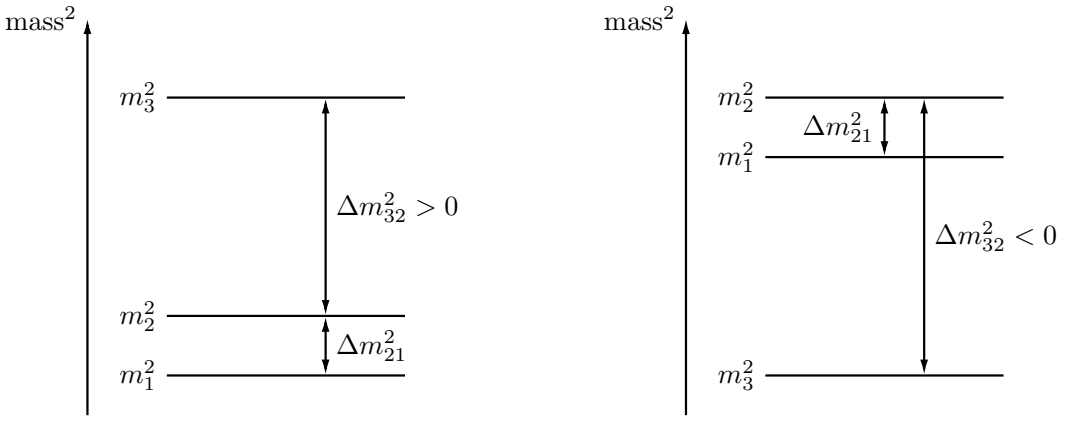

(a) Normal ordering (b) Inverted ordering

Figure 2.2.: Possible orderings of active neutrino masses allowed by experimental data. The sign of Δm_{21}^2 is known due to interactions of solar neutrinos with matter [8].

nesis and therefore worth to look at in more detail. From Eq. (2.10), which was derived by using the CI parametrization, we find

$$\left(h^\dagger h\right)_{ij} = \sqrt{\Lambda_i \Lambda_j}\left(R D_{\mathcal{M}_\nu} R^\dagger\right)_{ij} . \tag{2.20}$$

Thus, the parametric dependence nicely splits into $\widetilde{m} \coloneqq R D_{\mathcal{M}_\nu} R^\dagger$, which only depends on the masses of the active neutrinos through $D_{\mathcal{M}_\nu} \coloneqq \mathrm{diag}(m_1, m_2, m_3)$ and the (complex) CI parameters, and Λ_i that includes the other parameters like M_i and λ_5. Note that the matrix $h^\dagger h$ does not depend on the PMNS matrix U, which implies that the CP-violating phases in the PMNS matrix are not the ones that are driving leptogenesis[5]. Furthermore, this implies that the values of neutrino mixing angles are irrelevant for unflavored leptogenesis.

With all of the formulas above, we can now derive analytical expressions for leptogenesis in the scotogenic model. As we will see, there is a significant difference between the scotogenic model with two and three RHNs, so we will treat those cases separately.

2.4 Leptogenesis with Two Right-Handed Neutrinos

For the case of two RHNs, we have one massless active neutrino while the other two obtain a mass and we distinguish as usual between normal ordering (NO) and inverted ordering (IO), see Fig. 2.2. The active neutrino mass matrices are then given by

[5]This can change when flavor effects are taken into account. Then the contribution from $h_{\alpha i}^* h_{\alpha j}$ does not drop out of the CP asymmetry parameters $\varepsilon_{i\alpha}$ anymore (cf. Eq. (2.13)) and they depend on the CP-violating phases in the PMNS matrix.

$$
\begin{aligned}
D_{\mathcal{M}_\nu}^{\mathrm{NO}} &= \mathrm{diag}\left(0, \sqrt{\Delta m_{21}^2}, \sqrt{\Delta m_{31}^2}\right) , \\
D_{\mathcal{M}_\nu}^{\mathrm{IO}} &= \mathrm{diag}\left(\sqrt{-\Delta m_{31}^2}, \sqrt{\Delta m_{21}^2 - \Delta m_{31}^2}, 0\right) ,
\end{aligned}
\tag{2.21}
$$

with $\Delta m_{ij}^2 \coloneqq m_i^2 - m_j^2$. To avoid writing nearly identical equations twice, we will use the notation m_h for the heaviest active neutrino and m_l for the lightest (massive) active neutrino from now on. The matrix R (cf. Eq. (2.10)) is for two RHNs determined by one complex rotation parameter $z = z_R + iz_I$ (cf. [84] for the explicit form of R), where $z_R \in [0, 2\pi)$ and $z_I \in \mathbb{R}$.

Using the active neutrino mass matrix and the CI parametrization we can explicitly calculate the CP asymmetry ε_1 (cf. Eq. (2.17)) and maximize it over all possible values of z. Taking the approximation $F(r_{ji}, \eta_i) \approx -3/2$ for a hierarchical mass spectrum, we find an upper bound on the CP asymmetry of

$$
|\varepsilon_1| \lesssim \frac{3\pi}{4\lambda_5 v^2}\, \xi_2\, (m_h - m_l)\, M_1 , \tag{2.22}
$$

which is essentially the Davidson-Ibarra (DI) bound [31]. The difference is the additional factor of $(2\pi^2/\lambda_5)\,\xi_2$, which already appeared in Eq. (2.8) and is specific to the scotogenic model. Furthermore, the factor of $m_h - m_l$ implies that for the two RHNs case the CP asymmetry can be larger for NO than for IO.

In addition to the CP asymmetry ε_1, we need for the determination of the baryon-to-photon ratio η_B also the conversion factor $C \approx 0.01$ [34], which takes into account sphaleron conversion of the lepton into a baryon asymmetry as well as the evolution of the photon density after the production of the lepton asymmetry (related to the entropy generation during that time), and the efficiency factor κ_1, which represents the effect of the washout through inverse processes. As the efficiency factor κ_1 describes the influence of the washout, it is in general a function of the decay parameter K_1. Taking all of these factors together, the final baryon-to-photon ratio is given by [34]

$$
\eta_B = -C\varepsilon_1\kappa_1 . \tag{2.23}
$$

In our case, we get for the decay parameter

$$
K_1 = \frac{2\pi^2}{\lambda_5}\xi_1 \sqrt{\frac{45}{64\pi^5 g_*}}\frac{M_{\mathrm{Pl}}}{v^2}\widetilde{m}_{11}(1-\eta_1)^2 , \tag{2.24}
$$

and for the parameter values $0 \leq \lambda_5 \leq 4\pi$ and $3\, m_\eta \leq M_1$ (or $\eta_1 \leq 1/9$), it has a minimum of $K_1^{\min} \approx 10$, while being significantly larger ($K_1 \sim 10^3$ and above) in most parts of the parameter space. This means that we are always in the strong washout regime (cf. Sec. 2.3), enabling us to assume N_1-dominated leptogenesis and neglect washout through scattering effects. For these large values of K_1, the in general only numerically known relation between the efficiency factor and the decay parameter can be approximated by [34]

$$
\kappa_1(K_1) \approx \frac{1}{1.2 K_1 \left[\ln K_1\right]^{0.8}} . \tag{2.25}
$$

Putting all the pieces together, we can give a fully analytical expression of the baryon-to-photon ratio in the scotogenic model with two RHNs

$$\eta_B = C\sqrt{\frac{16\pi^3 g_*}{1.2^2 \cdot 45}}\frac{M_1}{M_{\rm Pl}}\frac{\xi_2}{\xi_1}\frac{F(r_{21},\eta_1)}{(1-\eta_1)^2}\frac{1}{[\ln K_1]^{0.8}}\cdot \frac{\left(m_h^2 - m_l^2\right)\sin(2z_R)\sinh(2z_I)}{\left[-(m_h-m_l)\cos(2z_R)+(m_h+m_l)\cosh(2z_I)\right]^2}\,, \tag{2.26}$$

where K_1 inside the logarithm is again given by the expression in Eq. (2.24). With this complete formula for η_B, we can now check whether it behaves as one might naively expect with regard to λ_5. Simply judging by the expression for the CP asymmetry, cf. Eq. (2.22), one might naively expect that λ_5 is important for leptogenesis and the smaller λ_5 is, the larger the generated baryon asymmetry can be. However, both of these expectations turn out not to be true for the two RHNs case. From the complete formula for η_B, Eq. (2.26), we find that it depends only logarithmically on λ_5 (through K_1), which means that the value of λ_5 has little impact on the generated baryon asymmetry. Furthermore, as $K_1 \sim 1/\lambda_5$ (cf. Eq. (2.24)), the baryon-to-photon ratio η_B actually decreases with decreasing λ_5, making the perturbative limit $\lambda_5 = 4\pi$ the optimal choice for a large baryon asymmetry.

For determining the minimal mass scale at which leptogenesis can be realized in the scotogenic model with two RHNs, we can start from Eq. (2.26), use the optimal value of $\lambda_5 = 4\pi$ and maximize over the CI parameters z_R and z_I. With the observed values for the neutrino masses (cf. [8]) and $\eta_B^{\rm obs} \approx 6.1 \cdot 10^{-10}$, the only variable left is the mass of the lightest RHN M_1 and we find for its lower limit (depending on the active neutrino mass ordering)

$$M_{1,\,\rm min}^{\rm NO} \sim 10^{10}\,{\rm GeV} \qquad \text{and} \qquad M_{1,\,\rm min}^{\rm IO} \sim 10^{12}\,{\rm GeV}\,. \tag{2.27}$$

These lower limits are essentially identical to the ones of standard leptogenesis in the strong washout regime ($K_1 \gtrsim 4$). This can be intuitively understood, as the main difference of the scotogenic model and standard scenario is the different Yukawa couplings $h_{\alpha i}$ (cf. Eq. (2.10)), however the baryon-to-photon ratio scales (up to logarithmic corrections) like $\eta_B \sim \varepsilon_1/K_1 \sim {\rm Im}\left[(h^\dagger h)^2\right]/(h^\dagger h)^2$ and thus all multiplicative prefactors of $h^\dagger h$, like λ_5, cancel. We conjecture this to be a generic feature of radiative neutrino mass models in which the active neutrino mass matrix is only modified by multiplicative factors. On the other hand, the whole argument relies on the fact that we are in the strong washout regime, which can depend on the mass of the lightest active neutrino and λ_5, as we will see in the next section in which we analyze the scotogenic model with three RHNs.

2.5 Leptogenesis with Three Right-Handed Neutrinos

With the introduction of a third RHN, we significantly open up our accessible parameter space, as the CI parametrization now includes three complex free parameters instead of one, as well as that the lightest active neutrino can now be massive and therefore have a mass below the value suggested by the smallest measured active neutrino mass square difference (cf. Fig. 2.2). Explicitly, the CI parametrization is now given by the product

of three complex rotation matrices $R(z_{23})$, $R(z_{13})$, and $R(z_{12})$ (cf. [84]) and the lightest active neutrino can be in principal arbitrarily light. This has important consequences for the decay parameter K_1 (cf. Eq. (2.24)), as in the relevant parameter space we have $(2\pi^2/\lambda_5)\,\xi_1 \gtrsim 1$ and from an explicit calculation we find $\widetilde{m}_{11} = \left(RD_{\mathcal{M}_\nu}R^\dagger\right)_{11} \geq m_l$. Thus, plugging in the numerical values, we can determine a lower limit for the decay parameter of

$$K_1 \gtrsim 10^3 \left(\frac{m_l}{\text{eV}}\right)(1-\eta_1)^2\,. \tag{2.28}$$

So for the hierarchical RHN mass spectrum we assume, we are necessarily in the strong washout regime as long as $m_l \gtrsim 10^{-3}\,\text{eV}$. In this regime, the three RHNs case behaves identically to the two RHNs NO case or standard leptogenesis and we find a lower limit on the lightest RHN mass of $M_1^{\text{min}} \sim 10^{10}\,\text{GeV}$. The only difference is that for three RHNs the distinction between NO and IO disappears, as the mass difference of the heaviest and lightest (massive) active neutrino is (nearly) independent of the ordering.

One aspect that becomes relevant once we leave the strong washout regime is the question of the initial N_1 abundance. In the case of strong washout the inverse decay processes that create the N_1 abundance are strong enough during the evolution of the universe to create a thermal initial abundance before the period relevant to leptogenesis begins (cf. Fig. 2.3). On the other hand, in the weak washout regime this is not the case anymore and one has to rely on other processes that help to establish a thermal initial abundance and then freeze out before the onset of leptogenesis. One example for such other processes that could help are gauge interactions mediated by a heavy Z' vector boson (cf. [85] and references therein). Thus, the standard choices for leptogenesis are to either assume a thermal or a vanishing initial abundance, so whether there are other processes than the inverse decays to create the thermal N_1 abundance or not. In the following, we will assume having a thermal initial abundance independent of the washout regime we are in, since the generated baryon asymmetry is always larger in this scenario and we want to investigate how low of a lightest RHN mass M_1 we can reach while still being able to explain the BAU. We will see that this choice is only relevant once we resort to the weak washout regime and $\Delta L = 2$ washout processes become important.

Aiming as a next and independent step for a DI-type bound, so an upper bound on solely the CP asymmetry, we can use the full expression of the CP asymmetry ε_1 to find that it does not depend on z_{23}. Furthermore, from an explicit parameter scan, we find that the optimal values of the CI parameters for NO are $z_{12} = 0$ and $z_{13_R} = \pm z_{13_I}$, with the relative sign of z_{13_I} determining the overall sign of the CP asymmetry. In the same way and for IO, we get on the other hand $z_{12_R} = \pi/2$, $z_{12_I} = 0$ and $z_{13_R} = \pi/2 \pm z_{13_I}$. Very similar to the two RHNs case, we find with the above determined CI parameters then a DI-type bound of

$$|\varepsilon_1| \lesssim \frac{3\pi}{4\lambda_5 v^2}\,\xi_3\,(m_h - m_l)\,M_1\,, \tag{2.29}$$

independent of the ordering and again including the additional factor of $(2\pi^2/\lambda_5)\xi_3$, which already appeared in the active neutrino mass matrix Eq. (2.8) and is specific to the scotogenic model.

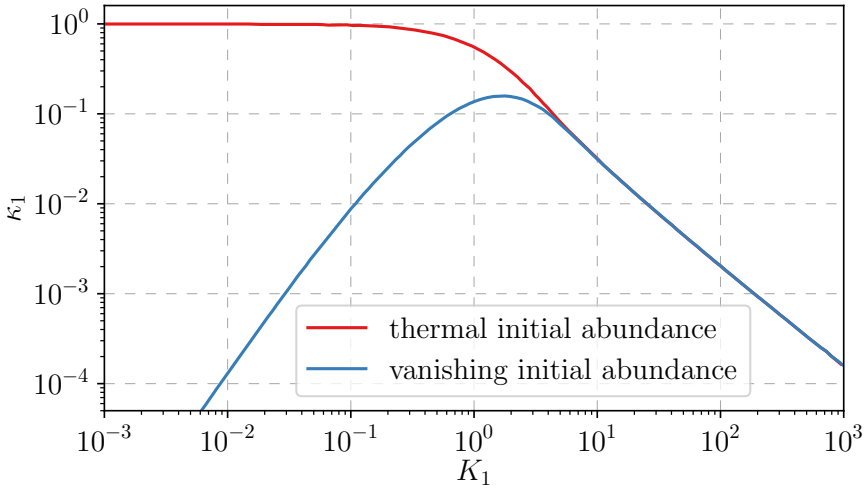

Figure 2.3.: Dependence of the efficiency κ_1 on the decay parameter K_1 as determined by [34] for the two options of a thermal initial abundance (red) and a vanishing initial abundance (blue) neglecting scattering effects. Note that for strong washout ($K_1 \gtrsim 4$) both curves are essentially identical as discussed in Sec. 2.5.

As an analytical solution including $\Delta L = 2$ washout is hard to come by, we will split our analysis of leptogenesis in the scotogenic model with three RHNs into two parts. First, we will analytically solve the case where the $\Delta L = 2$ washout is negligible and derive an estimate of when it becomes relevant. Second, we will use a full numerical analysis to confirm our results from the analytical calculation and also to extend them into the region where $\Delta L = 2$ washout is important.

2.5.1 Analytical Insights

To gain analytical insights into the scotogenic model with three RHNs in the case of negligible $\Delta L = 2$ washout, we can not derive a full analytic expression for the baryon-to-photon ratio η_B anymore and then maximize it (like we did in the two RHN scenario), because the analytic expression of the efficiency factor κ_1, Eq. (2.25), only holds in the strong washout regime. However, we can use that κ_1 is numerically known independent of the washout regime as a function of K_1, which will be very important for our new optimization strategy.

For optimizing the baryon-to-photon ratio $\eta_B = -C\varepsilon_1\kappa_1$ independent of the washout regime, we can use the freedom of the scalar coupling λ_5, together with the fact that there is a one-to-one correspondence between λ_5 and the decay parameter K_1 (cf. Eq. (2.24)). Assuming all parameters except for λ_5 to be fixed, the optimization of η_B reduces to determining the optimal value of λ_5, which we will call $\lambda_{5,\,\mathrm{opt}}$. As there is a one-to-one correspondence between λ_5 and K_1 this can also be seen as an optimization in K_1. To make this optimization explicit, we have to express the CP asymmetry ε_1, or its λ_5 dependence, in terms of K_1. Since we have $\varepsilon_1 \sim 1/\lambda_5$ (cf. Eq. (2.29), which also holds in the non-optimized case) and $K_1 \sim 1/\lambda_5$ (cf. Eq. (2.24)), we can conclude $\varepsilon_1 \sim K_1$ (in terms of λ_5) and thus $\eta_B \sim \kappa_1(K_1)\, K_1$, where we do not have to worry about the

precise prefactor at the moment. Hence, to maximize the baryon-to-photon ratio η_B, λ_5 (or correspondingly K_1) has to be chosen such that $\kappa_1(K_1)\, K_1$ becomes maximal. Using the numerical results for $\kappa_1(K_1)$ from [34] which are shown in Fig. 2.3, we find that the optimal value for thermal as well as for vanishing initial N_1 abundance are very similar and $K_{1,\,\mathrm{opt}} \approx 3$ suits both cases well. This value for K_1 corresponds to $\kappa_{1,\,\mathrm{opt}} \approx 0.15$ and thus leaves only ε_1 to be optimized over the CI parameters.

For the optimization of ε_1, we use $\lambda_{5,\,\mathrm{opt}}$ in the expression for ε_1 by recasting Eq. (2.24) as $\lambda_{5,\,\mathrm{opt}}(K_{1,\,\mathrm{opt}})$ before maximizing over the CI parameters. It turns out that the optimal CI parameters here are identical to the ones determined in the context of the DI-type bound, which are discussed above Eq. (2.29), with additionally z_{13_I} having an optimal value of $z_{13_I} \approx \sqrt{m_l/\,(2m_h)}$. One important realization to find this result is that we need $z_{13_I} \ll 1$ to get a small decay parameter K_1, which depends on z_{13_I} through $\widetilde{m}_{11}$ (cf. Eq. (2.24)), in addition to having a large CP asymmetry ε_1 at the same time. The same logic also enables us to intuitively understand why $z_{12} = 0$ (up to shifts of $\pi/2$ for IO) is optimal. For the CP asymmetry ε_1 the contribution from z_{12} is sub-dominant compared to the one of z_{13}, while any non-zero value of z_{12} would still increase the decay parameter K_1 in a non-negligible way.

Using the optimal values for the CI parameters, we can now determine a compact expression for the optimal value of λ_5, which is given by

$$\lambda_{5,\,\mathrm{opt}} \approx 4\pi\, \xi_1 \left(\frac{m_l}{10^{-3}\,\mathrm{eV}}\right) (1-\eta_1)^2\,. \tag{2.30}$$

With $\eta_1 \ll 1$ for a hierarchical mass spectrum and $\xi_1 \sim 1$, we rediscover our optimal solution for the strong washout regime, which we are in for $m_l > 10^{-3}\,\mathrm{eV}$, of $\lambda_{5,\,\mathrm{opt}} = 4\pi$ (cf. Sec. 2.4). Larger values for λ_5 might be desirable from an optimization point of view, but are not allowed as they would violate perturbativity.

For small active neutrino masses of $m_l < 10^{-3}\,\mathrm{eV}$ that enable us to reach regions below the strong washout regime, we get in combination with the experimental data from neutrino oscillation measurements of $m_h \gtrsim 5 \cdot 10^{-2}\,\mathrm{eV}$ [8] that $m_l \ll m_h$. Thus, we find for the upper limit of the baryon-to-photon ratio

$$\eta_B \lesssim 3 \cdot 10^{-21} \left(\frac{M_1}{\mathrm{GeV}}\right) \frac{\xi_3}{\xi_1} \frac{m_h}{m_l} \tag{2.31}$$

and therefore for the lower limit on the mass M_1

$$M_1^{\mathrm{min}} \approx \frac{\xi_1}{\xi_3} \frac{m_l}{m_h}\, 2 \cdot 10^{11}\,\mathrm{GeV}\,. \tag{2.32}$$

This formula holds for $m_l < 10^{-3}\,\mathrm{eV}$ down to masses of the lightest active neutrino for which $\Delta L = 2$ washout becomes important. As stated in Sec. 2.5, for $m_l > 10^{-3}\,\mathrm{eV}$ we are in the strong washout regime which leads to a limit of $M_1^{\mathrm{min}} \sim 10^{10}\,\mathrm{GeV}$.

Most notably, Eq. (2.32) clearly shows the importance of the mass of the lightest active neutrino and that it is possible to reach the correct BAU with smaller RHN masses than in standard leptogenesis. The reason why this is feasible is because the new parameter of the scotogenic model λ_5 enables us to tune the N_1 decay parameter to its sweet spot, $K_1 \to K_{1,\,\mathrm{opt}} \approx 3$, independently of the other parameters in the model. However,

this optimization method only works for $m_l < 10^{-3}\,\text{eV}$, since λ_5 has to stay within its perturbative limits. Additionally, it also increases the $\Delta L = 2$ washout [73], which becomes important for even lower lightest active neutrino masses. One last aspect we need to keep in mind is that making λ_5 smaller also increases the time it takes the RHNs N_1 to decay (cf. Eqs. (2.19, 2.20)). This will become important for the determination of an absolute lower limit on M_1, since the generation of the lepton asymmetry by the N_1 decays has to be finished before the $SU(2)$-sphalerons drop out of equilibrium, as the lepton asymmetry could otherwise not be converted into a baryon asymmetry.

Let us now turn to $\Delta L = 2$ washout processes and derive an estimate for when they become important. These processes are mediated by the RHNs and change the lepton number by two units, as their name suggests. In our case, the $\Delta L = 2$ processes are $\ell\eta \leftrightarrow \bar{\ell}\eta^*$ and $\ell\ell \leftrightarrow \eta^*\eta^*$ and involve the new scalar doublet η. To judge the strength of their contribution to the washout, we need to compute $\Gamma_{\Delta L=2}/(Hz_1)$, so their rate in comparison to Hz_1 (cf. discussion of the Boltzmann equations in Sec. 2.5.2). This can be done by taking the averaged matrix element squared from [34] and taking into account the modified CI parametrization of the Yukawa couplings as given by Eq. (2.10). Doing so, we find in similarity to [34] and [73]

$$\Delta W = \frac{\Gamma_{\Delta L=2}}{H\, z_1} = \frac{36\sqrt{5} M_{Pl}}{\sqrt{\pi} g_\ell \sqrt{g_*} v^4} \frac{1}{z_1^2} \frac{1}{\lambda_5^2} M_1 \overline{m}_\xi^2 \,, \tag{2.33}$$

where we for simplicity assumed $\eta_1 = m_\eta^2/M_1^2 \approx 0$ and $g_\ell = 2$ represents the number of internal degrees of freedom (dofs) per active neutrino ν_L^α or per charged lepton α_L. The effective mass parameter $\overline{m}_\xi$ is given by

$$\begin{aligned} \overline{m}_\xi^2 &\coloneqq \sum_{i,j} \xi_i \xi_j \,\text{Re}\Big[(R D_{\mathcal{M}_\nu} R^\dagger)_{ij}^2\Big] \\ &\approx 4\xi_1^2 m_l^2 + \xi_2^2 m_{h_2}^2 + \xi_3^2 m_h^2 \,, \end{aligned} \tag{2.34}$$

where the last line uses the previously determined optimal CI parameters. Our result for ΔW is identical to the one in [34][6], with the exception of an additional factor $(2\pi^2/\lambda_5)^2$ which is specific to the scotogenic model, and a slightly modified definition of the effective mass $\overline{m}_\xi$.

As a last step of preparation, we need to address the question how the additional washout due to $\Delta L = 2$ processes, ΔW, influences the efficiency parameter κ_1 of the whole evolution. To do so, we need to extract more knowledge from our optimal decay parameter $K_{1,\,\text{opt}} \approx 3$. As shown and numerically determined in [34], the decay parameter K_1 does not only quantify the efficiency κ_1 of the process, but also the time z_B from which on close to no additional asymmetry is generated and the asymmetry is predominantly washed out. For our optimal value of $K_{1,\,\text{opt}} \approx 3$, this translates into $z_B(K_1 \approx 3) \approx 3.5$. Another aspect which is helpful to us, is that one can assume for our case that the $\Delta L = 2$ washout becomes relevant at $z_{\Delta W} \gg 1$ [34]. In this case of $z_{\Delta W} \gtrsim z_B$, the washout contributions

[6] Note that in [34] the value $v = 174\,\text{GeV}$ is used whereas we use for the Higgs vev $v = 246\,\text{GeV}$.

can be separated and the total efficiency is given by [34]

$$\kappa_1^{\text{tot}} = \kappa_1 \, e^{-\int_{z_B}^{\infty} \mathrm{d}z \, \Delta W} \,. \tag{2.35}$$

This integral can be explicitly solved and by using Eq. (2.30) for λ_5 and Eq. (2.32) for M_1 we get

$$\int_{z_B}^{\infty} \mathrm{d}z \, \Delta W \approx \frac{9\sqrt{5} M_{Pl} \cdot 10^5 \, \text{GeV}}{7\pi^{\frac{5}{2}} g_l \sqrt{g_*} v^4} \frac{\text{eV}^2}{m_l m_h} \frac{1}{\xi_1 \xi_3} \, \overline{m}_\xi^2 \,. \tag{2.36}$$

To determine a value for m_l below which the $\Delta L = 2$ washout processes become important, we need to fix a numerical limit for the integral above which we call them important. In the following, we will do so when their influence on κ_1^{tot} is larger than 10%, corresponding to $\int_{z_B}^{\infty} \mathrm{d}z \, \Delta W > 0.1$. Using $\xi_i \sim 1$ as usual, we find that $\Delta L = 2$ washout processes become important below

$$m_l \lesssim 10^{-6} \, \text{eV} \,. \tag{2.37}$$

Thus, our analytic result for the minimal RHN mass M_1 to create the BAU via leptogenesis in Eq. (2.32) is valid in the range $10^{-6} \, \text{eV} \lesssim m_l \lesssim 10^{-3} \, \text{eV}$. We will verify this result in the next section with a numerical analysis and see that the validity of Eq. (2.32) even holds down to $m_l \lesssim 10^{-7} \, \text{eV}$. The reason is that in our derivation of the condition Eq. (2.37), we assumed the rigid relation of Eq. (2.30) between λ_5 and m_l, which is too restrictive below $m_l \sim 10^{-6} \, \text{eV}$ to achieve the optimal baryon-to-photon ratio η_B.

2.5.2 Numerical Insights

To verify and extend our results of Sec. 2.5.1, we perform a numerical analysis of leptogenesis in the scotogenic model with three RHNs. To do so, we work with the Boltzmann equations for N_1-dominated leptogenesis, where we include the effect of the $\Delta L = 2$ washout. A motivation of the Boltzmann equations together with the definitions of (and additional information on) the parameters we will be using throughout this section can be found in App. B.

Specifying Eqs. (B.57, B.54) to N_1 dominated leptogenesis with $\Delta L = 2$ washout, we find

$$\frac{\mathrm{d}N_{N_1}}{\mathrm{d}z_1} = -D_1 (N_{N_1} - N_{N_1}^{\text{eq}}) \tag{2.38a}$$

$$\frac{\mathrm{d}N_{B-L}}{\mathrm{d}z_1} = -\varepsilon_1 D_1 (N_{N_1} - N_{N_1}^{\text{eq}}) - W^{\text{tot}} N_{B-L} \,, \tag{2.38b}$$

with the z_1-dependent quantities

$$D_1 = K_1\, z_1\, \frac{\mathcal{K}_1(z_1)}{\mathcal{K}_2(z_1)}\,, \tag{2.39a}$$

$$W^{\text{tot}} = W_1 + \Delta W\,, \tag{2.39b}$$

$$W_1 = \frac{1}{4}\, K_1\, z_1^3\, \mathcal{K}_1(z_1)\,, \tag{2.39c}$$

$$N_{N_1}^{\text{eq}} = \frac{z_1^2}{2}\, \mathcal{K}_2(z_1)\,. \tag{2.39d}$$

For ε_1 and K_1 see Sec. 2.3, $\mathcal{K}_i(z_1)$ are the modified Bessel functions of the second kind and the contribution from $\Delta L = 2$ washout is included through ΔW as given by Eq. (2.33). From the final $B - L$ asymmetry N_{B-L}^f that is determined by the above Boltzmann equations, we can deduce the resulting baryon-to-photon ratio as $\eta_B = C N_{B-L}^f$. This is the same relation as Eq. (2.23), only that we directly find $N_{B-L}^f = -\varepsilon_1 \kappa_1$ from solving the Boltzmann equations. Being more precise than in the context of Eq. (2.23), the conversion factor C can be split into the sphaleron conversion factor C_{sph} and an entropy generation part as

$$C = \frac{3}{4} C_{\text{sph}} \frac{g_*^0}{g_*} \approx 0.0088\,, \tag{2.40}$$

with $C_{\text{sph}} = 8/23$ for two Higgs doublet models, $g_* = 116$ for three RHNs and $g_*^0 = 43/11$.

As we assumed for the Boltzmann equations that the η particles follow their equilibrium number density (cf. Eq. (B.18)), one might worry that they need to be modified due to the asymmetry induced by N_1 decays in the η-$\bar{\eta}$-sector. However, $\eta\eta \leftrightarrow HH$ interactions can effectively washout this asymmetry as long as they are strong enough (cf. [86]), which depends on the value of λ_5 (cf. Eq. (2.3)). For $\lambda_5 \gtrsim 10^{-4}$, which will turn out to be the relevant parameter range for us, this is the case.

The free parameters in our system of Boltzmann equations, Eq. (2.38), are the masses m_η, M_1, M_2, M_3 and m_l, the scalar couplings λ_3, λ_4 and λ_5 in addition to the generally complex CI parameters z_{12}, z_{13} and z_{23}. The masses of the other two active neutrinos are then fixed by the measured mass squared differences from neutrino oscillations in combination with the choice of an ordering (NO or IO), while m_η, together with the scalar couplings, determines the scalar masses via Eq. (2.4). Although this might seem like a large number of free parameters, we can fix most of them due to the analytical insights we gained and the hierarchical mass spectrum we are considering. Since we have N_1 dominated leptogenesis in a hierarchical mass spectrum, the masses of M_2 and M_3 only have a minor influence on leptogenesis and to be hierarchical we explicitly set $M_2 = 10^{0.5} M_1$ and $M_3 = 10^1 M_1$. Furthermore, the mass of the lightest scalar m_{η_I} has to fulfill Eq. (2.5) for it to be able to constitute DM, while we also want $m_\eta \ll M_1$ to be in the hierarchical regime. In this mass region, we can find from the formula for scalar masses, Eq. (2.4), that for scalar couplings of order one, m_η is the dominant contribution. Thus, we choose $m_\eta = 550\,\text{GeV}$, which ensures to stay in the range of Eq. (2.5) while being as hierarchical as possible. The scalar couplings then have only a small influence on the scalar masses and can be set to $\lambda_3 = 1$ and $\lambda_4 = -1$. On the other hand, λ_5 is very

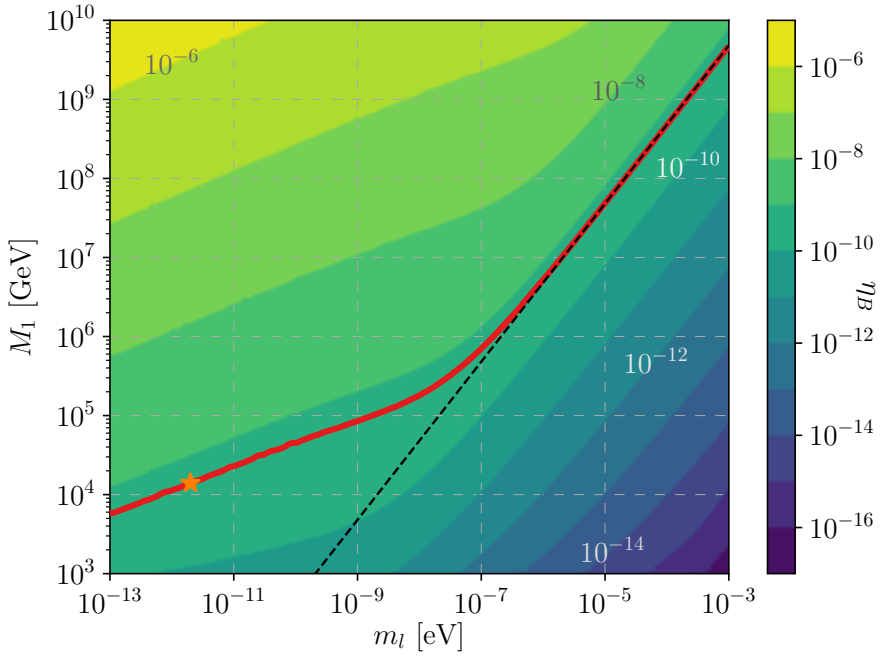

Figure 2.4.: Results for the baryon-to-photon ratio η_B maximized over $\lambda_5 \in [10^{-6}, 4\pi]$ shown as contours for the parameter scan in the m_l–M_1–plane, with $m_\eta = 550\,\text{GeV}$, $\lambda_3 = 1$, $\lambda_4 = -1$, $M_2 = 10^{0.5} M_1$, $M_3 = 10^{1} M_1$, $z_{12} = 0$, $z_{13_R} = \sqrt{m_l/(2m_h)} = z_{13_I}$, $z_{23} = 0$ and for NO. The red line highlights the minimal values of M_1 necessary to achieve the BAU, $\eta_B^{\text{obs}} \approx 6.1 \cdot 10^{-10}$, whereas the black dashed line shows the analytical result of Eq. (2.31) with $\xi_1/\xi_3 \approx 1.2$ that is valid for $m_l \gtrsim 10^{-6}\,\text{eV}$ (cf. Eq. (2.37)). The orange star denotes the last point on the red curve at which the baryon asymmetry is generated before the $SU(2)$-sphalerons fall out of equilibrium, so the smallest possible M_1.

important for the process of leptogenesis and will therefore be a free parameter in our scan. As we are interested in the lowest possible M_1 to achieve leptogenesis and know from our analytical investigation that m_l has a large influence on the generated baryon asymmetry, these two parameters will span our parameter plane.

The only parameters not accounted for in the above discussion are the CI parameters. For them, however, we found in Sec. 2.5.1 optimal values that are valid down to at least $m_l \sim 10^{-6}\,\text{eV}$. Therefore, we will in a first step assume that these optimal values hold for our entire parameter space and in a second step then explicitly check that this assumption is true for several points in the m_l–M_1–plane that produce the correct baryon asymmetry. Thus, the explicit check in the second step also validates our analytical results of Sec. 2.5.1 on the CI parameters.

Numerically solving the Boltzmann equations, Eq. (2.38), and optimizing over λ_5, we find for the maximally possible baryon-to-photon ratio the results depicted in Fig. 2.4. The numerical results show very clearly the importance of the smallest active neutrino mass m_l for leptogenesis, as well as the fact that our analytical expressions, Eqs. (2.31, 2.32), are able to accurately describe the upper limit on the baryon asymmetry, or, correspondingly,

the lower limit on the lightest RHN mass M_1 for $10^{-6}\,\text{eV} \lesssim m_l \lesssim 10^{-3}\,\text{eV}$. Note that, as Fig. 2.4 shows the maximally possible η_B, any parameter point with $\eta_B > \eta_B^{\text{obs}}$ (above the red line) is also viable to achieve the BAU, since a lower baryon asymmetry can always be realized by choosing other than the optimal values for λ_5 and the CI parameters. Furthermore, as commented on in Sec. 2.5, there is no significant difference between NO and IO for the three RHNs case, so our results do not depend on the choice of the ordering.

With the numerical results at hand we can also determine an approximate formula for the maximally possible baryon-to-photon ratio in the region where $\Delta L = 2$ washout is important, for which we find by fitting

$$\eta_B \lesssim 1.6 \cdot 10^{-14} \left(\frac{m_l}{\text{eV}}\right)^{-0.19} \left(\frac{M_1}{\text{GeV}}\right)^{0.58} . \tag{2.41}$$

This can be compared to Eq. (2.31) for the region with a negligible influence of $\Delta L = 2$ washout. As both the exponents of m_l and M_1 are closer to zero in the region with $\Delta L = 2$ washout, we observe that both variables have a comparably smaller influence on leptogenesis. This is reflected in Fig. 2.4 by a bigger spacing between the contours in the left part of the plot, where $\Delta L = 2$ washout is important, compared to the right part.

To verify our analysis of λ_5 and the optimal CI parameters for $m_l \gtrsim 10^{-6}\,\text{eV}$ and to justify our assumption that the optimal CI parameters do not change for smaller values of m_l, we choose specific points in the m_l–M_1–plane that correctly reproduce η_B^{obs} and perform a complete scan over all CI parameters and λ_5 for them. These scans do not point out a possibility to significantly improve η_B by varying the CI parameters or λ_5, thus verifying our analytical analysis and justifying the assumption on the optimal CI parameters. In the region where $\Delta L = 2$ washout is important, the scans point out that small improvements in η_B are possible, however, these improvements are not bigger than the systematic uncertainties of our simplified approach in which we focus on the most important effects (cf. the corresponding discussion in Sec. 2.3).

To gain a deeper understanding of the parameter dependencies, we depict in Fig. 2.5 the dependence of the decay parameter K_1 and the scalar coupling λ_5 on the RHN mass M_1 and lightest active neutrino mass m_l to get the correct baryon-to-photon ratio η_B in the optimal case (cf. red line in Fig. 2.4). We can see from Fig. 2.5 the clear transition between the regime in which $\Delta L = 2$ washout is negligible to when they become important as a kink in the decay parameter K_1. For negligible $\Delta L = 2$ washout, the optimal decay parameter has a constant value of $K_1 \approx 1.5$, whereas otherwise we need to resort to the weak washout regime $K_1 \lesssim 1$. The reason that the constant value of $K_1 \approx 1.5$ differs from $K_{1,\text{opt}} \approx 3$, as used in the analytical calculation of Sec. 2.5.1, is that $K_{1,\text{opt}} \approx 3$ enables us to get a reasonably accurate expression for η_B both for thermal and vanishing initial N_1 abundance. In addition, we can from the right plot of Fig. 2.5 also see the "less rigid relation" between λ_5 and m_l mentioned at the end of Sec. 2.5.1. While λ_5 follows a linear relation with m_l down to approximately $m_l \approx 10^{-6}\,\text{eV}$, it deviates from this relation for smaller active neutrino masses when $\Delta L = 2$ washout becomes important, enabling the baryon-to-photon ratio η_B to be well approximated by the analytical expression of Eq. (2.31) even down to $m_l \sim 10^{-7}\,\text{eV}$.

As apparent from Fig. 2.5, especially for small values of M_1 and m_l we also need small values of λ_5 to realize leptogenesis. Therefore, we need to check whether these small values

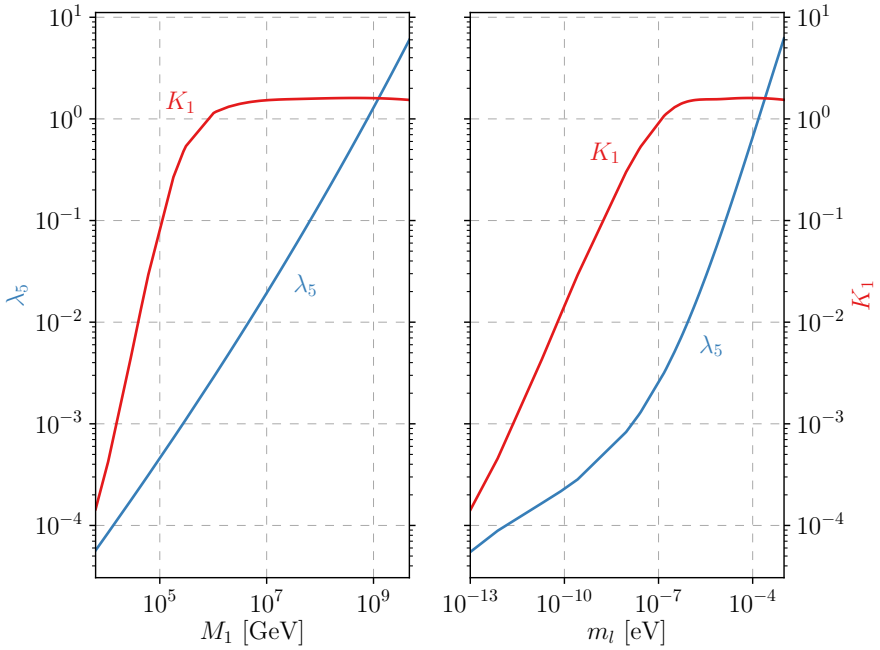

Figure 2.5.: Dependence of the optimal decay parameter K_1 and scalar coupling λ_5 on the RHN mass M_1 and lightest active neutrino mass m_l to achieve η_B^{obs} with the smallest RHN mass M_1 possible (cf. red line in Fig. 2.4). The underlying scan with the specification of all parameters can be found in Fig. 2.4.

of λ_5 are compatible with the limits from direct detection experiments due to inelastic scattering. This process is governed by the value of λ_5, since it defines the mass splitting between m_{η_R} and m_{η_I} (cf. Eqs. (2.4)), thereby determining how efficiently $\eta_{R/I}$ can scatter off a nucleus via Z boson exchange. With the expression for the limit of direct detection via inelastic scattering from [71] and the experimental data from XENON100 [87], we find a limit of $\lambda_5 \gtrsim 3 \cdot 10^{-6}$. Since this is smaller than the lowest value of $\lambda_5 \gtrsim 5 \cdot 10^{-5}$ appearing in Fig. 2.5, we are not restricted due to this bound from direct detection experiments.

In addition to demonstrating the crucial influence of the lightest active neutrino mass m_l on the baryon-to-photon ratio η_B as well as the very good agreement between our analytical and numerical results, Fig. 2.4 also shows that even in the regime in which $\Delta L = 2$ washout is important, the minimal necessary RHN mass M_1^{min} still decreases with m_l, which might come as a surprise. Although an analytical understanding of the region in which $\Delta L = 2$ washout is important (below $m_l \lesssim 10^{-7}\,\text{eV}$) is hard to come by, we can at least get an intuition for why M_1^{min} still decreases with m_l and determine an absolute lower bound on M_1^{min}. To do so, the relevant aspect is that small active neutrino masses are achieved in our model by a suppression of the N_1 Yukawa couplings. This implies that on the other hand also the N_1 decay width decreases (cf. Eq. (2.19)) and therefore its lifetime increases. The later decay of the RHNs N_1 thus leads to a partial circumvention of the $\Delta L = 2$ washout, which enables M_1^{min} to further decreases with m_l.

However, there is a limit to how much the N_1 decay can be delayed, because for leptogenesis to work the generated lepton asymmetry has to be converted into a baryon

asymmetry by $SU(2)$-sphaleron processes. As the $SU(2)$-sphalerons drop out of equilibrium around $T_{\text{sph}} \approx 130\,\text{GeV}$ [88], any later injection of lepton asymmetry by N_1 decays would remain solely in the lepton sector. Thus, we demand that the generation of the baryon asymmetry ends before $z_{B,\,\text{sph}} = M_1/T_{\text{sph}}$. Solving the Boltzmann equations several times for different but small m_l, with the corresponding optimal value of $\lambda_5 \sim 10^{-4}$, to determine the relation of z_B and m_l, we find approximately $z_B \approx 3.0 \cdot 10^{-5} (m_l/\text{eV})^{-0.56}$ and a fit to the small m_l region of Fig. 2.4 provides $M_1^{\text{min}} \approx 4.6 \cdot 10^7\,(m_l/\text{eV})^{0.30}$ GeV. Combining both fits with the constraint $z_B < z_{B,\,\text{sph}}$, we get in a first step $m_l \gtrsim 2 \cdot 10^{-12}\,\text{eV}$ and finally

$$M_1^{\text{min}} \sim 10^4\,\text{GeV}\,. \tag{2.42}$$

This is main result of this chapter, since it demonstrates that within the scotogenic model with three RHNs it is possible to realize leptogenesis for masses of the lightest RHN as low as $M_1 \sim 10\,\text{TeV}$.

One example for a complete set of parameters making this possible can be found in the description of Fig. 2.4 or our corresponding discussion above. Noticeably, creating the BAU via leptogenesis with a small mass of the lightest RHN N_1 requires an extremely light lightest active neutrino with a mass of $\sim 10^{-12}\,\text{eV}$. To get an impression of how the Yukawa matrix looks like for this case, we can determine it via the CI parametrization, cf. Eq. (2.10). To do so, we also need the PMNS matrix for which we use the best-fit PDG16 values [8] and set the Majorana phases to zero. In this way, we explicitly find

$$h = \begin{pmatrix} 1 \cdot 10^{-8} + 2 \cdot 10^{-9}\,i & 8 \cdot 10^{-4} + 0 \cdot i & -4 \cdot 10^{-4} + 7 \cdot 10^{-4}\,i \\ 1 \cdot 10^{-9} - 6 \cdot 10^{-9}\,i & 9 \cdot 10^{-4} + 7 \cdot 10^{-5}\,i & 4 \cdot 10^{-3} + 3 \cdot 10^{-15}\,i \\ 1 \cdot 10^{-8} - 6 \cdot 10^{-9}\,i & -7 \cdot 10^{-4} + 8 \cdot 10^{-5}\,i & 4 \cdot 10^{-3} + 1 \cdot 10^{-13}\,i \end{pmatrix}. \tag{2.43}$$

Since the above Yukawa matrix looks perfectly natural[7] we conclude that no particular tuning of parameters seems necessary to generate the BAU. The physical assumption which is represented by this Yukawa matrix is that the N_1 Yukawa couplings must be suppressed compared to those of the $N_{2,3}$ neutrinos, which we touched on in our discussion of the optimal CI parameters in Sec. 2.5.1. Essentially, this ties back to the Sakharov conditions we discussed in Sec. 2.1, as the small values of $h_{1\alpha} \ll 1$ ensure that the N_1 decays occur sufficiently out-of-equilibrium, while a sufficiently large CP-asymmetry is achieved by sizable $h_{2/3\,\alpha}$. Qualitatively similar observations can also be found in Ref. [52].

Compared to the charged-lepton Yukawa matrix, the hierarchies among the different entries of our neutrino Yukawa matrix in Eq. (2.43) are not much larger and the small absolute values can be seen as technically natural due to the global $U(1)$ symmetry which emerges as $h \to 0$. As the running of the Yukawa couplings is proportional to the Yukawa couplings themselves, the small absolute values are also stable against quantum corrections. Furthermore, we note that the optimization of the CI parameters is rather a technical trick than a fine-tuning of model parameters, as it should only be considered fine-tuning if the corresponding physical quantities like the Yukawa couplings show signs of fine-tuning.

The necessary small masses of the lightest active neutrino for low-scale leptogenesis

[7] The smallness of some of the imaginary parts is due to our choice of $z_{23} = 0$ and not necessary for successful leptogenesis.

($m_l \sim 10^{-12}\,\text{eV}$) are an interesting aspect of the model that makes this region of parameter space accessible to experiments, both earth bound and astrophysical. For example the tritium beta decay experiment KATRIN [89] is performing (cf. [90]) a direct measurement of the mass of the electron neutrino, $m_{\nu_e}^2 \coloneqq \sum_i |U_{ei}|^2\, m_i^2$. If their future measurements find evidence for a lightest active neutrino mass close to its design sensitivity, $m_l \sim 0.2\,\text{eV}$, this would falsify low-scale leptogenesis in the scotogenic model. On the other hand, astrophysical measurements like for example power spectrum data from galaxy surveys can be used to determine (an upper limit of) the sum of neutrino masses [91]. If any sum of neutrino masses above the minimal possible value determined from neutrino oscillation measurements (for NO or IO) is detected, this would imply $m_l \gg 10^{-12}\,\text{eV}$ and therefore also falsify low-scale leptogenesis in the scotogenic model.

2.6 Summary

In our above analysis of leptogenesis in the scotogenic model, which is the simplest model of radiative neutrino masses and also offers a candidate for DM, we demonstrated that it allows for the accommodation of low-scale leptogenesis in a hierarchical mass spectrum. To do so, we distinguished between the cases of two and three RHNs and derived in both cases a DI-type bound for the CP asymmetry. For two RHNs, we showed that leptogenesis inevitably occurs in the strong washout regime and consequently this scenario behaves similarly to standard leptogenesis in the type-I seesaw model. We argued that this follows from the fact that all new prefactors in the scotogenic model essentially cancel. Thus, for a normal ordering of SM neutrino masses (NO), the lightest RHN must have a mass of at least $M_1^{\text{min}} \sim 10^{10}\,\text{GeV}$, while for inverted ordering (IO), it must have a mass of at least $M_1^{\text{min}} \sim 10^{12}\,\text{GeV}$.

For three RHNs, the difference between normal and inverted hierarchy is negligible, as only the mass difference between the heaviest and lightest active neutrino matters, and the weak washout regime becomes accessible. We found that the minimal mass of the lightest RHN to realize the BAU strongly depends on the mass of the lightest active neutrino m_l. For $m_l \gtrsim 10^{-7\cdots-6}\,\text{eV}$, the effect of $\Delta L = 2$ washout is negligible and M_1^{min} is directly proportional to m_l, whereas for smaller values of m_l the $\Delta L = 2$ washout becomes important. Even in this regime, M_1^{min} can still be lowered by delaying the decay of the N_1 RHNs through suppressed N_1 Yukawa couplings. Due to the delay, the lepton asymmetry is generated later in time and therefore part of the washout is circumvented. However, this mechanism is limited by the fact that leptogenesis has to be completed before the $SU(2)$-sphalerons drop out of equilibrium, as they convert the generated lepton into a baryon asymmetry. Thus, we finally got an absolute lower limit on the mass of the lightest RHN of $M_1^{\text{min}} \sim 10^4\,\text{GeV}$. Comparing this to the lower limit from standard leptogenesis of $M_1^{\text{min}} \sim 10^9\,\text{GeV}$, we can conclude that the scotogenic model allows for leptogenesis significantly closer to experimentally accessible scales than the standard scenario. It is important to note that we used a hierarchical mass spectrum, so the lower scale of leptogenesis is not related to any kind of mass degeneracy.

An additional interesting aspect of our scenario is that successful low-scale leptogenesis for $M_1 \sim 10^4\,\text{GeV}$ requires very small masses of the lightest active neutrino of around $m_l \sim 10^{-12}\,\text{eV}$. This makes the intriguing scenario of low-scale leptogenesis in the

scotogenic model accessible to next generation experiments that aim at measuring the absolute neutrino mass scale. As the sensitivities of these experiments are of the order of $m_l \sim 10^{-2\cdots-1}\,\mathrm{eV}$, any measurement of the lightest active neutrino mass that is not compatible with zero would falsify low-scale leptogenesis in the scotogenic model.

In our analysis we focused on the most important effects for the generation – and the washout – of a lepton asymmetry: decays and inverse decays of RHNs as well as $\Delta L = 2$ washout processes. Therefore, we were able to perform most of our calculations analytically and gain insights into how the different parameters are intertwined. For future work, it will be interesting to refine the results of our analysis by incorporating several effects that were neglected in this paper. This includes mainly flavor effects and a more careful treatment of possible kinematic effects in the regime of large η masses, $m_\eta \sim M_1$. Such a refined analysis might disclose the remaining optimization potential to further lower the bound on M_1 by a factor of ~ 1 to ~ 10, similar to standard leptogenesis. The central finding of our analysis should however be unchanged: It is possible to realize low-scale leptogenesis in the scotogenic model of radiative neutrino masses without any degeneracy in the mass spectrum of the RHNs. As we will see in the next chapter, the scotogenic model is not the only model that permits such a realization of low-scale leptogenesis.

Chapter 3

Singlet Scalar Assisted Leptogenesis

In our investigation of models that allow for a low-scale explanation of the BAU, we found in the last chapter that the scotogenic model of radiative neutrino masses is able to accommodate low-scale leptogenesis even without a nearly degenerate mass spectrum. In this chapter, we will direct our attention to another model which does provide the possibility of low-scale leptogenesis. Instead of extending the Higgs sector by a new (dark) Higgs doublet like in the scotogenic model, we will add a real scalar singlet to it and therefore analyze low-scale leptogenesis assisted by a real scalar singlet. Note that the results displayed in this chapter are based on work published as Ref. [92].

The challenge to explain the BAU and the attractiveness to use leptogenesis to do so, which are both laid out in Sec. 2.1, remain for the singlet scalar assisted model the same as for the scotogenic model. Thus, we will be guided by the same principles also in this chapter: the experimental inaccessibility of high-scale leptogenesis drives us to look for options to realize the same mechanism at substantially lower scales, while we still do not want to rely on a nearly degenerate mass spectrum of the RHNs to do so.

In general, adding a scalar to the Higgs sector allows for leptogenesis to happen at significantly lower scales [93, 94] and we will demonstrate that in the simplest case of a real scalar singlet the BAU can be generated via leptogenesis even for RHN masses below the TeV scale. It turns out that even though the extension of the Higgs sector is simpler than in the scotogenic model of Ch. 2, the situation is analytically less accessible and we will need to rely more on numerical and semi-analytical analyses. Nevertheless, our analyses will equally well enable us to identify viable parameter regions that can be probed in on-going and future experiments.

The existence of an additional real scalar singlet is well motivated and appears oftentimes in more fundamental models. If the scalar S is stable, it represents for example a viable and simple DM candidate [95–98]. Alternatively, S can be identified with the inflaton field that drives inflation in the early universe [99–102] (see also Ref. [103]). Furthermore, it is possible to associate the field S with the dynamics of electroweak (EW) symmetry breaking. In particular, the EW phase transition can be turned into a strong first-order one [104–109], which has received a lot of attention in the literature. Similarly, in models in which the SM Higgs potential originates from a spontaneously broken approximate global

symmetry, the field S might correspond to a pseudo-Nambu-Goldstone boson (pNGB). In Ref. [110], it was shown that it is possible to connect low-scale leptogenesis to EW symmetry breaking and Goldstone-Higgs models, by coupling such a pNGB singlet to RHNs. From a theoretical standpoint, the singlet S can allow to ensure the absolute stability of the EW vacuum, as opposed to the meta-stability of the EW vacuum in the SM [111, 112]. Finally, the real scalar singlet extension of the SM represents an important experimental benchmark scenario for new physics searches at present and future colliders [113–119].

Despite this broad spectrum of theories in which an additional real scalar appears, it is sufficient for our purposes to view the field S as a low-energy effective description of some unknown ultraviolet (UV)-complete model. Thus, our analysis is not specific to a single model, but applies to all UV-complete models that are described by the same low-energy effective Lagrangian (cf. Eq. (3.3)). As we will see, the reason that adding a real scalar singlet to the model changes the picture of leptogenesis is due to its allowed coupling to the RHNs $\mathcal{L} \supset SNN$. This operator is renormalizable and trivially invariant under all SM gauge symmetries. Since it breaks the accidental global lepton number symmetry of the SM in the same way as the RHN Majorana mass term, we will assume that both of these couplings are present in our model. The only additionally allowed couplings of the real scalar singlet with the SM are through the Higgs potential, as all others are forbidden by gauge invariance.

Similarly to Ch. 2, we will focus on the most important aspects and neglect possible corrections to our calculation from thermal corrections, flavor effects and quantum kinetic effects (cf. Sec. 2.3). Furthermore, we can consider the minimal case of two RHNs $N_{1,2}$ and one real scalar S, to simplify the analysis while still capturing all relevant effects. At tree level, the presence of a light scalar S then leads to a new N_2 decay channel, $N_2 \to N_1 S$, which causes the N_2 number density to depart more strongly from its would-be value in thermal equilibrium. At the same time, the new N_2 decay channel also increases the amount of CP violation in N_2 decays at loop level. Together, these two effects enhance the efficiency of leptogenesis, such that the BAU can be successfully generated in N_2 decays for RHN masses even below the TeV scale. The general principle behind this mechanism has been described for the first time by Le Dall and Ritz [94].[1]

For our analysis, we build upon and extend this earlier work in two main ways. First, we perform a systematic scan of parameter space that allows us to determine the dependence of the final asymmetry on the choice of parameter values in the neutrino sector. Explicitly, we derive a semi-analytical fit function, allowing us to reproduce the exact numerical result with high precision (cf. Eqs. (3.23, 3.24)). Second, we ensure that our parameter values are consistent with the experimental data on neutrino oscillations by employing a CI parametrization [66], as also done in Ch. 2.

3.1 Couplings and Masses in the Real Singlet Scalar Model

For the real singlet scalar model we want to analyze, we have to take into account that the new field S can in principle have a non-zero vev. This is different to the additional

[1] The first discussion of N_2-dominated leptogenesis in the standard (type-I seesaw) leptogenesis scenario can be found in Ref. [120].

Higgs doublet η in the scotogenic model, since there a vev was prohibited by the imposed $\mathbb{Z}_2$ symmetry (cf. Ch. 2). Thus, the relevant quantities for leptogenesis can be different to the Lagrangian parameters above the scalar phase transition where all vevs are still zero. As we will focus on low-scale leptogenesis scenarios, the energy scale at which leptogenesis happens is going to be close to the EW phase transition[2] and therefore we will assume that leptogenesis happens between the temperature at which the singlet scalar field obtains its vev T_S and the temperature of the EW phase transition T_{ew}. Since we do not want these different processes to directly affect each other, we have to ensure $T_S \gg T_{\text{ew}}$.

Denoting the quantities for temperatures above T_S with a tilde, we get for the Lagrangian the standard type-I seesaw terms augmented by the interactions of the real scalar $\widetilde{S}$

$$-\mathcal{L} \supset \left[\widetilde{h}_{\alpha i}\,\ell_\alpha \widetilde{N}_i H + \frac{1}{2}\left(\widetilde{M}_{ij} + \widetilde{\alpha}_{ij}\widetilde{S}\right)\widetilde{N}_i \widetilde{N}_j + \text{h.c.}\right] + V\big(H, \widetilde{S}\big)\,, \tag{3.1}$$

where $i, j = 1, 2$ enumerates the RHNs and $\alpha = e, \mu, \tau$ the flavors. The fields $H = \big(H^+, H^0\big)^T$ and $\ell_\alpha = (\nu_\alpha, \alpha_L)^T$ correspond to the SM Higgs doublet and the three SM left-handed charged lepton doublets, respectively. We denote the usual RHN-lepton-Higgs Yukawa matrix by $\widetilde{h}$, $\widetilde{M}$ is the matrix of high scale RHN masses whose dynamical origin is left unspecified for the purposes of this work and $\widetilde{\alpha}$ characterizes the strength of the novel singlet-RHN Yukawa interactions.

The scalar potential $V\big(H, \widetilde{S}\big)$ can be separated into two parts, namely the part V_{even} containing all terms that are even with regard to $\widetilde{S}$ and the part V_{odd} with all correspondingly odd terms. Explicitly, we have $V\big(H, \widetilde{S}\big) = V_{\text{even}} + V_{\text{odd}}$, with

$$\begin{aligned} V_{\text{even}}\big(H, \widetilde{S}\big) &= \widetilde{m}_H^2\,|H|^2 + \frac{1}{2}\,\widetilde{m}_S^2\,\widetilde{S}^2 + \lambda_H\,|H|^4 + \frac{1}{2}\,\lambda_{SH}\,\widetilde{S}^2\,|H|^2 + \frac{1}{4}\,\lambda_S\,\widetilde{S}^4\,, \\ V_{\text{odd}}\big(H, \widetilde{S}\big) &= \widetilde{c}_S\,\widetilde{S} + \widetilde{\mu}_{SH}\,\widetilde{S}\,|H|^2 + \frac{1}{3}\,\widetilde{\mu}_S\,\widetilde{S}^3\,. \end{aligned} \tag{3.2}$$

It will turn out that the overall shape of the scalar potential is not crucial to successfully realize leptogenesis, with the exception of the trilinear coupling between the scalar and two SM Higgs fields. This trilinear coupling can in general appear from two different terms in the potential for the period of leptogenesis. Either due to the $\widetilde{\mu}_{SH}\,\widetilde{S}\,|H|^2$ term that is present already at high temperatures, or from the quartic term $\frac{1}{2}\,\lambda_{SH}\,\widetilde{S}^2\,|H|^2$ after the scalar gets a vev (cf. Eq. (3.2) and definition of the shifted scalar above Eq. (3.3)). The second option leads to a trilinear coupling even if there is a $\mathbb{Z}_2$ symmetry $\widetilde{S} \to -\widetilde{S}$. For the rest of our analysis we will assume this $\mathbb{Z}_2$ symmetry at high energies, since it decreases the number of free parameters in the scalar potential while not restricting the generality of our results. Thus, all terms of V_{odd} are not present in our scalar potential. As only the value of the trilinear coupling during the time of leptogenesis is relevant for our analysis, we are indifferent to how this value was generated from a potential at higher temperatures. However, since the coupling of the scalar to the RHNs explicitly breaks this $\mathbb{Z}_2$ symmetry, it can only be an approximate symmetry of our theory. On the other hand, this also provides us with some intuition regarding the size of the corresponding couplings $\widetilde{\alpha}$, as small values of $\widetilde{\alpha}$ are hence technically natural in the sense of 't Hooft [65].

[2] Strictly speaking the EW phase transition is a cross-over with a critical temperature of $T_c \approx 159\,\text{GeV}$ [88].

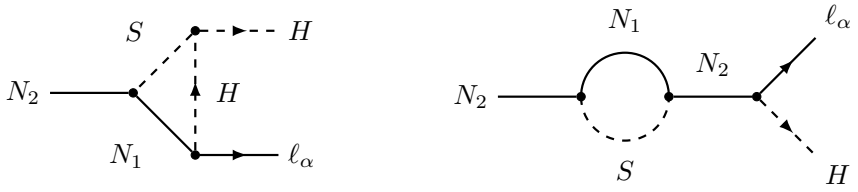

Figure 3.1.: Feynman diagrams for the decay $N_2 \to \ell_\alpha H$ that are mediated by the singlet scalar S and thereby enhance the CP asymmetry. The vertex correction to the left relies on the trilinear coupling $\mu\, S\, |H|^2$ together with the additional $\alpha_{12}\, S N_1 N_2$ interaction of the singlet scalar that is also crucial for the self-energy contribution to the right.

After the scalar phase transition at T_S, which breaks the $\mathbb{Z}_2$ symmetry, we assume that the scalar obtains a non-zero vev v_S. We thus define the shifted scalar S by $\widetilde{S} \to v_S + S$ and also diagonalize the RHN mass matrix for our calculations. This transforms the high temperature Lagrangian of Eq. (3.1) into the relevant one for leptogenesis

$$-\mathcal{L} \supset \left[h_{\alpha i}\, \ell_\alpha N_i H + \frac{1}{2} \left(\delta_{ij}\, M_j + \alpha_{ij}\, S\right) N_i N_j + \text{h.c.} \right] + V(H, S) \ , \tag{3.3}$$

where we dropped all tildes to indicate that it is valid after the scalar phase transition. As described before, the relevant part for leptogenesis of the scalar potential is the trilinear coupling

$$V(H, S) \supset \mu\, S\, |H|^2 \ , \tag{3.4}$$

where we suppressed the indices of the coupling strength μ_{SH} to simplify the notation. Note that the scalar S will only be able to modify the dynamics of leptogenesis if the diagonalization of the RHN mass matrix does not simultaneously also diagonalize α. If it would, the interactions of S with the RHNs would not induce any CP violation, because the off-diagonal coupling α_{12} would be zero. Diagrammatically, this can be seen from the Feynman diagrams shown in Fig. 3.1 that depict the additional possibilities to generate a CP asymmetry in the real singlet scalar model via the trilinear coupling and interactions parameterized by α. The standard diagrams to generate a CP asymmetry can be found from Fig. 2.1 by replacing the scotogenic model specific Higgs doublet η by the SM Higgs doublet H.

To connect the parameters of leptogenesis to the quantities that can be determined from current experiments, we have to keep in mind that the vev of the scalar v_S can receive corrections during the EW phase transition. This would make another shift of the scalar necessary, which implicitly defines the low-energy scalar s via $S \to v_S^0 - v_S + s$, in combination with another diagonalization of the RHN mass matrix. However, these corrections to v_S during the EW phase transition are related to α_{ij} and therefore small in our scenario, so we can safely neglect them for the analysis of leptogenesis. Nevertheless using a zero to indicate low-energy quantities valid today, we get after EW symmetry

breaking the low-energy Lagrangian of

$$-\mathcal{L} \supset \left[\frac{h^0_{\alpha i}}{\sqrt{2}}\,\nu_\alpha N^0_i h + \frac{1}{2}\left(\delta_{ij}\,M^0_j + \alpha^0_{ij}\,s\right) N^0_i N^0_j + \text{h.c.}\right] + V\left(h, s\right)\,, \tag{3.5}$$

where h denotes the physical SM Higgs boson with a mass of 125 GeV.

Similarly to what we did for the scotogenic model in Ch. 2, we can, by starting from the Lagrangian of Eq. (3.5), find a description of the active neutrino mass matrix m_ν and finally use a CI parametrization to express the Yukawa couplings h^0 in terms of measured quantities and free variables. The first step is, following along the lines of the type-I seesaw mechanism [26–30], to block-diagonalize the full neutrino mass matrix implicit in the Lagrangian of Eq. (3.5). In this way, we find the standard type-I seesaw formula

$$m_\nu = -m_D\, D_N^{-1}\, m_D^T\,, \tag{3.6}$$

where $m_D = h^0/\sqrt{2}\,v_{\text{ew}}$ is the active neutrino Dirac mass matrix and the diagonal RHN mass matrix is denoted by $D_N = \text{diag}\left(M^0_1, M^0_2\right)$. This mass matrix for the active neutrinos m_ν can be diagonalized in general by a matrix U via $D_\nu = U^T\, m_\nu\, U$, where U is the PMNS matrix [67, 68] if one is in the charged lepton flavor basis. Reshuffling terms and introducing the CI parametrization [66] through the 3×2 matrix R then allows us to express the Yukawa couplings as

$$\frac{h^0}{\sqrt{2}} = \frac{i}{v_{\text{ew}}}\, U^* D_\nu^{1/2} R\, D_N^{1/2}\,. \tag{3.7}$$

As in Sec. 2.4, the CI parametrization depends on one complex rotation angle z and satisfies $R^T R = \mathbb{1}$.

Since we will neglect flavor effects, the important quantity for leptogenesis is going to be $h^\dagger h \approx h^{0\dagger} h^0$ (cf. Ch. 2), which in this case is given by

$$\frac{h^{0\dagger} h^0}{2} = \frac{1}{v^2_{\text{ew}}}\, D_N^{1/2} R^\dagger D_\nu R\, D_N^{1/2} \tag{3.8}$$

and independent of the PMNS matrix. The right-hand side of Eq. (3.8) depends on the experimentally measurable quantities $v_{\text{ew}} = 246\,\text{GeV}$ together with the active neutrino mass squared differences Δm^2_{sol} and Δm^2_{atm}, for which we will take the values from the NuFIT global-fit analysis of [121]. In addition, it also depends on the RHN masses $M^0_1 \approx M_1$ and $M^0_2 \approx M_2$ as well as the CI parameter z, which we will treat as free input parameters.

3.2 CP Asymmetry Generation

The origin of the CP asymmetry in the real singlet scalar model are the CP violating decays of the RHNs $N_i \to \ell_\alpha H$ and $N_i \to \ell^\dagger_\alpha H^\dagger$, where the amount of CP violation is

quantified by the CP asymmetry parameter (cf. (B.51))

$$\varepsilon_i = \frac{\sum_\alpha \left[\Gamma(N_i \to \ell_\alpha H) - \Gamma(N_i \to \ell_\alpha^\dagger H^\dagger)\right]}{\sum_\alpha \left[\Gamma(N_i \to \ell_\alpha H) + \Gamma(N_i \to \ell_\alpha^\dagger H^\dagger)\right]} \,. \tag{3.9}$$

This can for the standard type-I seesaw case be explicitly calculated to be [83]

$$\varepsilon_i^0 = \frac{1}{8\pi \left(h^\dagger h\right)_{ii}} \sum_{j \neq i} \mathrm{Im}\left[\left(h^\dagger h\right)_{ji}^2\right] \mathcal{F}\left(\frac{M_j}{M_i}\right) \,, \tag{3.10}$$

where the loop function $\mathcal{F}(\cdot)$ is defined by

$$\mathcal{F}(x) = x\left[1 + \left(1 + x^2\right) \ln\left(\frac{x^2}{x^2+1}\right) - \frac{1}{x^2-1}\right] \,. \tag{3.11}$$

For the real scalar singlet model we have in addition to the standard CP violating diagrams leading to Eq. (3.10) also the diagrams depicted in Fig. 3.1 that account for the contribution of the scalar singlet. However, this extra contribution does not influence the CP asymmetry from N_1 decays because the decay $N_1 \to N_2 S$ is kinematically forbidden[3]. For ε_2 on the other hand, we get further vertex (v) and self-energy (s) contributions as displayed in Fig. 3.1. Thus we can write the total CP asymmetry parameters as

$$\varepsilon_1 = \varepsilon_1^0 \qquad\qquad \varepsilon_2 = \varepsilon_2^0 + \varepsilon_2^\mathrm{v} + \varepsilon_2^\mathrm{s} \tag{3.12}$$

and the additional terms have been determined by Ref. [94] to be

$$8\pi \left(h^\dagger h\right)_{22} \varepsilon_2^\mathrm{v} = \mathrm{Im}\left[\left(h^\dagger h\right)_{12} \beta_2\, \alpha_{21}\right] \mathcal{F}^\mathrm{v}_{21,\,R} + \mathrm{Im}\left[\left(h^\dagger h\right)_{12} \beta_2\, \alpha_{21}^*\right] \mathcal{F}^\mathrm{v}_{21,\,L} \,, \tag{3.13a}$$

$$\begin{aligned} 8\pi \left(h^\dagger h\right)_{22} \varepsilon_2^\mathrm{s} = {} & \mathrm{Im}\left[\left(h^\dagger h\right)_{12} \alpha_{21}\, \alpha_{11}\right] \mathcal{F}^\mathrm{s}_{211,\,RR} + \mathrm{Im}\left[\left(h^\dagger h\right)_{12} \alpha_{21}^*\, \alpha_{11}\right] \mathcal{F}^\mathrm{s}_{211,\,RL} \\ & + \mathrm{Im}\left[\left(h^\dagger h\right)_{12} \alpha_{21}\, \alpha_{11}^*\right] \mathcal{F}^\mathrm{s}_{211,\,LR} + \mathrm{Im}\left[\left(h^\dagger h\right)_{12} \alpha_{21}^*\, \alpha_{11}^*\right] \mathcal{F}^\mathrm{s}_{211,\,LL} \,, \end{aligned} \tag{3.13b}$$

where $\beta_2 \coloneqq \mu/M_2$ comes from the dimensionful parameter μ of the trilinear coupling in the scalar potential (cf. Eq. (3.4)). In App. C we provide the full expressions for the loop functions of Eq. (3.13). The appearing indices R and L denote whether the scalar field S interacts with left-chiral or right-chiral RHN spinor fields.

From the additional CP asymmetries given by Eq. (3.13) we can see the importance of the off-diagonal coupling α_{12} between the RHNs and the singlet, which we already touched on in our discussion of Fig. 3.1. Only if this coupling is non-vanishing can the CP asymmetry ε_2 be enhanced due to the presence of the additional real scalar singlet. Another important aspect is that the singlet scalar is in a sense secluded from the N_1 sector as the decay $N_1 \to N_2 S$ is kinematically forbidden for low energies. This implies

[3] In general, CP violation is linked to the imaginary part of the Feynman diagram and can therefore be calculated via the optical theorem (cf. e.g. [122]) or Cutkosky's cutting rules. They imply that for a CP asymmetry to be generated one needs a loop diagram in which the particles in the loop can go on-shell, which is not the case for the N_1 decay.

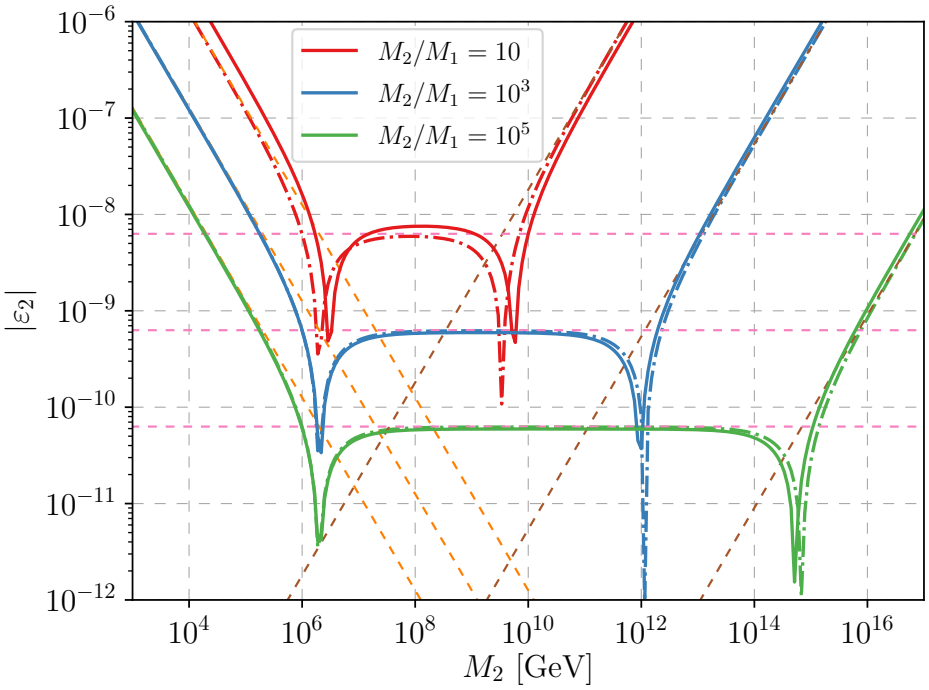

Figure 3.2.: Comparison of the absolute value of the CP asymmetry ε_2 in dependence on the heavy RHN mass M_2 in comparison to the approximations of the different contributions given by Eqs. (3.14, 3.15). For the comparison we choose $\alpha_{ij} = 10^{-3}$, $\mu = 1\,\text{TeV}$, $z = -\pi/4 + i$ and $m_S \ll M_2$. The solid lines represent the exact result, whereas the dashed lines show the approximations and the dot-dashed lines depict the sum of the approximations. The orange lines correspond to the approximation of ε_2^{v}, the pink lines to ε_2^{s} and the brown lines to ε_2^{0}.

that the asymmetry generated in the N_2 sector is not necessarily counteracted by an enhanced washout in the N_1 sector, as it would be in the standard leptogenesis scenario (cf. discussion on N_1 dominated leptogenesis in Ch. 2).

The expressions for ε_2^{v} and ε_2^{s} of Eq. (3.13) simplify significantly for a hierarchical RHN mass spectrum. Thus, in the case of $M_2 \gg M_1$, one obtains for a DI-type bound [94] with m_S being the mass of the new scalar

$$\begin{aligned} |\varepsilon_2^{\text{v}}| &\lesssim \frac{|\mu\,\alpha_{21}|}{8\pi M_2}\sqrt{\frac{M_1}{M_2}}\left(1-\frac{m_S^2}{M_2^2}\right), \\ |\varepsilon_2^{\text{s}}| &\lesssim \frac{|\alpha_{21}\,\alpha_{11}|}{16\pi}\sqrt{\frac{M_1}{M_2}}\left(1-\frac{m_S^2}{M_2^2}\right)^2. \end{aligned} \tag{3.14}$$

Furthermore, we can in the hierarchical regime similarly approximate Eq. (3.10) by a

DI-type bound, for which we find in the case of two RHNs (cf. [94][4])

$$\left|\varepsilon_2^0\right| \lesssim \frac{\sum_\alpha m_{\nu_\alpha}}{8\pi v \mathrm{ew}^2} M_2 \frac{M_1^2}{M_2^2} \log\left(\frac{M_2^2}{M_1^2}\right), \tag{3.15}$$

with the active neutrino masses m_{ν_α}. In Fig. 3.2, we show how the exact expressions for $|\varepsilon_2|$ of Eq. (3.12), with Eqs. (3.10, 3.13), compare to the DI-type bounds given by Eqs. (3.14, 3.15). As can be seen from Fig. 3.2, the CP asymmetry is larger for smaller differences between M_1 and M_2. Furthermore, the additional contributions due to the singlet scalar are significant for masses of N_2 below $\sim 10^6$ GeV and can lead to a substantial enhancement of the CP asymmetry. Especially, the new vertex contribution $\varepsilon_2^{\mathrm{v}}$ becomes important for very small masses of N_2 since it scales with $1/M_2$ (cf. Eq. (3.14)). Thus, from small to large values of M_2, first, the vertex contribution $\varepsilon_2^{\mathrm{v}}$ is dominant, before the self-energy contribution $\varepsilon_2^{\mathrm{s}}$ prevents a further decrease of the CP asymmetry, until finally the standard contribution ε_2^0 takes over and the CP asymmetry increases as usual with the RHN mass. However, in similarity to Ch. 2, when we use these new processes to lower the energy scale of leptogenesis, at some point $\Delta L = 2$ processes will lead to a stronger washout, thereby limiting the efficiency of leptogenesis. We will address this effect and its consequences in detail in Sec. 3.3.2, but first try to develop an understanding for the situation in which these scattering processes are still negligible.

3.3 Boltzmann Equations and a Semi-Analytical Solution

To gain a semi-analytical understanding of leptogenesis in the singlet scalar assisted model, we use the Boltzmann equations for the normalized number densities N_{N_i} and the $B-L$ asymmetry N_{B-L} for our set of assumptions and couplings as laid out in the introduction to Ch. 3 and Sec. 3.1. They include in addition to the standard decays and inverse decays of RHNs into Higgses and leptons also the processes induced by the new singlet scalar S. Furthermore, they capture the $\Delta L = 2$ washout through the scatterings $N_i N_j \to HH$ mediated by the singlet scalar S, which is the most relevant washout other than the one from inverse decays. For more information on Boltzmann equations and some of the appearing quantities see App. B[5].

Explicitly, the Boltzmann equations read [94]

$$\begin{aligned}\frac{\mathrm{d}N_{N_2}}{\mathrm{d}z_1} &= -(D_2 + D_{21})\,\Delta_{N_2} + D_{21}\,\Delta_{N_1} \\ &\quad - \Delta_{N_1N_2}\,S_{N_1N_2\to HH} - \Delta_{N_2N_2}\,S_{N_2N_2\to HH}\,,\end{aligned} \tag{3.16a}$$

$$\begin{aligned}\frac{\mathrm{d}N_{N_1}}{\mathrm{d}z_1} &= -(D_1 + D_{21})\,\Delta_{N_1} + D_{21}\,\Delta_{N_2} \\ &\quad - \Delta_{N_1N_2}\,S_{N_1N_2\to HH} - \Delta_{N_1N_1}\,S_{N_1N_1\to HH}\,,\end{aligned} \tag{3.16b}$$

$$\frac{\mathrm{d}N_{B-L}}{\mathrm{d}z_1} = -\sum_{i=1}^{2} \varepsilon_i\, D_i \Delta_{N_i} - W N_{B-L}\,, \tag{3.16c}$$

[4]The difference by a factor of two is related to the different definition of the vev v.

[5]Note that the conventions for the quantities in the Boltzmann equations can deviate slightly from App. B to match Ref. [94].

where the temperature (or time) dependence is encoded in

$$\Delta_{N_i}(z_1) \coloneqq \frac{N_{N_i}(z_1)}{N_{N_i}^{\mathrm{eq}}(z_1)} - 1\,, \tag{3.17a}$$

$$\Delta_{N_i N_j} \coloneqq \frac{N_{N_i} N_{N_j}}{N_{N_i}^{\mathrm{eq}} N_{N_j}^{\mathrm{eq}}} - 1\,, \tag{3.17b}$$

$$N_{N_i}^{\mathrm{eq}}(z_1) = \frac{z_i^2}{2}\,\mathcal{K}_2(z_i)\,, \tag{3.17c}$$

$$D_i(z_1) = K_i\, z_i\, \frac{\mathcal{K}_1(z_i)}{\mathcal{K}_2(z_i)} N_{N_i}^{\mathrm{eq}}(z_1)\,, \tag{3.17d}$$

$$D_{21}(z_1) = K_{21}\, z_2\, \frac{\mathcal{K}_1(z_2)}{\mathcal{K}_2(z_2)} N_{N_2}^{\mathrm{eq}}(z_1)\,, \tag{3.17e}$$

$$W(z_1) = \sum_i \frac{1}{4}\, K_i\, z_i^3\, \mathcal{K}_1(z_i) \tag{3.17f}$$

and $S_{N_1 N_2 \to HH}(z_1)$, which we will discuss in more detail in Sec. 3.3.2. The CP asymmetry parameter ε_i appearing in Eq. (3.16c) has been discussed in Sec. 3.2. Note that the inverse dimensionless temperature for the i-th RHN, $z_i \coloneqq M_i/T$, can be converted into a dependence on z_1 by using $z_i = z_1\, M_i/M_1$. Furthermore, $\mathcal{K}_a$ stands for the a-th modified Bessel function of the second kind.

The decay parameters are given by

$$K_i \equiv \frac{\Gamma(N_i \to LH)}{H(T = M_i)} = \sqrt{\frac{45}{64\pi^5 g_*}}\, \frac{M_{\mathrm{Pl}}}{v_{\mathrm{ew}}^2}\, \left(\mathcal{M}_\nu^R\right)_{ii}\,, \tag{3.18}$$

where we used the Hubble parameter from Eq. (A.10) and $\mathcal{M}_\nu^R$ represents the CI parametrization we introduced for the Yukawa couplings (cf. Eq. (3.7)) via

$$\mathcal{M}_\nu^R \equiv R^\dagger D_\nu R\,. \tag{3.19}$$

It is important to realize that the decay parameters K_i are independent of the RHN masses and that they generally fulfill $K_i \gtrsim 8$ for the case of two RHNs. Thus, we are always in the strong washout regime (cf. Sec. 2.3). The reason that the N_2 sector can nevertheless be relevant for leptogenesis is due to the singlet scalar S which modifies the N_2 sector in a different way than the N_1 sector, where the difference of the sectors is rooted in the fact that the decay $N_1 \to N_2 S$ is kinematically forbidden whereas $N_2 \to N_1 S$ is not. For the new decay channel we have a decay parameter of

$$K_{21} \coloneqq \frac{\Gamma(N_2 \to N_1 S)}{H(T = M_2)}\,, \tag{3.20}$$

with the decay width [94]

$$\Gamma(N_2 \to N_1 S) = \frac{|\alpha_{12}|^2\, M_2}{16\pi} \left[(1 + r_{12})^2 - \sigma_2\right] \sqrt{\delta_{12}}\,, \tag{3.21}$$

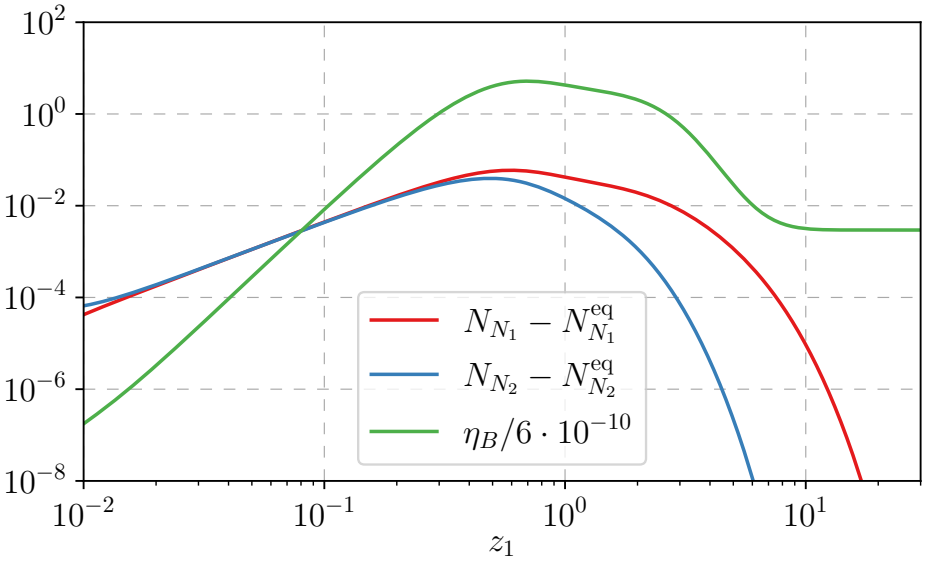

Figure 3.3.: Exemplary solution to the Boltzmann equations, Eqs. (3.16), in terms of the normalized RHN number densities (red and blue line) and baryon-to-photon ratio η_B (green line) for $M_1 = 2\,\mathrm{TeV}$, $M_2 = 6\,\mathrm{TeV}$, $m_S = 500\,\mathrm{GeV} = \mu$, $m_H = 0$ and $\alpha_{ij} = 10^{-3}$. The CI parameter was set to $z = 0.25i$ and results in $K_1 \approx 12$ and $K_2 \approx 51$, while we have $K_{21} \sim 10^6$.

where we used

$$r_{ij} \coloneqq (M_i/M_j)^2\,, \quad \sigma_i \coloneqq m_S^2/M_i^2\,, \quad \delta_{ij} \coloneqq (1 - r_{ij} - \sigma_j)^2 - 4\,r_{ij}\,\sigma_j\,. \tag{3.22}$$

The new decay parameter is in our parameter space of interest typically very large, for example we have $K_{21} \sim 10^6$ for $M_2 = 1\,\mathrm{TeV}$ and $\alpha_{12} = 10^{-3}$. This is very important for the RHN number densities N_{N_i} to be strongly out of equilibrium and thereby to help facilitating low-scale leptogenesis. We will now neglect the scattering terms $S_{N_1N_2\to HH}$ in the Boltzmann equations, whose influence we will address in Sec. 3.3.2, and develop a semi-analytical understanding of the situation in which scattering processes are negligible.

An exemplary solution to the Boltzmann equations, Eqs. (3.16), without $\Delta L = 2$ scatterings can be seen in Fig. 3.3, from which we can observe that the lepton or $B - L$ asymmetry generation proceeds in three steps. At first, the $B - L$ asymmetry is build up strongly by the N_2 decays until $z_1 \sim 0.5$, especially due to the enhanced CP asymmetry of the new decay channels. In a second phase until $z_1 \sim 2.5$, the N_1 decays also lead to a CP asymmetry that is however significantly smaller for $M_1 \lesssim 10^6\,\mathrm{GeV}$ (cf. Fig. 3.2 and [94]). At the same time, due to the large coupling of the N_1 and N_2 sector via K_{21}, the N_1 decays also create a deviation in the N_2 number density from equilibrium and thereby lead to additional CP violating decays. Both of these effects combined, together with the washout, lead to a slow decrease of the baryon-to-photon ratio η_B. Finally, in a third phase for $z_1 \gtrsim 2.5$, the washout dominates and exponentially suppresses the baryon asymmetry before it freezes out and becomes constant, as can be seen by the initially comparably

sharp decline of η_B before it flattens off in the corresponding region of Fig. 3.3.

Like in the usual case, the $B-L$ asymmetry generated in the RHN decays gets converted into a baryon asymmetry by $SU(2)$-sphalerons that are in equilibrium until a temperature of $T_{\rm sph} = 131\,\text{GeV}$ [88]. Thus, any process that happens at lower temperatures and does not explicitly violate baryon number can not influence the baryon asymmetry. This implies that the washout after $T_{\rm sph}$ will not affect the baryon-to-photon ratio, which can be used to circumvent part of the washout and to find low-scale leptogenesis scenarios with $M_1 \lesssim T_{\rm sph} \lesssim M_2$ (cf. Ref. [94]). However, we want to refrain from using this possibility and hence find for the final baryon-to-photon ratio $\eta_B \approx 0.01\, N_{B-L}(z=\infty)$ (cf. Ch. 2), where the prefactor takes into account sphaleron conversion and subsequent entropy generation.

Note that the example of Fig. 3.3 highlights the different regimes, but falls short of producing the BAU by roughly two orders of magnitude. Thus, it is either necessary to increase the amount of CP violating due to the RHN decays by an increase of the trilinear coupling μ (cf. Eq. (3.14)), which we will find to be limited by $\Delta L = 2$ scattering processes in Sec. 3.3.2, or to accept a smaller separation of the RHN masses, which will enhance the CP asymmetry (cf. Fig. 3.2) and suppress the washout (cf. discussion on Fig. 3.3), thereby increasing the efficiency of leptogenesis. To analyze both of these paths, it is helpful to develop a semi-analytical understanding for the baryon-to-photon ratio and determine its limits of validity in order to facilitate an analysis of the whole parameter space.

3.3.1 A Semi-Analytical Solution

Working in the regime where $\Delta L = 2$ scatterings are negligible and the N_1 and N_2 sectors are strongly coupled through large values of the decay parameter K_{21}, it turns out to be possible to separate the creation of a $B-L$ asymmetry into a generation in the N_2 sector combined with a washout from the N_1 sector. In terms of a formula this can be expressed by (cf. [34])

$$\eta_B \approx 0.01\, \varepsilon_2\, \kappa_2(K_2,\, r_{12})\, e^{-\omega(K_1,\, r_{12})}\,, \tag{3.23}$$

which depends on the squared mass ratio $r_{12} = (M_1/M_2)^2$ and the decay parameters K_1 and K_2. The reason this ansatz works for our case is that the dominant contribution to the CP violation and thus the $B-L$ asymmetry comes from the N_2 decays, while the N_1 sector mainly leads to a washout of the asymmetry.

In the standard case of a hierarchical RHN spectrum, the washout and efficiency functions are given by $\omega = 3\pi/8\, K_1$ and $\kappa_2 = 2/z_B(K_2)$ with $z_B(K_2) = 2 + 4\, {K_2}^{0.13}\, e^{-2.5/K_2}$ [34]. However, as one of our paths to reach a larger baryon asymmetry is by a smaller separation of RHN masses, these functions will be more complicated in our case since we want them to hold for RHN masses of the same order (but non-degenerate)[6]. Allowing these functions to have a more general form and to depend on the squared mass ratio r_{12}, we find as a

[6] A similar setting for the type-I seesaw case has been studied in Ref. [123].

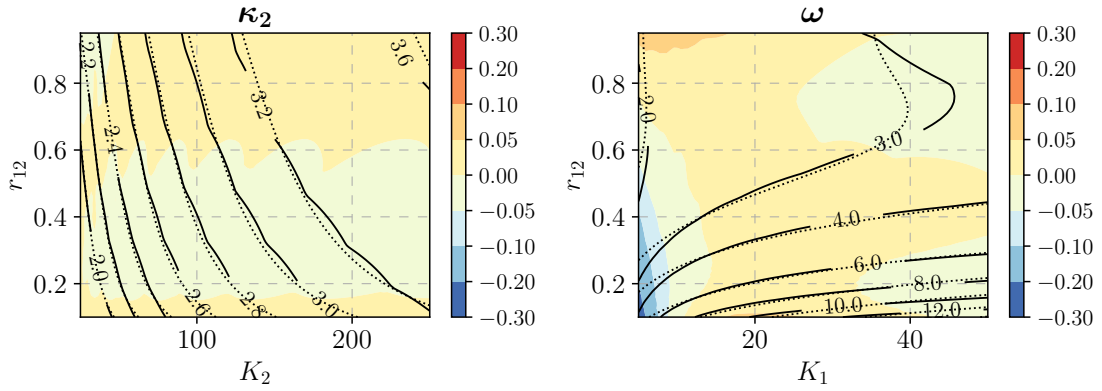

Figure 3.4.: Comparison of the efficiency factor κ_2 and the N_1 washout function ω between the numerical results (solid lines) and the fit functions presented in Eqs. (3.23, 3.24) (dashed lines). The color coding displays the relative deviation of the fit functions to the numerical results and is for nearly all of the parameter space less than 10 %.

good fit of the N_2 efficiency factor κ_2 and the N_1 washout function ω:

$$\kappa_2(K_2, r_{12}) = \frac{2}{z_B(K_2)} \frac{K_2^{0.44}\, r_{12}^{-0.2}}{0.3\, K_2 + 1.6\, r_{12}^{2.6}}\,, \tag{3.24a}$$

$$\omega(K_1, r_{12}) = \frac{3\pi}{8} \left(-K_1^{0.5} \left(1.4\, r_{12}^2 - 2.1\, r_{12} + 0.8\right) \ln(r_{12}) + 1.2\, K_1^{0.2}\right). \tag{3.24b}$$

A comparison of these semi-analytical solutions to the numerically determined values is shown in Fig. 3.4. The way that the efficiency κ_2 and the washout function ω are extracted from the numerical solution of the Boltzmann equations is by starting from the maximal $B-L$ asymmetry $N_{B-L}^{\max} \coloneqq \max_z N_{B-L}(z)$ and then extracting $\kappa_2 = N_{B-L}^{\max}/\varepsilon_2 \geq 0$ and $\omega = \ln(N_{B-L}^{\max}/N_{B-L}(\infty)) \geq 0$ in the spirit of Eq. (3.23). By means of Fig. 3.4, we find that the semi-analytical solutions of Eqs. (3.24) are accurate for nearly all of our region of interest with a deviation of less than 10 %. Note that in contrast to the standard formulas of [34], the efficiency κ_2 can in our case be larger than one. The reason for this is the strong coupling of the N_1 and N_2 sector through the large values of K_{21}, as described in Sec. 3.3, leading to additional CP violation in the N_2 sector.

This semi-analytical description of the final baryon-to-photon ratio enables us to describe the regime with a smaller separation of RHN masses and therefore one of the paths leading to a larger final baryon asymmetry. Furthermore, they can also describe the other path to a larger baryon asymmetry by an increase of the CP violation through larger values of the trilinear coupling μ as long as the $\Delta L = 2$ scatterings remain negligible. To verify this claim and to determine when the scatterings become important will be the guiding questions of the next section.

3.3.2 Washout from Scattering Processes

The most relevant washout other than the one by inverse decays is due to the $\Delta L = 2$ scatterings $N_i N_j \to HH$ mediated by the singlet scalar and encoded in the Boltzmann equations (cf. Eqs. (3.16) and [94]) by the term $S_{N_1 N_2 \to HH}$. The corresponding scattering cross section is given by [110]

$$\sigma_{N_i N_j \to HH}(s) = \frac{|(\alpha\alpha^\dagger)_{ji}|^2 \mu^2}{8\pi} \frac{s - (M_i + M_j)^2}{(s - m_S^2)^2 \sqrt{\delta_{M_i, M_j}(s)}}\,, \tag{3.25}$$

with

$$\delta_{M_i, M_j}(s) = (s - M_i^2 - M_j^2)^2 - 4 M_i^2 M_j^2\,. \tag{3.26}$$

This also quantifies the statement that the $\Delta L = 2$ scatterings increase with the trilinear coupling μ and therefore will limit the achievable baryon asymmetry for too large values of μ. Using the scattering cross section of Eq. (3.25), we can now give an explicit expression for the scattering functions $S_{N_1 N_2 \to HH}$ [94]

$$S_{N_i N_j \to HH} \equiv \frac{M_i}{64\pi^2 H(T = M_i)} \int_{w_{\min}}^{\infty} \mathrm{d}w \sqrt{w}\, K_1(\sqrt{w})\, \hat{\sigma}_{N_i N_j \to HH}\left(\frac{w M_i^2}{z_i^2}\right)\,, \tag{3.27}$$

with $w_{\min} = (M_i + M_j)^2$ and

$$\hat{\sigma}_{N_i N_j \to HH}(s) = \frac{1}{s}\, \delta_{M_i, M_j}(s)\, \sigma_{N_i N_j \to HH}(s)\,. \tag{3.28}$$

With the full expressions for the scattering functions $S_{N_1 N_2 \to HH}$ at hand, we can finally compare the full numerical results with $\Delta L = 2$ scatterings to the semi-analytic functions determined in Sec. 3.3.1. A sample of these comparisons is depicted in Fig. 3.5 and shows that the semi-analytical solutions agree well with the full numerical solution including scatterings for small enough values of the trilinear coupling μ. Explicitly, we can estimate that the semi-analytical solutions are an accurate description for

$$\mu < \mu_* \approx M_1 \left(\frac{0.5}{\delta_M}\right) \left(\frac{10^{-3}}{\alpha}\right)\,, \tag{3.29}$$

with

$$\delta_M \coloneqq \frac{M_2 - M_1}{M_1} \tag{3.30}$$

and we have fixed all couplings between the singlet scalar and the RHNs to be equal for simplicity $\alpha_{ij} \equiv \alpha$. We want to remark that Fig. 3.5 only represents a sample of parameter points investigated and we checked the estimate for μ_*, Eq. (3.29), to be accurate for a larger range of parameters.

There are two important aspects for our analysis that are visible from Fig. 3.5. First, to reiterate, the semi-analytical solution is a good approximation for the full numerical solution for $\mu \leq \mu_*$. Second, for values around $\mu \approx \mu_*$ the final baryon-to-photon ratio

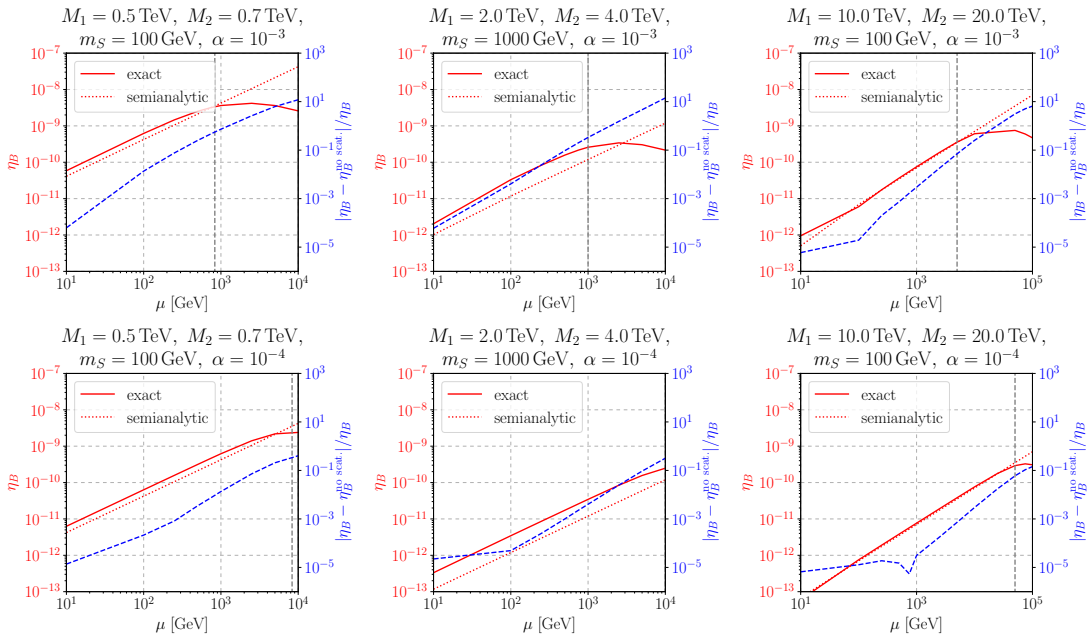

Figure 3.5.: Comparison of the full numerical solution to the Boltzmann equation for the final baryon-to-photon ratio η_B (cf. Eq. (3.16c)), displayed as a solid red line, to the semi-analytical solution (cf. Eqs. (3.23, 3.24)), shown as a dashed red line, in dependence on the trilinear coupling μ for several points in parameter space. The different rows display different values of $\alpha_{ij} \equiv \alpha$, while the columns correspond to different masses. The dashed gray line depicts μ_* as defined in Eq. (3.29) and thus an estimate of when $\Delta L = 2$ scatterings become important. In dashed blue, the relative deviation of the numerical solution with and without scatterings is shown. This relative deviation measures how important scatterings are and implicitly defines μ_* by the condition that the relative deviation is $\sim$0.1 for μ_*.

η_B reaches its maximal value, since for larger trilinear couplings the additional washout due to the $\Delta L = 2$ scattering processes is stronger than the additionally generated CP asymmetry. These two aspects combined enable us to use the semi-analytical functions, Eqs. (3.23, 3.24), to determine the viable parameter space for low-scale leptogenesis in our next and final step.

3.4 Viable Parameter Space for Low-Scale Leptogenesis

As detailed in Sec. 3.1, we consider for the parameter space analysis the minimal example of a $\mathbb{Z}_2$ symmetric potential with a real singlet scalar as specified by $V_{\text{even}}(H, \widetilde{S})$ in Eq. (3.2). Furthermore, we focus on the scenario of low-scale leptogenesis, so we want to show that the BAU can be created within the model for very low RHN masses. Therefore, we will fix in two benchmark scenarios $M_1 = 500\,\text{GeV}$ and $M_1 = 10\,\text{TeV}$, and demonstrate that for both of these masses successful leptogenesis is possible. However, we will see that

the parameter space in which this is the case is substantially bigger for $M_1 = 10\,\text{TeV}$ compared to $M_1 = 500\,\text{GeV}$, where only a very restricted combination of parameters enables leptogenesis. For M_2 we find that a mass splitting parameter (cf. Eq. (3.30)) of $\delta_M = 0.3$ is approximately optimal for the creation of a baryon asymmetry and we fix M_2 accordingly. This corresponds to a modest degeneracy of the RHN masses, which is necessary to strike an optimal balance between maximizing the CP asymmetry while minimizing the washout. For the CI parameter we choose $z = 0.25i$, as in Fig. 3.3, since this ensures a small decay parameter K_1 and therefore a not too strong washout in the N_1 sector.

This leaves us with the trilinear coupling μ and the new scalar mass during leptogenesis m_S as important parameters with simple bounds. As discussed in Sec. 3.3.2, the trilinear coupling has to be smaller than μ_* (cf. Eq. (3.29)) for the semi-analytical solutions to hold, and the scalar mass is restricted by the fact that for the singlet scalar to lead to additional CP violation, $\varepsilon_2^{\text{v/s}} \neq 0$, it needs to fulfill $m_S < M_2 - M_1$ (cf. Sec. 3.2). Due to this, we choose m_S and μ to span the parameter plane in which we will depict the scan results and limits. However, m_S and μ are not explicit parameters of our theory but depend on the scalar potential $V_{\text{even}}(H, \widetilde{S})$ (cf. Eq. (3.2)) with the quantities $\widetilde{m}_H$, $\widetilde{m}_S$, λ_H, λ_{SH} and λ_S. For our analysis we want to focus on the case in which the new scalar and the SM Higgs do not decouple at low energies, but instead mix. This implies that the present day scalar vev v_S^0 has to be non-vanishing, as we will see. We remark that a symmetry restoration scenario in which the scalar vev is non-zero for a limited time-period during the evolution of the universe could give rise to interesting phenomenology and therefore provides a potential starting point for further research.

Let us now provide the links of the fundamental parameters in the scalar potential to the ones we use for our leptogenesis parameter scan. The most direct link exists for the new scalar mass, which is simply

$$\widetilde{m}_S^2 = -\frac{1}{2} m_S^2 \,. \tag{3.31}$$

Furthermore, by taking λ_S to be a free parameter, we find for the scalar vev in the present day (low-energy) vacuum

$$v_S^0 = \sqrt{\frac{m_S^2 - \lambda_{SH} v_{\text{ew}}^2}{2\lambda_S}} \,, \tag{3.32}$$

which includes λ_{SH} and is showing that v_S^0 can only vanish for $\lambda_{SH} > 0$. Thus, we will distinguish the cases $\lambda_{SH} > 0$ and $\lambda_{SH} < 0$. The parameter λ_{SH} can be determined via

$$\lambda_{SH} = \frac{2\mu\mu_S}{3m_S^2} \,, \tag{3.33}$$

where the singlet self coupling μ_S is implicitly defined through

$$\lambda_S = 2\left(\frac{\mu_S}{3m_S}\right)^2 . \tag{3.34}$$

Additionally, we find for the mixing angle between the SM Higgs and the new singlet

$$\tan\theta = \frac{\lambda_{SH} v_S^0 v_{\text{ew}}}{2\lambda_S (v_S^0)^2 - m_{h_0}^2} \tag{3.35}$$

that can be easily converted into $\sin\theta$, which is the parameter for which experimental limits are usually given. Furthermore, in Eq. (3.35) the SM Higgs mass $m_{h_0} = 125.1\,\text{GeV}$ [8] appears and it also makes the statement explicit that for non-zero mixing we need $v_S^0 \neq 0$. Finally, we have for the quartic Higgs coupling

$$\lambda_H = \frac{m_{h_0}^2}{2v_{\text{ew}}^2} + \tan\theta\,\frac{\lambda_{SH} v_S^0}{2v_{\text{ew}}}\,, \tag{3.36}$$

for the low-energy new scalar mass

$$m_{s_0}^2 = m_S^2 + \tan\theta\,\lambda_{SH} v_{\text{ew}} v_S^0\,, \tag{3.37}$$

and for the Higgs mass parameter

$$\widetilde{m}_H^2 = -\frac{1}{2}\lambda_{SH}(v_S^0)^2 - \lambda_H v_{\text{ew}}^2\,. \tag{3.38}$$

The above relations will allow us to convert the theoretical and experimental limits from several sources into bounds on the viable parameter space.

From a theoretical perspective, the couplings in the scalar potential are not completely free, but need to adhere to certain restrictions. First, for the perturbative treatment to be valid, the quartic couplings have to fulfill $\lambda_H, \lambda_S, |\lambda_{SH}| < 4\pi$. However, in the light of perturbative unitarity bounds [124], we will use a more conservative limit of $|\lambda_i| < 3$. Second, as we want the scalar potential to be bounded from below, we need $\lambda_H, \lambda_S \geq 0$ together with $\lambda_{SH} > -2\sqrt{\lambda_H \lambda_S}$. It will turn out that of these restrictions, only $\lambda_H < 3$ will provide dominant limits to our parameter space.

Additionally, the mixing angle between the SM Higgs and the new scalar (cf. Eq. (3.35)) can be restricted by two different kinds of measurement at colliders. From signal strength measurements of the SM Higgs, one can derive a limit of $\sin\theta \lesssim 0.3$ [114, 125], while there are also limits from searches for resonant scalar singlet production at the LHC. Both of them will be relevant to restrict our parameter space and for the resonance searches we will work with the limits provided by the CMS collaboration based on $36\,\text{fb}^{-1}$ of data at 13 TeV [119, 126]. The resonance searches provide stronger limits than the Higgs signal strength measurements in the range of new scalar masses of $200\,\text{GeV} \lesssim m_S \lesssim 800\,\text{GeV}$. Another limit from collider physics appears for small scalar masses of $m_{s_0} < m_{h_0}/2$ because there the SM Higgs can decay into two new scalars. As this decay would be invisible at the LHC, the current bounds on invisible Higgs decays of $\text{BR}(h \to \text{inv}) \leq 0.23$ [127, 128] apply. To access the branching ratio, we need to compare the decay width of $h_0 \to s_0 s_0$ given by

$$\Gamma_{h_0 \to s_0 s_0} = \frac{\lambda_{SH}^2 v_{\text{ew}}^2}{32\pi m_{h_0}} \sqrt{1 - \frac{4m_{s_0}^2}{m_{h_0}^2}} \tag{3.39}$$

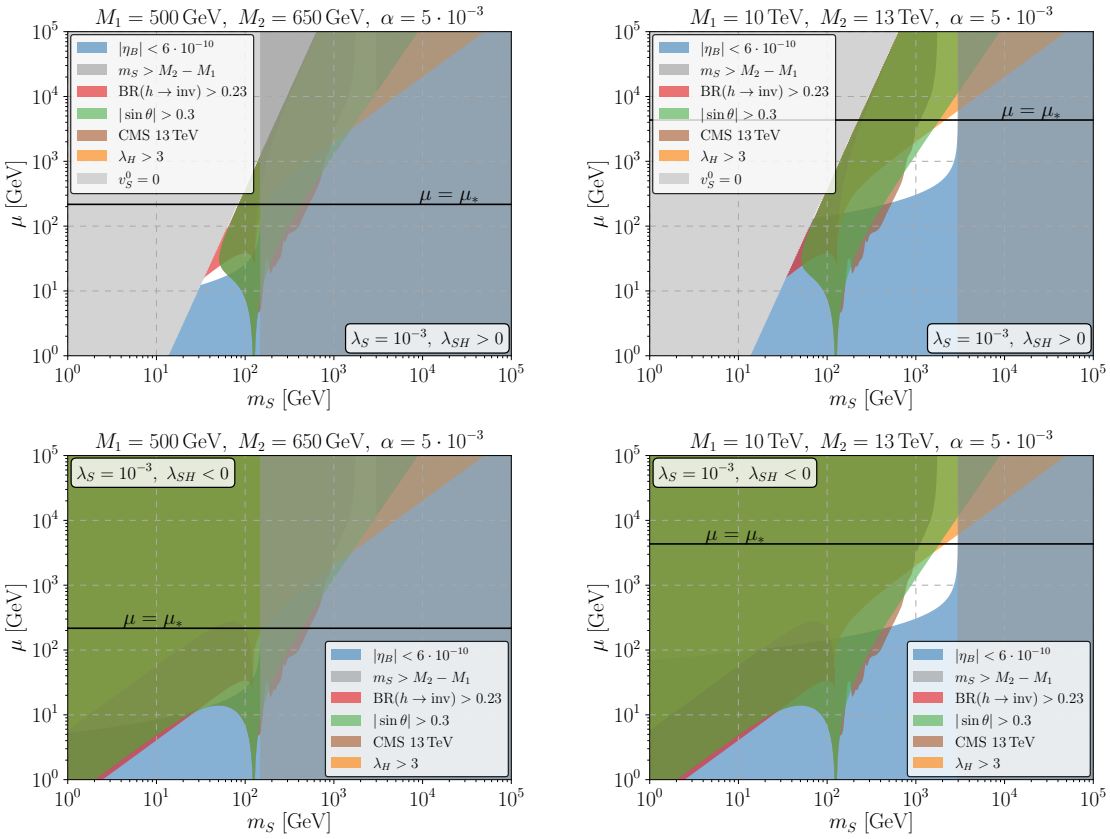

Figure 3.6.: Parameter space scans of the real scalar singlet model using the semi-analytical functions Eqs. (3.23, 3.24) to asses the viability of leptogenesis. The excluded regions due to different limits are shown in corresponding colors as laid out by the legends. Only the limits that are significant for at least one of the cases are shown. See text for details and parameter values.

to the total Higgs decay width including the visible SM channels that have a decay width of $\Gamma_{h_0} \approx 4.03\,\text{MeV}$ for m_{h_0} [129].

Besides the already mentioned limits of $m_S < M_2 - M_1$ for the $N_2 \to N_1 S$ decay to be kinematically allowed and $v_S^0 > 0$ to not be in a symmetry restoration scenario, this leaves us with the choice of λ_S. As λ_S does not influence the resulting baryon asymmetry, we can use its numerical values to ensure the desired phase transition pattern as laid out in Sec. 3.1. To do so, we fix $\lambda_S = 10^{-3}$ since this leads to smaller thermal corrections for the singlet mass parameter in comparison to the Higgs mass parameter (cf. [107, 109])[7].

With all the relevant bounds at hand, we can scan the parameter space with the help of our semi-analytical solutions, Eqs. (3.23, 3.24), and identify viable regions. The results of this parameter scan are shown in Fig. 3.6, from which we can see that singlet scalar assisted leptogenesis can create the BAU for RHN masses of as low as $\sim 500\,\text{GeV}$ with corresponding scalar masses of $m_S \sim 50\,\text{GeV}$. Note that for the results of Fig. 3.6 we have

[7] If a higher scalar phase transition temperature is necessary to realize leptogenesis, it can be achieved by picking a smaller λ_S.

set the RHN mass splitting to $\delta_M = 0.3$ and thereby admitted a modest degeneracy of RHN masses. A lower degeneracy is also possible, but comes at the expense of higher necessary RHN masses. Although in the viable (white) region of Fig. 3.6 the baryon asymmetry is strictly speaking too large, it can always be reduced to the measured BAU by adjusting the mass splitting between the RHNs or the CI parameters. For masses below $M_1 \sim 500\,\text{GeV}$, singlet scalar assisted leptogenesis soon becomes under pressure as the window due to the restriction on the scalar mass closes and the conversion of a lepton into a baryon asymmetry has to finished before $T_{\text{sph}} \approx 130\,\text{GeV}$ [88]. On the other hand, larger RHN masses like $M_1 = 10\,\text{TeV}$ (cf. right panels of Fig. 3.6) allow for a larger viable region of parameter space with corresponding scalar masses in the range $600\,\text{GeV} \lesssim m_S \lesssim 3\,\text{TeV}$. It is interesting to note that both of these mass ranges for M_1 or m_S are accessible to current (and future) experiments, with the main restrictions coming from collider limits on the Higgs sector in contrast to Ch. 2 where the experimental accessibility was through the active neutrino sector.

3.5 Summary

In this chapter, we have, by analyzing the singlet scalar assisted model, investigated another option to create the BAU via low-scale leptogenesis, while following the same guiding principles as in Ch. 2. The singlet scalar assisted model enlarges the SM by two RHNs and a real singlet scalar that modifies the scalar potential through interactions with the Higgs field and serves as the low-energy effective theory of a large class of UV-complete models. It therefore represents a simple and rather general modification to the standard type-I seesaw framework. The possible coupling of the new scalar S to the two RHNs N_1 and N_2, opens up the additional decay channel $N_2 \to N_1 S$, which leads to an increased lepton (or baryon) asymmetry created in the N_2 sector through a larger CP asymmetry and stronger deviation from thermal equilibrium. Combined with a not too strong washout in the N_1 sector, this effect enables low-scale leptogenesis even below the TeV scale without the need for a strongly degenerate RHN mass spectrum.

For the analysis, we developed a semi-analytical solution for the resulting baryon-to-photon ratio, Eqs. (3.23, 3.24), that accurately reproduces the full numerical result and allows for an efficient study of the parameter space. These solutions also incorporate the data on the low-energy active neutrino sector by employing a CI parametrization. We used the semi-analytical solutions to study in more detail the viable parameter space for two benchmark scenarios, covering a very-low-scale leptogenesis scenario of $M_1 = 500\,\text{GeV}$ with scalar masses (at the time of leptogenesis) of around $m_S \sim 50\,\text{GeV}$ and a low-scale leptogenesis scenario of $M_1 = 10\,\text{TeV}$ with scalar masses in the range $600\,\text{GeV} \lesssim m_S \lesssim 3\,\text{TeV}$. The main result we found is that leptogenesis can account for the BAU in both of these scenarios, with the viable parameter space being significantly smaller for the very-low-scale version. Thus $M_1 \sim 500\,\text{GeV}$ provides a rough estimate of how small the lightest RHN mass can be in the singlet scalar assisted model to allow for successful leptogenesis. Furthermore, both of these benchmark regions turn out to be accessible by current and future experiments, mostly through measurements of the Higgs sector.

In addition to the mentioned symmetry restoration scenario, in which the scalar vev

is only non-zero during a limited part of the evolution of the universe during which also leptogenesis happens, further studies can also aim at a more precise determination of the lower bound on M_1. This would imply to extend Eq. (3.23) to take into account flavor effects, as well as a more detailed treatment of the effects due to the electroweak phase transition shortly before the $SU(2)$-sphaleron freeze-out. Moreover, it would be interesting to embed the singlet scalar assisted model into a concrete UV-complete model, allowing to predict important model parameters like the RHN-singlet Yukawa matrix α_{ij} or the trilinear coupling μ from fundamental parameters.

With this, we want to conclude the discussion of SM extensions enabling low-scale leptogenesis and therefore providing a possible explanation for the BAU. In our discussion, we have analyzed two models that not only make low-scale leptogenesis possible, but are also accessible by current and future experiments. While leptogenesis in the scotogenic model can be probed by measurements of the neutrino sector and especially the lightest active neutrino mass, singlet scalar assisted leptogenesis can potentially show up in LHC measurements of the Higgs sector. This second kind of experiments will also be the focus of our investigations in the next chapter, where we will shift our attention to DM as another puzzling new physics effect and look at so-called next generation simplified DM models, which we will compare by studying their LHC signatures.

Chapter 4

Two Higgs Doublet Model + Scalar or Pseudoscalar

In our study of low-scale new physics phenomena beyond the SM, we will, after looking at leptogenesis as a possibility to explain the BAU, now change our focus to DM searches at the LHC. Beside the discovery and analysis of the Higgs boson [130, 131], searches for DM have been, and remain, one of the prime goals for studies of LHC data (cf. e.g. [132] for a review), with weakly interacting massive particles (WIMPs) [133] being a common candidate to look for. These WIMPs can escape the detector unnoticed and can therefore lead to signatures with a substantial amount of missing transverse energy (MET), as the particles recoiling against the WIMPs can oftentimes be detected. Although these MET searches can generally be kept independent of specific theoretical models, a theoretical framework is necessary to highlight important regions of parameter space, characterize a possible discovery and enable a comparison to non-collider results like direct detection (DD) and indirect detection (ID) [134].

Historically, supersymmetry was for a long time the main theoretical framework for DM searches at the LHC to compare results in. With the non-discovery of supersymmetric particles at the LHC [135] and also over time, the focus for the theoretical framework shifted to DM effective field theories (EFTs) because they allow for a simple and model independent way to account for the interaction of the SM with DM [136–141]. By construction, EFTs are a good description for processes as long as the relevant momentum transfer is substantially smaller than the mass scale of the particles mediating this process, which is for example the case for DD [142]. However, this assumption does not necessarily hold at colliders, where the momentum transfer can be of a similar order as the mass scale of the mediating particle [143–148]. Due to this fact, the focus changed from DM EFTs to the framework of simplified models [148, 149] (cf. e.g. [150] for a review) that includes not only a DM candidate, but also a particle mediating the DM interactions. Although improving on the DM EFTs by taking the mediating particle into account, simplified models face problems of their own right. Besides allowing due to their simplicity only for a limited set of experimental signatures and being already very constrained by measurements, they also often violate theoretical restrictions like gauge invariance, unitarity and renormalizability [151–157]. Therefore, with the next-generation DM models, a new theoretical framework beyond the DM simplified models was developed to overcome

these shortcomings, while still having a not too large set of free parameters. As laid out by Ref. [134], the guiding principles for the next-generation DM models are:

(I) the model should preferably be a theoretically consistent extension of one of the DM simplified models already used by the LHC collaborations;

(II) the model should still be generic enough to be used in the context of broader, more complete theoretical frameworks;

(III) the model should have a sufficiently varied phenomenology to encourage comparison of different experimental signals and to search for DM in new, unexplored channels;

(IV) the model should be of interest beyond the DM community, to the point that other direct and indirect constraints can be identified.

The 2HDM+S and 2HDM+PS, which we will analyze in this chapter, are two notable examples of these next-generation DM models. Within these models, as their name suggests, we have in addition to a second Higgs doublet a singlet scalar or pseudoscalar, which couples to a fermionic singlet DM particle. Since the scalar or pseudoscalar can mix with the CP-even or CP-odd states of the two Higgs doublets sector, their interactions with the DM are not secluded from the SM sector. Thus, both of these next-generation DM models lead to a rich collider phenomenology beyond the expected simple MET signatures (cf. [134, 142, 158–161]).

In an effort to better understand the LHC phenomenology of both models, we will analyze the LHC channels that provide the strongest bounds, namely $t\bar{t}$ resonance, mono-Z and mono-h searches. Although the 2HDM+S and 2HDM+PS are very similar by construction and all of these signatures appear in both models, we will show that there can be sizable differences between the signal rates of the scalar and pseudoscalar version. Our aim is thus to characterize and understand the similarities and differences of the respective signatures of the two models, by contrasting the limits on the parameter space that can be derived from current LHC data and analyses. Furthermore, we will project the reach of the mono-Z limits for LHC upgrades and comment on possibilities to distinguish between the 2HDM+S and 2HDM+PS in case of a signal detection. Our analysis goes beyond the existing literature by updating some of the available LHC results on the 2HDM+PS (cf. [134, 160]) and providing new results for the 2HDM+S, together with a comparison of both of these models. We remark that the work and results presented in this chapter are based on Ref. [162].

4.1 Model Description of the 2HDM + Scalar / Pseudoscalar

The two models we want to analyze and compare both have an enlarged scalar sector by including a second Higgs doublet together with an additional singlet scalar and therefore a more complex scalar potential than the SM. Additionally, the new scalars can interact via Yukawa interactions with the SM fermions, which we will look at after considering the effects of the modified scalar potential. Furthermore, these models have been widely studied in the literature (cf. e.g. [142, 153, 160, 163–166]), so we will keep the following model description brief as it serves to lay out our parameter space and the notation we will be using.

4.1.1 Scalar Potential

As the scalar potentials of the 2HDM+S and 2HDM+PS are very similar, we will use the notation for the 2HDM+S, but discuss them together as a general two Higgs doublet model with an additional (pseudo)scalar. After having laid out our general assumptions and identified the coefficient that discriminates between the scalar and pseudoscalar model, we will then introduce the equations for the pseudoscalar case, such that each parameter associated with the singlet sector can be clearly identified as belonging to the 2HDM+S or 2HDM+PS.

In general, the scalar potential can be split up into

$$V(\Phi_1, \Phi_2, S) = V_{2\text{HDM}}(\Phi_1, \Phi_2) + V_S(S) + V_{S2\text{HDM}}(\Phi_1, \Phi_2, S)\,, \tag{4.1}$$

with $V_{2\text{HDM}}$ being the standard 2HDM potential, V_S the potential of the scalar singlet and $V_{S2\text{HDM}}$ the potential responsible for interactions between the scalar singlet and the doublets. The two Higgs doublets in $V_{2\text{HDM}}$ have identical charges and thus allow us the freedom to choose a specific base Φ_1, Φ_2 in terms of which to write the potential. A general $SU(2)$ basis change,

$$\begin{pmatrix} \Phi_1 \\ \Phi_2 \end{pmatrix} \to \begin{pmatrix} \Phi_1^{'} \\ \Phi_2^{'} \end{pmatrix} = U \begin{pmatrix} \Phi_1 \\ \Phi_2 \end{pmatrix} \tag{4.2}$$

where U is an arbitrary $SU(2)$ matrix, leads to a potential that results in the same physics but enables us to shift the weight of different terms as their coefficients change due to the $SU(2)$ transformation. Although it is possible to get rid of this residual freedom by basis independent methods [167–169], we will focus on two reference bases that are suited for our purposes. First, we have the flavor basis, which is well suited to analyze the interactions of the doublets with the fermions under the assumption that the Yukawa interactions in the 2HDM are of the usual types: I, II, X, Y or Inert. We will describe the Yukawa interactions and their different types mentioned here in more detail in Sec. 4.1.3. Then, the basis Φ_1, Φ_2 is defined by which of the two Higgs doublets interacts with the different fermions. Second, there is the Higgs basis, which simplifies the treatment of the Higgs doublets as one of them does not have a vev in that basis. To distinguish these two bases, we will label the coefficients differently depending on which basis we are in. For the coefficients in the flavor basis we will use λ_i, M_{ij}, whereas the same quantities with a hat $\hat{\lambda}_i, \hat{M}_{ij}$ express the coefficients in the Higgs basis. For the doublets we will use the above mentioned Φ_1, Φ_2 in the flavor basis, while in the Higgs basis we will refer to them as Φ_h, Φ_H.

For the 2HDM potential in the flavor basis we have

$$\begin{aligned} V_{2\text{HDM}}(\Phi_1, \Phi_2) = {} & M_{11}^2 \Phi_1^\dagger \Phi_1 + M_{22}^2 \Phi_2^\dagger \Phi_2 + (M_{12}^2 \Phi_2^\dagger \Phi_1 + \text{h.c.}) + \frac{\lambda_1}{2}(\Phi_1^\dagger \Phi_1)^2 + \frac{\lambda_2}{2}(\Phi_2^\dagger \Phi_2)^2 \\ & + \lambda_3 (\Phi_1^\dagger \Phi_1)(\Phi_2^\dagger \Phi_2) + \lambda_4 (\Phi_2^\dagger \Phi_1)(\Phi_1^\dagger \Phi_2) + \frac{1}{2}\left(\lambda_5 (\Phi_2^\dagger \Phi_1)^2 + \text{h.c.}\right), \end{aligned} \tag{4.3}$$

where a $\mathbb{Z}_2$ symmetry $\Phi_1 \to \Phi_1,\ \Phi_2 \to -\Phi_2$ has been imposed to suppress flavor changing neutral currents (FCNCs), thus removing the additionally possible terms $\lambda_{6,7}$ containing

three Φ_1 doublets and one Φ_2 doublet and vice versa. However, we still allow for a soft breaking of the $\mathbb{Z}_2$ symmetry via the M_{12}^2 term, which is necessary for the minimum to be the global minimum of the scalar potential [153, 161, 170]. Furthermore, we also assume that the potential does not break CP explicitly. This implies that $(M_{12}^2)^2$ and λ_5 are required to have the same phase (up to a relative sign) and we can absorb this phase by a field redefinition into Φ_2. Thus, we take the parameters λ_i, M_{ij} to be real and the freedom of the $SU(2)$ basis change mentioned above reduces to $SO(2)$ rotations:

$$\begin{pmatrix} \Phi_1 \\ \Phi_2 \end{pmatrix} \to \begin{pmatrix} \Phi_1' \\ \Phi_2' \end{pmatrix} = \begin{pmatrix} \cos\beta & \sin\beta \\ -\sin\beta & \cos\beta \end{pmatrix} \begin{pmatrix} \Phi_1 \\ \Phi_2 \end{pmatrix}. \tag{4.4}$$

This leaves us with the other two terms of Eq. (4.1) that are, in their most general form, given by

$$V_S(S) = \frac{1}{2}M_{SS}^2 S^2 + \frac{1}{3}\mu_S S^3 + \frac{1}{4}\lambda_S S^4\,, \tag{4.5}$$

$$\begin{aligned} V_{S2\text{HDM}}(\Phi_1,\Phi_2,S) = {} & \mu_{11S}(\Phi_1^\dagger\Phi_1)S + \mu_{22S}(\Phi_2^\dagger\Phi_2)S + (\mu_{12S}\Phi_2^\dagger\Phi_1 S + \text{h.c.}) \\ & + \frac{\lambda_{11S}}{2}(\Phi_1^\dagger\Phi_1)S^2 + \frac{\lambda_{22S}}{2}(\Phi_2^\dagger\Phi_2)S^2 + \frac{1}{2}(\lambda_{12S}\Phi_2^\dagger\Phi_1 S^2 + \text{h.c.})\,. \end{aligned} \tag{4.6}$$

Here, again, a $\mathbb{Z}_2$ symmetry can lead to a smaller number of allowed terms in these parts of the scalar potential. For a $\mathbb{Z}_2$ symmetry of the kind $S \to -S$, the terms with the coefficients μ_S, μ_{11S} and μ_{22S} would be forbidden, except for the case of a soft breaking of the $\mathbb{Z}_2$ symmetry. On the other hand, the λ_{12S} term is always forbidden due to the assumed $\mathbb{Z}_2$ symmetry of the Higgs fields. However, as these terms only affect the scalar trilinear and quartic interactions, their impact on the LHC phenomenology we will discuss is negligible and we will therefore, in line with [160], not include them (set them to zero) in our analysis.

The coefficients of the scalar interaction potential, Eq. (4.6), need to be real as well, except for λ_{12S} and μ_{12S}. Since λ_{12S} is forced to zero by the assumed $\mathbb{Z}_2$ symmetry on the Higgs doublet fields, the only remaining possible phase is the one of μ_{12S} (after appropriate rotations of the Higgs doublets to absorb all phases in Eq. (4.3)). To conserve CP, there are then only two possible choices for this coefficient, either purely real or imaginary. If it is purely real, the CP-even states in the Higgs doublets Φ_1 and Φ_2 can mix with the singlet scalar, while if it is purely imaginary, the corresponding CP-odd states can mix with the (then pseudo)scalar. Consequently, this is the coefficient that differentiates the 2HDM+S and 2HDM+PS, by being purely real for the scalar case and purely imaginary for the pseudoscalar case.

Thus, we will now restate the relevant equations for the 2HDM+PS, which was introduced in [163] and had its LHC bounds discussed in [160], where we use instead of an index S now an index P to make the parameters distinguishable and emphasize the pseudoscalar nature of the singlet. For the potential we have

$$V(\Phi_1,\Phi_2,P) = V_{2\text{HDM}}(\Phi_1,\Phi_2) + V_P(P) + V_{P2\text{HDM}}(\Phi_1,\Phi_2,P)\,, \tag{4.7}$$

where V_{2HDM} is identical to Eq. (4.3), while

$$V_P(P) = \frac{1}{2}\, M_{PP}^2 P^2 + \frac{1}{4}\,\lambda_P P^4\,, \tag{4.8}$$

$$V_{P2\text{HDM}}(\Phi_1,\Phi_2,P) = \frac{\lambda_{11P}}{2}\,(\Phi_1^\dagger\Phi_1)P^2 + \frac{\lambda_{22P}}{2}\,(\Phi_2^\dagger\Phi_2)P^2 + \mu_{12P}P(i\Phi_1^\dagger\Phi_2 + \text{h.c.})\,, \tag{4.9}$$

with

$$\Phi_i = \begin{pmatrix} \Phi_i^+ \\ \frac{v_i+\rho_i+i\eta_i}{\sqrt{2}} \end{pmatrix}, \qquad P = \eta_3\,, \tag{4.10}$$

and $v_{1,2}$ are usually parameterized in terms of

$$\tan\beta = \frac{v_2}{v_1}\,, \qquad \text{with} \qquad v_1^2 + v_2^2 = v^2 \tag{4.11}$$

and $v = 246\,\text{GeV}$ is the SM Higgs vev. In these equations, $\rho_{1,2}$ are CP-even scalar particles and $\eta_{1,2,3}$ are CP-odd scalar particles, but they do not have to be mass eigenstates.

As mentioned in our discussion of the different bases, we can rotate the flavor basis doublets $\{\Phi_1,\Phi_2\}$ into the Higgs basis $\{\Phi_h,\Phi_H\}$, in which we have $\langle\Phi_H\rangle = 0$ and $\langle\Phi_h\rangle = v$. This turns out to be handy and changes the potential to

$$\hat{V}(\Phi_h,\Phi_H,P) = \hat{V}_{2\text{HDM}}(\Phi_h,\Phi_H) + \hat{V}_P(P) + \hat{V}_{P2\text{HDM}}(\Phi_h,\Phi_H,P)\,, \tag{4.12}$$

where the different contributions are given by

$$\begin{aligned}\hat{V}_{2\text{HDM}}(\Phi_h,\Phi_H) = {}& \hat{M}_{hh}^2\Phi_h^\dagger\Phi_h + \hat{M}_{HH}^2\Phi_H^\dagger\Phi_H + (\hat{M}_{hH}^2\Phi_H^\dagger\Phi_h + \text{h.c.}) \\ & + \frac{\hat{\lambda}_h}{2}(\Phi_h^\dagger\Phi_h)^2 + \frac{\hat{\lambda}_H}{2}(\Phi_H^\dagger\Phi_H)^2 \\ & + \hat{\lambda}_3(\Phi_h^\dagger\Phi_h)(\Phi_H^\dagger\Phi_H) + \hat{\lambda}_4(\Phi_H^\dagger\Phi_h)(\Phi_h^\dagger\Phi_H) + \frac{\hat{\lambda}_5}{2}\left((\Phi_H^\dagger\Phi_h)^2 + \text{h.c.}\right) \\ & + \hat{\lambda}_6\Phi_h^\dagger\Phi_h\left((\Phi_H^\dagger\Phi_h)^2 + \text{h.c.}\right) + \hat{\lambda}_7\Phi_H^\dagger\Phi_H\left((\Phi_H^\dagger\Phi_h)^2 + \text{h.c.}\right),\end{aligned} \tag{4.13}$$

$$\hat{V}_P(P) = \frac{1}{2}\,\hat{M}_{PP}^2 P^2 + \frac{\hat{\lambda}_P}{4}\,P^4\,, \tag{4.14}$$

$$\begin{aligned}\hat{V}_{P2\text{HDM}}(\Phi_h,\Phi_H,P) = {}& \frac{\hat{\lambda}_{HHP}}{2}\,\Phi_H^\dagger\Phi_H P^2 + \frac{\hat{\lambda}_{hhP}}{2}\,\Phi_h^\dagger\Phi_h P^2 + \frac{\hat{\lambda}_{hHP}}{2}P^2(\Phi_H^\dagger\Phi_h + \text{h.c.}) \\ & + \mu_{12P}P\left(i\Phi_h^\dagger\Phi_H + \text{h.c.}\right).\end{aligned} \tag{4.15}$$

For the two Higgs doublets, we then have

$$\Phi_h = \cos\beta\;\Phi_1 + \sin\beta\;\Phi_2 = \begin{pmatrix} G^+ \\ \frac{v+\hat{\rho}_1+iG^0}{\sqrt{2}} \end{pmatrix}, \tag{4.16}$$

$$\Phi_H = -\sin\beta\;\Phi_1 + \cos\beta\;\Phi_2 = \begin{pmatrix} H^+ \\ \frac{\hat{\rho}_2+i\hat{\eta}_2}{\sqrt{2}} \end{pmatrix}, \tag{4.17}$$

with the SM Goldstone bosons $G^{\pm}$ and G^0, and the charged scalar $H^{\pm}$, which are all mass eigenstates. The CP-even scalars $\hat{\rho}_{1,2}$ can in general mix and result in the mass eigenstates of the SM Higgs boson h and an additional heavy scalar H. Similarly, the CP-odd scalars $\hat{\eta}_2, \hat{\eta}_3$ also mix due to the μ_{12P} coupling and lead to the pseudoscalar mass eigenstates a and A, where we choose our notation such that in general we have $M_a < M_A$. Note that the terms $\lambda_6, \lambda_7, \lambda_{hHP}$ can arise due to the change of basis and that the coefficient of the term $P\left(i\Phi_h^\dagger \Phi_H + \text{h.c.}\right)$ is invariant under this basis change.

For the 2HDM+S there are in principle two possible ways to obtain the mixing between the different CP-even or CP-odd states. One option would be to proceed analogously to the 2HDM+PS described above, only with μ_{12S} being purely real valued. However, we will follow the second way here, as done by [142, 153], where the mixing is due to a vev of the singlet and not the μ_{12S} term (cf. Ch. 3, where also the singlet vev leads to mixing). In this second way, one assumes a spontaneously broken $\mathbb{Z}_2$ symmetry $S \to -S$, which removes all odd terms with respect to S in the potential, including the μ_{12S} term. This could for example arise in theories where S is part of a complex scalar charged under a dark $U(1)$ gauge group. Following [142], the potential given directly in the Higgs basis is

$$\hat{V}(\Phi_h, \Phi_H, S) = \hat{V}_{2\text{HDM}}(\Phi_h, \Phi_H) + \hat{V}_S(S) + \hat{V}_{S2\text{HDM}}(\Phi_h, \Phi_H, S)\,, \tag{4.18}$$

with

$$\begin{aligned}\hat{V}_{2\text{HDM}}(\Phi_h, \Phi_H) = {} & \hat{M}_{hh}^2 \Phi_h^\dagger \Phi_h + \hat{M}_{HH}^2 \Phi_H^\dagger \Phi_H + (\hat{M}_{hH}^2 \Phi_H^\dagger \Phi_h + \text{h.c.}) \\ & + \frac{\hat{\lambda}_h}{2}(\Phi_h^\dagger \Phi_h)^2 + \frac{\hat{\lambda}_H}{2}(\Phi_H^\dagger \Phi_H)^2 + \hat{\lambda}_3 (\Phi_h^\dagger \Phi_h)(\Phi_H^\dagger \Phi_H) \\ & + \hat{\lambda}_4 (\Phi_H^\dagger \Phi_h)(\Phi_h^\dagger \Phi_H) + \frac{\hat{\lambda}_5}{2}\left((\Phi_H^\dagger \Phi_h)^2 + \text{h.c.}\right),\end{aligned} \tag{4.19}$$

$$\hat{V}_S(S) = \frac{1}{2}\hat{M}_{SS}^2 S^2 + \frac{\hat{\lambda}_S}{4} S^4\,, \tag{4.20}$$

$$\hat{V}_{S2\text{HDM}}(\Phi_h, \Phi_H, S) = \frac{\hat{\lambda}_{HHS}}{2}\,\Phi_H^\dagger \Phi_H S^2 + \frac{\hat{\lambda}_{hhS}}{2}\,\Phi_h^\dagger \Phi_h S^2 + \frac{1}{2}\left(\hat{\lambda}_{hHS} \Phi_H^\dagger \Phi_h S^2 + \text{h.c.}\right), \tag{4.21}$$

and

$$\Phi_h = \begin{pmatrix} G^+ \\ \frac{v + \hat{\rho}_1 + iG^0}{\sqrt{2}} \end{pmatrix}, \tag{4.22}$$

$$\Phi_H = \begin{pmatrix} H^+ \\ \frac{\hat{\rho}_2 + iA}{\sqrt{2}} \end{pmatrix}, \tag{4.23}$$

$$S = v_s + \hat{\rho}_3\,. \tag{4.24}$$

Here, we have in addition to the SM Goldstone bosons $G^{0,\pm}$ and the charged scalars $H^{\pm}$, a single CP-odd scalar A and three CP-even scalars $\hat{\rho}_{1,2,3}$. These CP-even scalars can all mix and result in the SM Higgs boson h together with two new scalar particles $S_{1,2}$. In comparison to the 2HDM+PS, the role of the lighter new (pseudo)scalar particle is now

filled by S_2, so in general we have $M_{S_2} < M_{S_1}$. Note that in terms of the potential and in contrast to the pseudoscalar case, the terms $\hat{\lambda}_{6,7}$ are generally absent in the Higgs basis.

4.1.2 Scalar Mass Spectrum, Couplings and Alignment Limit

As the Higgs boson observed at the LHC [130, 131] behaves experimentally very similar to the Higgs boson predicted by the SM, the models we want to investigate have to include a SM Higgs-like boson with $M_h = 125\,\text{GeV}$. In this way, the model automatically fulfills most of the constraints from Higgs physics. To ensure that our model parameters lead to such a Higgs-like bosons we will work in the so-called alignment limit [171, 172]. The alignment limit restricts the accessible parameter space in a way such that the mixing between $\hat{\rho}_1$ and $\hat{\rho}_2$ is negligible and $\hat{\rho}_1$ can be identified with the experimentally observed (CP-even) Higgs boson at 125 GeV.

For our models, there are two possible ways to achieve this. One way is to set β, the parameter associated to the ratio of the Higgs vevs, to (cf. e.g. [153])

$$\cos(2\beta) = -\frac{\lambda_1 - \lambda_2}{\lambda_1 + \lambda_2 - 2(\lambda_3 + \lambda_4 + \lambda_5)}\,, \tag{4.25}$$

while it is also possible to assume a CP2 symmetry [173] that enforces

$$\lambda_1 = \lambda_2 = \lambda_3 + \lambda_4 + \lambda_5\,. \tag{4.26}$$

The CP2 symmetry alignment limit comes with the additional benefit of simplifying the basis change between the flavor and the Higgs basis, as one finds the relations $\lambda_1 = \hat{\lambda}_h$, $\lambda_2 = \hat{\lambda}_H$, $\lambda_i = \hat{\lambda}_i$ for $i = 3, 4, 5$ and $\hat{\lambda}_{6,7} = 0$. Furthermore, as Eq. (4.26) is independent of $\tan\beta$ whereas Eq. (4.25) is not, enforcing the CP2 symmetry makes it possible to vary $\tan\beta$ independent of the couplings λ_i, which is why we will use it in our analysis. Since we achieved mixing in the 2HDM+S through a non-zero singlet vev and therefore differently to the 2HDM+PS, we need for the alignment limit in the 2HDM+S in addition to Eq. (4.25) or (4.26) also the condition [153]

$$\hat{\lambda}_{hhS} = 0\,. \tag{4.27}$$

By employing the alignment limit through Eq. (4.25) or (4.26) (together with Eq. (4.27) in the scalar case), the corresponding mass matrix becomes block-diagonal. For the 2HDM+PS, we find two zero eigenvalues that correspond to the Goldstone bosons G^0, $G^\pm$, the CP-even non-mixing part of the two Higgs doublets result in M_h^2, $M_{H^\pm}^2$, M_H^2, and the CP-odd mixing part results after a diagonalization in two pseudoscalar particles with squared masses M_a^2, M_A^2. The corresponding mixing angle between the two pseudoscalar particles θ is then given by

$$\sin(2\theta) = \frac{2\,v\,\mu_{12P}}{M_A^2 - M_a^2}\,. \tag{4.28}$$

This procedure enables us to switch to a more intuitive set of parameters, by changing from the original parameters $\lambda_{1,2,4,5}$, M_{11}^2, M_{22}^2, M_{12}^2, M_{PP}^2, μ_{12P} to the new set of parameters M_h, M_H, $M_{H^\pm}$, M_A, M_a, θ, $\tan\beta$, v, together with the alignment condition. Of the

remaining parameters, λ_{11P}, λ_{22P}, λ_P stay free parameters of the theory, while λ_3 gets fixed if the CP2 symmetry version of the alignment condition is chosen (cf. Eq. (4.26)).

Following the same steps for the 2HDM+S, we find in the block-diagonal matrix two zeroes for the Goldstone bosons G^0, $G^\pm$, the mixing independent squared masses M_h^2, $M_{H^\pm}^2$, M_A^2 and a CP-even mixing part resulting after a diagonalization in two scalar particles with squared masses $M_{S_2}^2$, $M_{S_1}^2$. The corresponding mixing angle between the two scalar particles, which we will also refer to as θ, is similarly (in the Higgs basis) given by

$$\sin(2\theta) = \frac{2\hat{\lambda}_{hHs}\, v\, v_S}{M_{S_1}^2 - M_{S_2}^2}\,. \tag{4.29}$$

Again, this enables switching to more intuitive parameters, through going from $\lambda_{1,2,4,5}$, M_{11}^2, M_{22}^2, M_{12}^2, M_{SS}^2, v_S to the parameters M_h, M_{S_1}, $M_{H^\pm}$, M_A, M_{S_2}, θ, $\tan\beta$, v, together with the alignment condition. By means of the additional alignment condition in the scalar case, Eq. (4.27), the parameter λ_{11S} is fixed. Similar to the pseudoscalar case, of the remaining parameters, λ_{22S}, λ_S stay free parameters of the theory, while λ_3 gets fixed if the CP2 symmetry version of the alignment condition is chosen (cf. Eq. (4.26)).

As we will discuss later on, electroweak precision constraints are very restrictive if the scalars that are mostly doublet do not have very similar masses. Thus we will work with the degenerate masses assumption $M_H = M_{H^\pm} = M_A > M_a$ and $M_A = M_{H^\pm} = M_{S_1} > M_{S_2}$, where the last relations refer to the above mentioned mass ordering we assume for the particles that result from the mixing. These relations also show one of the correspondences between the different particles in the 2HDM+PS and 2HDM+S. While the heavy pseudoscalar A, the charged Higgses $H^\pm$ and the heavy scalar $H \leftrightarrow S_1$ appear in both models, corresponding roles are taken on by the light pseudoscalar a and light scalar S_2, such that we have the correspondence $a \leftrightarrow S_2$.

Since we want to compare the 2HDM+PS and 2HDM+S, we need to ensure that the parameters are comparable. To do so, we choose the CP2 symmetry version of the alignment condition (cf. Eq. (4.26)), which fixes λ_3, and decide to set from now on

$$\hat{\lambda}_{hhS} = 0 = \hat{\lambda}_{HHS}\,, \tag{4.30}$$

$$\hat{\lambda}_{hhP} = 0 = \hat{\lambda}_{HHP}\,, \tag{4.31}$$

or equivalently

$$\lambda_{11S} = 0 = \lambda_{22S}\,, \tag{4.32}$$

$$\lambda_{11P} = 0 = \lambda_{22P}\,. \tag{4.33}$$

Ensuring these comparable values for the above couplings (and their particular value) is most relevant for the Aah vertex in the pseudoscalar model and the $S_1 S_2 h$ vertex in the scalar model, which are both relevant vertices for the corresponding mono-h searches (cf. Fig. 4.11 in Sec. 4.3.4 on mono-h searches). Explicitly, these vertices depend on the

respective couplings g_{Aah} and $g_{S_1S_2h}$ that depend on the above parameters via (cf. App. D)

$$\hat{\lambda}_{hhS} = \lambda_{11S}\cos^2\beta + \lambda_{22S}\sin^2\beta\,, \tag{4.34}$$

$$\hat{\lambda}_{hhP} = \lambda_{11P}\cos^2\beta + \lambda_{22P}\sin^2\beta\,. \tag{4.35}$$

The last parameters which we have not discussed above, are the quartic self-couplings λ_P and λ_S. However, both of them do not play a role for the $t\bar{t}$, mono-Z and mono-h resonance signatures we will be looking at.

4.1.3 Yukawa Sector

After having discussed the scalar potential and its couplings, we now turn to the interactions of the SM fermions with the two Higgs doublets. These Yukawa interactions can be expressed in the Lagrangian

$$L_{\text{Yukawa}} = -\sum_{n=1,2}\left(Y^u_{n,ij}\bar{Q}^i_L u^j_R\widetilde{\Phi}_n + Y^d_{n,ij}\bar{Q}^i_L d^j_R\Phi_n + Y^l_{n,ij}\bar{L}^i_L l^j_R\Phi_n + \text{h.c.}\right), \tag{4.36}$$

with the Yukawa coupling matrices to up-type quarks / down-type quarks / leptons $Y^{u/d/l}_{n,ij}$, the left-handed quark doublets Q^i_L, the right-handed quarks u^j_R / d^j_R, the left-handed lepton doublets L^i_L and the right-handed leptons l^j_R. As common for 2HDMs, we need to choose the Yukawa matrices in a way such that flavor violating processes are suppressed.

Since we are interested in how the Yukawa interactions look like with respect to the Higgs mass eigenstates h and H, we rewrite Eq. (4.36) in the Higgs basis and obtain

$$L_{\text{Yukawa}} = -\sum_{n=h,H}\left(\hat{Y}^u_{n,ij}\bar{Q}^i_L u^j_R\widetilde{\Phi}_n + \hat{Y}^d_{n,ij}\bar{Q}^i_L d^j_R\Phi_n + \hat{Y}^l_{n,ij}\bar{L}^i_L l^j_R\Phi_n + \text{h.c.}\right). \tag{4.37}$$

To reproduce the Yukawa interactions of the SM Higgs, the corresponding Yukawa matrices $\hat{Y}^{u/d/l}_h$ have to be identical to the SM ones, so

$$\hat{Y}^{u/d/l}_h = \hat{Y}^{u/d/l}_{\text{SM}}\,, \tag{4.38}$$

while to avoid FCNCs, we can choose the Yukawa couplings associated with the new heavy Higgs H to be proportional to the SM ones

$$\hat{Y}^{u/d/l}_H = \varepsilon_{u/d/l}\hat{Y}^{u/d/l}_{\text{SM}}\,, \tag{4.39}$$

with the Yukawa scaling factors $\varepsilon_{u/d/l}$. These values for the Yukawa matrices are the so-called aligned Yukawa model [174–180], which reduces for specific values of the Yukawa scaling factors $\varepsilon_{u/d/l}$ to the different $\mathbb{Z}_2$ symmetric Yukawa structures (type I, II, X or Y), as shown in Tab. 4.1. The underlying assumption of the $\mathbb{Z}_2$ symmetric Yukawa structures is that there is a $\mathbb{Z}_2$ symmetry in the Yukawa sector, which allows only one of the two Higgs doublets $\Phi_{1,2}$ to couple to a certain type of quarks / leptons and is usually referred to as natural flavor conservation (NFC). However, there can still be flavor violation at loop level through the presence of the charged Higgs $H^\pm$, which in principle allows to

Model	ε_d	ε_u	ε_l
Type I	$\cot\beta$	$\cot\beta$	$\cot\beta$
Type II	$-\tan\beta$	$\cot\beta$	$-\tan\beta$
Type X	$\cot\beta$	$\cot\beta$	$-\tan\beta$
Type Y	$-\tan\beta$	$\cot\beta$	$\cot\beta$
Inert	0	0	0

Table 4.1.: Values of the Yukawa scaling factors $\varepsilon_{u,d,l}$ that correspond to the different $\mathbb{Z}_2$ symmetric Yukawa structures.

set limits on $\tan\beta$ and $M_{H^\pm}$ (cf. e.g. [174, 181]). For our analysis, we will focus on the parameter region $0.3 \leq \tan\beta \leq 3$, which has the advantage that the different types of Yukawa structures of Tab. 4.1 all behave very similar, except for the inert one, and our results hold (approximately) irrespective of which specific type is chosen. Whenever necessary to specify a type, for example for the explicit formulas of branching ratios, we will use the type-I scenario of the Yukawa structures.

In addition to the Yukawa couplings of the two Higgs doublets, there is also a Yukawa coupling of the singlet to the DM particle χ with mass m_χ. In the flavor basis, these interactions are described either by

$$\mathcal{L}_{\text{DM}} = -y_\chi^S \, S \, \bar{\chi}\chi \,, \tag{4.40}$$

for the scalar model, or by

$$\mathcal{L}_{\text{DM}} = -y_\chi^P \, P \, \bar{\chi}\gamma^5\chi \,, \tag{4.41}$$

for the pseudoscalar model. These interactions with the DM are passed on via the mixing of the (pseudo)scalar singlet to the (CP-odd) CP-even part of the scalar doublets. Thus, the DM particle is not secluded from the 2HDM part of the model.

4.1.4 Decay Widths and Branching Ratios

With the masses and couplings at hand, we can now look in more detail at the branching ratios (BRs) of the four neutral scalar states in the 2HDM+PS (h, a, H, A) and 2HDM+S (h, S_2, S_1, A), which will be helpful for our analysis of the different LHC signatures later on. The corresponding analytic expressions for the dominant decay widths are, together with the ones for the charged scalars, given in App. D. For the model parameters of all BR plots shown here, we choose the values given by the parameter overview of Eq. (4.46) and additionally set $M_A = 500\,\text{GeV}$ and $\tan\beta = 1$, where the value of $\tan\beta$ implies that the results are applicable to all types of the Yukawa structure except for the inert one (cf. Tab. 4.1). These values are representative of our parameter space of interest and therefore allow us to gain insight into how the BRs behave in the region of interest. Since the mass of the light new (pseudo)scalar M_{a/S_2} is the most important quantity with the masses of the heavy scalars and pseudoscalars fixed, we will look at the different BRs in terms of its mass.

Starting out with the SM Higgs-like scalar h, we find for the BRs the results depicted in

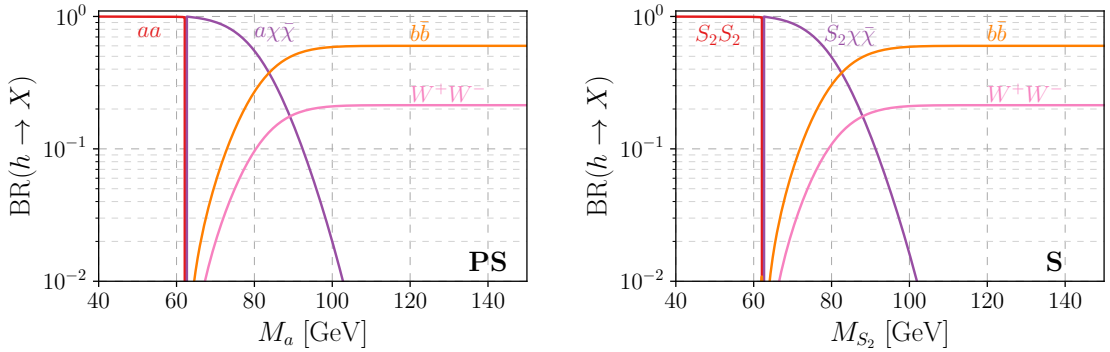

Figure 4.1.: Dominant branching ratios of the SM Higgs-like scalar h for $M_A = 500\,\text{GeV}$, $\tan\beta = 1$, $m_\chi = 10\,\text{GeV}$ and other parameter values as given by the parameter overview of Eq. (4.46) in the 2HDM+PS (left) and 2HDM+S (right).

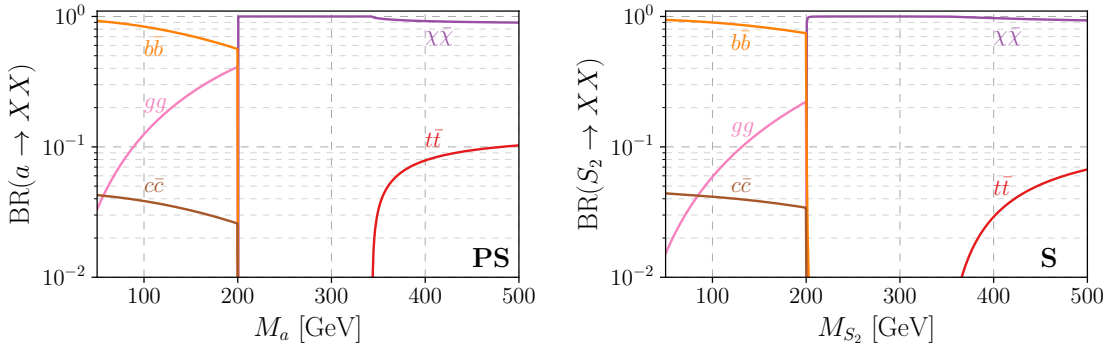

Figure 4.2.: Dominant branching ratios of the light (pseudo)scalar (a) S_2 for $M_A = 500\,\text{GeV}$, $\tan\beta = 1$, $m_\chi = 100\,\text{GeV}$ and other parameter values as given by the parameter overview of Eq. (4.46) in the 2HDM+PS (left) and 2HDM+S (right). The DM mass m_χ was set to 100 GeV to also show the decay channels below $2m_\chi$.

Fig. 4.1. As we work in the alignment limit (cf. Sec. 4.1.2), the couplings of h essentially coincide with the couplings of the SM Higgs boson. However, the total decay width can differ from the SM value due to additional possible decay channels. These additional decay channels are dominantly $h \to aa$ or respectively $h \to S_2S_2$, if these decays are kinematically allowed, and the three body decays $h \to a\chi\bar{\chi}$ or respectively $h \to S_2\chi\bar{\chi}$ above the kinematically accessible region of the two-body decays (half the SM Higgs mass). For the $h \to SM$ decays, we only show the two largest BRs to $b\bar{b}$ and W^+W^-. Comparing the 2HDM+PS and 2HDM+S, we see that both models behave practically identical, except for the particles h can decay to having different names.

The BRs for a/S_2, shown in Fig. 4.2, are especially in the region above $M_{a/S_2} > 2m_\chi$ also very similar, except for a slight preference to decay into $t\bar{t}$ for the 2HDM+PS. Both BRs are dominated by the decay into DM ($\chi\bar{\chi}$) as long as that channel is kinematically

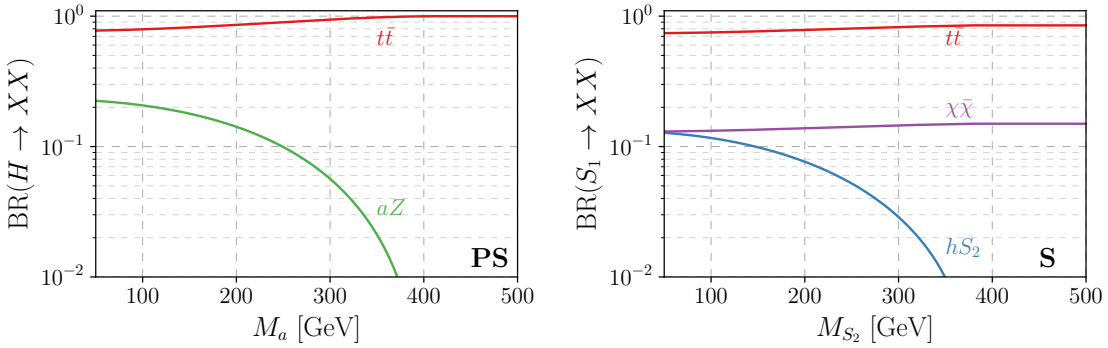

Figure 4.3.: Dominant branching ratios of the heavy scalar H / S_1 for $M_A = 500\,\text{GeV}$, $\tan\beta = 1$, $m_\chi = 10\,\text{GeV}$ and other parameter values as given by the parameter overview of Eq. (4.46) in the 2HDM+PS (left) and 2HDM+S (right).

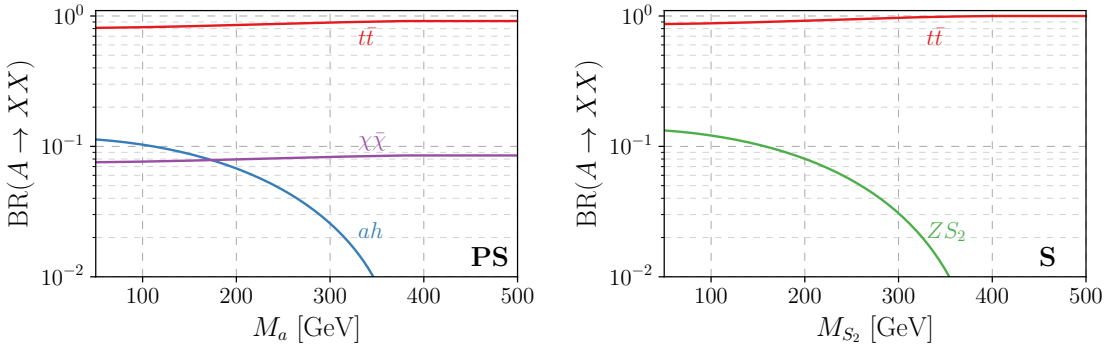

Figure 4.4.: Dominant branching ratios of the heavy pseudoscalar A for $M_A = 500\,\text{GeV}$, $\tan\beta = 1$, $m_\chi = 10\,\text{GeV}$ and other parameter values as given by the parameter overview of Eq. (4.46) in the 2HDM+PS (left) and 2HDM+S (right).

allowed. This behavior is expected, since the light (pseudo)scalar state is mostly singlet like and therefore the coupling to DM is nearly unsuppressed (by $\cos^2\theta$), while the other decay channels are introduced by mixing and thus scale like $\sin^2\theta$. The region below $M_{a/S_2} < 2m_\chi$ is shown for completeness and will not be relevant to our analysis since we assume the DM to be light.

For the decay channels of the heavy scalars H/S_1 and pseudoscalars A, we can find from Fig. 4.3 (H/S_1) and Fig. 4.4 (A) that they are exchanged between the 2HDM+PS and 2HDM+S. This correspondence of decay channels comes as no surprise because in both cases the component that is involved in the mixing couples to the DM (albeit suppressed by $\sin^2\theta$), so the heavy pseudoscalar A in the 2HDM+PS and the heavy scalar S_1 in the 2HDM+S. Similarly, also the non-mixing components show a comparable behavior. One feature that all of the four depicted decay channels share is that they are dominated by the decay to top quarks, which reflects the comparably large top-Yukawa coupling with respect to the other fermions. For the mono-h and mono-Z signatures that we will be looking at, the important decay channels are $A \to ah$ and $H \to aZ$ in the 2HDM+PS together

with $S_1 \to S_2 h$ and $A \to S_2 Z$ in the 2HDM+S. While the corresponding processes have a similar shape in all cases and the absolute values of the BRs are similar for the decays leading to mono-h signatures, $\mathrm{BR}(H \to Za)$ in the pseudoscalar model is bigger by roughly a factor of two in comparison to $\mathrm{BR}(A \to ZS_2)$ in the scalar model. The reason is that scalar particles have a smaller decay width to quarks than pseudoscalar particles, thus leading to a smaller total decay width of the scalar particle H in the 2HDM+PS, which finally results in a larger BR for the process $H \to Za$ compared to $A \to ZS_2$. This effect will become important when we interpret and compare our results for different signatures.

4.2 Overview of Model Constraints

Before we look at the constraints due to collider searches for $t\bar{t}$, mono-Z and mono-h resonance signatures in the next section, we will discuss other collider and non-collider constraints on the 2HDM+PS and 2HDM+S here. The focus of this section is to assess how the parameter space of the two models is restricted due to these other searches and thereby to guide us in choosing sensible parameter ranges for our analysis. A more detailed discussion of the different limits can be found in Ref. [162].

4.2.1 Non-Collider Constraints

In terms of non-collider constraints, we have in general constraints from DD and ID experiments together with searches for flavor violation, as well as parameter space restriction to achieve the correct DM relic density and theoretical bounds from considerations of perturbativity and unitarity.

The DD phenomenology is rather different for the 2HDM+PS and 2HDM+S, due to the (pseudo)scalar character of the additional scalar singlet that couples to DM. While the spin independent (SI) interactions, which are most strongly constrained by experiments, appear at tree level for the scalar model (cf. [142, 153, 182]), they are only present at loop level for the pseudoscalar model (cf. [164, 165, 182–187]). Thus, DM masses in the typical WIMP range of a few hundred GeV are tightly constrained for the scalar model but only within the range of next-generation DD experiments like XENONnT and DARWIN for the pseudoscalar model (cf. [163, 188]). Therefore, we will focus on the complementary region of parameter space of light DM, explicitly $m_\chi = 10\,\mathrm{GeV}$, for our analysis of collider signatures.

For ID and relic density bounds, both in the scalar [142] and pseudoscalar model [134], there are no constraining limits for light DM due to ID and it is usually possible to achieve the correct relic density by an appropriate choice of the model parameters. In the region of higher DM masses (190 to 400 GeV), FERMI-LAT bounds [189] can restrict the parameter space of the pseudoscalar model through ID searches [134].

Although we are working in the alignment limit of the 2HDM extensions we are considering, FCNCs do appear at loop level and can lead to bounds on the parameter space, as there are tight experimental limits on such processes (cf. Sec. 4.1.3 and see [181] for a detailed discussion). These bounds are most pronounced for type-II and type-Y models but also appear for type-I and type-X models. Generally, they restrict especially very small ($\lesssim 0.1$) and moderate to large values ($> \mathcal{O}(10)$) of $\tan\beta$ as well as leading to a lower bound of $M_{H^\pm} \gtrsim 570\,\mathrm{GeV}$ in type-II and type-Y models. The choice of

$0.3 < \tan\beta < 3$ does allow for the flavor constraints to generally be fulfilled, while we do not explicitly take into account the lower bound on $M_{H^\pm}$.

Furthermore, the theoretical bounds due to perturbativity and unitarity constraints limit the allowed ranges for the couplings of the scalar potential together with the requirement for the scalar potential to be bounded from below. They cannot be too large ($\lesssim \mathcal{O}(1)$) to fulfill perturbativity and unitarity, while also the couplings associated with the highest exponents that dominate for large field values have to be positive and their combinations need to exceed the couplings of the terms that link different fields, to guarantee that the potential is bounded from below. These bounds for the scalar and pseudoscalar model have been studied in [153, 190, 191] and [155], and an overview of the explicit relations for the couplings is shown for example in [162]. As the region of parameter space we are interested in does not require any particularly large or otherwise "special" couplings, these limits do not restrict our analysis.

4.2.2 Collider Constraints

Besides the restrictions from non-collider constraints, there are also collider measurements like electroweak precision measurements that can guide us in terms of which part of the parameter space is still accessible and therefore of special interest for our analysis. Moreover, we will also briefly comment on sub-dominant channels like $t\bar{t} + \not{E}_\mathrm{T}$ (MET) and mono-jet, which will not be part of our main analysis that deals with $t\bar{t}$, mono-Z and mono-h searches in Sec. 4.3.

Most importantly, we find constraints from electroweak precision measurements determining the ρ parameter. Since both the 2HDM+S and 2HDM+PS break the custodial symmetry [192–197] (in particular the λ_4, λ_5 and λ_{hHS} terms) they would in general imply a deviation of the ρ parameter from $\rho = 1$. These additional contributions to the ρ parameter depend on the mass splitting of the heavy (pseudo)scalars and therefore restrict the masses and the mixing angle to fulfill $M_{S_1} \sim M_A \sim M_{H^\pm}$ and $0 \leq \theta \lesssim \pi/4$ for the 2HDM+S and $M_A \sim M_H \sim M_{H^\pm}$ and $0 \leq \theta \lesssim \pi/4$ for the 2HDM+PS (cf. [142, 160]). Thus, our choice of degenerate masses $M_H = M_{H^\pm} = M_A > M_a$ and $M_A = M_{H^\pm} = M_{S_1} > M_{S_2}$, as touched upon in Sec. 4.1.2, allows us to ensure that our parameter space does not violate electroweak precision constraints, while the hierarchies given by the last relations ($M_A > M_a$ and $M_{S_1} > M_{S_2}$) are necessary to not suppress the mono-Z and mono-h signals.

Furthermore, searches for $t\bar{t} + \not{E}_\mathrm{T}$ (and $b\bar{b} + \not{E}_\mathrm{T}$) are carried out by the experiments at LHC with recent results being reported in [198, 199]. Their results have been interpreted in simplified DM models and can be recast to our next-generation simplified models for a sufficient hierarchy between the heavy and light scalars (cf. [134]). As an example, the scaling relation between the DM simplified model (abbreviated by DMF, referring to the dark matter forum) and the 2HDM+PS reads

$$\frac{\sigma(pp \to t\bar{t} + \not{E}_\mathrm{T})_\mathrm{2HDM+PS}}{\sigma(pp \to t\bar{t} + \not{E}_\mathrm{T})_\mathrm{DMF}} = \left(\frac{y_\chi \sin\theta}{g_\chi g_q \tan\beta}\right)^2, \tag{4.42}$$

where the factor of $\tan\beta$ needs to be replaced according to Tab. 4.1 if one looks at limits for $b\bar{b} + \not{E}_\mathrm{T}$. Generally, it turns out that these limits are subdominant for the extended

2HDMs we are considering [200] and thus they do not constrain our parameter space and we will not derive explicit bounds for them.

Finally, we consider mono-jet searches whose experimental results are, like the $t\bar{t} + \not{E}_{\mathrm{T}}$ searches, typically interpreted in simplified DM models. If the heavy (pseudo)scalars of the 2HDM sector are significantly heavier than the mostly singlet-like states, comparable scaling relations to Eq. (4.42) hold. However, this condition is not valid for the whole parameter space. Therefore, we used the CheckMate [201] implementation of the latest Atlas search [202] and found no excluded points for $\tan\beta = 1$ for both the 2HDM+S and the 2HDM+PS. This implies that initial state radiation signatures in general should not be of importance in this parameter region, because mono-jet signatures provide usually the strongest bounds among them [203]. The analysis of [160] supports this finding by showing that mono-jet limits arise only for $\tan\beta < 1$ in the 2HDM+PS. However, this parameter region of $\tan\beta < 1$ is strongly constrained by $t\bar{t}$ searches, as we will find in our corresponding analysis, so that we will focus on the limits due to $t\bar{t}$ and not further investigate the mono-jet searches.

4.3 Comparison of LHC Signatures

After this general overview, let us now turn to the most important LHC signatures for the 2HDM+PS and 2HDM+S and the limits we can derive from comparing dedicated collider simulations to results by experimental searches. We will start out by discussing some general aspects relevant to all signatures before dealing with $t\bar{t}$, mono-Z and mono-h searches in detail.

4.3.1 General Aspects

Beside the decay side of the processes we want to analyze, which we described in Sec. 4.1.4, also the production side of the mediating particles is important to understand the resulting limits. This is what we are going to address in this section together with an overview of our parameter space and how we simulated the expected signals for both models.

Resonant Production Using the narrow width approximation, we can write the production cross section for a (pseudo)scalar X with mass M_X as [204]

$$\sigma(pp \to X) = \frac{1}{M_X s} \sum_i C_i \Gamma(X \to i)\,, \tag{4.43}$$

where a further decay to a state Y can be incorporated by including a factor $\mathrm{BR}(X \to Y)$. Here, the sum over i refers to all possible partonic initial states, like quark or gluon pairs, C_i are weight factors taking into account color factors and the parton distribution functions (PDFs) of the (initial state) protons, and $s = (13\,\mathrm{TeV})^2$ refers to the squared

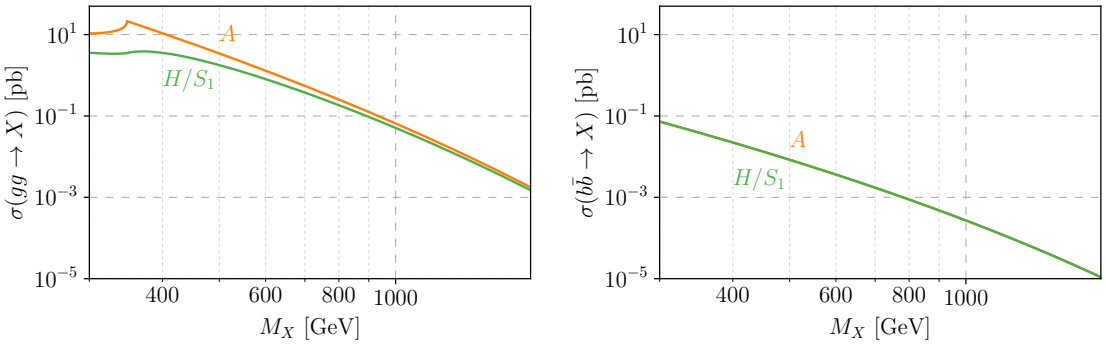

Figure 4.5.: Comparison of the production cross sections (cf. Eq. (4.43)) in the 2HDM+PS and 2HDM+S for the heavy scalars H/S_1 and pseudoscalars A in the case of gluon fusion (left) and $b\bar{b}$ initial state (right) for $\tan\beta = 1$.

center of mass energy. Explicitly, the weight factors C_i for gluons and quarks are given by

$$C_{gg} = \frac{\pi^2}{8} \int_{M_X^2/s}^1 \frac{\mathrm{d}x}{x} g(x)\, g\left(\frac{M_X^2}{sx}\right), \tag{4.44}$$

$$C_{q\bar{q}} = \frac{4\pi^2}{9} \int_{M^2/s}^1 \frac{\mathrm{d}x}{x} \left[q(x)\, \bar{q}\left(\frac{M_X^2}{sx}\right) + q\left(\frac{M_X^2}{sx}\right) \bar{q}(x)\right], \tag{4.45}$$

with the PDFs of the quarks $q(x)$ (anti-quarks $\bar{q}(x)$) and gluons $g(x)$ depending on the Bjorken scaling variable x.

The dominant contribution to the production cross section of the (pseudo)scalars is in general given by gluon fusion and $b\bar{b}$ initial states. Their dependence on the (pseudo)scalar mass M_X is shown in Fig. 4.5, which is based on Eq. (4.43). From Fig. 4.5, we can see that the production cross section due to gluon fusion is for the depicted case of $\tan\beta = 1$ about 100 times larger than for $b\bar{b}$ initial states. Although this dominance of gluon fusion depends on both the Yukawa structure (cf. Tab. 4.1) and the value of $\tan\beta$, it holds for our whole parameter space of interest ($0.3 \leq \tan\beta \leq 3$), allowing us to safely neglect the contributions to the production cross section from $b\bar{b}$ initial states. Furthermore, Fig. 4.5 also shows that it is always easier (by gluon fusion) to create a pseudoscalar particle in comparison to a scalar particle. The reason for this is that a pseudoscalar particle has a larger effective coupling to gluons than a scalar particle under the same assignment of Yukawa couplings (cf. e.g. [205, 206]). This enhancement of intermediary pseudoscalars, independent of whether that pseudoscalar is part of the 2HDM+PS or 2HDM+S, will play a significant role for the limits we find, as we will see later on.

Parameter Overview To provide a better overview of the model parameters we use, and therefore the parameter space we focus on, we list all choices of model parameters here. These choices are based on constraints mostly discussed in Sec. 4.2 and leave as remaining (mostly unconstrained) parameters to span our parameter space the light (pseudo)scalar masses M_{a/S_2} together with the heavy ones $M_{A,H^\pm,H/S_1}$ or $\tan\beta$. For the light (pseudo)scalar masses M_{a/S_2} we will find a lower limit of $M_{a/S_2} \sim 100\,\mathrm{GeV}$ from

Higgs-to-invisible searches, which will be discussed in Sec. 4.3.5, and is just stated here for completion, since it will guide our choice of the corresponding parameter range. In summary, we take for our model parameters the values

$$\begin{aligned} &M_A = M_{H^\pm} = M_{H/S_1} \\ &\lambda_3 = M_h^2/v^2 \\ &\lambda_{iiS/P} = 0 \\ &y_\chi^{S,PS} = 1 \\ &m_\chi = 10\,\text{GeV} \\ &\sin\theta = 0.3 \\ &\tan\beta \in [0.3, 3]\,. \end{aligned} \tag{4.46}$$

Signal Generation Lastly in this overview of general aspects, we want to comment on how exactly we ran our simulations that we compared to the results of the experimental analyses. To simulate a potential signal in the 2HDM+PS and 2HDM+S, we used MadGraph5_aMC@NLO [207–211] at next-to-leading order (NLO) in quantum chromo dynamics (QCD) using the 263000 PDF set (NNPDF3.0) [212] provided through LHAPDF6 [213]. The parton-showering was done within MadGraph via the built-in Pythia 8.2 [214] and for the fast detector simulation we used Delphes 3.4.2 [215] together with the provided CMS detector card. Finally, we implemented the appropriate cuts in MadAnalysis 5 [216, 217]. As a test that the program chain for the simulations and analyses is working as intended, we reproduced the mono-Z and mono-h exclusion limits in the 2HDM+PS presented in [134, 200]. Therefore, we are confident that our simulation and analysis procedure is reliable and stable.

4.3.2 $t\bar{t}$ Resonances

In general, $t\bar{t}$ resonances are powerful tools to search for models in which intermediately created particles decay dominantly into top pairs. In our case, these are the heavy scalars or pseudoscalars H/S_1 or A that mostly decay to $t\bar{t}$ (cf. Sec. 4.1.4) if their masses are above the top threshold $M_{H/S_1,\,A} > 2\,m_t$. What complicates such an analysis of $t\bar{t}$ resonances is that the signal processes interfere non-trivially with the SM background, however these effects are taken properly into account by recent experimental analyses of ATLAS [218] and CMS [219].

The ATLAS analysis [218] uses the $s = \sqrt{8}\,\text{TeV}$ dataset and interprets it in two different cases. First, they analyze a 2HDM of type-II (cf. Sec. 4.1.3) in which the different mediators can be considered independently and second, a mass degenerate scenario in which both contributions are analyzed simultaneously. By comparing the two scenarios, we can see that the mass degenerate one gives significantly stronger constraints. This means that considering the two mediators independently can be seen as a conservative estimate.

The CMS analysis [219] is more recent, takes into account a wider range of mediator masses and uses the $s = \sqrt{13}\,\text{TeV}$ dataset with $35.9\,\text{fb}^{-1}$. They analyze the data in simplified models containing either a scalar or a pseudoscalar, thereby being similar to the ATLAS analysis in which the mediators are distinguished. Furthermore, they also provide limits for interpreting the data in the hMSSM, resembling the mass degenerate case of the

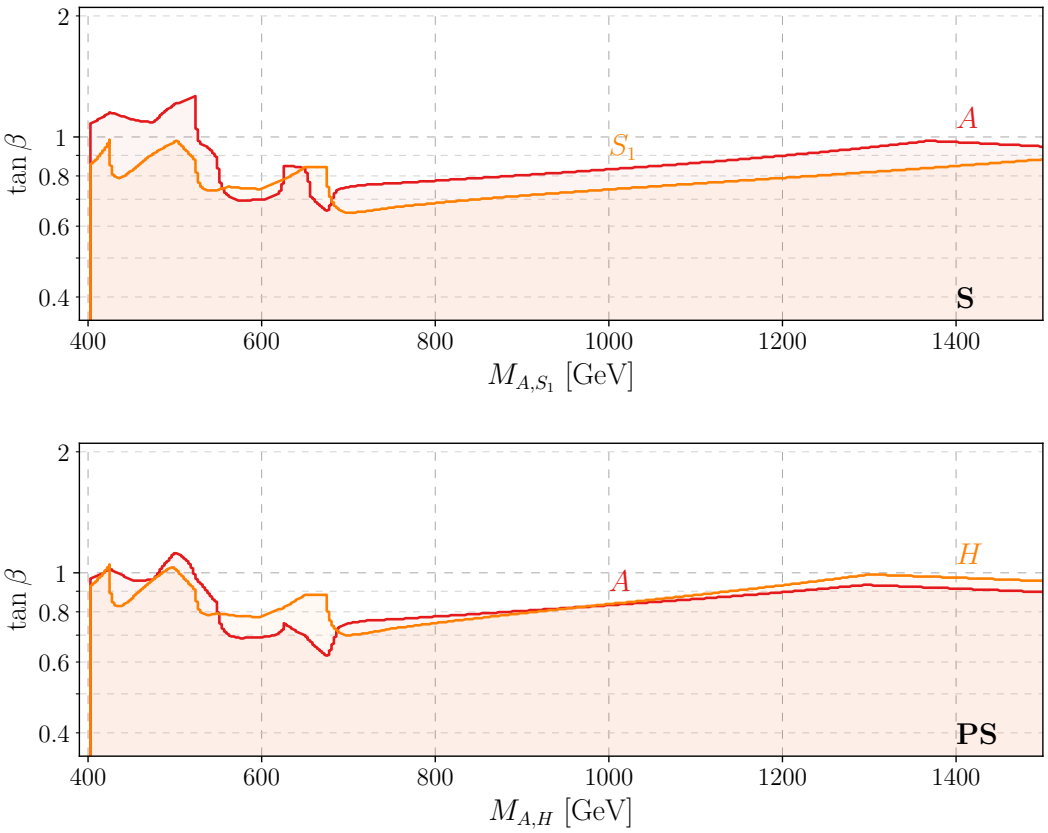

Figure 4.6.: Exclusion limits on $\tan\beta$ (at $2\,\sigma$) depending on $M_{A,\,H/S_1}$ from $t\bar{t}$ resonance searches by CMS [219] for the 2HDM+S (top) and 2HDM+PS (bottom). The limits from searches for a scalar are depicted in orange, while the limits for pseudoscalars are shown in red. The parameters are fixed to $M_{a/S_2} = 400\,\text{GeV}$ and the values given by the parameter overview of Eq. (4.46).

ATLAS analysis. However, as the CMS analysis finds a $1.9\,\sigma$ "signal-like deviation" that would fit a pseudoscalar with a mass of around 400 GeV, their limits do not improve as significant as one might expect upon the limits found by ATLAS.

The mixing with the additional (pseudo)scalar singlet that leads to the light new (pseudo)scalar a/S_2 can in principle also have a non-trivial impact due to interference effects, as laid out in Sec. 7.1 of [134]. However, thanks to our choice of small mixing ($\sin\theta = 0.3$), these interference effects are expected to be small and we will therefore neglect them. We leave a detailed analysis of the appearing interference effects and the combination of the limits for the heavy scalar and pseudoscalar for future work and derive our limits by recasting the CMS results of [219] for single mediators to our parameter space. To do so, we interpolate between the different exclusion limits given for specific total width to mass ratios. Since combining the limits for the scalar and pseudoscalar mediators significantly strengthens the resulting limit, as mentioned in the context of our discussion of the ATLAS results above, our method can be seen as a conservative estimate. In this way, we find the limits depicted in Fig. 4.6 in the $M_{A,\,H/S_1}$–$\tan\beta$–plane.

Even though the limits on $\tan\beta$ shown in Fig. 4.6 show some dependence on the heavy (pseudo)scalar mass $M_{A,\,H/S_1}$, they are always in the range $\tan\beta \sim 1$, which is the strong constraint we referred to in Sec. 4.2.2. In addition to the dependence on the heavy (pseudo)scalar mass, there is also a small dependence on the light (pseudo)scalar mass $M_{a,\,S_2}$, which appears in Figs. 4.13 and 4.14 where we compare the 2HDM+S and 2HDM+PS. Furthermore, we can see that in the 2HDM+S, the pseudoscalar mediator leads to generally stronger limits than the scalar mediator, while in the 2HDM+PS both mediators lead to comparably strong limits on $\tan\beta$. This behavior is caused by two effects. First, for masses above the top threshold, the decay width of pseudoscalars to quarks and in particular $t\bar{t}$ is bigger than the one for scalars (cf. Sec. 4.1.4, App. D and [220]), while also the effective coupling for the gluon fusion production is larger (cf. Sec. 4.3.1 or Eq. (4.43) and [221]). This leads to an enhancement of the limits from pseudoscalar searches. Second, we have to take into account the mixing of the light and heavy (pseudo)scalar in the 2HDM+S (2HDM+PS). It leads to a suppression of the cross section of the mixing particle by a factor of $\cos^2\theta$ (cf. Sec. 4.1.4 and App. D), thus decreasing the strength of the scalar channel in the 2HDM+S and the pseudoscalar channel in the 2HDM+PS. Therefore, for the 2HDM+S both of these effects pull into the same direction, namely making the limit from pseudoscalar searches more constraining than the one from scalar searches (cf. Fig. 4.6), while in the 2HDM+PS the enhancement of the pseudoscalar searches due to the first effect is canceled by the second one, leading to similar exclusion results of the scalar and pseudoscalar searches.

In summary, we find that $t\bar{t}$ resonance searches provide strong limits on $\tan\beta$ and, especially for masses of the heavy (pseudo)scalar Higgses of 500 GeV (which is often used as a benchmark value), can exclude values of $\tan\beta \lesssim 1$.

4.3.3 Mono-Z Searches

The dominant contribution to the mono-Z signal is via the resonantly produced non-mixing heavy (pseudo)scalar decaying to a Z boson and the light state a/S_2, as shown in Fig. 4.7. Thus, the mediating particle is a scalar in the 2HDM+PS and a pseudoscalar in the 2HDM+S. The light state a/S_2 continues to decay predominantly into DM (cf. Sec. 4.1.4), while for the Z decay we focus on the decays to electrons and muons, which provide the cleanest signatures. Searches for this (comparably) clean final state of the decay to DM, leading to MET ($\not{E}_{\mathrm{T}}$), and leptons (electrons and muons), have been carried out by both the ATLAS and CMS collaborations [222, 223].

The main idea of the analysis is to compare the MET distribution expected from SM backgrounds to the measured / simulated one, because a potential signal of the 2HDM+S or 2HDM+PS might leave its footprint there. Thus we will first discuss the MET distribution expected in both of our models, then comment on the backgrounds expected from the SM, before finally showing the results we find by comparing them. Strictly speaking, by comparing the simulated signal to the SM backgrounds in this way, we obtain the expected exclusion limits, so the limits one would expect to get by an experimental search. This is different to the $t\bar{t}$ and mono-h searches where our results are observed limits. However, as the expected limits we find are very similar to the observed ones where available (cf. [200]), we can use them for our comparison of limits from the different search channels.

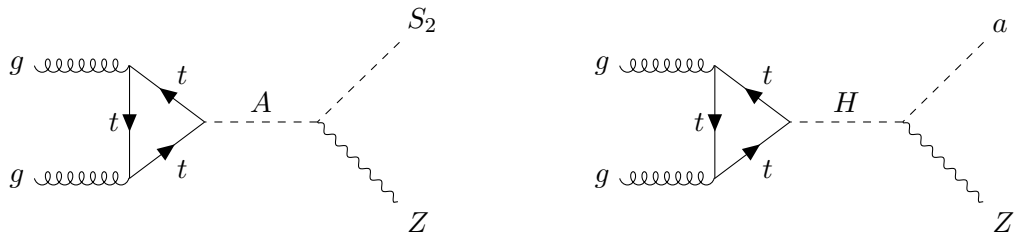

Figure 4.7.: Feynman diagrams for the dominant contribution to a mono-Z signal in the 2HDM+S (left) and 2HDM+PS (right). The consecutive decay of the light (pseudo)scalar a/S_2 to DM and of the Z boson to electrons or muons is not depicted, but necessary for a (comparably) clean MET + leptons signature.

MET Spectrum in the 2HDM+S/PS The MET spectrum of the mono-Z process we are interested in "is a steeply rising function with a sharp cut-off at $\not{E}_T^{\text{max}}$" [158], where the maximal MET is given by [158, 160]

$$\not{E}_T^{\text{max}} = \frac{\lambda^{1/2}(M_{A/H}, M_{S_2/a}, M_Z)}{2M_{A/H}}\,, \tag{4.47}$$

with $\lambda(m_1, m_2, m_3)$ as given by Eq. (D.17) and the first (second) subscript corresponds to the 2HDM+S (2HDM+PS). However, this sharp cut-off is smeared out by detector effects, leading to to a MET distribution that is peaked close to $\not{E}_T^{\text{max}}$, rather than having a cut-off there. If the heavy (pseudo)scalar mass $M_{A/H}$ is the dominant mass related to this process, so $M_{A/H} \gg M_{S_2/a}$ and $M_{A/H} \gg M_Z$, the expression for the maximal MET simplifies significantly to $\not{E}_T^{\text{max}} \approx M_{A/H}/2$.

To find the MET distributions in our models, we use the signal generation process as described in Sec. 4.3.1. Two examples for them, in the case of an $e^+e^- + \not{E}_{\text{T}}$ final state in the 2HDM+PS, are shown together with the predicted SM backgrounds and the observed number of events provided by ATLAS [222] in Fig. 4.8. Nearly identical MET spectra exist both for the $\mu^+\mu^- + \not{E}_{\text{T}}$ final state as well as the corresponding processes in the 2HDM+S. From Fig. 4.8 we see that the signal consists of a peak a bit below $\not{E}_{\text{T}} = M_A/2$ above a smoothly falling SM background, which we discuss next.

Backgrounds As laid out by [222] and depicted in Fig. 4.8, the main irreducible background for mono-Z searches is the production of two Z bosons of which one decays to neutrinos which lead to a MET signature. Another relevant contribution comes from WZ production in which one lepton of the W decay escapes detection or a τ decays hadronically. Furthermore, there are additional, but significantly smaller, background contributions from Z+jets processes with poor MET reconstruction and non-resonant $\ell\ell$ production (two leptons that do not originate from a Z). The background estimates of [222] are based on simulations as well as data-driven methods and the dominant uncertainty on the total background is systematic and mostly due to uncertainties on the Z+jets contribution.

Current Constraints For our analysis and the constraints we want to derive, we can now work with MET spectra like the ones shown in Fig. 4.8 and compare the experimentally

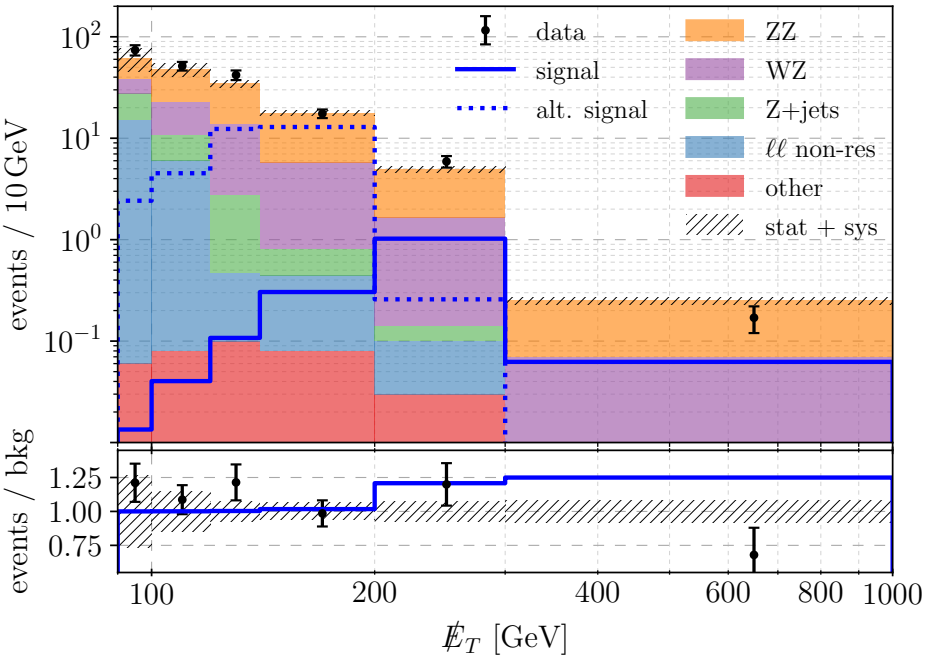

Figure 4.8.: Top panel: MET spectra for $gg \to e^+e^-\chi\bar{\chi}$ in the 2HDM+PS for $M_a = 250\,\text{GeV}$, $M_A = 700\,\text{GeV}$ (solid blue line) and $M_a = 150\,\text{GeV}$, $M_A = 400\,\text{GeV}$ (dotted blue line), with the other parameters having the values of Eq. (4.46). The expected SM backgrounds and observed events are taken from [222] and shown in different colors with their combined uncertainty displayed as a hatched region on top.
Lower panel: ratios of the observed events (points with error-bars) and signal + background expectation (solid blue line) to the background expectation plotted together with the background uncertainty (hatched region).

and with simulations determined backgrounds with our simulated results for the 2HDM+S and 2HDM+PS. To do so, we use the results of [222], since they are also used by the LHC dark matter working group (DMWG) [134] and in terms of the applied cuts easier to reproduce than the (slightly stronger) CMS results of [223]. Explicitly, the significance with which a specific point in parameter space is excluded is given by [134, 224]

$$Z_i = \sqrt{2\left((s+b)\ln\left[\frac{(s+b)(b+\sigma_b^2)}{b^2+(s+b)\sigma_b^2}\right] - \frac{b^2}{\sigma_b^2}\ln\left[1+\frac{\sigma_b^2 s}{b\,(b+\sigma_b^2)}\right]\right)}\,, \tag{4.48}$$

where b is the expected number of background events with corresponding uncertainty σ_b (both given by [222]), s is the number of signal events we find from our simulations and the index i of Z_i refers to the different MET bins as shown in Fig. 4.8. To find the (square of the) total significance Z^2, the values Z_i for the different bins have to be added up quadratically, and parameter points with $Z > 2$ are excluded at 95% confidence level. We would like to note that Eq. (4.48) can be understood as a likelihood-inspired generalization

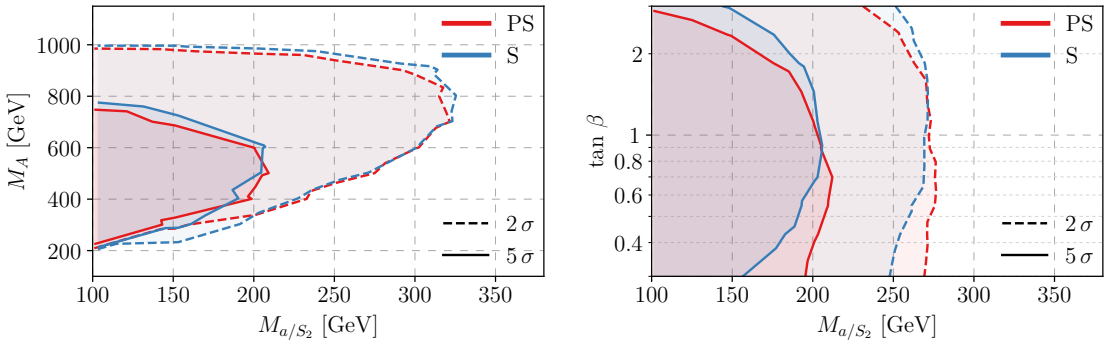

Figure 4.9.: Exclusion limits at $2\,\sigma$ (dashed) and $5\,\sigma$ (solid) from mono-Z searches for the 2HDM+S (blue) and 2HDM+PS (red) in the M_{a/S_2}–M_A–plane (left) and M_{a/S_2}–$\tan\beta$–plane (right). The model parameters are given by the values specified in Eq. (4.46), while for the left plot we fixed $\tan\beta = 1$ and for the right one $M_A = 500\,\text{GeV}$.

of the standard expression for the significance of $Z = s/\sqrt{b + \sigma_b^2}$ (cf. [224]). Furthermore and as described above, this procedure results in the expected exclusion limits, which are however very similar to the experimental ones where available (cf. [200]), thus enabling us to use these limits for comparison with the other experimental limits of $t\bar{t}$ resonances and mono-h searches in Sec. 4.3.5.

The resulting constraints on the parameter space of our analysis are shown in Fig. 4.9, from which we can see that they are similar both in shape and reach for the 2HDM+PS and 2HDM+S. This similarity however might come as a surprise, since the production cross section for pseudoscalar mediators is larger than for scalar mediators (cf. Sec. 4.3.1) and one might thus expect that the exclusion limits for the 2HDM+S are stronger than for the 2HDM+PS (cf. dominant Feynman diagrams in Fig. 4.7). That this is not the case is related to the branching ratios discussed in Sec. 4.1.4. There, we found that the branching ratio $\text{BR}(A \to ZS_2)$ in the scalar model is smaller by roughly a factor of two in comparison to $\text{BR}(H \to Za)$ in the pseudoscalar model, approximately canceling the enhancement due to the larger production cross section. Thus, we get similar exclusion limits from the mono-Z channel for both the 2HDM+PS and 2HDM+S.

In addition to the general similarity of the exclusion limits, we can also understand several distinct features of the exclusion plots shown in Fig. 4.9. In the M_{a/S_2}–$\tan\beta$–plane, the limits on the light new Higgs mass M_{a/S_2} are only moderately dependent on $\tan\beta$, with weaker limits for larger values of $\tan\beta$. This is a reflection of the type-I Yukawa couplings we use as a default (cf. Sec. 4.1.3), for which the top coupling scales like $(\tan\beta)^{-1}$. The top Yukawa is very important to the process since it is the coupling involved in the production of the mediator (cf. Fig. 4.7). In the M_{a/S_2}–M_A–plane, there are three different features in terms of the shape of the exclusion limits that can be understood. First, there is an upper bound on the exclusion limits in terms of the heavy Higgs mass, which is simply rooted in the fact that the heavy Higgs is the mediator of the process (cf. Fig. 4.7) and the cross section of the process is therefore suppressed by its mass. Second, the "diagonal" lower bound of the excluded region is due to kinematics, as for $M_A \lesssim M_{a/S_2} + M_Z$ not

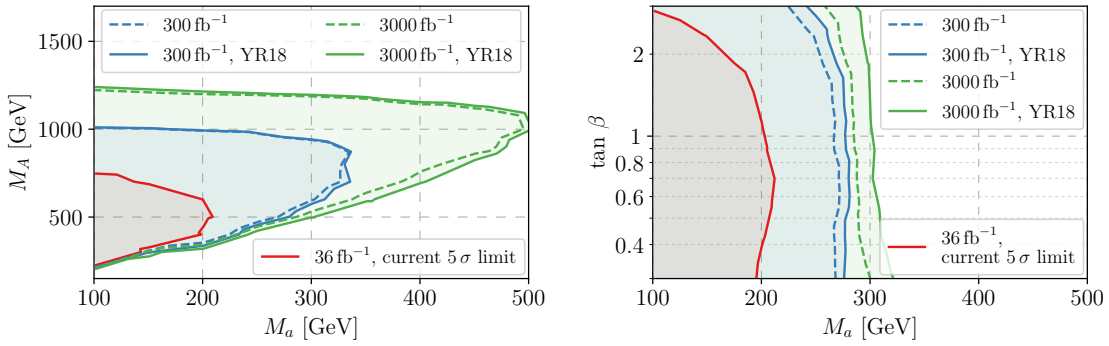

Figure 4.10.: Current $5\,\sigma$ exclusion limits for the 2HDM+PS (in red) and projected ones for the high-luminosity LHC (in blue and green) for mono-Z searches in the in the M_a–M_A–plane (left) and M_a–tan β–plane (right). The 2HDM+S limits are nearly identical and therefore not shown. The dashed lines correspond to a scenario without any improvement in the systematic uncertainties, whereas the solid lines assume a reduction by 50 %, called YR18 scenario. For the other parameters, the numerical values used are identical to Fig. 4.9.

all three of those particles can be on-shell, leading to a strong suppression of a potential signal. Third, the triangular shaped exclusion limit which might be expected from the first two features is smoothed out due to kinematics, since a heavier light new Higgs (a/S_2) leaves less energy available for the Z, which kinematically suppresses its production.

Projected Sensitivity Thanks to having access to the detailed data of the experimental analysis of [222], we can in addition to determining the current limits also estimate the projected sensitivity for the high luminosity phase of the LHC (HL-LHC). The results for the projected sensitivity can be found in Fig. 4.10 and are shown for integrated luminosities of 300 fb^{-1} and 3000 fb^{-1}, while for the systematic uncertainties we distinguished between having them unchanged and a reduction by 50 %, which is the so-called YR18 scenario [225]. From Fig. 4.10, we can see that the increased luminosity will lead to significantly stronger limits on the parameter space for both the 2HDM+PS and 2HDM+S, where the latter is not shown explicitly in Fig. 4.10 because the resulting limits look the same. The general shape of the limits remains identical to the one of the current limits as discussed above. In case of the masses, the maximal reach is estimated to increase by a factor of roughly 1.5 for the heavy Higgses and 2.5 for M_{a/S_2}. That this is not reflected in the corresponding plot in the M_a–tan β–plane, and that there seems to be little improvement from 300 fb^{-1} to 3000 fb^{-1}, is due to our parameter choice of $M_A = 500$ GeV. For this value, the 300 fb^{-1} case already reaches down close to the lower "diagonal" kinematical limit ($M_A \lesssim M_{a/S_2} + M_Z$), making any further progress in terms of the excluded parameter space hard to reach through larger integrated luminosities. On the other hand, the impact of reducing the systematic uncertainties will likely be small.

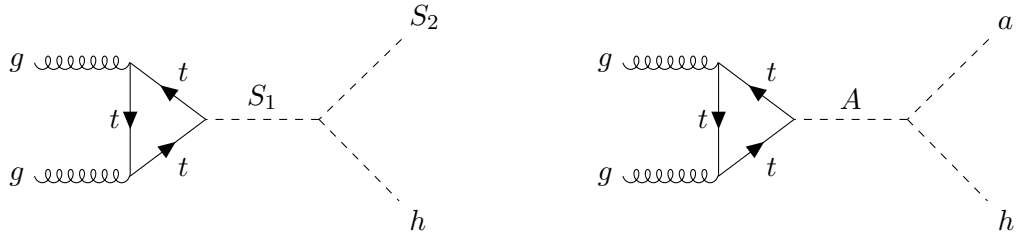

Figure 4.11.: Feynman diagrams for the dominant contribution to a mono-h signal in the 2HDM+S (left) and 2HDM+PS (right). The consecutive decay of the light (pseudo)scalar a/S_2 to DM and of the SM Higgs to $b\bar{b}$ is not depicted.

4.3.4 Mono-h Searches

Similar, but in contrast to the mono-Z searches described in Sec. 4.3.3, for which the dominant contribution comes from a resonance of the non-mixing heavy (pseudo)scalar (cf. Fig. 4.7), the mono-h signal gets its dominant contribution from the heavy (pseudo)scalar that is mixing. The corresponding Feynman diagrams of the dominant channels are depicted in Fig. 4.11 and lead to a similar MET signature and spectrum as the mono-Z case (cf. Fig. 4.8). This is due to the fact that the resulting light new (pseudo)scalar from the vertex involving the SM Higgs-like boson decays mostly to DM. For a heavy enough light new (pseudo)scalar as in our case, the SM Higgs-like boson decays mostly into $b\bar{b}$ pairs like in the SM (cf. Sec. 4.1.4), which makes the $h \to b\bar{b}$ channel well suited to search for the mono-h + MET signature. Corresponding searches for $h \to b\bar{b}$ by ATLAS and CMS can be found in [226, 227], while searches for mono-h with $h \to b\bar{b}$, $\gamma\gamma$, $\tau^+\tau^-, W^+W^-$, ZZ are performed in [228], however the limits are also dominated by the contribution of $h \to b\bar{b}$. For our analysis, we work with the model-independent upper limit on the cross section for $h + \not{E}_{\mathrm{T}}$ as derived by ATLAS in [226] and compare it to the cross section we find from our simulations.

This procedure is the same as followed by the LHC DMWG [134] and encapsulated in the formula for the resulting sensitivity in bin i [134]

$$S_i = \frac{\sigma_i\big(pp \to h + \not{E}_{\mathrm{T}}\big)_{\mathrm{sim}} \cdot \mathrm{BR}(h \to b\bar{b})_{\mathrm{SM}} \cdot (\mathcal{A} \cdot \epsilon)_i}{\sigma_i\big(pp \to h + \not{E}_{\mathrm{T}} \to b\bar{b} + \not{E}_{\mathrm{T}}\big)_{\mathrm{exp}}}\,, \tag{4.49}$$

where we have in the numerator the simulated cross section $\sigma(\cdot)_{\mathrm{sim}}$, the SM branching ratio of the Higgs $\mathrm{BR}(h \to b\bar{b})_{\mathrm{SM}} \approx 58\,\%$, and the kinematic acceptance of the event selection $\mathcal{A}$ together with the detection efficiency ϵ (both given by [226]), and in the denominator the experimentally determined limit on the cross section $\sigma(\cdot)_{\mathrm{exp}}$. Note that the sensitivity S_i here is not identical to the significance Z_i discussed for mono-Z searches in Sec. 4.3.3, but the different sensitivities need to be added up in order to get the total sensitivity $S = \sum_i S_i$, for which any parameter point with $S > 1$ is excluded at more than $2\,\sigma$ [134].

Since the experimental data is directly combined with the corresponding background expectations into upper limits on the cross section by [226], we do not need to address the MET spectrum or the backgrounds as for the mono-Z searches (cf. Sec. 4.3.3). However, we still want to briefly comment on the dominant background contributions before discussing the current constraints.

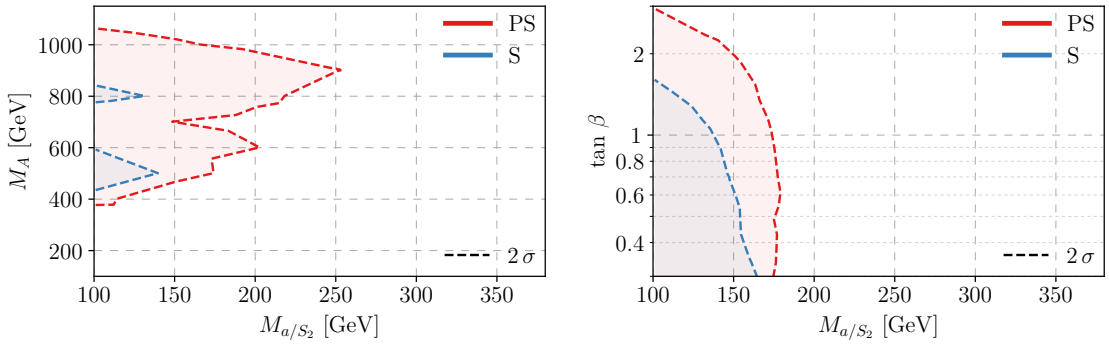

Figure 4.12.: Exclusion limits at $2\,\sigma$ (dashed) from mono-h searches for the 2HDM+S (blue) and 2HDM+PS (red) in the M_{a/S_2}–M_A–plane (left) and M_{a/S_2}–$\tan\beta$–plane (right). The model parameters are given by the values specified in Eq. (4.46), while for the left plot we fixed $\tan\beta = 1$ and for the right one $M_A = 500\,\text{GeV}$.

Backgrounds The main backgrounds for mono-h searches with a following $h \to b\bar{b}$ decay come from top pairs or single tops as well as leptonically decaying vector boson + jets processes [226]. For top pairs or single tops, a top decaying to a bottom can look like it came from a Higgs decay in combination with another b-tagged jet, while the missing energy escapes via neutrinos. Similarly, decaying vector bosons can also induce MET via decays to neutrinos or missed charged leptons, and the jets can be misreconstructed as a Higgs decay. These processes are important to derive limits on the cross section for mono-h + MET and to generate them Monte-Carlo simulations are used in [226].

Current Constraints By determining the sensitivity according to Eq. (4.49), plugging in our simulation results and the experimental findings of [226], we get the exclusion limits on the parameter space shown in Fig. 4.12. It is important to note that the experimental analysis of [226] only uses one MET bin at a time to minimize the model dependency, while also, within each bin, sampling the kinematic dependencies as well as the acceptance and efficiency for several parameter points and using only the least stringent limits in the end. Both of these measures lead to conservative estimates for the limits derived from the experimental data.

From Fig. 4.12, we can see that the limits behave similarly to the mono-Z searches (cf. Fig. 4.9), which are discussed in the corresponding Sec. 4.3.3, with weaker exclusion limits for larger values of $\tan\beta$, M_A and M_{a/S_2} as well as strongly suppressed ones for $M_A \lesssim M_{a/S_2} + M_h$. Another striking feature is the dip in the exclusion limit for masses of the heavy (pseudo)scalar of $M_A \sim 700\,\text{GeV}$ as visible in the M_{a/S_2}–M_A–plane plot of Fig. 4.12. This is a binning effect, caused by the relatively large MET bins used in the experimental analysis (150 to 200 GeV, 200 to 350 GeV, 350 to 500 GeV and $> 500\,\text{GeV}$) together with the fact that their corresponding experimental limits on the cross section differ significantly from bin to bin. Around $M_A \sim 700\,\text{GeV}$, there are mainly two effects that play a role. First, the production cross section decreases for a larger mass M_A, thus suppressing the exclusion power. Therefore, $M_A = 700\,\text{GeV}$ leads to a

weaker limit than $M_A = 600\,\text{GeV}$, as both of their MET spectra fall dominantly into the 200 to 350 GeV bin since they are peaked around $\not{E}_\text{T} = M_A/2$ (cf. corresponding discussion in Sec. 4.3.3). Second, the 350 to 500 GeV bin is significantly stronger constrained than the 200 to 350 GeV bin (cf. [226]). This results for $M_A = 800\,\text{GeV}$ in an overcompensation of the decrease in cross section, since its MET spectrum falls mostly in the 350 to 500 GeV bin (being again peaked around $M_A/2$), which brings about a stronger limit than for $M_A = 700\,\text{GeV}$ and leads to the dip.

The last relevant feature, which is also in contrast to the mono-Z searches, is that the exclusion limits for the mono-h searches lead to significantly different results for the 2HDM+PS and 2HDM+S, while being stronger for the pseudoscalar model. Its explanation however, goes along the same lines as the explanation of why the mono-Z searches lead to similar results for both models. From the production of the intermediate particle, we can for the mono-h searches expect that the 2HDM+PS leads to a stronger limit, because its mediating particle is the pseudoscalar A, which has a larger production cross section than the scalar S_1 in the 2HDM+S (cf. Sec. 4.3.1 and the Feynman diagrams of Fig. 4.11). The difference to the mono-Z searches is that this comparably larger production cross section for the pseudoscalar model is however not counteracted by a smaller branching ratio, as we find from Sec. 4.1.4 that $\text{BR}(S_1 \to S_2 h) \approx \text{BR}(A \to a h)$. Thus, the exclusion limits due to mono-h searches for the 2HDM+PS are stronger than for the 2HDM+S.

4.3.5 Combined Constraints

In addition to the constraints from the searches for $t\bar{t}$ resonances as well as mono-Z and mono-h signatures, we also take limits from Higgs-to-invisible searches into account for our analyses, even though so far only implicitly. Namely, for our models, both the two-body decays $h \to aa/S_2S_2$ and the three-body decays $h \to a/S_2\,\chi\bar{\chi}$, discussed in Sec. 4.1.4, lead to Higgs-to-invisible signatures, since the light (pseudo)scalar a/S_2 decays nearly exclusively into DM. We can thus find, with the help of the decay width formulas of App. D, the Higgs-to-invisible branching ratio for each point in parameter space and compare this to the experimental limit for the combined corresponding searches given by [229]

$$\text{BR}(h \to \text{inv}) < 0.26 \;\; \left(0.17^{+0.07}_{-0.05}\right), \tag{4.50}$$

as the observed (expected) upper limit at 95 % confidence level. Doing so results in a lower limit of $M_{a/S_2} \sim 100\,\text{GeV}$ for $m_\chi = 10\,\text{GeV}$, which has a slight dependence on the mass scale of the heavy Higgses $M_A = M_{H^\pm} = M_{H/S_1}$. As already mentioned in our discussion of the parameter space in Sec. 4.3.1, this limit guides our choice of the lowest values of M_{a/S_2} we consider.

Combining all our constraints into a single plot of the corresponding parameter plane for each model, we find the results depicted in Figs. 4.13 and 4.14. Having addressed the differences between the 2HDM+PS and 2HDM+S in each of the searches in the respective sections, we want to now focus on the comparison of the different constraints within each model. Starting with the 2HDM+PS in the M_a–M_A–plane (cf. left panel of Fig. 4.13), we see that the dominant exclusion limits come from searches for mono-Z signatures, while for small masses of M_a and large masses of the heavy Higgses, the mono-h limits are of

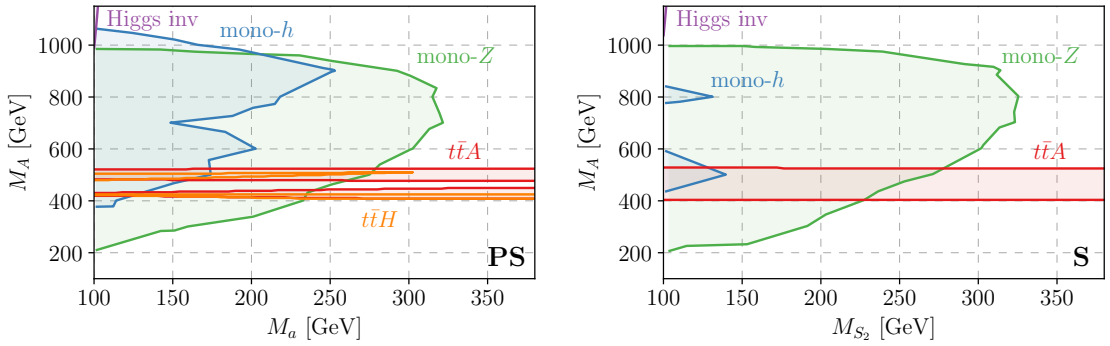

Figure 4.13.: Combined constraints at $2\,\sigma$ for searches of $t\bar{t}$ resonances as well as mono-Z and mono-h signatures, together with limits from Higgs-to-invisible decays in the M_{a/S_2}–M_A–plane for the 2HDM+PS (left) and 2HDM+S (right). The model parameters are given by the values specified in Eq. (4.46), while fixing $\tan\beta = 1$.

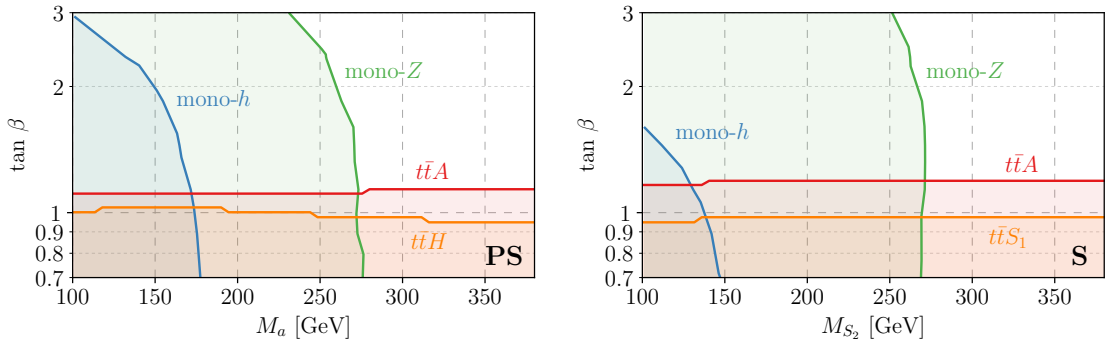

Figure 4.14.: Combined constraints at $2\,\sigma$ for searches of $t\bar{t}$ resonances as well as mono-Z and mono-h signatures in the M_{a/S_2}–$\tan\beta$–plane for the 2HDM+PS (left) and 2HDM+S (right). The model parameters are given by the values specified in Eq. (4.46), while fixing $M_{H/S_1} = M_{H^\pm} = M_A = 500\,\text{GeV}$.

similar order or can even be stronger. The Higgs-to-invisible limits essentially provide us with a lower bound on M_a, which becomes only relevant for very small or large masses of the heavy Higgses, where the other limits disappear. Furthermore, even for $\tan\beta = 1$, we see the limits from $t\bar{t}$ resonance searches start to appear in the parameter space as a (patchy) band for values of $M_H = M_{H^\pm} = M_A$ between 400 and 500 GeV.

For the 2HDM+S in the M_{S_2}–M_A–plane (cf. right panel of Fig. 4.13), we find a nearly identical behavior of $t\bar{t}$, mono-Z and Higgs-to-invisible limits, only with the band of the $t\bar{t}$ limits being less patchy due to the slightly stronger limits (cf. 4.3.2 and Fig. 4.14). In contrast to the 2HDM+PS, the mono-h limits are completely subdominant to the mono-Z limits for the 2HDM+S, thus not providing any additional excluded parameter space.

A similar picture as in the M_{S_2}–M_A–plane emerges from the limits in the M_{a/S_2}–$\tan\beta$–plane (cf. Fig. 4.14), with the masses of the heavy Higgses fixed to 500 GeV. We find for

both the 2HDM+PS and 2HDM+S that the mono-Z limits dominate over the mono-h limits, with both searches making it possible to find exclusion limits for parameter points with $\tan\beta > 1$, however depending on the value of the light (pseudo)scalar Higgs mass M_{a/S_2}. In contrast to that, the limits from $t\bar{t}$ resonances are nearly independent of the light (pseudo)scalar Higgs mass M_{a/S_2} and provide thus the strongest limits on $\tan\beta$ for large values of M_{a/S_2}.

We want to remark that for values of $\tan\beta > 3$, which we did not analyze in our parameter scan, it is important which type of $\mathbb{Z}_2$ symmetric Yukawa structure is used (cf. Tab. 4.1). This is due to the fact that for type-II and type-Y (the types with enhanced couplings of b quarks for $\tan\beta > 1$), in addition to the gluon fusion production also the $b\bar{b}$ production channel becomes important, leading to stronger limits for larger values of $\tan\beta$. On the other hand, type-I and type-X do not have this strengthening of constraints, as there the $b\bar{b}$ production channel is not enhanced.

Finally, there is a potential upshot of the exclusion limits being weaker for mono-h searches in the 2HDM+S compared to the 2HDM+PS. Assuming a potential signal discovery in the future, one could use the weaker constraints for the mono-h searches in the 2HDM+S to distinguish between the two models, as there is a large part of parameter space in which both models would see a signal in the mono-Z channel, but only the 2HDM+PS would see one in the mono-h channel as well. Thus, this difference in sensitivity to the different signatures could potentially be used to distinguish between the two models by looking at their collider signatures and in particular the respective signal strength ratios.

4.4 Summary

In an effort to better understand the LHC phenomenology of the 2HDM+PS and 2HDM+S, as two notable examples of next-generation DM models, we analyzed the exclusion limits from $t\bar{t}$ resonances as well as mono-Z and mono-h searches. The next-generation DM models are benchmark models used by ATLAS and CMS to interpret their experimental data and extend the simplified DM models used before, by offering a richer phenomenology and overcoming some of their shortcomings. For the 2HDM+PS and 2HDM+S in particular, this richer phenomenology is due to an added additional doublet and (pseudo)scalar singlet to the field content of the SM.

Guided by existing experimental results on Higgs physics, FCNCs and electroweak precision data, and the intention to compare the 2HDM+PS and 2HDM+S, we restricted our parameter space in the same way as done by experimental collaborations (cf. [134]). At the same time, we tried to stay as general as possible in terms of the Yukawa coupling structure, however at the expense of limiting the allowed range for $\tan\beta$ that represents the ratio of the vevs of the two Higgs doublets. We focused on rather light DM of $m_\chi = 10\,\text{GeV}$, since for larger masses especially signatures from direct detection experiments can provide stronger limits than collider searches.

With the help of data from experimental analyses, we derived exclusion limits for both the 2HDM+PS and 2HDM+S for Higgs-to-invisible and $t\bar{t}$ resonance searches as well as mono-Z and mono-h signatures, which we compared both between and within the models. While Higgs-to-invisible searches provide a lower bound of $\sim 100\,\text{GeV}$ on the light (pseudo)scalar mass, $t\bar{t}$ resonance searches are best suited to exclude values of $\tan\beta \lesssim 1$

irrespective of it. Mono-Z searches are generally dominant over mono-h searches and provide strong exclusion limits in all cases, however they are getting weaker the larger the light (pseudo)scalar mass is. Comparing the strength of the different signatures, especially the mono-Z and mono-h one, would in case of a signal detection allow for a discrimination between the 2HDM+PS and 2HDM+S.

As the experimental data analysis of the LHC collaborations is an ongoing effort, one possible avenue of future research would be to recast their coming results to interesting benchmark models, which would help in getting a better understanding of these models. Furthermore, also for the experimental data at hand there is the potential for improvement. For example in case of the $t\bar{t}$ resonance searches, getting a combined limit including both mediators would improve the limits derived here, however, such an analysis requires a dedicated effort.

This concludes our investigation of possible signatures of next-generation DM models including a rather light DM candidate and we will see in the next chapter that the scale of 10 GeV is by far not a low one for possible DM candidates. However, the common particle DM picture including interactions with the SM used in this chapter, will not be well suited to look at (pseudo)scalar and vector DM with curvature couplings discussed in the next chapter.

Chapter 5

Dark Matter from Gravitational Couplings

The lack of a suitable DM candidate in the SM provides a strong motivation to search for possible SM extensions that include such a candidate, as well as their corresponding signatures in experiments (cf. Ch. 4). Oftentimes, the most relevant couplings in the production and decay of these DM candidates are the ones to SM particles. However, we want to pursue a different approach here, by using the fact that (very) light (pseudo)scalars and vectors, which are very weakly coupled to the SM, can be viable dark matter candidates [230–236] (cf. e.g. [237] for a review). Due to their (very) light mass and very weak couplings to the SM, they usually require different experiments and search strategies than the conventional SM extensions (cf. [238–242] for overviews) and are automatically stable on cosmological time scales even without an additional symmetry protecting them.

Creating DM in this way is closely tied to the cosmological period of inflation and several mechanism are able to generate a sufficient DM density. Which of them are viable and lead to the dominant contribution depends on the parameters of inflation as well as the ones governing the DM candidate. For our investigation, we will focus on two options: the misalignment mechanism [230–232, 234–236] and the stochastic scenario [243–248]. In general there can also be contributions from inflationary fluctuations [249–254] as well as from decays of precursor particles [255–259]. While most of the previous studies have focused on the case of a minimal coupling to gravity for a (pseudo)scalar field (cf. e.g. [230–232]) and the corresponding situation for a vector field (cf. [235, 260]), we will instead allow in both cases for a non-minimal coupling to gravity, represented by the Ricci scalar R. This will enable us to significantly enlarge the parameter space that allows for the creation of the correct amount of DM. Note that the results presented in this chapter are based on work published as Ref. [261].

For our discussion of DM from curvature couplings, we will first describe the actions (and thereby Lagrangians) underlying our analysis and the mechanisms to generate DM, before dealing first with the (pseudo)scalar case and then with the vector case in detail.

5.1 Curvature Coupling Models

The action including a curvature coupling for the (pseudo)scalar case reads

$$S = \int \mathrm{d}^4x \sqrt{-g} \left(\frac{1}{2}(m_{\mathrm{Pl}}^2 - \xi\phi^2)R - \frac{1}{2}\partial_\mu\phi\partial^\mu\phi - \frac{1}{2}m_\phi^2\phi^2 \right), \tag{5.1}$$

where g is the determinant of the metric $g_{\mu\nu}$ with signature $(+,-,-,-)$, m_{Pl} the reduced Planck mass, ξ the respective coupling strength of the gravitational coupling and m_ϕ the mass of the (pseudo)scalar field ϕ. Similarly, we have for the vector case

$$S = \int \mathrm{d}^4x \sqrt{-g} \left(\frac{1}{2}\left(m_{\mathrm{Pl}}^2 + \frac{\kappa}{6}X_\mu X^\mu\right) R - \frac{1}{4}X_{\mu\nu}X^{\mu\nu} - \frac{1}{2}m_X^2 X_\mu X^\mu \right), \tag{5.2}$$

with the respective coupling strength κ of the gravitational coupling as well as the field strength tensor $X_{\mu\nu}$ and mass m_X of the vector field X_μ. For both cases we assume any potential coupling to the SM to be negligible, at least for the purposes of our analysis.

In the expression of the action for the vector case, Eq. (5.2), we choose the normalization of the non-minimal coupling κ in line with the convention of [235, 262–264], implying that the components of the vector field behave like a minimally coupled scalar field for $\kappa = 1$, as we will discuss in detail in Sec. 5.3. With Eq. (5.1), we can now also make explicit that a minimal coupling to gravity refers to the case $\xi = 0$. Furthermore, it is helpful to note that the (pseudo)scalar and vector non-minimal coupling come with a different sign, hence $\xi < 0$ corresponds to $\kappa > 1$ and vice versa. As the pseudoscalar case behaves identically to the scalar one, we will from now on drop the "(pseudo)" and only refer to the scalar case.

One important aspect of the actions we are considering, Eqs. (5.1) and (5.2), is that both of them are in the Jordan frame that includes a term linking the (scalar / vector) field to the Ricci scalar, in contrast to the Einstein frame in which the couplings to gravity are canonically normalized (cf. [254] for a short discussion on such actions in the Jordan and Einstein frame). These two frames are linked by a transformation of the metric and a field redefinition, necessary to have both gravity and the field canonically normalized. However, as we do not want to significantly change or influence GR through our assumed coupling with a scalar or vector field, we can directly work in the Jordan frame and identify the mass scale linked to the Ricci scalar with the reduced Planck mass m_{Pl}, as done above. For this to be valid however, the field value should have at least no transplanckian excursions, assuming a coupling of order one. To determine the size of the corrections or additional interactions due to the non-minimal coupling, we need to perform the above mentioned transformation to the Einstein frame. Doing so, we find that they scale with $1/m_{\mathrm{Pl}}^2$ (cf. [254]), which is the naturally expected size of such terms in theories of quantum gravity.

Especially for the scalar case represented by Eq. (5.1) there exist several works that motivate such a non-minimal coupling to gravity (the Ricci scalar). For example [265] argues that such couplings need to be considered if one views GR as an effective field theory. Furthermore, the quantization of a scalar field theory in a gravitational background produces such couplings [266] and they are essential for the renormalizability of the energy-momentum tensor in curved backgrounds [267]. Finally, such scalar couplings scaling with $1/m_{\mathrm{Pl}}^2$ as described above, generically arise in theories like asymptotic safety (cf. [268, 269]

for reviews) aiming at the quantization of gravity [270–276].

For the action of the vector field, the situation is more complicated. One aspect is that to generate the mass term of the vector field (cf. Eq. (5.2)) in a gauge invariant way, we need to employ a Stueckelberg (or Higgs) mechanism. However, the terms necessary for such a Stueckelberg mechanism can lead to a violation of unitarity already at energies below the Planck scale [255]. Additionally, in the vector theory, the kinetic term of the longitudinal modes becomes negative for a specific range of momenta of the corresponding particles, reminiscent of a ghost, which is a scalar particle with a negative kinetic term. Such ghosts are normally unwanted in any theory as they destabilize the vacuum [277, 278]. Since the negative sign of the kinetic term is only realized for a specific range of momenta and a sufficiently large Ricci scalar, it cannot directly be concluded that the vacuum would be destabilized. This feature together with an appearing singularity in the kinetic term have been discussed in dedicated works [264, 279, 280], but no final verdict on the viability has been reached. Understanding these issues better would be a suitable topic for further research that is however beyond the scope of our analysis in this chapter. While acknowledging the potential issues with the vector scenario, we will nevertheless analyze it alongside the scalar one.

Non-minimal couplings as we are considering, have been studied for a variety of reasons in the literature so far. Originally, they have been mostly used to construct models of inflation (e.g. [281, 282]), which received a lot of attention with the realization that large values of the non-minimal coupling $\xi \sim 10^4$ allow the Higgs boson to take on the role of the inflaton [283, 284]. Also the possibility to realize inflation with the help of a non-minimally coupled vector field was studied, cf. [260]. More recently and as in our case, the focus for these kind of couplings shifted to the possible connection to DM. Here, their connections to the creation of DM during inflation [249–254] or at preheating and reheating [285–293] have been studied.

As mentioned in the introduction to this chapter, both the misalignment mechanism and the stochastic scenario are closely tied to the cosmological period of inflation. The reason is that for both mechanisms to work, they need to have a non-zero homogeneous field value at the end of inflation to represent a viable dark matter candidate, however they differ with regard to how this non-zero homogeneous field value is reached. It needs to be non-zero to lead to the DM energy density of the universe, as we will see when explicitly calculating the energy density stored in the scalar or vector field non-minimally coupled to gravity, and it needs to be homogeneous to correspond to cold DM, as experimentally required for structure formation to be efficient enough [294]. That a homogeneous field represents very cold matter is easiest understood by thinking about the quantum mechanical momentum operator which is essentially the spatial derivative of the field, thereby implying that if the field derivative is close to zero, the corresponding particle also has close to zero momentum and is thus very cold. In the misalignment scenario, the underlying assumption is that the field has a random (and therefore expectedly non-zero) initial state. Through inflation, this field gets stretched until an initially tiny, nearly constant patch covers the whole observable universe, resulting in a non-zero but very homogeneous field value. In the stochastic scenario on the other hand, inflation is long enough for this initial non-zero field value to relax back to zero, so the contribution from the misalignment mechanism is negligible, while all the fluctuations that get stretched to super-horizon scales during inflation add up in a random walk like process and thus slowly build up the non-zero

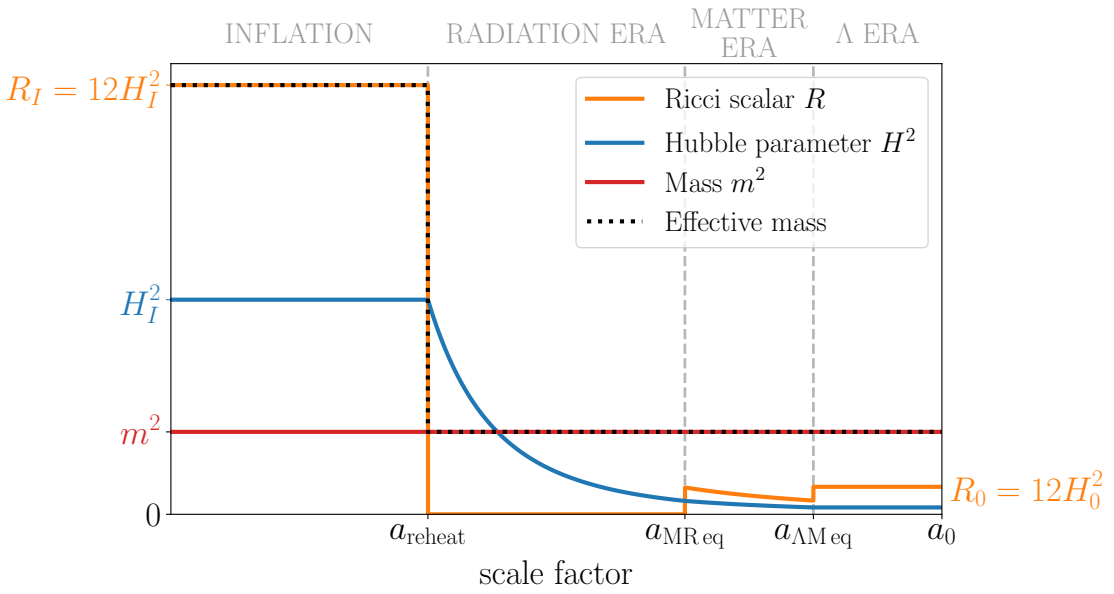

Figure 5.1.: Illustration of the evolution of the effective mass over the history of the universe (the lengths of the different eras are not to scale) under the assumption of $\xi = 1$ for illustrative purposes, displayed together with the quantities determining it. While being dominated during inflation by the contribution due to the coupling to the Ricci scalar R, for later eras the mass parameter $m \equiv m_{\phi/X}$ is dominant if it is larger than the Hubble parameter at matter-radiation-equality $m > H_{\text{eq}} \approx 2 \cdot 10^{-28}\,\text{eV}$ [296]. The present day Hubble parameter during the era of the cosmological constant Λ is given by $H_0 \approx 10^{-33}\,\text{eV}$ [296], while we take its value during inflation H_I to be a free parameter of the theory.

homogeneous field value.

For our following analysis, we will assume inflation to be described by a perfect de Sitter (exponential) expansion with a constant Hubble parameter H_I, followed by instantaneous reheating. This significantly simplifies our calculations and keeps the results qualitatively valid as long as the small spectral tilt measured at CMB scales [295], which indicates that H_I is a slowly decreasing function of time, remains small for all relevant scales. Quantitatively, the effect of a slowly decreasing value for H_I can be compensated by slightly larger values of the non-minimal coupling in the scalar case and slightly smaller ones in the vector case.

Before continuing with our detailed discussion of the scalar and vector model, we can already provide an intuitive understanding of why such non-minimal couplings to gravity can alter the evolution of the corresponding field and thereby enlarge the parameter space that allows for the creation of the correct amount of DM. As depicted in Fig. 5.1 together with the evolution of the Ricci scalar R, the non-minimal couplings lead to a (positive or negative) contribution to the mass and can therefore strongly influence the effective mass of the field, which is very important to its evolution. Thus, by means of this effective mass, the field value during inflation can be significantly enhanced or suppressed, making new regions of parameter space accessible.

5.2 Non-Minimally Coupled Scalar Fields

For the discussion of the non-minimally coupled scalar fields, we will first focus on the misalignment scenario and look at the homogeneous scalar field value and the resulting relic density, before turning to the scalar fluctuations that provide a limit through measurements of the isocurvature fluctuations of the CMB by PLANCK and finally addressing how the stochastic scenario could be realized with a non-minimal coupling to gravity.

5.2.1 Homogeneous Scalar Field Value and Relic Density

The equation of motion (EOM) for the homogeneous scalar field can be derived from Eq. (5.1) or found by analogy to, e.g., [235]. When viewing the non-minimal coupling as an additional mass term, cf. Fig. 5.1, we can follow the standard derivation for the minimal coupling case and simply replace $m_\phi^2 \to m_\phi^2 + \xi R$ to find

$$\ddot{\phi} + 3H\dot{\phi} + \left(m_\phi^2 + \xi R\right)\phi = 0\,. \tag{5.3}$$

As we can see from Fig. 5.1, the additional mass term due to the non-minimal coupling is only important during inflation, which implies that the equations of motion and the dynamics of the scalar field after inflation are described by the same equations as the minimally coupled case. Therefore, we can follow [235] to derive an expression for the energy density stored in the scalar field. Oftentimes, this is expressed in terms of the density parameter $\Omega_\phi = \rho_\phi/\rho_{\text{crit}}$ as the fraction of the critical energy density $\rho_{\text{crit}} = 3m_{\text{Pl}}^2 H_0^2 \approx 3 \cdot 10^{-47}\,\text{GeV}^4$. Since we want our field to explain the DM content of the universe, we are especially interested in the ratio of the density parameter of the scalar field to the density parameter of the DM in the universe $\Omega_{\text{DM}} \approx 0.26$ [295]. Thus, we aim for a compact expression for

$$\frac{\Omega_\phi}{\Omega_{\text{DM}}} = \frac{\rho_\phi(t_0)}{\rho_{\text{crit}}\,\Omega_{\text{DM}}}\,, \tag{5.4}$$

with the energy density in the scalar field today $\rho_\phi(t_0)$. It can be expressed using a WKB approximation as [235]

$$\rho_\phi(t_0) \approx \frac{1}{2} m_\phi^2 \phi^2(t_{\text{WKB}}) \frac{a^3(t_{\text{WKB}})}{a^3(t_0)}\,, \tag{5.5}$$

where t_{WKB} denotes the time where we begin using the WKB approximation and $a(t)$ refers to the scale factor. Transforming the fraction of scale factors with the help of comoving entropy conservation [235]

$$S = sa^3 = \frac{2\pi}{45} g_{*,s}(T) T^3 a^3 = \text{const}\,, \tag{5.6}$$

where s is the comoving entropy density, $g_{*,s}$ is the effective number of entropy dofs and T is the temperature, we get

$$\frac{a^3(t_{\mathrm{WKB}})}{a^3(t_0)} = \frac{g_{*,s}(T_0)\, T_0^3}{g_{*,s}(T_{\mathrm{WKB}})\, T_{\mathrm{WKB}}^3}\,. \tag{5.7}$$

Furthermore, using the condition implicitly defining T_{WKB}, $3H(T_{\mathrm{WKB}}) = m_\phi$, combined with the equation for the Hubble parameter during radiation domination, Eq. (A.10), we find that the energy density scales like

$$\rho_\phi(t_0) \sim \phi^2(t_{\mathrm{WKB}})\, m_\phi^{\frac{1}{2}}\, \mathcal{F}(T_{\mathrm{WKB}})\,, \tag{5.8}$$

where the hidden proportionality factor depends on $T_0 = 2.73\,\mathrm{K}$ ($1\,\mathrm{K} = 8.62 \cdot 10^{-14}\,\mathrm{GeV}$) and we introduced

$$\mathcal{F}(T_{\mathrm{WKB}}) \coloneqq \left(\frac{g_*(T_{\mathrm{WKB}})}{3.38}\right)^{\frac{3}{4}} \left(\frac{3.94}{g_{*,s}(T_{\mathrm{WKB}})}\right)\,, \tag{5.9}$$

which is approximately one and encodes the change in relativistic dofs from t_{WKB} until today. In difference to [235], we use a more careful matching of the initial conditions (cf. [262]) resulting in a slightly altered relation between the field value at the end of inflation ϕ_e and $\phi(t_{\mathrm{WKB}})$. In this way we find $\phi_e^2 \approx 3\phi^2(t_{\mathrm{WKB}})$, leading finally to

$$\frac{\Omega_\phi}{\Omega_{\mathrm{DM}}} \approx 5\,\mathcal{F}(T_{\mathrm{WKB}}) \left(\frac{\phi_e}{10^{12}\,\mathrm{GeV}}\right)^2 \sqrt{\frac{m_\phi}{\mathrm{eV}}}\,. \tag{5.10}$$

Note that due to the non-minimal coupling to gravity, the field value at the end of inflation ϕ_e is in general not identical to the field value at the start of inflation ϕ_s. Furthermore, assuming from now on that the scalar field makes up all of the DM in the universe, $\Omega_\phi = \Omega_{\mathrm{DM}}$, Eq. (5.10) provides a possibility to link the mass of the scalar field m_ϕ to ϕ_e.

Let us now turn to the evolution of the scalar field during inflation, as this is the only era really being affected by the non-minimal coupling. Since we assume a perfect de Sitter expansion, we have during inflation $R = 12H_I^2$ (cf. Fig. 5.1) and the EOM, Eq. (5.3), is one of a damped harmonic oscillator. However, we can not assume $\dot{\phi}_s = 0$ like for the minimally coupled case, as the non-minimal coupling generally allows for the field value to change during inflation[1]. Taking this into account, we find for the general solution of the scalar field evolution during inflation

$$\phi(t) = \phi_s \left(c_1\, \mathrm{e}^{-\frac{1}{2}\alpha_- H_I t} + c_2\, \mathrm{e}^{-\frac{1}{2}\alpha_+ H_I t}\right)\,, \tag{5.11}$$

where t denotes the time from the start of inflation, we have $c_1 + c_2 = 1$ with their exact expressions being given by Eq. (F.2) and encoding the dependence on the initial conditions,

[1] For a minimal coupling, the damping of any non-zero $\dot{\phi}_s$ is so strong that it quickly becomes $\dot{\phi} \approx 0$ and one usually neglects this short initial period of inflation and works directly with $\dot{\phi}_s = 0$. The possibility for the field value to change during inflation implies that this strong damping is not there for the non-minimally coupled case and we can therefore not assume $\dot{\phi}_s = 0$.

and we introduced[2]

$$\alpha_{\pm} \coloneqq 3 \pm \sqrt{9 - 48\xi}\,. \tag{5.12}$$

Since $\alpha_{\pm}$ appears in the exponential, its influence is very strong and our region of interest are values of ξ relatively close to zero. Thus, we generally have $\xi < 3/16$, leading to $\alpha_{\pm}$ being both real and positive and $\alpha_+ > \alpha_-$. Therefore, the first term of Eq. (5.11) will after a short amount of time become dominant and we can approximate the field value during (later times of) inflation by

$$\phi(a) \approx c_1 \phi_s \left(\frac{a}{a_s}\right)^{-\frac{1}{2}\alpha_-} = c_1 \phi_s \, \mathrm{e}^{-\frac{1}{2}\alpha_- N(a)}, \tag{5.13}$$

where we used in the first step that for exponential inflation we have the relation $a = a_s \mathrm{e}^{H_I t}$ and in the second one the definition of the number of e-folds $N(a) \coloneqq \ln(a/a_s)$. In particular, the field value at the end of inflation is given by

$$\phi_e \approx c_1 \phi_s \mathrm{e}^{-\frac{1}{2}\alpha_- N_{\mathrm{tot}}}\,, \tag{5.14}$$

where the total number of e-folds of inflation N_{tot} can potentially be very large [297, 298] depending on the scenario of inflation, allowing even in the case of small values of ξ (and thereby α_-) for a substantial impact of the exponential factor. Another difference with regard to the minimally coupled scenario is the fact that the scalar field has a non-zero time derivative at the end of inflation, directly linked to the size of ξ via α_-

$$\dot{\phi}_e = -\frac{1}{2}\alpha_- H_I \phi_e\,, \tag{5.15}$$

which can be relevant to the post-inflationary evolution of the field.

As discussed in Sec. 5.1, we have to ensure that the field value does not grow beyond the Planck scale for our treatment to be valid. This limits the allowed values for ξ, as negative values would lead to negative values of α_- (cf. Eq. (5.12)) and thereby to a growing field value during inflation. We show the corresponding limits in Fig. 5.2 under the conservative assumptions of minimal inflation, $N_{\mathrm{tot}} = N_{\mathrm{min}}(H_I)$ (cf. App. E), and initial de Sitter vacuum fluctuations, $\phi_s = H_I/2\pi$ and $\dot{\phi}_s = 0$. From Fig. 5.2 we find that the bound is usually in the range of $\xi \sim -1$ to -0.1, depending on the value of H_I. For lower scales of inflation, $H_I \lesssim 10^{-14}\,\mathrm{GeV}$, it can be a bit looser. Since the depicted limit is calculated for minimal inflation, we want to remark that it can for longer periods of inflation become significantly stronger (cf. Eq. (5.14)).

5.2.2 Scalar Fluctuations and Isocurvature Perturbations

Besides the constraint that the scalar field value has to remain below the Planck scale, the second important constraint is given by the non-detection of isocurvature perturbations by the Planck satellite [295]. These kind of perturbations are expected to appear in models like ours, where in addition to the inflaton field there is a second field present

[2]This definition of $\alpha_{\pm}$ implicitly assumes $m_\phi^2/H_I^2 \ll \xi$, which is usually the case.

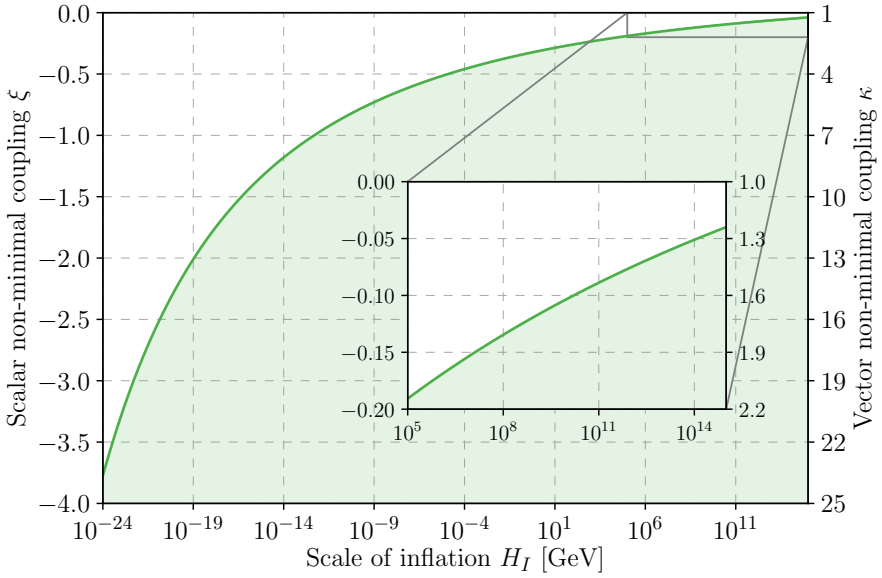

Figure 5.2.: Limits on the non-minimal coupling to gravity for the scalar case (left axis) and the vector case (right axis) depending on the Hubble parameter during inflation H_I from the constraint that the field value has to remain below the Planck scale $m_{\rm Pl}$. The depicted limits assume minimal inflation, $N_{\rm tot} = N_{\rm min}(H_I)$, and initial de Sitter vacuum fluctuations, $\phi_s = H_I/2\pi$ and $\dot{\phi}_s = 0$.

during inflation. As both of these fields acquire perturbations over the course of inflation imprinted in their corresponding energy densities, both of them could in general manifest in the CMB measurements done by Planck. The perturbations stemming from the inflaton field are called adiabatic or curvature perturbations and are identical for all particles, since all of them originate from the decay of the inflaton field. Thus, with respect to a reference particle species (usually photons), there is no spatial variation. This is different for entropy or isocurvature perturbations, because they are independent of the inflaton field and one would therefore expect spatial variation with respect to photons. For this reason, we will look in this section at the energy density contrast power spectrum related to the fluctuations of the scalar field and use it to derive constraints for the parameter space of our model, focused on the misalignment mechanism.

In a first step towards the energy density contrast power spectrum, we will look at the power spectrum of the scalar field fluctuations themselves. This was analyzed in [254] in the context of DM generated from fluctuations, but is identically valid for our analysis of the misalignment mechanism and given by

$$\mathcal{P}_\phi(k, a_k) = \left(\frac{H_I}{2\pi}\right)^2 F(\alpha_-)\,, \tag{5.16}$$

with the comoving wavenumber k and

$$F(\alpha_-) \coloneqq \frac{2^{2-\alpha_-}}{\pi}\,\Gamma^2\left(\frac{3-\alpha_-}{2}\right), \tag{5.17}$$

where $\Gamma(\cdot)$ refers to the Gamma function. Furthermore, we introduced $a_k \coloneqq k/H_I$ that denotes at which time the power spectrum is evaluated, with a_k referring to the point in time that the scale k left the horizon. Looking at Eq. (5.16) for the power spectrum, we see that it is the same as the usual scale invariant result $(H_I/2\pi)^2$ for the minimally coupled case, except for the additional factor $F(\alpha_-) \sim 1$. This similarity can be understood by the fact that within the horizon we have $k/a \gg H_I$ and therefore the non-minimal coupling term, which scales with H_I by means of the Ricci scalar R, is actually subdominant.

After horizon exit however, this changes very quickly when the fluctuations have the same EOMs as the homogeneous field value and the power spectrum evolves according to [254]

$$\mathcal{P}_\phi(k,a) = \mathcal{P}_\phi(k,a_k)\left(\frac{\phi(k,a)}{\phi(k,a_k)}\right)^2. \tag{5.18}$$

Using the evolution equation for the homogeneous field, Eq. (5.13), we can evaluate the above expression to find

$$\mathcal{P}_\phi(k,a) = \mathcal{P}_\phi(k,a_k)\left(\frac{k}{a\,H_I}\right)^{\alpha_-} \tag{5.19}$$

and in particular for the end of inflation

$$\mathcal{P}_\phi(k,a_e) = \mathcal{P}_\phi(k,a_k)\,\mathrm{e}^{-\alpha_- N(k)}, \tag{5.20}$$

with $N(k)$ being the number of e-folds between the mode k exiting the horizon and the end of inflation, cf. Eq. (E.1). In comparison to the evolution of the homogeneous field, as laid out by Eq. (5.14), we see that the fluctuations only behave similar when superhorizon in scale. This is a distinct difference, as in contrast to N_{tot} one can (under certain assumptions) derive an upper limit for the corresponding number of e-folds $N(k)$ for the modes of interest in cosmology [296].

With the help of the above formula for the power spectrum of the scalar field fluctuations, we can now find an expression for the corresponding energy density contrast power spectrum, which is constrained by Planck measurements. The energy density contrast represents the deviations from the mean energy density $\langle\rho\rangle$ and is thus in general given by

$$\delta(\vec{x}) \coloneqq \frac{\rho(\vec{x}) - \langle\rho\rangle}{\langle\rho\rangle} \equiv \frac{\delta\rho(\vec{x})}{\langle\rho\rangle}, \tag{5.21}$$

where we will drop the spatial dependence from now on and introduced the deviation from the average energy density $\delta\rho$. In our situation of the misalignment scenario things simplify, as the homogeneous field value is dominant compared to the fluctuations and we can therefore identify $\langle\rho\rangle = \rho_\phi$, so the energy density of the homogeneous field. Furthermore,

since the energy density generally scales with ϕ^2 (cf. Eq. (5.5))[3], the leading contribution due to the fluctuations scales in the same way with $\delta\rho_\phi \propto 2\phi\,\delta\phi$. With this, we get in a first step for the energy density contrast of the scalar field

$$\delta_\phi \equiv \frac{\delta\rho_\phi}{\rho_\phi} \approx 2\frac{\delta\phi}{\phi} \tag{5.22}$$

and in a second step for the energy density contrast power spectrum

$$\mathcal{P}_{\delta_\phi}(k) \approx \frac{4}{\phi^2}\mathcal{P}_\phi(k,a)\,. \tag{5.23}$$

Here we intentionally did not write a scale factor dependence for the energy density contrast power spectrum on the left side, since in terms of the scale factor $\mathcal{P}_\phi(k,a)$ scales like ϕ^2 (cf. Eq. (5.18)) and therefore the scale factor dependence of the right side cancels. Due to this, we can evaluate the energy density power spectrum at any time, in particular at horizon exit, and find with the help of Eqs. (5.16) and (5.13) for CMB scales

$$\begin{aligned}\mathcal{P}_{\delta_\phi}(k_{\mathrm{CMB}}) &\approx \frac{4}{c_1^2\phi_s^2\,\mathrm{e}^{-\alpha_-(N_{\mathrm{tot}}-N_{\mathrm{CMB}})}}\left(\frac{H_I}{2\pi}\right)^2 F(\alpha_-)\\ &\approx \frac{4}{\phi_e^2\,\mathrm{e}^{\alpha_- N_{\mathrm{CMB}}}}\left(\frac{H_I}{2\pi}\right)^2 F(\alpha_-)\,,\end{aligned} \tag{5.24}$$

where we used Eq. (5.14) in the second step. As detailed in App. E, $N_{\mathrm{CMB}} \equiv N_{\mathrm{CMB}}(H_I)$ is (under common assumptions) a function only of the scale of inflation H_I and thereby fixed once H_I is chosen. Furthermore, we display the result both in terms of ϕ_s and ϕ_e to highlight once more the difference of the scalar field value at the start and end of inflation.

Using the expression for the energy density contrast power spectrum provided by Eq. (5.24), we can derive limits on the non-minimally coupled scalar field scenario from the non-observation of isocurvature perturbations by Planck [295]. From Eq. (5.24), we find with ϕ_e, H_I and ξ the same set of important parameters as in our whole analysis so far. Since ξ is in principle arbitrary, up to the bounds presented in Fig. 5.2, and our requirement for the scalar field to explain all of the DM ($\Omega_\phi = \Omega_{\mathrm{DM}}$) links m_ϕ and ϕ_e, we choose m_ϕ and H_I as the fundamental parameters of our parameter space. Defining the parameter space with m_ϕ instead of ϕ_e has the advantage that it provides a natural lower cutoff of $m_\phi \gtrsim 10^{-22}\,\mathrm{eV}$ [299], due to the restriction that the wavelength of the DM candidate has to fit within a galaxy (size $\sim$1kpc) to be able to be confined to it. For the upper end we choose the cutoff $m_\phi = 1\,\mathrm{eV}$, which reflects our focus on the potential to realize (extremely) light DM candidates.

The isocurvature limits from Planck provide an upper bound on the energy density contrast power spectrum (cf. e.g. [262]) and we use the "axion II" case of the Planck CDI scenario [295] because it reflects the non-zero spectral index and uncorrelatedness with adiabatic perturbations of our scenario. In this way we get the limits presented in Fig. 5.3, where in addition to the constraint from isocurvature perturbations we also include the constraint that the initial homogeneous field value has to be smaller than the Planck scale

[3] This scaling is true for the envelope of the WKB approximation or if one uses the relation between $\dot{\phi}$ and ϕ to express everything in terms of ϕ.

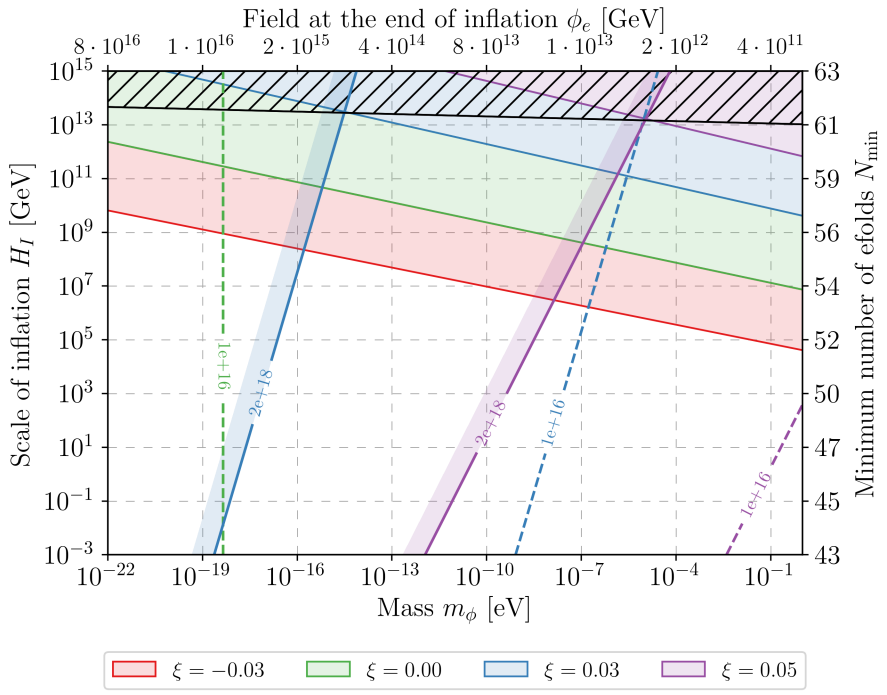

Figure 5.3.: Constraints on the scalar misalignment scenario depicted in the m_ϕ–H_I–plane for several values of the non-minimal coupling ξ. The colored regions indicate which part of the parameter space is excluded due to isocurvature constraints, while the colored lines denote the necessary initial field value under the assumption of minimal inflation to get the correct DM energy density (solid lines for $\phi_s = m_{\mathrm{Pl}}$ and dashed ones for $\phi_s = 10^{16}\,\mathrm{GeV}$). The black hatched region depicts the part of parameter space in which there exists no combination of ξ and $\phi_s < m_{\mathrm{Pl}}$ that reproduces the observed amount of DM while fulfilling the isocurvature constraints by Planck. As there is a one-to-one correspondence of the scalar mass parameter m_ϕ and the scalar field value at the end of inflation ϕ_e (cf. Eq. (5.10)) as well as the scale of inflation H_I and the minimal number of e-folds $N_{\min}$ (cf. Eq. (E.2)), their respective values are given on the top and right axis.

m_{Pl}, where we assume the shortest possible duration of minimal inflation (cf. App. E). Overall, we find that a large enough non-minimal coupling can relax the isocurvature bounds to a degree that the misalignment mechanism provides a viable way to create the correct abundance of DM for scales of inflation up to $H_I \sim 10^{13}\,\mathrm{GeV}$, irrespective of the scalar mass m_ϕ. In comparison to the minimal coupling case, represented by $\xi = 0$ in Fig. 5.3, this is significantly different, as especially for larger values of m_ϕ the scale of inflation has to be considerably lower in the minimal coupling case. For each specific value of ξ, the two bounds from isocurvature perturbations and non-transplanckian field values exclude different parts of parameter space. The non-transplanckian field value restriction dominantly excludes low scalar masses m_ϕ, as very light DM masses require larger field values to recreate the correct abundance of DM (cf. Eq. (5.10)), while

isocurvature perturbations mostly exclude large scales of inflation (cf. dependence on H_I of Eq. (5.24)).

5.2.3 Stochastic Scenario

In the addition to the misalignment scenario discussed in the last sections, it is also possible to generate the correct abundance of DM in the stochastic scenario [245, 246] as briefly described in Sec. 5.1. The underlying idea is that for long periods of inflation the small fluctuations that get stretched to superhorizon scales during inflation can add up in a random walk like process and thereby create a non-zero homogeneous field value. To describe this random walk, one can assume that the homogeneous field value receives a "kick" every Hubble time $t_H = 1/H_I$ from the modes that exit the horizon at that time. This gets counteracted by the relaxation of the homogeneous field value driven by the effective mass of the scalar as described in Sec. 5.2.1. In our discussion here, we will focus on the case in which equilibrium between these two effects is reached, even though, in general, this is not a strict requirement for the stochastic scenario to work.

Similarly to the misalignment scenario, we will extend the existing literature by taking into account a non-minimal coupling of the scalar to gravity. To do so, we will follow along the lines of [246], considering that the (squared) effective mass $m_{\text{eff}}^2 \equiv m_\phi^2 + \xi R \approx 12\xi H_I^2$ is generally non-negligible compared to the (squared) scale of inflation H_I^2. This will most strongly affect the last N_{min} e-folds of inflation, during which the stretched fluctuations cannot contribute to the homogeneous field value any more, as they would not be stretched enough to cover the whole horizon and therefore not lead to a homogeneous field value. On the other hand, the superhorizon homogeneous field value continues to be driven towards its minimum by the effective mass of the field. For the details of our calculation we refer to App. F, while we here focus on the main results and consequences of the non-minimal coupling.

For a long enough period of inflation, the probability distribution of the homogeneous field value created from summing up small contributions from stretched fluctuations approaches a Gaussian distribution with a mean of zero and a variance of (cf. Eq. (F.9) for the exact expression)

$$\left\langle \phi_\delta^2 \right\rangle \approx \frac{F(\alpha_-)}{\alpha_-} \left(\frac{H_I}{2\pi}\right)^2 \mathrm{e}^{-\alpha_- N_{\text{min}}} , \tag{5.25}$$

valid for our range of interest of $0 \lesssim \xi \lesssim 3/16$. Note that for extremely small values of ξ (or α_-) the implicit assumption $m_\phi^2/H_I^2 \ll \xi$ can be violated and our results would reduce to the minimally coupled case by taking an effective $\xi_{\text{eff}} \sim m_\phi^2/H_I^2$ (cf. App. F and [246]). From the result of Eq. (5.25) we can deduce the expected typical value of the homogeneous field, since its size is given by $\sqrt{\left\langle \phi_\delta^2 \right\rangle}$. Additionally, we remark that only modes are taken into account that are still superhorizon today and therefore correspond to a homogeneous field value, as mentioned above. Furthermore, we can also identify both contributions resulting in an equilibrium from Eq. (5.25). While the first part corresponds to the creation of a homogeneous field value from fluctuations (cf. Eq. (5.16)), the exponential suppression corresponding to the second part represents the field evolution during the last N_{min} e-folds of inflation (cf. Eq. (5.14)). From the exponential character of this suppression, we can

already infer that a non-minimal coupling has a substantial influence on the stochastic scenario.

While the suppression of the homogeneous field value during the last e-folds of inflation favors the minimally coupled case, the time it takes to reach the equilibrium between creation and relaxation of the homogeneous field value can be substantially shorter. For our calculation of this time, or number of e-folds, we require two things. First, the equilibrium between creation and relaxation of the homogeneous field value from fluctuations has to be reached and second, the stochastic contribution has to be dominant over the misalignment contribution which is in principle also there. From the requirement of having reached the equilibrium we find for the necessary extra number of e-folds (cf. App. F)

$$\Delta N \coloneqq N_{\mathrm{tot}} - N_{\mathrm{min}} > \frac{1}{\alpha_-}\,, \tag{5.26}$$

while for the stochastic contribution to be bigger by a factor of γ, we get the expression (cf. App. F)

$$\Delta N > \frac{1}{\alpha_-} \ln\left[\gamma \frac{2^{2+\alpha_-}\pi^3}{\Gamma^2\left(\frac{3-\alpha_-}{2}\right)} \frac{\alpha_-}{(\alpha_+ - \alpha_-)^2}\left(\frac{\dot{\phi}_s}{H_I^2} + \frac{1}{2}\alpha_+ \frac{\phi_s}{H_I}\right)^2 + 1\right]. \tag{5.27}$$

The results of Eqs. (5.25) and (5.26)/(5.27) are our main results for the description of the stochastic scenario and generalize the results found in [245, 246] to arbitrary initial conditions and large effective masses, e.g. due to a non-minimal coupling to gravity. With these results at hand, we can now proceed by looking at possible restrictions of the stochastic scenario. Since the subhorizon fluctuations in the stochastic scenario lead to isocurvature perturbations in the CMB in the same way as we analyzed for the misalignment mechanism, our corresponding discussion for the energy density contrast power spectrum carries over and Eq. (5.24) remains valid. The only difference is that ϕ_e is now not a free parameter of the theory, but determined by the fluctuations themselves through $\phi_e \approx \sqrt{\langle \phi_\delta^2 \rangle}$ (cf. Eq. (5.25)). Thus we find for the energy density contrast power spectrum (assuming enough e-folds of inflation)

$$\mathcal{P}_{\delta_\phi}(k_{\mathrm{CMB}}) \approx 4\alpha_- \, \mathrm{e}^{\alpha_-(N_{\mathrm{min}} - N_{\mathrm{CMB}})}\,, \tag{5.28}$$

where the exponential factor appears due to the difference of the largest observable scales and the ones accessible by the CMB, and corresponds to about 7 e-folds (cf. App. E). For small values of α_-, this exponential contribution is subdominant and $\mathcal{P}_{\delta_\phi}(k_{\mathrm{CMB}}) \approx \alpha_-$, which reflects the fact that the accumulated field variance is enhanced by a factor of $1/\alpha_-$ in comparison to the amplitude of the fluctuations of an individual mode (cf. comparison of Eqs. (5.25) and (5.16)).

Again using the Planck constraint on isocurvature perturbations [295], we find explicitly for the limit $\mathcal{P}_{\delta_\phi}(k_{\mathrm{CMB}}) = \mathcal{P}_I(k_{\mathrm{CMB}}) \lesssim 10^{-9}$ and thus the strong bound of $\xi \lesssim 10^{-10}$, corresponding to $\Delta N \gtrsim 10^9$. This implies that any non-minimal coupling of the scalar field to gravity makes it hard to realize such a stochastic scenario. Since we only used the fact that the effective mass is non-negligible in comparison to the scale of inflation to derive this strong bound, we conjecture that this difficulty to realize a stochastic scenario

is not specific to models with a non-minimal coupling to gravity but holds for all models for which the effective mass is non-negligible.

5.3 Non-Minimally Coupled Vector Fields

For our discussion of non-minimally coupled vector fields, we will follow the same route as we did for the scalar case, by first focusing on the misalignment scenario and looking at the evolution of the homogeneous field value together with the relic density, before addressing the generated isocurvature perturbations and how they limit the available parameter space. Afterwards we will conclude our discussion by analyzing the stochastic scenario also for non-minimally coupled vector fields. While most of the results for the vector case can be found following the same steps as in the scalar case, especially the treatment of fluctuations will need some additional effort.

5.3.1 Homogeneous Vector Field Value and Relic Density

From the action of the non-minimally coupled vector model, Eq. (5.2), we can derive in the same way as for the scalar model the EOMs for the homogeneous field value [235, 260, 262]

$$\chi_0 = 0 \quad \text{and} \quad \ddot{\chi}_i + 3H\dot{\chi}_i + \left(m_X^2 + \frac{1-\kappa}{6}R\right)\chi_i = 0\,, \tag{5.29}$$

where we introduced the physical field $\chi_\mu \equiv X_\mu/a$ (cf. [260][4]) to express them. This turns the energy density (for an approximately homogeneous field) into [235, 260, 262]

$$\rho_\chi = \sum_{i=1}^{3}\left[\frac{1}{2}\dot{\chi}_i^2 + \frac{1}{2}m_X^2\chi_i^2 + (1-\kappa)\left(\frac{1}{2}H^2\chi_i^2 + H\dot{\chi}_i\chi_i\right)\right]. \tag{5.30}$$

The advantage of introducing the physical field as done above is that the EOM for each spatial component is identical to the one of the scalar field (cf. Eq. (5.3)) once we identify

$$\frac{(1-\kappa)}{6} \longleftrightarrow \xi\,. \tag{5.31}$$

This correspondence is very important, as it will enable us to establish connections between our calculations done for the scalar case and the ones for the vector case. In particular, we find that a non-minimally coupled vector with $\kappa = 1$ behaves identical to a minimally coupled scalar ($\xi = 0$).

Making use of the correspondence between the scalar and vector case through Eq. (5.31), we can directly transfer our results found for the scalar case in Sec. 5.2.1 to the vector case discussed here. This includes in particular all evolution equations given by Eq. (5.11) and following. By denoting the absolute value of the vector field by $\chi \equiv |\vec{\chi}|$, we thus find

[4]Strictly speaking, the physical field χ is usually only introduced for the spatial components χ_i, however, because we find $X_0 = 0$ from the EOMs, we can extend the definition to the time component to simplify the notation.

for the relic density

$$\frac{\Omega_\chi}{\Omega_{\rm DM}} \approx 5\,\mathcal{F}(T_\star)\left(\frac{\chi_e}{10^{12}\,\mathrm{GeV}}\right)^2\sqrt{\frac{m_X}{\mathrm{eV}}}, \tag{5.32}$$

where we remind the reader that in general $\chi_e \neq \chi_s$ because of the non-minimal coupling to R and the resulting superhorizon evolution. Their relation is defined by the non-minimal coupling κ through

$$\chi_e \approx c_1 \chi_s\, \mathrm{e}^{-\frac{1}{2}\beta_- N_{\rm tot}}\,, \tag{5.33}$$

where we introduced (corresponding to $\alpha_\pm$ in the scalar case)

$$\beta_\pm \coloneqq 3 \pm \sqrt{1+8\kappa}\,. \tag{5.34}$$

Also for reference to other works, we note that β_- defined here is related to ν used in [262, 263] by $\beta_- = 3 - 2\nu$ and we assumed $m_X^2/H_I^2 \ll 1-\kappa$.

From Eq. (5.33), we see that the evolution during inflation can lead to a substantial enhancement or suppression of the field value, depending on whether we have $\kappa > 1$ or $\kappa < 1$. As this potentially growing field value has to remain below the Planck scale $m_{\rm Pl}$ (cf. Sec. 5.1), we can derive limits on $\kappa > 1$. These limits are depicted in Fig. 5.2 under the conservative assumptions of minimal inflation, $N_{\rm tot} = N_{\rm min}(H_I)$ (cf. App. E), and initial de Sitter vacuum fluctuations, $\chi_s = H_I/2\pi$ and $\dot{\chi}_s = 0$. In the vector case they are usually in the range of $\kappa \sim 1.5$ to 10, with larger values being allowed for low scales of inflation H_I. Again, we note that they become significantly stronger for longer periods of inflation (cf. Eq. (5.14)) and are independent of whether or not we assume the vector field to represent DM.

5.3.2 Vector Fluctuations and Isocurvature Perturbations

Similar to the scalar case, also a non-minimally coupled vector field results in isocurvature perturbations that would be imprinted in the CMB and could therefore be detected by Planck. Thus, the non-detection of these isocurvature perturbations [295] leads to constraints on the parameter space of the non-minimally coupled vector scenario. To calculate the expected amount of isocurvature perturbations and the resulting limit, we will split our calculation into two parts, since the multicomponent nature of the vector field complicates the treatment. First, we will look into the generation of fluctuations during inflation, before we will address in detail their evolution after inflation. For both regimes, it is best to split the fluctuations into transverse ($\perp$) and longitudinal ($\parallel$) modes and address each of these polarizations separately. Additionally, the treatment is furthermore simplified by working in momentum space by Fourier transforming the equations.

5.3.2.1. Generation During Inflation

For the generation of vector fluctuations we start out by looking at the transversal fluctuations before considering the more involved longitudinal ones.

Transversal Fluctuations The EOMs of the two transversal polarizations $\delta\chi_i^\perp$ of the fluctuations, are in momentum space given by (cf. [262])

$$\ddot{\delta\chi_i}^\perp + 3H\dot{\delta\chi_i}^\perp + \left(m_X^2 + \frac{1-\kappa}{6}R + \frac{k^2}{a^2}\right)\delta\chi_i^\perp = 0\,, \tag{5.35}$$

which is identical to the expression in the scalar case (cf. [254]), using the usual identification $(1-\kappa)/6 \leftrightarrow \xi$. Thus, we can transfer our result from Sec. 5.2.2 and find for the power spectrum of the transversal fluctuations

$$\mathcal{P}_{\chi_i}^\perp(k,a) = \left(\frac{H_I}{2\pi}\right)^2 F(\beta_-)\left(\frac{k}{aH_I}\right)^{\beta_-}\,, \tag{5.36}$$

with $F(\cdot)$ as defined in Eq. (5.17).

Longitudinal Fluctuations In addition to working in momentum space, we can simplify the treatment of the EOM for longitudinal fluctuations further by introducing conformal time τ via $\mathrm{d}t/\tau = a$ and $a = -1/(\tau H_I)$ as well as working with the original field $\delta X^\parallel = a\,\delta\chi^\parallel$. Doing so, we find the EOM (cf. [262])

$$0 = \left[\partial_\tau^2 - \frac{2\tau k^2 H_I^2}{\tau^2 k^2 H_I^2 + m_X^2 - 2\kappa H_I^2}\partial_\tau + \frac{m_X^2 - 2\kappa H_I^2}{\tau^2 H_I^2} + k^2\right]\delta X^\parallel\,. \tag{5.37}$$

Since it turns out that this EOM is hard to solve in its complete form, we will focus on the limiting cases of the sub- and superhorizon limit, in which it can be solved analytically, and then use numerical methods to accurately link the two.

Starting with the subhorizon limit, for which $k/(aH_I) = -k\tau \gg 1$, the EOM simplifies to

$$0 = \left[\partial_\tau^2 - \frac{2}{\tau}\partial_\tau + \frac{\widetilde{m}^2}{\tau^2 H_I^2} + k^2\right]\delta X^\parallel\,, \tag{5.38}$$

where we also introduced the shifted mass $\widetilde{m}^2 \coloneqq m_X^2 - 2\kappa H_I^2$. Furthermore redefining $\widetilde{\delta X}_i^\parallel \equiv -|\widetilde{m}|/(\tau k H_I)\;\delta X_i^\parallel$ (cf. [263]) removes the term proportional to ∂_τ and results in

$$0 = \left[\partial_\tau^2 + \frac{m_X^2 - 2(\kappa+1)H_I^2}{\tau^2 H_I^2} + k^2\right]\widetilde{\delta X}^\parallel\,. \tag{5.39}$$

The correct physical solution to this equation requires the Bunch-Davies vacuum as initial condition (cf. [263]), which is given by

$$\widetilde{\delta X}^\parallel \xrightarrow{\tau\to-\infty} \frac{1}{\sqrt{2k}}\mathrm{e}^{-ik\tau}\,. \tag{5.40}$$

Explicitly solving Eq. (5.39) with the initial condition of Eq. (5.40), results in the solution

(cf. [262])

$$\delta X^{\parallel} \equiv -\frac{\tau k H_I}{|\widetilde{m}|}\widetilde{\delta X}^{\parallel} = -\frac{\tau k H_I}{|\widetilde{m}|}\sqrt{-\pi\tau}\frac{\mathrm{e}^{i\frac{\pi}{2}\left(\widetilde{\nu}+\frac{1}{2}\right)}}{1-\mathrm{e}^{2i\pi\widetilde{\nu}}}\left[J_{\widetilde{\nu}}(-k\tau)-\mathrm{e}^{i\pi\widetilde{\nu}}J_{-\widetilde{\nu}}(-k\tau)\right], \tag{5.41}$$

with $J_{\pm\widetilde{\nu}}(\cdot)$ being Bessel functions of the first kind and we introduced the expression $\widetilde{\nu} \coloneqq 1/2\sqrt{1+8(\kappa+1)-4m_X^2/H_I^2}$. Thus, we have found an explicit solution in the subhorizon limit, which will be important for linking the sub- and superhorizon regime.

In the superhorizon limit, for which $-\tau k \ll 1$, the EOM Eq. (5.37) reduces to

$$0 = \left[\partial_\tau^2 - \frac{2\tau k^2 H_I^2}{\widetilde{m}^2}\partial_\tau + \frac{\widetilde{m}^2}{\tau^2 H_I^2} + k^2\right]\delta X^{\parallel}, \tag{5.42}$$

which can be explicitly solved in terms of confluent hypergeometric functions of the first kind. For our purposes however, it is more practical to use $m_X^2 \ll 2\kappa H_I^2$ and $-\tau k \ll 1$ to find the approximate solution

$$\begin{aligned}\delta X^{\parallel} &\approx 2^{-2-\frac{1}{2}\beta_-}(k\tau)^{-1+\frac{1}{2}\beta_-}\left[\widetilde{C}_1\,(k\tau)^{3-\beta_-} + \widetilde{C}_2\,2^{3-\beta_-}\right] \\ &\approx \widetilde{C}_2\,2^{1-\frac{1}{2}\beta_-}(k\tau)^{-1+\frac{1}{2}\beta_-},\end{aligned} \tag{5.43}$$

where the approximation of the second line is valid long after horizon exit and the appearing coefficients $\widetilde{C}_1$ and $\widetilde{C}_2$ are in general functions of k and κ. One important realization is that for the superhorizon solution to fit to the subhorizon one, the coefficients need to scale in terms of k like $\widetilde{C}_{1,2} \sim 1/\sqrt{k}$, as can be seen from trying to analytically match them. Extracting this dependence on k, we are left with a dependence on κ and thus define $\widetilde{C}_2 \equiv 1/\sqrt{k}\; f(\kappa)$. Switching back to the physical field and scale factor (instead of conformal time), the solution becomes

$$\delta\chi^{\parallel} \approx f(\kappa)\,2^{1-\frac{1}{2}\beta_-}\frac{H_I}{k^{3/2}}\left(\frac{k}{aH_I}\right)^{\frac{1}{2}\beta_-}. \tag{5.44}$$

Importantly, this superhorizon solution depends in the same way on time as the solution for the homogeneous field and the transversal fluctuations.

The last remaining step is to link the sub- and superhorizon solution by numerically solving the full EOM Eq. (5.37). To do so, we use the subhorizon solution as the initial condition, evolve it numerically to the superhorizon regime and then choose $f(\kappa)$ such that the analytical superhorizon solution fits the numerical one. A particular example of this is depicted in Fig. 5.4 for $\kappa = 1$, showing how the numerical solution at first agrees well with the subhorizon one before shortly after horizon exit (at $\tau k = -1$) the superhorizon solution represents the evolution better. Furthermore, we can also see that the subhorizon solution provides a very accurate description for $\tau k \lesssim -10$, while the superhorizon solution does so for $\tau k \gtrsim -0.1$, where $\tau k \to -\infty$ represents the Big Bang and $\tau k = 0$ the infinite future.

Extracting several values for $f(\kappa)$ in the range $\kappa \in [10^{-4}, 10]$, which extensively covers our region of interest, we can determine an accurate fit to the numerical results. This fit

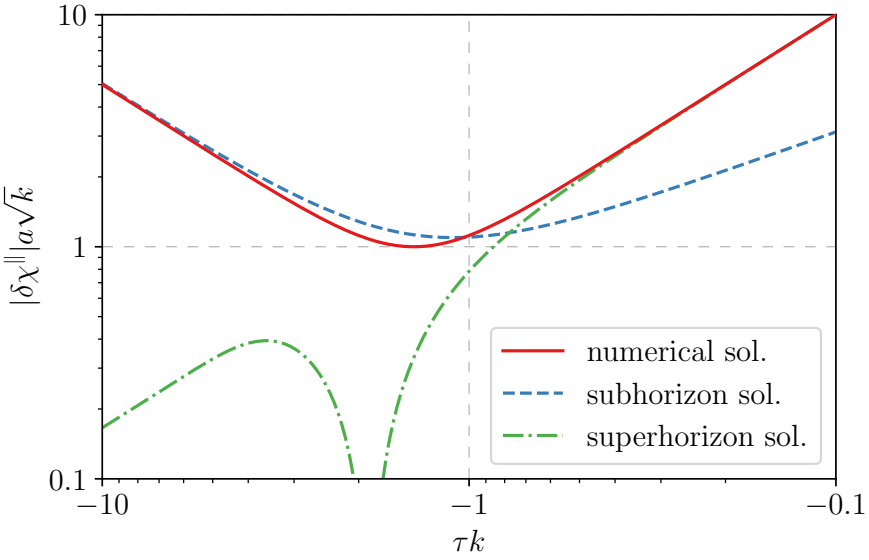

Figure 5.4.: Evolution of the subhorizon (early time), superhorizon (late time) and numerical solution to the EOM Eq. (5.37) for $\kappa = 1$. The value for $f(\kappa)$ is chosen such that the superhorizon solution agrees with the numerical one for late times.

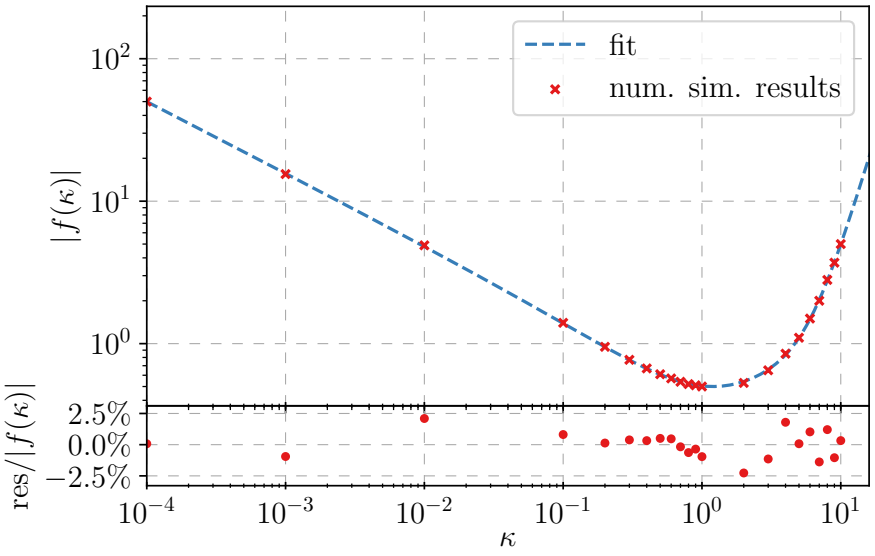

Figure 5.5.: Numerical results for $f(\kappa)$ determined from figures like Fig. 5.4 depicted together with a fit to these numerical results (cf. Eq. (5.45)) in the top panel. The bottom panel shows the relative deviation of this fit (residuals) to the numerical results themselves.

function representing $f(\kappa)$ is given by

$$|f(\kappa)| \approx 0.502\kappa^{-0.5} - 0.224 + 0.262\kappa - 0.0411\kappa^2 + 0.00654\kappa^3\,, \tag{5.45}$$

which is displayed together with the underlying data and the residuals in Fig. 5.5. With deviations of less than 2.5 % from the numerical results, the fit function represents an accurate representation of the real dependence. Note that we chose to directly work with the absolute value of $f(\kappa)$, since this is the quantity appearing in the power spectrum and easier to handle numerically.

With this result we can now calculate the power spectrum of the longitudinal fluctuations given by $\mathcal{P}_\chi^\parallel = k^3/(2\pi^2)|\delta\chi^\parallel|^2$ and find in the superhorizon limit

$$\mathcal{P}_\chi^\parallel(k,a) \approx 2^{3-\beta_-}|f(\kappa)|^2 \left(\frac{H_I}{2\pi}\right)^2 \left(\frac{k}{aH_I}\right)^{\beta_-}\,, \tag{5.46}$$

which is similar to the power spectrum of the transversal perturbations and we can identify the relation

$$\mathcal{P}_\chi^\parallel = \frac{2\pi|f(\kappa)|^2}{\Gamma^2\left(\frac{3-\beta_-}{2}\right)}\,\mathcal{P}_{\chi_i}^\perp\,. \tag{5.47}$$

This relation generalizes the result $\mathcal{P}_\chi^\parallel = 2\,\mathcal{P}_{\chi_i}^\perp$ for $\kappa = 1$ found in [263, 264] to arbitrary values of κ and is our central result of this section. We therefore found that the power spectra from longitudinal and transversal perturbations are proportional to each other and since the proportionality constant is of order one, especially around $\kappa \sim 1$, they are usually also similar to each other in size. However, this similarity does not necessarily hold for the evolution of the power spectra after inflation, to which we will turn next.

5.3.2.2. Evolution After Inflation

As we did for the discussion of the generation of vector fluctuations during inflation, we will also split the analysis of their evolution after inflation into transversal and longitudinal fluctuations.

Transversal Fluctuations In the same way as the generation of transversal perturbations during inflation is identical to the scalar case, their evolution after inflation is also the same, since they have the identical EOMs after we identify $\kappa \leftrightarrow 1 - 6\xi$ (cf. Eq. (5.35) and [254]). Thus, for large scales like the ones of the CMB, we can follow one to one our analysis of the scalar case from Sec. 5.2.2. Keeping in mind that there are two transversal polarizations that each behave like a scalar field, we get an additional factor of two and therefore for the energy density contrast power spectrum representing the induced isocurvature perturbations is

$$\mathcal{P}_{\delta_\chi}^\perp(k_{\mathrm{CMB}}) \approx \frac{8}{\chi_e^2\,\mathrm{e}^{\beta_- N_{\mathrm{CMB}}}} \left(\frac{H_I}{2\pi}\right)^2 F(\beta_-)\,. \tag{5.48}$$

In correspondence to the scalar case, we find a suppression of the isocurvature perturbations for $\kappa < 1$ and an enhancement for $\kappa > 1$.

Longitudinal Fluctuations To analyze the evolution of the longitudinal fluctuations, we start from the EOM Eq. (5.37), but in proper time and with setting $R \equiv 0$ for radiation domination or using R, $\dot{R} \ll m_X^2$ for later eras (cf. Fig. 5.1). The EOM then reads

$$\ddot{\delta\chi}^{\parallel} + \left(3 + \frac{2k^2}{k^2 + a^2 m_X^2}\right) H \dot{\delta\chi}^{\parallel} + \left(\frac{2k^2}{k^2 + a^2 m_X^2} H^2 + \frac{k^2}{a^2} + m_X^2\right) \delta\chi^{\parallel} = 0\,. \tag{5.49}$$

Since we assume reheating to be approximately instantaneous, this EOM covers the whole evolution of the perturbations until today.

Already a simple comparison of the EOMs in the transversal and longitudinal case, cf. Eqs. (5.35) and (5.49), suggests that their behavior can be substantially different from each other and thus we have to study the evolution of the longitudinal modes in detail. What helps to simplify the discussion is that we are interested in rather large-scale modes that become non-relativistic before reentering the horizon, since these are the ones connected to the CMB. Thus, we have to analyze their behavior in three different regimes:

(i) $H \gg k/a \gg m_X$

In the superhorizon and relativistic[5] regime, the EOM Eq. (5.49) reduces to

$$\ddot{\delta\chi}^{\parallel} + 5H\dot{\delta\chi}^{\parallel} + 2H^2 \delta\chi^{\parallel} = 0\,, \tag{5.50}$$

which can be solved by using that in this regime we have to be in the radiation dominated era for our masses of interest $m_X \gtrsim 10^{-22}\,\mathrm{eV}$ [299] (cf. Fig. 5.1). Thus, we can use $H_{\mathrm{rad}} = 1/(2t)$ (and $a_{\mathrm{rad}} \sim t^{1/2}$) to find

$$\delta\chi^{\parallel} \approx \frac{\tilde{c}_1}{\sqrt{t}} + \frac{\tilde{c}_2}{t} = \tilde{c}_1' a^{-1} + \tilde{c}_2' a^{-2} \tag{5.51}$$

and after a short while the term scaling with a^{-1} will be the dominant one. However, modes that become non-relativistic before the end of inflation will skip this regime completely, since they violate $k/a \gg m_X$. In particular, the CMB modes of interest skip this regime if

$$m_X \gtrsim \frac{k_{\mathrm{CMB}}}{a_r} \approx 2 \cdot 10^{-4}\,\mathrm{eV} \sqrt{\frac{H_I}{6.6 \cdot 10^{13}\,\mathrm{GeV}}}\,, \tag{5.52}$$

where we used the Planck pivot scale as a typical CMB scale, $k_{\mathrm{CMB}} = 0.05\,\mathrm{Mpc}^{-1}$, and a_r denotes the scale factor at reheating. The scale factor at reheating can, assuming instantaneous reheating as we do, be expressed as $a_r = \mathrm{e}^{-N_{\min}(H_I)}$ (cf. App. E for $N_{\min}(H_I)$). For the scale of inflation H_I we choose as normalization the upper limit compatible with the non-observation of tensor modes [295], $H_I < 6.6 \cdot 10^{13}\,\mathrm{GeV}$. Thus, we conclude that the relativistic and superhorizon regime will not be entered

[5] Note that k/a is not only related to the size of the horizon, but also represents the momentum of the particle $p = k/a$.

by the CMB scale modes of the longitudinal fluctuations if the mass parameter is large enough, $m_X \gtrsim 10^{-4}\,\mathrm{eV}$ (or less for smaller H_I), and if they do enter, the solution tends to scale with a^{-1}.

(ii) $H \gg m_X \gg k/a$

For the superhorizon and non-relativistic regime, we can simplify the EOM Eq. (5.49) to

$$\ddot{\delta\chi}^{\parallel} + 3H\dot{\delta\chi}^{\parallel} = 0\,, \tag{5.53}$$

for which we find the solution (again using the fact that we are in the radiation dominated era like for regime (i))

$$\delta\chi^{\parallel} \approx c_1' + c_2' a^{-1}\,. \tag{5.54}$$

Therefore, one would naively expect that the constant term[6] quickly becomes the dominant one and one could drop the term scaling with a^{-1}. However, as argued by [249], this is not necessarily the case and depends in our situation strongly on how long the fluctuations evolved in regime (i). If they spend enough time in regime (i), their solution becomes nearly perfectly proportional to a^{-1}, leading to a large hierarchy of the coefficients, $c_1' \ll c_2'$, from demanding continuity of the solution and its derivative between regimes (i) and (ii).

Thus, we have to distinguish two different cases. One option is that the fluctuations skip regime (i) completely, which would lead them to follow the constant branch of Eq. (5.54) and hence there is no suppression of the fluctuations. The other option is that they enter regime (i) and the power spectrum gets suppressed. Carefully matching the field value and its derivative through regimes (i) and (ii), we find

$$\delta\chi^{\parallel}(k_{\mathrm{CMB}}, a_{(\mathrm{ii})}) \approx \left(\frac{m_X}{k_{\mathrm{CMB}}/a_r}\right)^2 \delta\chi^{\parallel}(k_{\mathrm{CMB}}, a_r)\,, \tag{5.55}$$

with $a_{(\mathrm{ii})}$ being the scale factor at the end of regime (ii). Here, the appearance of $m_X/(k_{\mathrm{CMB}}/a_r)$ can be intuitively understood, since it gives a measure of how long regime (i) is traversed (cf. discussion on regime (i)) and thus is related to how well the solution scales like a^{-1} before entering regime (ii).

(iii) $m_X \gg H, k/a$

In this non-relativistic regime the Hubble parameter has become small enough for the field to overcome the Hubble friction and therefore the EOM Eq. (5.49) becomes that of pressureless matter

$$\ddot{\delta\chi}^{\parallel} + 3H\dot{\delta\chi}^{\parallel} + m_X^2\delta\chi^{\parallel} = 0\,, \tag{5.56}$$

being identical to the EOM of the homogeneous field and transversal fluctuations. Therefore we can use the results found in the corresponding discussions and combine the different regimes in the next step.

[6] This corresponds to a growing $\delta X_i^{\parallel}$ (cf. [249]), however, not to a real growth of the density perturbations.

Since the influence of the evolution through regimes (i) and (ii) is covered by the potential suppression factor of Eq. (5.55) and regime (iii) behaves as in the transversal case, we can combine all three regimes and find with respect to the transversal result

$$\mathcal{P}^{\parallel}_{\delta_\chi}(k_{\mathrm{CMB}}) \simeq \frac{1}{2}\,\mathcal{P}^{\perp}_{\delta_\chi}(k_{\mathrm{CMB}}) \cdot \frac{2\pi|f(\kappa)|^2}{\Gamma^2\left(\frac{3-\beta_-}{2}\right)} \cdot \begin{cases} 1\,, & \text{if } m \gtrsim k_{\mathrm{CMB}}/a_r \\ \left(\frac{m}{k_{\mathrm{CMB}}/a_r}\right)^4, & \text{if } m \lesssim k_{\mathrm{CMB}}/a_r\,. \end{cases} \tag{5.57}$$

Here, the factor of 1/2 in front accounts for the change in dofs from two transversal ones to one longitudinal one, the central factor reflects the change in the generation of the longitudinal fluctuations during inflation (cf. Sec. 5.3.2.1) and the final distinction between cases is due to the evolution after inflation (cf. Sec.5.3.2.2). The total energy density contrast power spectrum is then given by the sum of the individual polarizations, hence

$$\mathcal{P}_{\delta_\chi}(k_{\mathrm{CMB}}) = \mathcal{P}^{\perp}_{\delta_\chi}(k_{\mathrm{CMB}}) + \mathcal{P}^{\parallel}_{\delta_\chi}(k_{\mathrm{CMB}})\,. \tag{5.58}$$

Like in the scalar case, we can now derive limits from the non-observation of isocurvature perturbations by Planck [295]. The resulting limits are depicted in Fig. 5.6 and are very similar to the scalar limits shown in Fig. 5.3, with the difference that the standard scenario now corresponds to $\kappa = 1$. However, this implies that a non-minimal coupling is essential for the vector scenario to provide a viable DM candidate. One noticeable feature of the depicted limits is a small kink in the isocurvature exclusion limits that stems from the suppression of the longitudinal modes for small enough masses as given by Eq. (5.57).

5.3.3 Stochastic Scenario

Similar to the stochastic scenario discussed for a scalar field in Sec. 5.2.3, it can also be realized for a vector field. While the calculation follows along the same lines, it is, like in the previous sections, helpful to split the contributions of the vector field fluctuations into transversal and longitudinal polarizations.

For the transversal fluctuations, we find again a behavior identical to scalar fluctuations with the usual replacements $\alpha_\pm \leftrightarrow \beta_\pm$ and $\xi \leftrightarrow (1-\kappa)/6$. Thus we can use the result of the scalar case from Sec. 5.2.3 (see also App. F) and find

$$\left\langle {\chi^{\perp}_{\delta}}^2 \right\rangle \approx 2\,\frac{F(\beta_-)}{\beta_-}\left(\frac{H_I}{2\pi}\right)^2 \mathrm{e}^{-\beta_- N_{\min}}\,, \tag{5.59}$$

where the factor of two accounts for the two transversal polarizations.

For the longitudinal fluctuations, we can use (cf Eq. (5.44))

$$\delta\chi^{\parallel} \approx f(\kappa)\,2^{1-\frac{1}{2}\beta_-}\,\frac{H_I}{k^{3/2}}\left(\frac{k}{aH_I}\right)^{\frac{1}{2}\beta_-}\,. \tag{5.60}$$

as derived in Sec. 5.3.2.1. While strictly speaking this result was derived for late times of inflation, it is still a reasonable approximation around horizon exit (cf. Fig. 5.4). Thus, we can follow App. F in finding the accumulated field value at the end of inflation from the longitudinal fluctuations by integrating over all modes that are still superhorizon today.

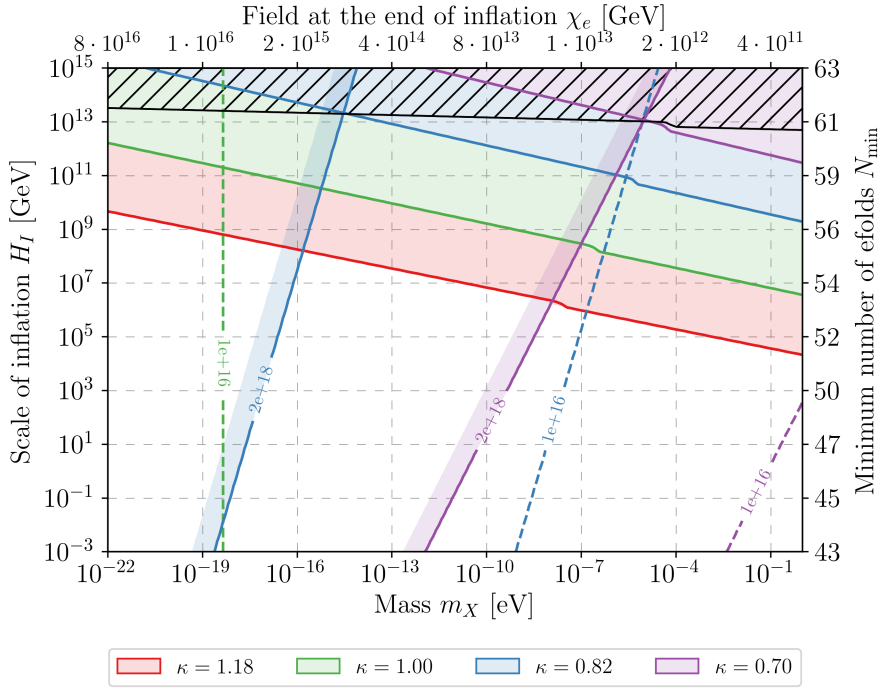

Figure 5.6.: Constraints on the vector misalignment scenario depicted in the m_X–H_I–plane for several values of the non-minimal coupling κ. The colored regions indicate which part of the parameter space is excluded due to isocurvature constraints, while the colored lines denote the necessary initial field value under the assumption of minimal inflation to get the correct DM energy density (solid lines for $\chi_s = m_{\mathrm{Pl}}$ and dashed ones for $\chi_s = 10^{16}\,\mathrm{GeV}$). The black hatched region depicts the part of parameter space in which there exists no combination of κ and $\chi_s < m_{\mathrm{Pl}}$ that reproduces the observed amount of DM while fulfilling the isocurvature constraints by Planck. As there is a one-to-one correspondence of the vector mass parameter m_X and the vector field value at the end of inflation χ_e (cf. Eq. (5.32)) as well as the scale of inflation H_I and the minimal number of e-folds $N_{\min}$ (cf. Eq. (E.2)), their respective values are given on the top and right axis.

However, as we have seen in Sec. 5.3.2.2, the post-inflationary evolution of transversal and longitudinal perturbations can substantially differ, depending on the mass parameter m_X. As we assume equilibrium between the creation and relaxation of the homogeneous field value, the integral over all modes that are still superhorizon today is dominated by the largest scales (cf. App. F), which means that the present horizon scale k_0 is the dominant one. Therefore, the suppression of the longitudinal fluctuations discussed in Sec. 5.3.2.2 (see also [249]) is slightly modified and we find that no suppression occurs for

$$m_X \gtrsim \frac{k_0}{a_r} \sim 10^{-7}\,\mathrm{eV}\sqrt{\frac{6.6 \cdot 10^{13}\,\mathrm{GeV}}{H_I}}\,, \tag{5.61}$$

where $k_0^{-1} \sim 10\text{Gpc}$ is the size of the observable universe. Accounting for the possible suppression, the resulting variance of the superhorizon longitudinal fluctuations is then

$$\left\langle {\chi_\delta^\parallel}^2 \right\rangle \simeq \frac{1}{2} \left\langle {\chi_\delta^\perp}^2 \right\rangle \cdot \frac{2\pi |f(\kappa)|^2}{\Gamma^2\left(\frac{3-\beta_-}{2}\right)} \cdot \begin{cases} 1\,, & \text{if } m \gtrsim k_0/a_r \\ \left(\frac{m}{k_0/a_r}\right)^4, & \text{if } m \lesssim k_0/a_r\,. \end{cases} \tag{5.62}$$

The total variance is simply given by adding up the two contributions from the transversal and longitudinal polarizations

$$\langle {\chi_\delta}^2 \rangle = \left\langle {\chi_\delta^\perp}^2 \right\rangle + \left\langle {\chi_\delta^\parallel}^2 \right\rangle , \tag{5.63}$$

and a typical stochastically generated field value is $\sqrt{\langle {\chi_\delta}^2 \rangle}$.

Demanding that the equilibrium between creation and relaxation of the homogeneous field value from fluctuations has been reached and that the stochastic contribution is dominant over the misalignment contribution, which is in principle also there, requires an extra number of e-folds ΔN in addition to the minimally necessary one $N_{\min}$. Like in the scalar case, an extra number of e-folds of

$$\Delta N > \frac{1}{\beta_-} \tag{5.64}$$

is required to attain equilibrium, while for the created homogeneous field value to be dominant by a factor of γ over the misalignment contribution we find the constraint

$$\Delta N > \frac{1}{\beta_-} \ln \left[\gamma \left(\frac{\pi |f(\kappa)|^2}{\Gamma^2\left(\frac{3-\beta_-}{2}\right)} + 1 \right)^{-1} \frac{2^{1+\beta_-}\pi^3}{\Gamma^2\left(\frac{3-\beta_-}{2}\right)} \frac{\beta_-}{(\beta_+ - \beta_-)^2} \left(\frac{\dot{\chi_s}}{H_I^2} + \frac{1}{2}\beta_+ \frac{\chi_s}{H_I} \right)^2 + 1 \right] . \tag{5.65}$$

Finally, we can use the above results to look at possible restrictions of the stochastic scenario due to isocurvature perturbations. Like in the scalar case, we can employ the energy density contrast power spectrum found when discussing the misalignment mechanism (cf. Eq. (5.58) with Eqs. (5.48) and (5.57)) together with $\chi_e \approx \sqrt{\langle \chi_\delta^2 \rangle}$ (cf. Eq. (5.63) with Eqs. (5.59) and (5.62)) to get

$$\mathcal{P}_\delta(k_{\text{CMB}}) \approx 4\,\beta_-\, \mathrm{e}^{\beta_-(N_{\min} - N_{\text{CMB}})}\,, \tag{5.66}$$

where we neglected a small effect due to the different scales appearing in Eq. (5.57) and Eq. (5.62) (k_{CMB} vs k_0). The equation for the energy density contrast power spectrum reflects again the enhancement of the accumulated field variance by a factor of $1/\beta_-$ with respect to the amplitude of the fluctuations of an individual mode, while it also implies that the stochastic scenario is hard to realize for deviations from $\kappa = 1$. Explicitly, we find from the isocurvature constraint of Planck [295] a limit of $1 - \kappa \lesssim 10^{-10}$ and thus any deviation from the minimally coupled scalar like case is strongly constrained.

5.4 Summary

This chapter was devoted to the study of DM consisting of very light (pseudo)scalar and vector fields that have non-minimal couplings to gravity by means of the Ricci scalar R. The strongest impact of these couplings is during inflation, when they have a significant impact on the effective mass of the fields, resulting in effective masses in the order of the Hubble parameter. This does not only influence the evolution of the homogeneous field value, but also the evolution of the fluctuations, having a profound impact on both the misalignment and stochastic scenario. After inflation, the Ricci scalar ceases to be the dominant scale as it becomes negligible compared to the mass parameter, and thus the influence of the non-minimal coupling is only a consequence of inflation.

For (pseudo)scalar fields, we found that the non-minimal coupling to gravity can substantially alleviate the bound from isocurvature fluctuations for the misalignment mechanism, as the perturbations get suppressed at CMB scales. To do so, a non-minimal coupling of $\xi \sim 0.05$ is sufficient, while negative values strengthen the isocurvature limits and larger negative values are excluded as they would lead to transplanckian field excursions. With respect to the stochastic scenario, which requires inflation to last sufficiently long to build up a homogeneous field value from fluctuations that get stretched to superhorizon scales during inflation, we were able to generalize the existing results to arbitrary non-minimal couplings (or effective masses). However, the isocurvature constraints lead in this scenario to a strong bound on the non-minimal coupling of $\xi \lesssim 10^{-10}$, showing that the stochastic scenario is hard to realize for non-minimally coupled models.

For the vector case, we found in general similar results as for the scalar one, since the evolution of the homogeneous field value is identical to the scalar case after identifying $\kappa \leftrightarrow 1-6\xi$. Thus a minimally coupled scalar field corresponds to a non-minimally coupled vector field with $\kappa = 1$. As remarked in the introduction, the non-minimally coupled vector field has the potential issue that its longitudinal component has a negative kinetic term for a finite range of momenta. This is an interesting issue but beyond the scope of our presented analysis and thus left for future work.

In the calculation of the vector fields, we split the analysis into transversal and longitudinal polarizations, of which the transversal ones behave like a scalar field, while the behavior of the longitudinal ones can differ. This applies both to the generation of longitudinal fluctuations during inflation, as well as their evolution after inflation. For the generation during inflation, we were able to provide a fit formula that accurately describes the behavior of the longitudinal fluctuations for late times and arbitrary non-minimal couplings, and thus allowed us to describe the generated isocurvature perturbations. Evolving this power spectrum through time, we find a suppression factor for the longitudinal modes for light mass parameters below $m_X \sim 10^{-4}\,\mathrm{eV}$ (depending on the scale of inflation). When not being suppressed, the longitudinal fluctuations are similar or slightly bigger in size compared to the transversal perturbations. Properly accounting for both contributions, we find similar to the scalar case that a non-minimally coupled vector field can substantially alleviate the bound from isocurvature perturbations for the misalignment mechanism. In agreement with the identification $\kappa \leftrightarrow 1 - 6\xi$, non-minimal couplings of around $\kappa \sim 0.7$ are necessary to do so, while couplings larger than one become at some point constrained by avoiding transplanckian excursions. For the stochastic scenario we find equally strong bounds as in the scalar case, again showing that it is hard to realize for any deviation in

the couplings from their standard value.

Summarizing one can say that non-minimal curvature couplings allow for the generation of DM both for scalar and vector fields in a large part of parameter space for the misalignment mechanism, while the stochastic scenario can only be realized in a very small range of non-minimal couplings. This provides an additional possibility to accommodate for DM even without any sizable couplings to the SM and thus beyond the standard DM particle picture.

Chapter 6

Conclusions

In this work, we examined a set of BSM models that allow for a low-scale explanation of the BAU or DM. For both of these phenomena there is ample observational evidence and their full explanation requires BSM physics. While especially for the BAU there are well studied theories that can explain it by introducing new particles at high scales, we focused on low-scale realizations that are accessible to current and future experiments in the spirit of the motto of the Royal Society *Nullius in verba*. For DM, these low-scale realizations can provide new pathways besides the standard WIMP paradigm.

With regard to low-scale theories that explain the BAU, we first analyzed the scotogenic model in Ch. 2 for both cases of two and three RHNs. For two RHNs, we found to be bound to the strong washout regime and derived a fully analytical solution for the baryon-to-photon ratio by which we determined a lower limit for the RHN mass scale of $\sim 10^{10}\,\text{GeV}$, similar to the limit in standard leptogenesis. We furthermore argued that the possible enhancement of the CP asymmetry, as apparent from the DI-type bound we derived, mostly cancels out in the calculation of the baryon-to-photon asymmetry and thus does not help in creating a baryon asymmetry. For three RHNs, we are able to access the weak washout regime and the situation fundamentally changes. As long as $\Delta L = 2$ washout remains negligible, we were able to work analytically and show that the lower limit on the smallest RHN mass is proportional to the lightest active neutrino mass and can thus be substantially decreased. This remains true down to lightest active neutrino masses of $m_l \gtrsim 10^{-7\ldots-6}\,\text{eV}$, at which point a numerical treatment became necessary to include the $\Delta L = 2$ washout. Below these lightest active neutrino masses, it is possible to lower the necessary RHN mass scale for successful leptogenesis even further down to $\sim 10\,\text{TeV}$ by delaying the decay of the lightest RHNs until right before the $SU(2)$-sphalerons freeze out via a decrease of the corresponding Yukawa couplings. Any later conversion of a baryon into a lepton asymmetry is impossible as it is mediated by the $SU(2)$-sphalerons. Since low-scale leptogenesis in the scotogenic model requires a very small mass of the lightest active neutrino, any detection of a non-zero mass for it would make this mechanism (at low scales) impossible.

In the singlet scalar assisted model of leptogenesis in Ch. 3, we realized low-scale leptogenesis by introducing an additional source of CP violation via the new RHN decay channels that opened up due to the scalar singlet. To make a parameter scan of the model feasible, we first derived a semi-analytical fit function of the final baryon-to-photon

ratio by numerical methods. With the help of this fit function, we were able to compare the parameters necessary for successful leptogenesis to exclusion limits from collider measurements and theoretical considerations like perturbativity and unitarity, all while taking recent neutrino data into account. Doing so revealed the possibility to realize singlet scalar assisted leptogenesis at RHN mass scales even below 1 TeV and evading all limits at the same time. However, especially for such low scales, the available parameter space for a successful creation of the BAU is tightly constrained and thus accessible to future more precise measurement of the Higgs sector at colliders.

Next, we turned from the BAU to DM and compared the LHC signatures of two benchmark models, given by the 2HDM+PS and 2HDM+S. Although DM is represented within these models in the standard way of vector-like DM, we focused on the parameter region of light DM with a mass of a few GeV, which is only weakly constrained by other types of experiments and can lead to a rich phenomenology at colliders. Studying this rich collider phenomenology in detail, we investigated the limits from $t\bar{t}$, mono-Z and mono-h searches and compared these limits between the models as well as between each other. As the bounds from $t\bar{t}$ searches strongly constrain regions of parameter space with values of $\tan\beta < 1$ for both models, they also start to exclude parameter points in the commonly considered case of $\tan\beta = 1$. Mono-Z and mono-h searches on the other hand, are strongest for small masses of the light new pseudoscalar or scalar and lead to significant constraints mostly independent of $\tan\beta$. While mono-Z searches are dominant over mono-h searches for both models, their relative signal strength significantly differs in the 2HDM+PS and 2HDM+S, thus making it generally possible to distinguish between the two models by their collider signatures in case of a future signal detection.

Lastly, we considered the possibility that DM is not linked to couplings to the SM but related to couplings between (pseudo)scalar or vector fields and gravity by means of the Ricci scalar R. In particular, we analyzed the misalignment and stochastic scenario for non-minimally coupled (pseudo)scalar and vector fields. As known from the minimally coupled scenario for the (pseudo)scalar ($\xi = 0$) and the corresponding one for the vector ($\kappa = 1$), both of these mechanisms generally allow for an explanation of the observed DM relic density even for DM mass scales as low as the sub-eV regime, while evading their strongest constraint from the non-observation of isocurvature fluctuations in the CMB. We found that the generalization to non-minimal couplings in the misalignment scenario allows for a substantially larger part of parameter space to evade the isocurvature limits, while reproducing the correct amount of DM. This improvement over the minimally coupled scenario gets more significant for larger mass parameters of the (pseudo)scalar and vector fields. For the stochastic scenario on the other hand, it turned out that the minimally coupled case (corresponding to $\kappa = 1$ for the vector field) represents the least constrained value for the coupling, even though very small deviations from this value in the order of 10^{-10} are allowed. To derive these results for the vector field, we developed a semi-analytical fit function that generalizes the literature result for the power spectrum of the longitudinal fluctuations generated during inflation to a large range of the non-minimal coupling κ. Thus, our investigation of DM from non-minimal curvature couplings led to new insights into the evolution of longitudinal fluctuations of a vector field as well as showing that such non-minimal couplings can open up new viable regions of parameter space.

For all of our above studies there are possible improvements that we already touched

upon in the respective chapters. In the case of leptogenesis, this usually implies including sub-leading contributions like flavor corrections. However, since these contributions normally do not qualitatively change the workings of leptogenesis, the more intriguing question might be how it could be linked to other phenomena and what that might tell us about leptogenesis itself, especially for the low-scale version. These links to other phenomena were in principle present in both of our low-scale leptogenesis models, by a link to DM in the scotogenic model and a singlet scalar S that could be related to a rich phenomenology in the singlet scalar assisted model, but may deserve more attention. One option would be, for example, to try to learn more about leptogenesis by studying its connection to gravitational waves (cf. [300] for recent work in this direction).

In regard to DM, our study of two benchmark models can be seen as a small piece in a bigger puzzle, which tries to develop a sensible theoretical framework to analyze experimental data in. This is not only important for the analysis of models themselves, but also as a mean to compare different models to each other. Since new experimental data will rule out old models and shift the focus to new ones, this puzzle is likely to never be completely finished, but will continue to be work in progress. For the study of DM from curvature couplings, an interesting question would be to assess the viability of the non-minimally coupled vector field, which has been picked up by some works but is still a subject of ongoing discussion. On a bigger scale, it reminds us of the far reaching consequences that a unified theory of gravity and quantum field theory can potentially have and that it is worth to always look for new mechanism that could explain unresolved phenomena like DM.

With phenomena like the BAU and DM lacking an explanation (and experimental confirmation thereof), the field of astroparticle physics will remain an active and attractive field of research searching for a solution to these challenges. The presented possible low-scale explanations for these phenomena in this thesis provide one approach that might be particularly interesting thanks to the many currently ongoing experimental efforts. However, as often (probably falsely) attributed to Niels Bohr, "it's very difficult to make predictions, especially about the future".

Appendices

Appendix A

Equilibrium Thermodynamics

Here we give a brief overview over the important relations from equilibrium thermodynamics that can come in handy in the study of processes in thermal baths, like leptogenesis in the thermal bath of the early universe. This overview is based on the standard literature, e.g. [301], which also provides further details. The most fundamental quantity of equilibrium thermodynamics is probably the phase space distribution function $f(\vec{p})$ depending on the momentum $\vec{p}$. It is normally given by Fermi-Dirac oder Bose-Einstein statistics

$$f(|\vec{p}|) = \frac{1}{e^{\frac{E-\mu}{T}} \pm 1}, \tag{A.1}$$

where the former refers to the plus sign and the latter to the minus sign. Here E is the energy which depends on the absolute value of the momentum $|\vec{p}|$, μ the chemical potential and T the temperature (with $k_B = 1$). In the classical limit of quantum statistics (sufficiently small number density or sufficiently large temperature while the total number of particles is fixed) we have $e^{\frac{E-\mu}{T}} \gg 1$ and both simplify to the Maxwell-Boltzmann distribution

$$f(|\vec{p}|) = e^{\frac{-(E-\mu)}{T}}. \tag{A.2}$$

With the phase space distribution function one can determine the number density n, energy density ρ and the pressure p of a dilute, weakly-interacting gas of particles with g internal degrees of freedom (e.g. spin) as[1]

$$\begin{aligned} n &= \frac{g}{(2\pi)^3} \int f(\vec{p})\, \mathrm{d}^3 p \\ \rho &= \frac{g}{(2\pi)^3} \int E(\vec{p}) f(\vec{p})\, \mathrm{d}^3 p \\ p &= \frac{g}{(2\pi)^3} \int \frac{|\vec{p}|^2}{3E(\vec{p})} f(\vec{p})\, \mathrm{d}^3 p. \end{aligned} \tag{A.3}$$

The relation for the pressure is interesting because it leads in the relativistic limit

[1] The factor of $(2\pi)^3$ is due to the volume a single state occupies in phase space.

($T \gg m$) and negligible chemical potential ($T \gg \mu$) to the relation

$$p = \frac{\rho}{3}. \tag{A.4}$$

For the other quantities we get under the same assumptions

$$\begin{aligned} n &= \begin{cases} \frac{\zeta(3)}{\pi^2} g T^3 & \text{for bosons} \\ \frac{3}{4}\frac{\zeta(3)}{\pi^2} g T^3 & \text{for fermions} \end{cases} \\ \rho &= \begin{cases} \frac{\pi^2}{30} g T^4 & \text{for bosons} \\ \frac{7}{8}\frac{\pi^2}{30} g T^4 & \text{for fermions,} \end{cases} \end{aligned} \tag{A.5}$$

with the Riemann zeta function $\zeta(3) \approx 1.202$.

In the non-relativistic case ($m \gg T$) we get

$$\begin{aligned} n &= g \left(\frac{mT}{2\pi}\right)^{\frac{3}{2}} e^{-\frac{m-\mu}{T}} \\ \rho &= mn \\ p &= Tn \ll \rho, \end{aligned} \tag{A.6}$$

where there is no difference between fermions and bosons. Comparing these expressions to the one for relativistic species, we see that the non-relativistic ones are exponentially suppressed. Therefore, the total energy density and pressure can be well approximated by only taking into account the relativistic species. Since the different species of particles might have different temperatures T_i compared to the bath of photons with temperature T, due to energy injection from particle decay (e.g. $e^+ + e^- \to \gamma + \gamma$), we can define the effective number of relativistic dofs

$$g_* \coloneqq \sum_{\text{bosons}} g_i \left(\frac{T_i}{T}\right)^4 + \frac{7}{8} \sum_{\text{fermions}} g_i \left(\frac{T_i}{T}\right)^4 \tag{A.7}$$

and write in a very compact way

$$\begin{aligned} \rho_{\mathrm{R}} &= \frac{\pi^2}{30} g_* T^4 \\ p_{\mathrm{R}} &= \frac{\rho_{\mathrm{R}}}{3} = \frac{\pi^2}{90} g_* T^4. \end{aligned} \tag{A.8}$$

In the scotogenic model we have $g_* = 114.25$ for two RHNs and $g_* = 116$ for three RHNs.

The relation for the total energy density is especially handy when combining it with the first Friedmann equation for a flat ($k = 0$) universe with neglected cosmological constant ($\Lambda = 0$), which is given by

$$H^2 = \frac{8\pi}{3M_{Pl}^2} \rho_{\mathrm{R}} \tag{A.9}$$

and we used that in natural units ($\hbar = 1$, $c = 1$) the Planck mass is given by $M_{Pl} =$

$\sqrt{G}^{-1} \simeq 1.22 \cdot 10^{19}\,\mathrm{GeV}$. Plugging in the above relation for ρ_{R}, we find for the radiation dominated regime during which dark matter and dark energy do not play an important role that

$$H = \sqrt{\frac{8\pi^3 g_*}{90}} \frac{T^2}{M_{Pl}}. \tag{A.10}$$

Appendix B

Boltzmann Equations

This appendix serves as a collection of information on Boltzmann equations, which are the equations that track the phase space distribution function $f_X(\vec{p}_X)$ of a particle species X, and builds upon App. A on equilibrium thermodynamics. For further information on the topic and as a source of this overview see for example [301] and [302, Appendix A].

Integrated over a phase space volume, $f_X(\vec{p}_X)$ gives the average number of X particles in that phase space volume at a specific time. In general, it depends on all phase space coordinates as well as time t. However, after imposing homogeneity (all points in space are equal) and isotropy (no preferred direction), the phase space distribution function only depends on the momentum of the corresponding particle species[1] $|\vec{p}_X| \equiv p$ (the particle species index is implicitly understood) and t. In this case the Boltzmann equation reads

$$\hat{\mathcal{L}}[f_X(p,t)] \equiv E_X \left(\frac{\partial}{\partial t} - Hp\frac{\partial}{\partial p} \right) f_X(p,t) = \mathcal{C}_X[f_X(p,t)]\,, \tag{B.1}$$

with the Liouville operator $\hat{\mathcal{L}}$, the collision operator $\mathcal{C}_X$, $E_X = \sqrt{p^2 + m_X^2}$ with mass m_X and the Hubble rate H. Essentially, the equation states that changes in the phase space distribution function have to come from interactions - tracked by the collision operator $\mathcal{C}_X$ - or are due to the momentum of the particles or the expansion of space - tracked by the second part of the Liouville operator $\hat{\mathcal{L}}$.

The collision operator can be split into the different interactions by

$$\begin{aligned} \mathcal{C}_X &= \sum_{ab\ldots} \sum_{ij\ldots} C_X(Xab\ldots \leftrightarrow ij\ldots) \\ &= \sum_{ij\ldots} C_X(X \leftrightarrow ij\ldots) + \sum_{a} \sum_{ij\ldots} C_X(Xa \leftrightarrow ij\ldots) + \ldots\,, \end{aligned} \tag{B.2}$$

while each C_X is determined from QFT in terms of the matrix element and multi-particle

[1] Note the difference in notation to App. A in which p is referring to the pressure and not the absolute value of the momentum of the particle.

phase-space by

$$C_X(Xab\ldots \leftrightarrow ij\ldots) = \frac{1}{2}\int \mathrm{d}\Pi(X|a,b,\ldots,i,j,\ldots)(2\pi)^4\delta\left(\sum p_{\mathrm{in}} - \sum p_{\mathrm{out}}\right) \\ \left[f_i f_j \ldots (1\pm f_X)(1\pm f_a)(1\pm f_b)\ldots |\mathcal{M}(ij\ldots \to Xab\ldots)|^2 \right. \\ \left. - f_a f_b \ldots f_X(1\pm f_i)(1\pm f_j)\ldots |\mathcal{M}(Xab\ldots \to ij\ldots)|^2\right] , \tag{B.3}$$

where we introduced

$$\mathrm{d}\Pi(X|a,b,\ldots,i,j,\ldots) \equiv S(X,a,b,\ldots,i,j,\ldots)\mathrm{d}\tilde{p}_a\mathrm{d}\tilde{p}_b\ldots\mathrm{d}\tilde{p}_i\mathrm{d}\tilde{p}_j\ldots , \tag{B.4}$$

with S being the appropriate symmetry factor for identical particles in the initial or final state (n identical particles lead to a factor of $1/n!$) and $\mathrm{d}\tilde{p}_\alpha \equiv g_\alpha/(2\pi)^3\cdot\mathrm{d}^3p_\alpha/(2E_\alpha)$ is the Lorentz invariant momentum space element. The matrix elements $|\mathcal{M}|^2$ are understood as summed (not averaged; cf. [303, p. 80]) over initial and final spins and the quantum mechanical factors of $(1+f_\alpha)$ for Bose enhancement and $(1-f_\alpha)$ for Pauli blocking have normally only a minor influence [304] (order of 10% at $T=m$ according to [303, p. 78]) and can therefore often be neglected in the sense that $(1\pm f_\alpha)\approx 1$. Furthermore, there is another way to split the C_X according to the direction the process proceeds in

$$C_X(Xab\ldots \leftrightarrow ij\ldots) = C_X(ij\ldots \to Xab\ldots) - C_X(Xab\ldots \to ij\ldots) . \tag{B.5}$$

It is important to mention that the above expression for C_X is a phenomenological approximation. That it works and is sufficiently accurate has been shown in [305] by comparing it to the full Kadanoff-Baym equations. Under certain assumptions, a derivation of the Boltzmann equations from Kadanoff-Baym equations also seems to be possible [306].

To arrive at the more common version of the integrated Boltzmann equation, we take it in the form of Eq. (B.1), divide both sides by E_X, multiply by $g_X/(2\pi)^3$ and integrate over d^3p. Using the relation for the number density, Eq. (A.3), and integration by parts, we get

$$\dot{n}_X + 3Hn_X = \hat{\gamma}_X = \sum_{ab\ldots}\sum_{ij\ldots}\gamma_X(Xab\ldots \leftrightarrow ij\ldots) , \tag{B.6}$$

where we introduced the interaction density

$$\gamma_X(Xab\ldots \leftrightarrow ij\ldots) = \frac{g_X}{(2\pi)^3}\int\frac{\mathrm{d}^3p}{E_X}C_X(Xab\ldots \leftrightarrow ij\ldots) . \tag{B.7}$$

To further simplify these equations, we have to take a closer look at the phase space distribution functions.

It will be helpful to introduce a Maxwell-Boltzmann phase space distribution function with zero chemical potential, so we define

$$f_\alpha^{\mathrm{eq}}(p) \coloneqq e^{-\frac{E_\alpha}{T}} . \tag{B.8}$$

One important realization is that we can, after approximating the Fermi-Dirac and Bose-

Einstein distributions as Maxwell-Boltzmann distributions $f_\alpha(p) \approx e^{-\frac{E_\alpha - \mu_\alpha}{T}}$, rewrite the phase space distribution function as

$$f_X(p,t) = R(t) f_X^{\text{eq}}(p,t) \quad \text{with} \quad R(t) \coloneqq e^{\frac{\mu_X}{T}} \tag{B.9}$$

and use Eq. (A.3) for the number density to realize that

$$R(t) \coloneqq e^{\frac{\mu_X}{T}} = \frac{n_X}{n_X^{\text{eq}}} \,. \tag{B.10}$$

This means that we can replace $f_\alpha(p)$ with $f_\alpha^{\text{eq}}(p)$ in terms of

$$f_\alpha(p) = \frac{n_\alpha}{n_\alpha^{\text{eq}}} f_\alpha^{\text{eq}}(p) \,, \tag{B.11}$$

where we did not mention the time dependence explicitly.

Plugging this into the interaction density γ_X we get

$$\begin{aligned}
&\gamma_X(Xab\ldots \leftrightarrow ij\ldots) = \\
&\quad S(X,a,b,\ldots,i,j,\ldots) \int \mathrm{d}\tilde{p}_X \mathrm{d}\tilde{p}_a \mathrm{d}\tilde{p}_b \ldots \mathrm{d}\tilde{p}_i \mathrm{d}\tilde{p}_j \ldots (2\pi)^4 \delta\left(\sum p_{\text{in}} - \sum p_{\text{out}}\right) \\
&\quad \left[\frac{n_i}{n_i^{\text{eq}}} \frac{n_j}{n_j^{\text{eq}}} \ldots f_i^{\text{eq}} f_j^{\text{eq}} \ldots (1 \pm f_X)(1 \pm f_a)(1 \pm f_b) \ldots |\mathcal{M}(ij\ldots \to Xab\ldots)|^2 \right. \\
&\quad \left. - \frac{n_a}{n_a^{\text{eq}}} \frac{n_b}{n_b^{\text{eq}}} \ldots \frac{n_X}{n_X^{\text{eq}}} f_a^{\text{eq}} f_b^{\text{eq}} \ldots f_X^{\text{eq}} (1 \pm f_i)(1 \pm f_j) \ldots |\mathcal{M}(Xab\ldots \to ij\ldots)|^2 \right] .
\end{aligned} \tag{B.12}$$

In the following, we want to show how to derive the Boltzmann equation for two specific cases from this expression. However, the relations and approximations we will use are helpful in general. The first example we are looking at is the Boltzmann equation for a sterile neutrino N_i that can decay to a Higgs boson η and a lepton ℓ as in the scotogenic model. So we identify $X \to N_i$, $i \to \eta$ and $j \to \ell$, where we, for simplicity, do not explicitly write the sums over all possible η and ℓ. In this case the integrated Boltzmann equation, Eq. (B.6), for N_i reads

$$\dot{n}_{N_i} + 3Hn_{N_i} = \gamma_{N_i}(N_i \leftrightarrow \eta\ell) \,. \tag{B.13}$$

Plugging in the interaction density, Eq. (B.12), and neglecting all quantum mechanical factors $(1 \pm f_\alpha) \approx 1$, we find (the symmetry factor is $S(N_i, \eta, \ell) = 1$)

$$\begin{aligned}
\dot{n}_{N_i} + 3Hn_{N_i} = &\int \mathrm{d}\tilde{p}_{N_i} \mathrm{d}\tilde{p}_\eta \mathrm{d}\tilde{p}_\ell (2\pi)^4 \delta(p_{N_i} - p_\eta - p_\ell) \\
&\left[\frac{n_\eta}{n_\eta^{\text{eq}}} \frac{n_\ell}{n_\ell^{\text{eq}}} f_\eta^{\text{eq}} f_\ell^{\text{eq}} |\mathcal{M}(\eta\ell \to N_i)|^2 - \frac{n_{N_i}}{n_{N_i}^{\text{eq}}} f_{N_i}^{\text{eq}} |\mathcal{M}(N_i \to \eta\ell)|^2 \right] .
\end{aligned} \tag{B.14}$$

To further simplify this expression we can use energy conservation to get

$$f_\eta^{\mathrm{eq}} f_\ell^{\mathrm{eq}} = e^{-\frac{E_\eta + E_\ell}{T}} = e^{-\frac{E_{N_i}}{T}} = f_{N_i}^{\mathrm{eq}} \tag{B.15}$$

and follow [307, p. 3] to see that the matrix elements are identical up to CP violating effects. Explicitly, we have

$$\begin{aligned} &\mathcal{M}(i \to j) = \mathcal{M}(\bar{j} \to \bar{i}) \quad \text{by charge, parity and time conjugation (CPT) invariance} \\ &\mathcal{M}(i \to j) = \mathcal{M}(\bar{i} \to \bar{j}) = \mathcal{M}(j \to i) \quad \text{by first CP and second CPT invariance.} \end{aligned} \tag{B.16}$$

Since the non CP violating part is much larger than the part that can appear due to CP violation we can safely neglect the latter and approximate

$$|\mathcal{M}(\eta\ell \to N_i)|^2 \approx |\mathcal{M}(N_i \to \eta\ell)|^2 \,, \tag{B.17}$$

where the matrix element is summed and not averaged over the initial states as noted above. Finally, as n_α only deviates from n_α^{eq} around $m_\alpha = T$ and we assume $m_\eta \ll m_{N_1}$ as well as $m_\ell \ll m_{N_1}$, we can set

$$\frac{n_\eta}{n_\eta^{\mathrm{eq}}} \approx 1 \qquad\qquad \frac{n_\ell}{n_\ell^{\mathrm{eq}}} \approx 1 \,. \tag{B.18}$$

This deviation from equilibrium happens around $m_\alpha = T$, because at this temperature the Boltzmann suppression $e^{-\frac{E_\alpha}{T}}$ in the phase space distribution function "kicks in" and the number density cannot directly follow the equilibrium number density due to the finite lifetime of the particles.

Using these relations for the equilibrium phase space distribution functions, matrix elements and number densities in the Boltzmann equation of our example, Eq. (B.14), we get

$$\dot{n}_{N_i} + 3Hn_{N_i} = \int \mathrm{d}\tilde{p}_{N_i} \mathrm{d}\tilde{p}_\eta \mathrm{d}\tilde{p}_\ell (2\pi)^4 \delta(p_{N_i} - p_\eta - p_\ell) |\mathcal{M}(N_i \to \eta\ell)|^2 f_{N_i}^{\mathrm{eq}} \left(1 - \frac{n_{N_i}}{n_{N_i}^{\mathrm{eq}}}\right) \tag{B.19}$$

and it is important to remember that the factor $n_{N_i}/n_{N_i}^{\mathrm{eq}} \equiv R(t)$ depends only on time and therefore is not relevant for evaluating the integral. Inserting a factor of $2m_{N_i}g_{N_i}/(2m_{N_i}g_{N_i})$ and splitting the integral up into the different parts, leads to

$$\begin{aligned} \dot{n}_{N_i} + 3Hn_{N_i} = &\left(1 - \frac{n_{N_i}}{n_{N_i}^{\mathrm{eq}}}\right) 2m_{N_i} g_{N_i} \int \mathrm{d}\tilde{p}_{N_i} f_{N_i}^{\mathrm{eq}} \\ &\frac{1}{2m_{N_i}} \int \mathrm{d}\tilde{p}_\eta \mathrm{d}\tilde{p}_\ell (2\pi)^4 \delta(p_{N_i} - p_\eta - p_\ell) \frac{1}{g_{N_i}} |\mathcal{M}(N_i \to \eta\ell)|^2 \,. \end{aligned} \tag{B.20}$$

From Peskin & Schroeder [122, p. 107] we find that the second line is by definition $\Gamma_{\mathrm{avg}}(N_i \to \eta\ell)$ - note that due to the factor of $\frac{1}{g_{N_i}}$ this is now the over initial states

averaged decay width (still summed over final states though). The integral in the first line can be explicitly calculated to be

$$\int \mathrm{d}\tilde{p}_{N_i} f_{N_i}^{\mathrm{eq}} = \int \frac{\mathrm{d}^3 p}{2E_{N_i}(2\pi)^3} f_{N_i}^{\mathrm{eq}} = \frac{1}{2}\frac{T^2}{2\pi^2} z_i \mathcal{K}_1(z_i)\,, \tag{B.21}$$

where we introduced $z_i \coloneqq m_{N_i}/T$ and $\mathcal{K}$ is the modified Bessel function of the second kind[2].

To end up with a very compact expression, it is helpful to also have the explicit results for the equilibrium number density n_X^{eq} and the number density for a relativistic particle species n_X^{rel} (with Maxwell-Boltzmann distribution)

$$\begin{aligned} n_X^{\mathrm{eq}} &= g_X \frac{T^3}{2\pi^2} z_i^2 \mathcal{K}_2(z_i) \\ n_X^{\mathrm{rel}} &= g_X \frac{T^3}{\pi^2} \end{aligned} \tag{B.22}$$

that can be derived from Eq. (A.3) together with the specific expression of the phase space distribution function. Comparing these expressions with the result of the integration in Eq. (B.21) we find

$$2m_{N_i} g_{N_i} \int \mathrm{d}\tilde{p}_{N_i} f_{N_i}^{\mathrm{eq}} = n_{N_i}^{\mathrm{eq}} \frac{\mathcal{K}_1(z_i)}{\mathcal{K}_2(z_i)}\,, \tag{B.23}$$

which finally leads us to the compact Boltzmann equation

$$\dot{n}_{N_i} + 3Hn_{N_i} = \frac{\mathcal{K}_1(z_i)}{\mathcal{K}_2(z_i)} \Gamma_{\mathrm{avg}}(N_i \to \eta\ell)(n_{N_i}^{\mathrm{eq}} - n_{N_i})\,. \tag{B.24}$$

However, this equation has still one significant drawback, which is that $z_i \coloneqq m_{N_i}/T$ implicitly depends on time by means of the Temperature T. Therefore, it is helpful to rewrite the equation as a differential equation in z_i instead of t.

As a first step, it is useful to rewrite the left-hand side of the Boltzmann equation in a more compact way. This is achieved by switching from n_{N_i} to $N_{N_i}^{(\mathrm{eq})} \coloneqq n_{N_i}^{(\mathrm{eq})}/n_{N_i}^{\mathrm{rel}}$, so by normalizing the number density of the sterile neutrinos by its relativistic number density. For the normalized number density we have

$$\dot{N}_{N_i} = \frac{\dot{n}_{N_i} n_{N_i}^{\mathrm{rel}} - n_{N_i}\dot{n}_{N_i}^{\mathrm{rel}}}{(n_{N_i}^{\mathrm{rel}})^2} = \frac{\dot{n}_{N_i}}{n_{N_i}^{\mathrm{rel}}} - \frac{n_{N_i}}{n_{N_i}^{\mathrm{rel}}}\frac{\dot{n}_{N_i}^{\mathrm{rel}}}{n_{N_i}^{\mathrm{rel}}} = \frac{1}{n_{N_i}^{\mathrm{rel}}}\left(\dot{n}_{N_i} + 3Hn_{N_i}\right)\,, \tag{B.25}$$

where in the last step we used (with $a(t)$ being the scale factor)

$$\frac{\dot{n}_{N_i}^{\mathrm{rel}}}{n_{N_i}^{\mathrm{rel}}} = -3\frac{\dot{a}(t)}{a(t)} =: -3H\,. \tag{B.26}$$

This can be derived using the assumption of homogeneity, meaning that $n_{N_i}^{\mathrm{rel}}$ scales with

[2]For the modified Bessel functions of the second kind we use $\mathcal{K}$ instead of the usual K to distinguish it from the later appearing decay parameter called K.

the volume V of space, so $n_{N_i}^{\mathrm{rel}} \sim V \sim a(t)^3$ and $\dot{n}_{N_i}^{\mathrm{rel}} \sim -\frac{\mathrm{d}}{\mathrm{d}t} a(t)^3 = -3\frac{\dot{a}(t)}{a(t)} a(t)^3$, where the minus sign reflects the fact that the number density decreases if the volume of space increases.

After plugging $\dot{n}_{N_i} + 3Hn_{N_i} = n_{N_i}^{\mathrm{rel}} \dot{N}_{N_i}$ into the Boltzmann equation and by using the definition of $N_{N_i}^{(\mathrm{eq})}$, we get

$$\dot{N}_{N_i} = \frac{\mathcal{K}_1(z_i)}{\mathcal{K}_2(z_i)} \, \Gamma_{\mathrm{avg}}(N_i \to \eta\ell) \, (N_{N_i}^{\mathrm{eq}} - N_{N_i}) \,, \tag{B.27}$$

nevertheless we are still left with a differential equation in t. To change that we have to quickly dive into GR. In GR energy conservation is given by $\nabla_\mu T^{\mu\nu} = 0$, which together with the Robertson-Walker metric (using homogeneity and isotropy) and the assumption of a perfect fluid[3] (with stress-momentum-tensor $T_{\mu\nu} = \mathrm{diag}(\rho, -p, -p, -p)$) leads to the energy conservation equation

$$\dot{\rho} + 3H(\rho + p) = 0 \,. \tag{B.28}$$

For the radiation dominated universe we have, as mentioned in Eq. (A.4), $p = \frac{\rho}{3}$ and therefore $\dot{\rho} + 4H\rho = 0$ or $\rho \sim a(t)^{-4}$. Comparing this to the Stefan-Boltzmann law $\rho = \alpha T^4$, we can deduce that $T \sim a(t)^{-1}$. The same result can also be found by using an argument about adiabatic expansion. For adiabatic expansion we have $\delta S = 0$, which implies $S \sim a(t)^3 s = \mathrm{const}$, where s denotes the entropy density and S the entropy. The entropy density can in the radiation dominated era be determined to be

$$s = \frac{\rho + p}{T} = \frac{2\pi^2}{45} g_{*,s} \, T^3 \,, \tag{B.29}$$

which implies

$$g_{*,s} \, a(t)^3 \, T^3 = \mathrm{const} \tag{B.30}$$

or $T \sim a(t)^{-1}$ as long as we have adiabatic expansion and $g_{*,s} = \mathrm{const}$. This insight can be used via

$$\frac{\mathrm{d}z_i}{\mathrm{d}t} = m_{N_i} \frac{\mathrm{d}}{\mathrm{d}t} \frac{1}{T} = -\frac{m_{N_i}}{T^2} \frac{\mathrm{d}T}{\mathrm{d}t} = -z_i \frac{1}{T} \frac{\mathrm{d}T}{\mathrm{d}t} \tag{B.31}$$

and

$$-\frac{1}{T} \frac{\mathrm{d}T}{\mathrm{d}t} = -a(t) \frac{\mathrm{d}\left(\frac{1}{a(t)}\right)}{\mathrm{d}t} = H \tag{B.32}$$

to get

$$\frac{\mathrm{d}z_i}{\mathrm{d}t} = H z_i \,, \tag{B.33}$$

[3] Here and for the next couple of lines about GR p refers to the pressure and not the momentum of a particle.

which implies

$$\dot{N}_{N_i} = \frac{\mathrm{d}N_{N_i}}{\mathrm{d}z_i} H z_i \,. \tag{B.34}$$

This translates the Boltzmann equation into

$$\frac{\mathrm{d}N_{N_i}}{\mathrm{d}z_i} = \frac{\Gamma_{\mathrm{avg}}(N_i \to \eta\ell)}{H z_i} \frac{\mathcal{K}_1(z_i)}{\mathcal{K}_2(z_i)} (N_{N_i}^{\mathrm{eq}} - N_{N_i}) \,, \tag{B.35}$$

where only the Hubble parameter is left as being dependent on time t. Using Eq. (A.10) for the Hubble parameter, we can rewrite it as[4]

$$H = \sqrt{\frac{8\pi^3 g_*}{90}} \frac{T^2}{M_{Pl}} = H(z_i = 1) \frac{1}{z_i^2} \tag{B.36}$$

and by defining the decay parameter

$$K_i \coloneqq \frac{\Gamma_{\mathrm{avg}}(N_i \to \eta\ell)}{H(z_i = 1)} \tag{B.37}$$

we finally end up with the Boltzmann equation in its normally for leptogenesis used form

$$\frac{\mathrm{d}N_{N_i}}{\mathrm{d}z_i} = -K_i z_i \frac{\mathcal{K}_1(z_i)}{\mathcal{K}_2(z_i)} (N_{N_i} - N_{N_i}^{\mathrm{eq}}) \,, \tag{B.38}$$

with (cf. Eqs. (B.22))

$$N_{N_i}^{\mathrm{eq}} \coloneqq \frac{n_{N_i}^{\mathrm{eq}}}{n_{N_i}^{\mathrm{rel}}} = \frac{z_i^2}{2} \mathcal{K}_2(z_i) \,. \tag{B.39}$$

The second Boltzmann equation we want to derive is the one for the $B - L$ asymmetry, which is conserved by all SM processes. Here we will stick to the simplest case[5] with only one sterile neutrino N_i and one lepton ℓ_1, without taking into account flavor effects or scatterings, and follow the derivation of [79, pp. 6 sq.]. If one wants to account for flavor effects, the usual approach is to work with N_{Δ_α}, with $\Delta_\alpha \coloneqq \frac{1}{3}B - L_\alpha$, instead of N_{B-L} and include flavor branching ratios (cf. [79, 80]) and a flavor coupling matrix.

The first step is to ignore the reprocessing action of sphalerons, which distributes the lepton asymmetry generated by the decays of the sterile neutrino N_i in the whole lepton and baryon sector, allowing us to write

$$\frac{\mathrm{d}N_{B-L}}{\mathrm{d}z_i} = \frac{\mathrm{d}N_{\bar{\ell}_1}}{\mathrm{d}z_i} - \frac{\mathrm{d}N_{\ell_1}}{\mathrm{d}z_i} \,. \tag{B.40}$$

This is of course equivalent to assuming $N_{B-L} = N_{\bar{\ell}_1} - N_{\ell_1}$ and implies that only the N_i decays lead to a lepton (or baryon) asymmetry. In this way, we linked the Boltzmann equation for the $B-L$ asymmetry to Boltzmann equations for the leptons and anti-leptons.

[4] $H(z_i = 1)$ means to set $T = m_{N_i}$ in the expression for H.
[5] The indices are given to show how the formulas generalize.

For this reason, we go back to the general integrated Boltzmann equation, Eq. (B.6) or (B.13), and use $X \to \bar{\ell}_1/\ell_1$, $a \to \eta$ and $i \to N_i$ (this is the only significant CP violating process generating a lepton asymmetry), to get

$$\dot{n}_{\ell_1} + 3Hn_{\ell_1} = \gamma_{\ell_1}(\ell_1\eta \leftrightarrow N_i) \tag{B.41}$$

and the same for $\bar{\ell}_1$. We will give only the equations for ℓ_1 from here on and it is understood that each one is also valid for $\ell_1 \to \bar{\ell}_1$. Following the exact same steps as above, except for not using $n_{\ell_1}/n_{\ell_1}^{\mathrm{eq}} \approx 1$, leads to

$$\dot{n}_{\ell_1} + 3Hn_{\ell_1} = \frac{\mathcal{K}_1(z_i)}{\mathcal{K}_2(z_i)}\,\Gamma_{\mathrm{avg}}(N_i \to \eta\ell_1)\left(n_{N_i} - n_{N_i}^{\mathrm{eq}}\frac{n_{\ell_1}}{n_{\ell_1}^{\mathrm{eq}}}\right), \tag{B.42}$$

which has an additional minus sign compared to Eq. (B.24) because the roles of initial and final particles are exchanged. Switching again to a differential equation in z_i and using $N_{N_i}^{(\mathrm{eq})} \coloneqq n_{N_i}^{(\mathrm{eq})}/n_{N_i}^{\mathrm{rel}}$, $N_{\ell_1}^{(\mathrm{eq})} \coloneqq n_{\ell_1}^{(\mathrm{eq})}/n_{N_i}^{\mathrm{rel}}$, gives us

$$\frac{\mathrm{d}N_{\ell_1}}{\mathrm{d}z_i} = \frac{\Gamma_{\mathrm{avg}}(N_i \to \eta\ell_1)}{Hz_i}\frac{\mathcal{K}_1(z_i)}{\mathcal{K}_2(z_i)}\left(N_{N_i} - N_{N_i}^{\mathrm{eq}}\frac{N_{\ell_1}}{N_{\ell_1}^{\mathrm{eq}}}\right). \tag{B.43}$$

Defining

$$\langle\Gamma_i\rangle \coloneqq \Gamma_{\mathrm{avg}}(N_i \to \eta\ell_1)\,\frac{\mathcal{K}_1(z_i)}{\mathcal{K}_2(z_i)} \qquad \left\langle\bar{\Gamma}_i\right\rangle \coloneqq \Gamma_{\mathrm{avg}}\left(N_i \to \eta\bar{\ell}_1\right)\,\frac{\mathcal{K}_1(z_i)}{\mathcal{K}_2(z_i)} \tag{B.44}$$

and (ID stands for "inverse decay")

$$\left\langle\Gamma_i^{\mathrm{ID}}\right\rangle \coloneqq \langle\Gamma_i\rangle\,\frac{N_{N_i}^{\mathrm{eq}}}{N_{\ell_1}^{\mathrm{eq}}} \qquad \left\langle\bar{\Gamma}_i^{\mathrm{ID}}\right\rangle \coloneqq \left\langle\bar{\Gamma}_i\right\rangle\,\frac{N_{N_i}^{\mathrm{eq}}}{N_{\bar{\ell}_1}^{\mathrm{eq}}} \tag{B.45}$$

finally leads to the equations given in [79, pp. 6 sq.]

$$\frac{\mathrm{d}N_{\ell_1}}{\mathrm{d}z_i} = \frac{\langle\Gamma_i\rangle}{Hz_i}N_{N_i} - \frac{\left\langle\Gamma_i^{\mathrm{ID}}\right\rangle}{Hz_i}N_{\ell_1} \qquad \frac{\mathrm{d}N_{\bar{\ell}_1}}{\mathrm{d}z_i} = \frac{\left\langle\bar{\Gamma}_i\right\rangle}{Hz_i}N_{N_i} - \frac{\left\langle\bar{\Gamma}_i^{\mathrm{ID}}\right\rangle}{Hz_i}N_{\bar{\ell}_1}\,. \tag{B.46}$$

Note that the definition given above for $\langle\Gamma\rangle$ is equivalent to the expectation value for the decay width Γ of a Maxwell-Boltzmann distributed collection of particles. The expectation value of a quantity $Q(p)$ with phase space distribution function $f(p)$ is generally given by

$$\langle Q\rangle_{f(p)} = \frac{\int \mathrm{d}^3p\; Q(p)f(p)}{\int \mathrm{d}^3p\; f(p)}\,, \tag{B.47}$$

which specializes to $\langle Q\rangle_{\mathrm{MB}}$ for $f(p) = e^{-\frac{E}{T}}$ or $f(p) = e^{-\frac{E-\mu}{T}}$ because the part of the chemical potential μ does not depend on p and therefore cancels out. Using the relation for the Lorentz factor $\gamma = \frac{E}{m}$ and time dilation $t = \gamma\tilde{t}$ (quantities with a tilde are in the rest frame of the particle) from special relativity together with $\Gamma = 1/\tau$, with the lifetime

τ of the particle, we get

$$\langle\Gamma\rangle = \left\langle\frac{1}{\tau}\right\rangle = \left\langle\frac{1}{\gamma\tilde{\tau}}\right\rangle = \left\langle\frac{1}{\gamma}\right\rangle\frac{1}{\tilde{\tau}} = \left\langle\frac{m}{E}\right\rangle\Gamma(T=0) = \frac{\mathcal{K}_1(z)}{\mathcal{K}_2(z)}\,\Gamma(T=0)\,, \tag{B.48}$$

which is equivalent to the above given definition.

Continuing with the derivation of our Boltzmann equation, we have for a vanishing asymmetry $0 = N_{B-L} \equiv N_{\bar{\ell}_1} - N_{\ell_1}$ that $N_{\bar{\ell}_1} = N_{\ell_1} \equiv N_\ell^{\mathrm{eq}}$, which implies $N_{\bar{\ell}_1} \approx N_{\bar{\ell}_1}^{\mathrm{eq}} \equiv N_\ell^{\mathrm{eq}}$ and $N_{\ell_1} \approx N_{\ell_1}^{\mathrm{eq}} \equiv N_\ell^{\mathrm{eq}}$ up to CP violating effects. The linear parts of these differences due to CP violation have different signs, while the quadratic parts have the same sign. This suggests that $\frac{1}{2}(N_{\ell_1} + N_{\bar{\ell}_1}) = N_\ell^{\mathrm{eq}} + \mathcal{O}\left(N_{B-L}^2\right)$ and therefore

$$\begin{aligned} N_{\ell_1} &= \frac{1}{2}(N_{\ell_1} + N_{\bar{\ell}_1}) + \frac{1}{2}(N_{\ell_1} - N_{\bar{\ell}_1}) = N_\ell^{\mathrm{eq}} - \frac{1}{2}N_{B-L} + \mathcal{O}\left(N_{B-L}^2\right) \\ N_{\bar{\ell}_1} &= \frac{1}{2}(N_{\ell_1} + N_{\bar{\ell}_1}) - \frac{1}{2}(N_{\ell_1} - N_{\bar{\ell}_1}) = N_\ell^{\mathrm{eq}} + \frac{1}{2}N_{B-L} + \mathcal{O}\left(N_{B-L}^2\right)\,. \end{aligned} \tag{B.49}$$

Plugging these relations into Eq. (B.46) and using Eqs. (B.40, B.45), while neglecting the $\mathcal{O}\left(N_{B-L}^2\right)$ terms, we get

$$\frac{\mathrm{d}N_{B-L}}{\mathrm{d}z_i} = \frac{\langle\bar{\Gamma}_i\rangle - \langle\Gamma_i\rangle}{\langle\bar{\Gamma}_i\rangle + \langle\Gamma_i\rangle}\frac{\langle\bar{\Gamma}_i\rangle + \langle\Gamma_i\rangle}{Hz_i}\left(N_{N_i} - N_{N_i}^{\mathrm{eq}}\right) - \frac{1}{2}\frac{\langle\bar{\Gamma}_i^{\mathrm{ID}}\rangle + \langle\Gamma_i^{\mathrm{ID}}\rangle}{Hz_i}N_{B-L}\,. \tag{B.50}$$

To achieve a more compact notation, we define the CP asymmetry

$$\varepsilon_i \coloneqq \frac{\Gamma_i - \bar{\Gamma}_i}{\Gamma_i + \bar{\Gamma}_i}\,, \tag{B.51}$$

where the averaging over the phase space distribution functions canceled out, the decay term

$$D_i(z_i) \coloneqq \frac{\langle\bar{\Gamma}_i\rangle + \langle\Gamma_i\rangle}{Hz_i} \tag{B.52}$$

and the washout term

$$W_i(z_i) \coloneqq \frac{1}{2}\frac{\langle\bar{\Gamma}_i^{\mathrm{ID}}\rangle + \langle\Gamma_i^{\mathrm{ID}}\rangle}{Hz_i}\,, \tag{B.53}$$

and finally end up with the compact Boltzmann equation for the $B-L$ asymmetry

$$\frac{\mathrm{d}N_{B-L}}{\mathrm{d}z_i} = -\varepsilon_i D_i(z_i)\,(N_{N_i} - N_{N_i}^{\mathrm{eq}}) - W_i(z_i)\,N_{B-L}\,. \tag{B.54}$$

Often it is helpful to have expressions for the decay and washout term in terms of the decay parameter K_i introduced in Eq. (B.37) and not in terms of the decay rates Γ_i. Under the usual assumption that the leptons are relativistic in the period we are interested in and that the internal number of degrees of freedom are the same for the sterile neutrinos and the leptons ($g_{N_i} = 2 = g_{\ell_j}$), we can deduce from its definition that $N_\ell^{\mathrm{eq}} = 1$ and we have to zeroth order of the CP asymmetry $N_{\ell_j}^{\mathrm{eq}} = N_\ell^{\mathrm{eq}} = N_{\bar{\ell}_j}^{\mathrm{eq}}$. Note that

we only take into account the zeroth order of the CP asymmetry for $W_i(z_i)$ because N_{B-L} is an effect in first order of the CP asymmetry and in this way all terms of Eq. (B.54) are of the same (first) order in the CP asymmetry. Furthermore, it is important to note that the decay parameter as defined in Eq. (B.37) does not differentiate between decay to particles and anti-particles, so it refers to the sum of those two decay rates. Plugging in the above definitions of the inverse decay rate, using Eq. (B.39) for $N_{N_i}^{\mathrm{eq}}$ and rewriting the Hubble parameter in terms of z_i, leads to

$$W_i(z_i) = \frac{1}{4} K_i z_i^3 \mathcal{K}_1(z_i) \tag{B.55}$$

for the washout term, whereas similar steps give

$$D_i(z_i) = K_i z_i \frac{\mathcal{K}_1(z_i)}{\mathcal{K}_2(z_i)} \tag{B.56}$$

for the decay term. With the help of this expression for the decay term, we can also express the first Boltzmann equation we derived for sterile neutrinos, Eq. (B.38), in a more compact form as

$$\frac{\mathrm{d}N_{N_i}}{\mathrm{d}z_i} = -D_i(N_{N_i} - N_{N_i}^{\mathrm{eq}})\,. \tag{B.57}$$

To be able to write one single Boltzmann equation for several sterile neutrinos, one has to use the fact that $z_i/z_1 = m_{N_i}/m_{N_1}$ is a constant and therefore $\frac{\mathrm{d}}{\mathrm{d}z_i} = m_{N_1}/m_{N_i}\frac{\mathrm{d}}{\mathrm{d}z_1} = z_1/z_i\frac{\mathrm{d}}{\mathrm{d}z_1}$. Since the equations for the different sterile neutrinos are otherwise well separated for a hierarchical sterile neutrino mass spectrum $m_{N_{i+1}} \geq 3m_{N_i}$, we can write

$$\frac{\mathrm{d}}{\mathrm{d}z_1} N_{B-L} = \sum_i \frac{z_i}{z_1} \left[\varepsilon_i D_i (N_{N_i} - N_{N_i}^{\mathrm{eq}}) - W_i N_{B-L}\right]\,. \tag{B.58}$$

Well separated means in this context that except for $m_{N_i} \approx T$ we have $N_{N_i} \approx N_{N_i}^{\mathrm{eq}}$ and $W_i \approx 0$, so the contributions from the other sterile neutrinos are negligible and we can use Eq. (B.54) for each sterile neutrino and use its final result as initial condition for the next lighter sterile neutrino.

Finally, let us for completeness also mention how to extend the Boltzmann equation(s) to also take into account flavor effects by introducing flavor branching ratios $P_{i\alpha}$ and the flavor coupling matrix $C_{\alpha\beta}$. With these corrections the Boltzmann equation(s) then read

$$\frac{\mathrm{d}}{\mathrm{d}z_1} N_{\Delta_\alpha} = \sum_i \frac{z_i}{z_1} \left[\varepsilon_{i\alpha} D_i (N_{N_i} - N_{N_i}^{\mathrm{eq}}) - W_i \sum_\beta P_{i\alpha} C_{\alpha\beta} N_{\Delta_\beta}\right]\,. \tag{B.59}$$

Thus, the interplay of the different flavors changes how the washout effects the evolution of the $B-L$ asymmetry.

Appendix C

Loop Functions of the Singlet Scalar Model

Here we want to state the full expressions for the loop functions that are relevant for the CP asymmetry in the singlet scalar model. They have been determined in [94] and read

$$\mathcal{F}^{\mathrm{v}}_{ij,\,R} = \sqrt{r_{ji}}\,\ln\left[\frac{(1+\eta_i)(1-r_{ji})-(1-\eta_i)(\sigma_i+\sqrt{\delta_{ji}})}{(1+\eta_i)(1-r_{ji})-(1-\eta_i)(\sigma_i-\sqrt{\delta_{ji}})}\right], \tag{C.1}$$

$$\mathcal{F}^{\mathrm{v}}_{ij,\,L} = -\sqrt{\delta_{ji}} + \frac{r_{ji}-\eta_i}{1-\eta_i}\ln\left[\frac{(1+\eta_i)(1-r_{ji})-(1-\eta_i)(\sigma_i+\sqrt{\delta_{ji}})}{(1+\eta_i)(1-r_{ji})-(1-\eta_i)(\sigma_i-\sqrt{\delta_{ji}})}\right], \tag{C.2}$$

$$\mathcal{F}^{\mathrm{s}}_{ijk,\,RR} = \frac{\sqrt{r_{ji}}\sqrt{r_{ki}}\sqrt{\delta_{ji}}}{1-r_{ji}}, \tag{C.3}$$

$$\mathcal{F}^{\mathrm{s}}_{ijk,\,RL} = \frac{1}{2}\frac{\sqrt{r_{ki}}\sqrt{\delta_{ji}}(1+r_{ji}-\sigma_i)}{1-r_{ji}}, \tag{C.4}$$

$$\mathcal{F}^{\mathrm{s}}_{ijk,\,LL} = \frac{\sqrt{r_{ji}}\sqrt{\delta_{ji}}}{1-r_{ji}}, \tag{C.5}$$

$$\mathcal{F}^{\mathrm{s}}_{ijk,\,LR} = \frac{1}{2}\frac{\sqrt{\delta_{ji}}(1+r_{ji}-\sigma_i)}{1-r_{ji}}, \tag{C.6}$$

where we defined $r_{ij} \coloneqq M_i^2/M_j^2$, $\sigma_i \coloneqq m_S^2/M_i^2$, $\eta_i \coloneqq m_h^2/M_i^2$ and $\delta_{ij} \coloneqq (1-r_{ij}-\sigma_j)^2 - 4\,r_{ij}\sigma_j$. Note that since leptogenesis happens before the EW phase transition, we have a vanishing mass of the SM Higgs boson $m_h = 0$. This can be different if another Higgs doublet is involved in leptogenesis as for example in the scotogenic model (cf. Ch. 2).

Appendix D

Formulae for the Decay Widths

This appendix serves as an overview of the formulae for the decay widths in the 2HDM+S and 2HDM+PS, as discussed (in parts) by Sec. 4.1.4. Like Ch. 4, this appendix is based on Ref. [162].

We focus in the analysis of the decay widths on a mass spectrum of the type $M_A \sim M_{H/S_1} \sim M_{H^\pm} > M_{a/S_2}, M_h$ as it also appears in Sec. 4.1.4. Furthermore, we use $\tan\beta \sim 1$, implying that we are nearly independent of the specific type of the Yukawa structures, except for the inert one. Nevertheless, we will mostly use ε_f for a (type of) fermion f to indicate the Yukawa scaling factors as laid out by Tab. 4.1 and note that the SM value for the Yukawa coupling is given by $y_f = \sqrt{2}\, m_f/v$. Additionally, we introduce the regularly appearing kinematic quantity $\tau_{i,j} \coloneqq 4M_i^2/M_j^2$.

D.1 Scalar Model

Higgs Boson h As discussed in Sec. 4.1.2, the alignment or decoupling limit ensures that the couplings of h with the SM states coincide with the ones of the SM Higgs boson. However, its total width can deviate from the SM prediction, because of possible additional decay channels. The most relevant, if kinematically allowed, is the one into a pair of S_2 states. Since the Higgs width is small, also three-body decays can be relevant and the additional widths are given by

$$\Gamma(h \to S_2 S_2) = \frac{1}{32\pi}\, g_{hS_2S_2}^2\, M_h\, \sqrt{1-\tau_{S_2,h}}\,, \tag{D.1}$$

$$\Gamma(h \to S_2 \chi \bar{\chi}) = \frac{y_\chi^2}{32\pi^3}\, g_{hS_2S_2}^2\, M_h\, g(\tau_{S_2,h}) \cos^2\theta\, (1-\tau_{\chi,S_2})^{3/2}\,, \tag{D.2}$$

$$\Gamma\big(h \to S_2 f \bar{f}\big) = \frac{N_c^f\, \varepsilon_f^2\, y_f^2}{16\pi^3}\, g_{hS_2S_2}^2\, M_h\, g(\tau_{S_2,h}) \sin^2\theta\, (1-\tau_{f,S_2})^{3/2}\,, \tag{D.3}$$

with [220]

$$g(\tau) = \frac{\tau-4}{8}\left[4 - \ln\left(\frac{\tau}{4}\right)\right] - \frac{5\tau-4}{4\sqrt{\tau-1}}\left[\arctan\left(\frac{\tau-2}{2\sqrt{\tau-1}}\right) - \arctan\left(\frac{1}{\sqrt{\tau-1}}\right)\right], \tag{D.4}$$

$$g_{hS_2S_2} = \frac{1}{M_h v}\left(M_h^2 - 2\left(M_{S_1}^2 - M_{S_2}^2\right)\cos^2\theta\right)\sin^2\theta\,. \tag{D.5}$$

Light Scalar S_2 The light scalar S_2 mostly decays into gg, $f\bar{f}$ and $\chi\bar{\chi}$ (direct couplings with gauge boson are forbidden in the alignment limit), depending on the mass. We quote below the corresponding decay widths and the loop-induced one into gluons, which is useful for the interpretation of our collider studies:

$$\Gamma(S_2 \to gg) = \frac{\alpha_s^2}{16\pi^3} M_{S_2} \sin^2\theta \sum_q \varepsilon_q^2\, y_q^2\, F_S(\tau_{q,S_2})\,, \tag{D.6}$$

$$\Gamma(S_2 \to f\bar{f}) = \frac{N_c^f\, \varepsilon_f^2\, y_v^2}{16\pi} M_{S_2} \sin^2\theta\,(1-\tau_{f,S_2})^{3/2}\,, \tag{D.7}$$

$$\Gamma(S_2 \to \chi\bar{\chi}) = \frac{y_\chi^2}{8\pi} M_{S_2} \cos^2\theta\,(1-\tau_{\chi,S_2})^{3/2}\,, \tag{D.8}$$

with

$$F_S(x) = x\left|1 + (1-x)\arctan^2\frac{1}{\sqrt{x-1}}\right|^2. \tag{D.9}$$

Heavy Scalar S_1 The couplings of the heavy scalar to the SM fields are similar to the usual 2HDM formulas, with an additional factor of $\cos^2\theta$ that appears due to the mixing between the scalar singlet and the doublets. Furthermore, we have the additional decay channels $S_1 \to \chi\bar{\chi}$, which is suppressed by $\sin^2\theta$, $S_1 \to S_2S_2$, which is very small for our choice of parameters, and $S_1 \to S_2 h$, which turns out to be important for the mono-h bounds. The analytic expressions are given by

$$\Gamma(S_1 \to gg) = \frac{\alpha_s^2}{16\pi^3} M_{S_1} \cos^2\theta \sum_q \varepsilon_q^2\, y_q^2\, F_S(\tau_{q,S_1})\,, \tag{D.10}$$

$$\Gamma\big(S_1 \to f\bar{f}\big) = \frac{N_c^f\, \varepsilon_f^2\, y_f^2}{16\pi} M_{S_1} \cos^2\theta\,(1-\tau_{f,S_1})^{3/2}\,, \tag{D.11}$$

$$\Gamma(S_1 \to \chi\bar{\chi}) = \frac{y_\chi^2}{8\pi} M_{S_1} \sin^2\theta\,(1-\tau_{\chi,S_1})^{3/2}\,, \tag{D.12}$$

$$\Gamma(S_1 \to S_2S_2) = \frac{1}{32\pi} g_{S_1S_2S_2}^2\, M_{S_1}\sqrt{1-\tau_{S_2,S_1}}\,, \tag{D.13}$$

$$\Gamma(S_1 \to S_2 h) = \frac{1}{16\pi}\frac{\lambda^{1/2}(M_{S_1}, M_h, M_{S_2})}{M_{S_1}}\, g_{S_1S_2h}^2\,, \tag{D.14}$$

with

$$g_{S_1S_2S_2} = \frac{1}{M_{S_1} v_S} \left(M_{S_1}^2 + 2M_{S_2}^2 - \frac{2 - 3\sin^2\theta}{\cos^2\theta}\, \hat{\lambda}_{HHS}\, v_S^2 \right) \sin\theta\, \cos\theta\,, \tag{D.15}$$

$$g_{S_1S_2h} = \frac{1}{M_{S_1} v} \left(M_h^2 + \left(M_{S_1}^2 - M_{S_2}^2 \right) \cos 2\theta \right) \sin\theta\, \cos\theta\,. \tag{D.16}$$

Furthermore, we introduced

$$\lambda(m_1, m_2, m_3) \coloneqq \left(m_1^2 - m_2^2 - m_3^2 \right)^2 - 4\, m_2^2\, m_3^2\,. \tag{D.17}$$

Pseudoscalar A In addition to the decay channels known from 2HDMs, the pseudoscalar has a further one to S_2Z. Their decay widths are found to be

$$\Gamma(A \to gg) = \frac{\alpha_s^2}{16\pi^3}\, M_A \sum_q \varepsilon_q^2\, y_q^2\, F_P(\tau_{q,A})\,, \tag{D.18}$$

$$\Gamma\left(A \to f\bar{f}\right) = \frac{N_c^f\, \varepsilon_f^2\, y_f^2}{16\pi}\, M_A\, (1 - \tau_{f,A})^{1/2}\,, \tag{D.19}$$

$$\Gamma(A \to S_2 Z) = \frac{1}{16\pi}\, \frac{\lambda^{3/2}(M_A, M_{S_2}, M_Z)}{M_A^3\, v^2}\,, \tag{D.20}$$

with

$$F_P(x) = x \left| \arctan^2 \frac{1}{\sqrt{x-1}} \right|^2. \tag{D.21}$$

Charged Scalar $H^\pm$ For completeness, we also list the partial widths of $H^\pm$ to quarks and the new scalars in combination with a $W^\pm$. The $H^\pm h W^\pm$ vertex, and therefore the corresponding partial width, vanishes in the alignment limit.

$$\Gamma\left(H^+ \to t\bar{b}\right) = \frac{N_c^t |V_{tb}|^2 \varepsilon_t^2\, y_t^2}{16\pi}\, M_{H^\pm} \left(1 - \tau_{t,H^\pm}/4\right)^2\,, \tag{D.22}$$

$$\Gamma\left(H^\pm \to S_1 W^\pm\right) = \frac{1}{16\pi}\, \frac{\lambda^{3/2}(M_{H^\pm}, M_{S_1}, M_W)}{M_{H^\pm}^3 v^2}\, \cos^2\theta\,, \tag{D.23}$$

$$\Gamma\left(H^\pm \to A W^\pm\right) = \frac{1}{16\pi}\, \frac{\lambda^{3/2}(M_{H^\pm}, M_A, M_W)}{M_{H^\pm}^3 v^2}\,, \tag{D.24}$$

$$\Gamma\left(H^\pm \to S_2 W^\pm\right) = \frac{1}{16\pi}\, \frac{\lambda^{3/2}(M_{H^\pm}, M_{S_2}, M_W)}{M_{H^\pm}^3 v^2}\, \sin^2\theta\,, \tag{D.25}$$

where in the case of $H^+ \to t\bar{b}$ we have neglected terms of $\mathcal{O}(m_b^2/M_{H^\pm}^2)$.

D.2 Pseudoscalar Model

The results in this section are taken from [160] and transferred into our notation. In general, the decay width formulas and their behavior is very similar to the scalar ones

presented in the previous section.

Higgs Boson h Similarly to the 2HDM+S, the couplings of h to $f\bar{f}$ and gauge boson pairs are fixed to their SM values by the alignment limit. Nevertheless, due to the additional two and three body decay channels, the total decay width is enlarged and we find the expressions [220]:

$$\Gamma(h \to aa) = \frac{1}{32\pi}\, g_{haa}^2\, M_h\, (1-\tau_{a,h})^{1/2}\,, \tag{D.26}$$

$$\Gamma(h \to a\chi\bar{\chi}) = \frac{y_\chi^2}{32\pi^3}\, g_{haa}^2\, M_h\, g(\tau_{a,h}) \cos^2\theta\, (1-\tau_{\chi,a})^{1/2}\,, \tag{D.27}$$

$$\Gamma\big(h \to af\bar{f}\big) = \frac{N_c^f\, \varepsilon_f^2\, y_f^2}{16\pi^3}\, g_{haa}^2\, M_h\, g(\tau_{a,h}) \sin^2\theta\, (1-\tau_{f,a})^{1/2}\,, \tag{D.28}$$

with $g(\tau)$ given by Eq. (D.4) and

$$g_{haa} = \frac{1}{M_h v}\Big[\left(M_h^2 - 2M_H^2 + 4M_{H^\pm}^2 - 2M_a^2 - 2\lambda_3 v^2\right)\sin^2\theta \\ - \left(\lambda_{11P}\cos^2\beta + \lambda_{22P}\sin^2\beta\right) v^2 \cos^2\theta\Big].$$

Light Pseudoscalar a The partial widths to gg, $f\bar{f}$ and $\chi\bar{\chi}$ are given by

$$\Gamma(a \to gg) = \frac{\alpha_s^2}{16\pi^3}\, M_a\, \sin^2\theta \sum_q \varepsilon_q^2\, y_q^2\, F_P(\tau_{q,A})\,, \tag{D.29}$$

$$\Gamma\big(a \to f\bar{f}\big) = \frac{N_c^f\, \varepsilon_f^2\, y_f^2}{16\pi}\, M_a\, (1-\tau_{f,a})^{1/2}\,, \tag{D.30}$$

$$\Gamma(a \to \chi\bar{\chi}) = \frac{y_\chi^2}{8\pi}\, M_a \cos^2\theta\, (1-\tau_{\chi,a})^{1/2}\,, \tag{D.31}$$

with F_P as given in Eq. (D.21).

Heavy Pseudoscalar A For the heavy pseudoscalar we find for the partial widths to gg, $f\bar{f}$, $\chi\bar{\chi}$ and ah

$$\Gamma(A \to gg) = \frac{\alpha_s^2}{16\pi^3}\, M_A\, \cos^2\theta \sum_q \varepsilon_q^2\, y_q^2\, F_P(\tau_{q,A})\,, \tag{D.32}$$

$$\Gamma\big(A \to f\bar{f}\big) = \frac{N_c^f\, \varepsilon_f^2\, y_f^2}{16\pi}\, M_A\, \cos^2\theta\, (1-\tau_{f,A})^{1/2}\,, \tag{D.33}$$

$$\Gamma(A \to \chi\bar{\chi}) = \frac{y_\chi^2}{8\pi}\, M_A\, \sin^2\theta\, (1-\tau_{\chi,A})^{1/2}\,, \tag{D.34}$$

$$\Gamma(A \to ah) = \frac{1}{16\pi}\, \frac{\lambda^{1/2}(M_A, M_a, M_h)}{M_A}\, g_{Aah}^2\,, \tag{D.35}$$

with

$$g_{Aah} = \frac{1}{M_A\, v}\Big[M_h^2 - 2M_H^2 - M_A^2 + 4M_{H^\pm}^2 - M_a^2 \\ + \left(\lambda_{11P}\cos^2\beta + \lambda_{22P}\sin^2\beta - 2\lambda_3\right) v^2\Big]\sin\theta\,\cos\theta\,. \tag{D.36}$$

Heavy Scalar H In this case, the partial widths to gg, $f\bar{f}$, aa and aZ are given by

$$\Gamma(H\to gg) = \frac{\alpha_s^2}{16\pi^3}\, M_H \sum_q \varepsilon_q^2\, y_q^2\, F_S(\tau_{q,H})\,, \tag{D.37}$$

$$\Gamma\big(H\to f\bar{f}\big) = \frac{N_c^f\,\varepsilon_f^2\, y_f^2}{16\pi}\, M_H\,(1-\tau_{f,H})^{3/2}\,, \tag{D.38}$$

$$\Gamma(H\to aa) = \frac{1}{32\pi}\, g_{Haa}^2\, M_H\,(1-\tau_{a,H})^{1/2}\,, \tag{D.39}$$

$$\Gamma(H\to aZ) = \frac{1}{16\pi}\,\frac{\lambda^{3/2}(M_H,M_a,M_Z)}{M_H^3 v^2}\,\sin^2\theta\,, \tag{D.40}$$

with $\lambda(\cdot)$ as defined by Eq. (D.17) and the Haa coupling

$$g_{Haa} = \frac{1}{M_H v}\Big[\cot(2\beta)\left(2M_h^2 - 4M_H^2 + 4M_{H^\pm}^2 - 2\lambda_3 v^2\right)\sin^2\theta \\ + \sin(2\beta)\cos^2\theta\, v^2\,\left(\lambda_{11P} - \lambda_{22P}\right)/2\Big]. \tag{D.41}$$

Charged Scalar $H^\pm$ Finally, we find for the decay width of the charged scalar

$$\Gamma\left(H^+\to t\bar{b}\right) = \frac{N_c^t\,|V_{tb}|^2\,\varepsilon_t^2\, y_t^2}{16\pi}\, M_{H^\pm}\left(1-\tau_{t,H^\pm}/4\right)^2\,, \tag{D.42}$$

$$\Gamma\big(H^\pm\to HW^\pm\big) = \frac{1}{16\pi}\,\frac{\lambda^{3/2}(M_{H^\pm},M_H,M_W)}{M_{H^\pm}^3 v^2}\,, \tag{D.43}$$

$$\Gamma\big(H^\pm\to AW^\pm\big) = \frac{1}{16\pi}\,\frac{\lambda^{3/2}(M_{H^\pm},M_A,M_W)}{M_{H^\pm}^3 v^2}\,\cos^2\theta\,, \tag{D.44}$$

$$\Gamma\big(H^\pm\to aW^\pm\big) = \frac{1}{16\pi}\,\frac{\lambda^{3/2}(M_{H^\pm},M_a,M_W)}{M_{H^\pm}^3 v^2}\,\sin^2\theta\,, \tag{D.45}$$

where in the case of $H^+\to t\bar{b}$ we have again neglected terms of $\mathcal{O}(m_b^2/M_{H^\pm}^2)$. Note that in the alignment limit the $H^\pm hW^\pm$ vertex, and therefore the corresponding partial width, vanishes. Additionally, these decay widths of the charged scalar $H^\pm$ are mostly relevant for small $\tan\beta$.

Appendix E

Inflation Scale and Minimal Number of e-Folds

Since inflation is the central focus of our analysis, we want to address here several points about the number of e-folds of inflation and their connection to the scale of inflation H_I. For our discussion, we will closely follow [296] and rely on some common assumptions in cosmology.

We denote the number of e-folds between the comoving scale (wavenumber) k leaving the horizon at $k = aH$ during inflation and the end of inflation by $N(k)$, while $N_{\rm tot}$ represents the total number of e-folds of inflation. From the present horizon scale $k_0 = a_0 H_0$, which is the largest scale that we can access observationally, we find a lower limit $N_{\rm tot} \geq N(k_0)$, however $N_{\rm tot}$ can in principle be much larger. To be able to get quantitative results, we have to specify in some cases the total number of e-folds $N_{\rm tot}$, for which we will then use the assumption of minimal inflation, meaning to choose $N_{\rm tot} = N_{\rm min} = N(k_0)$.

In general $N(k)$ can be expressed as [296]

$$N(k) = -\ln\left(\frac{k}{a_0 H_0}\right) + \frac{1}{3}\ln\left(\frac{\rho_{\rm reh}}{\rho_{\rm end}}\right) + \frac{1}{4}\ln\left(\frac{\rho_{\rm eq}}{\rho_{\rm reh}}\right) + \ln\left(\frac{H_k}{H_{\rm eq}}\right) + \ln(219\,\Omega_m h)\,, \quad \text{(E.1)}$$

where $\rho_{\rm end}$, $\rho_{\rm reh}$, $\rho_{\rm eq}$ are the energy density at the end of inflation, at reheating and at matter-radiation equality, H_k and $H_{\rm eq}$ are the Hubble parameters at the time when the scale k exits the horizon during inflation and at matter radiation equality, and Ω_m is the matter density. To simplify the above expression we will rely on two common assumptions in cosmology. First, we assume $H_k = H_{\rm end} \equiv H_I$, thus an exactly exponential expansion during inflation. Second, $\rho_{\rm reh} = \rho_{\rm end}$, thus instantaneous reheating at the end of inflation. Additionally, we can make use of the first Friedmann equation for a flat universe, $\rho = 3m_{\rm Pl}^2 H^2$ with the reduced Planck mass $m_{\rm Pl}$, and the numerical values $H_{\rm eq} \approx 2 \cdot 10^{-37}\,\text{GeV}$, $\Omega_m \approx 0.3$ and $h \approx 0.7$. In this way we find for minimal inflation ($k = k_0$) the nicely simple expression

$$N_{\rm min} = 62 + \frac{1}{2}\ln\left(\frac{H_I}{6.6 \cdot 10^{13}\,\text{GeV}}\right). \quad \text{(E.2)}$$

Here, the chosen normalization for H_I refers to the largest scale of inflation allowed by

observations (using the 95 % confidence limit from [295]). An important aspect of this result for the minimal number of e-folds is that we can directly see that $N_{\min}$ decreases for smaller scales of inflation.

In addition to the minimal number of e-folds, we are also interested in the number of e-folds that the scales related to the CMB left the horizon before the end of inflation, $N(k_{\mathrm{CMB}})$. With the PLANCK pivot scale $k_{\mathrm{CMB}} = k_\star = 0.05\,\mathrm{Mpc}^{-1}$, we find

$$N_{\min} - N(k_{\mathrm{CMB}}) = 7.26\,. \tag{E.3}$$

To conclude and for comparison, we also give the expression for the minimal number of e-folds without any assumptions on reheating and assuming slow-roll inflation:

$$N_{\min} = 62 + \frac{1}{2}\ln\left(\frac{H_I}{6.6\cdot 10^{13}\,\mathrm{GeV}}\right) + \frac{1}{4}\ln\left(\frac{V_{k_0}}{\rho_{\mathrm{end}}}\right) + \frac{1}{12}\ln\left(\frac{\rho_{\mathrm{reh}}}{\rho_{\mathrm{end}}}\right). \tag{E.4}$$

The slow-roll approximation implies $H_k = 8\pi V_k/3m_{\mathrm{Pl}}^3$ and we reformulated the result in terms of the energy scale of inflation instead of the Hubble scale. Note that for a longer period of preheating we generally have $\rho_{\mathrm{reh}} \leq \rho_{\mathrm{end}}$, leading to a decrease in $N_{\min}$, while a deviation from pure de Sitter expansion means that $V_{k_0} \geq \rho_{\mathrm{end}}$ and results in a larger value for $N_{\min}$.

Appendix F

Stochastic Scenario

This appendix provides the details of the calculation for the stochastic scenario, following along the lines of [246]. While we provide all formulas here for the scalar case, note that the calculation works essentially identical for the vector case for which we partially use formulas from [262].

As the stochastic scenario relies on an equilibrium between the accumulation of fluctuations that get stretched to superhorizon scales and the relaxation of the so generated homogeneous field value, we will need for our calculations the exact form of the homogeneous field evolution during inflation. Taking general initial conditions ϕ_s and $\dot{\phi}_s$, it is given by

$$\phi(t) = \phi_s \left(c_1 \mathrm{e}^{-\frac{1}{2}\alpha_- H_I t} + c_2 \mathrm{e}^{-\frac{1}{2}\alpha_+ H_I t} \right), \tag{F.1}$$

with

$$\begin{aligned} c_1 &= \frac{1}{\alpha_+ - \alpha_-} \left(\alpha_+ + \frac{\dot{\phi}_s}{H_I \, \phi_s} \right), \\ c_2 &= -\frac{1}{\alpha_+ - \alpha_-} \left(\alpha_- + \frac{\dot{\phi}_s}{H_I \, \phi_s} \right), \end{aligned} \tag{F.2}$$

and identical equations being valid in the vector case for $\chi_i(t)$, only exchanging $\alpha_\pm$ for $\beta_\pm$. Using $\alpha_+ > \alpha_-$ ($\beta_+ > \beta_-$), we can for late times approximate the solutions by

$$\phi(t) \approx \frac{2}{H_I(\alpha_+ - \alpha_-)} \left(\dot{\phi}_s + \frac{1}{2}\alpha_+ H_I \phi_s \right) \mathrm{e}^{-\frac{1}{2}\alpha_- H_I t} \tag{F.3}$$

$$\dot{\phi}(t) \approx -\frac{\alpha_-}{\alpha_+ - \alpha_-} \left(\dot{\phi}_s + \frac{1}{2}\alpha_+ H_I \phi_s \right) \mathrm{e}^{-\frac{1}{2}\alpha_- H_I t} . \tag{F.4}$$

Note that the time t appearing here is defined such that at the end of inflation $H_I t = N_{\mathrm{tot}}$. Furthermore, we find for the time derivative in general

$$\dot{\phi}(t) = -\frac{1}{2}\alpha_- H_I \phi(t) , \tag{F.5}$$

implying for the initial conditions that the assumption $\dot{\phi}_s \sim H_I \phi_s$ is reasonable as long as $\alpha_- \not\approx 0$.

For the computation of the variance of the field value sourced by fluctuations, we, in a first step, identify how the notation used in [246] relates to our notation. The quantity ν, used by [246, 262], is in terms of our α_- given by $\alpha_- = 3 - 2\nu$, or directly in terms of ξ by $\nu \approx 3/2\sqrt{1 - 16/3\xi}$, with $0 \lesssim \xi \lesssim 3/16$. Solving the EOM of the fluctuations, which is very similar to the one solved in [246], we find a solution that depends on a Hankel function. Splitting this Hankel function into Bessel functions, it turns out that the contribution scaling with the Bessel function of the first kind $J_{-\nu}(\cdot)$ is dominant and thus, after approximating $J_{-\nu}(\cdot)$, the (late time) field values of the fluctuations turn out to be

$$|\delta\phi_k|^2 \approx \frac{H_I^2}{4\pi}\,\Gamma^2\!\left(\frac{3-\alpha_-}{2}\right)\left(\frac{1}{aH_I}\right)^3\left(\frac{2aH_I}{k}\right)^{3-\alpha_-} . \tag{F.6}$$

However, the fluctuations do only contribute to the homogeneous field value as long as inflation stretches their size to scales that are still superhorizon today. The accumulated effect of all these sufficiently long wavelength modes then results in a Gaussian distribution for the homogeneous field value with variance

$$\begin{aligned}\left\langle\phi_\delta^2\right\rangle_{\text{horizon}} &= \int_{a(t_i)H_I}^{a(t_{\text{horizon}})H_I} \frac{\mathrm{d}^3\vec{k}}{(2\pi)^3}\,|\delta\phi_k|^2_{a=a_{\text{horizon}}} \\ &= \frac{2^{-\alpha}}{\pi^3\alpha_-}\Gamma^2\!\left(\frac{3-\alpha_-}{2}\right)H_I^2\left[1-\mathrm{e}^{-\alpha_-(N_{\text{tot}}-N_{\text{min}})}\right],\end{aligned} \tag{F.7}$$

where the subscript "horizon" indicates the quantity at horizon exit of the present horizon scale k_0. Note that we implicitly assumed in this expression (through the definition of $\alpha_\pm$) that $m_\phi^2/H_I^2 \ll \xi$ (cf. [246, 262]). For smaller values of ξ, this result and the ones below still hold but for an effective $\xi_{\text{eff}} \sim m_\phi^2/H_I^2$. Thus it is not possible to make α_- arbitrarily small to retrieve an arbitrarily large variance.

The homogeneous field value that is realized in our universe and created in this way is thus a draw from this Gaussian distribution. Naturally assuming that the Gaussian distribution has a mean of zero, the "typical" result of such a draw is $\phi_{\text{horizon}} = \sqrt{\left\langle\phi_\delta^2\right\rangle}$. However, the presence of a non-minimal coupling can significantly change this homogeneous field value between the time of horizon exit of the present horizon scale and the end of inflation. Assuming equilibrium has been reached (we will specify an exact condition for this below), we have $\dot{\phi}_{\text{horizon}} = 0$ and the subsequent evolution can be described by (cf. Eq. (F.3))

$$\phi_e \approx \frac{\alpha_+}{\alpha_+ - \alpha_-}\,\mathrm{e}^{-\frac{1}{2}\alpha_- N_{\text{min}}}\phi_{\text{horizon}} . \tag{F.8}$$

As this subsequent evolution lasts for the last N_{min} e-folds of inflation, we find for the (square of the) typical homogeneous field value at the end of inflation

$$\left\langle\phi_\delta^2\right\rangle = \frac{F(\alpha_-)}{\alpha_-}\left(\frac{H_I}{2\pi}\right)^2\left[1-\mathrm{e}^{-\alpha_-(N_{\text{tot}}-N_{\text{min}})}\right]\left(\frac{\alpha_+}{\alpha_+-\alpha_-}\,\mathrm{e}^{-\frac{1}{2}\alpha_- N_{\text{min}}}\right)^2 . \tag{F.9}$$

From Eq. (F.9) we can also deduce an exact condition what it means for equilibrium to be reached. In general, and also in the way we used the term above, equilibrium means that a state does not change (any more) with time. Since time refers for us to the duration of inflation during which the homogeneous field value is built up $\Delta N \coloneqq N_{\mathrm{tot}} - N_{\mathrm{min}}$, equilibrium happens when Eq. (F.9) is (approximately) independent of ΔN, so for $\Delta N \gtrsim 1/\alpha_-$. This is equivalent to demanding that the integral of Eq. (F.7) is dominated by the upper limit (or independent of the lower limit), corresponding to the superhorizon modes with the shortest wavelengths that just span the observable universe. Thus, assuming equilibrium, the term in the square brackets in Eq. (F.9) becomes one and to simplify things further we can use $\alpha_+ > \alpha_-$ to approximate $\alpha_+/(\alpha_+ - \alpha_-) \approx 1$.

To compare the homogeneous field value created through the stochastic scenario to the one from the misalignment mechanism, it is best to evaluate both at t_{horizon}, since afterwards their evolution is identical. Using Eq. (F.3) after ΔN e-folds of inflation for the misalignment field value and Eq. (F.7) for the stochastic field value, we need to specify, as a last ingredient, how much larger the stochastic field value should be compared to the misalignment one. Calling this factor γ, we end up with a single equation that can be readily solved for ΔN. The corresponding result is given in the respective sections of the stochastic scenario for the scalar and vector case.

For the calculations of the stochastic scenario in the case of a vector field, we simply have to split the contributions into transverse and longitudinal modes, while following the same lines as above.

Disclaimer

The scientific findings presented in this thesis are based on work performed by the author in collaboration with others. As most of these scientific findings have been part of publications, we indicate the corresponding publication in the respective introduction to the chapter. In summary,

- chapter 2, from Sec. 2.2 onward, is based on Ref. [1],
- while chapter 3 is rooted in Ref. [2],
- chapter 4 is adapted from Ref. [3]
- and chapter 5 is based on Ref. [4].

While all of the above papers are published, Refs. [1, 2, 4] are available in peer-reviewed journals, whereas Ref. [3] is (as of submission of this thesis) in the peer-review process.

In addition to the above mentioned works, the author also contributed to the peer-reviewed Refs. [5, 6] and was part of the CONUS collaboration with a focus on data analysis.

Note that the reference numbers here are not identical to the main text.

References

[1] Thomas Hugle, Moritz Platscher, and Kai Schmitz. "Low-Scale Leptogenesis in the Scotogenic Neutrino Mass Model". In: *Phys. Rev.* D98.2 (2018), p. 023020. DOI: 10.1103/PhysRevD.98.023020. arXiv: 1804.09660 [hep-ph].

[2] Tommi Alanne et al. "Low-scale leptogenesis assisted by a real scalar singlet". In: *JCAP* 1903.03 (2019), p. 037. DOI: 10.1088/1475-7516/2019/03/037. arXiv: 1812.04421 [hep-ph].

[3] Giorgio Arcadi et al. "Comparing 2HDM + Scalar and Pseudoscalar Simplified Models at LHC". In: (2020). arXiv: 2001.10540 [hep-ph].

[4] Gonzalo Alonso-Álvarez, Joerg Jaeckel, and Thomas Hugle. "Misalignment & Co.: (Pseudo-)scalar and vector dark matter with curvature couplings". In: *JCAP* 02.02 (2020), p. 014. DOI: 10.1088/1475-7516/2020/02/014. arXiv: 1905.09836 [hep-ph].

[5] Giorgio Arcadi, Thomas Hugle, and Farinaldo S. Queiroz. "The Dark $L_\mu - L_\tau$ Rises via Kinetic Mixing". In: *Phys. Lett. B* 784 (2018), pp. 151–158. DOI: 10.1016/j.physletb.2018.07.028. arXiv: 1803.05723 [hep-ph].

[6] Tommi Alanne et al. "A fresh look at the gravitational-wave signal from cosmological phase transitions". In: *JHEP* 03 (2020), p. 004. DOI: 10.1007/JHEP03(2020)004. arXiv: 1909.11356 [hep-ph].

List of Figures

List of Tables

List of Abbreviations

ΛCDM standard model of cosmology

2HDM two Higgs doublet model

2HDM+PS two Higgs doublet model with an additional pseudoscalar

2HDM+S two Higgs doublet model with an additional scalar

BAU baryon asymmetry of the universe

BBN big bang nucleosythesis

BR branching ratio

BSM beyond the standard model

C charge conjugation

CI Casas-Ibarra

CMB cosmic microwave background

CP charge and parity conjugation

CPT charge, parity and time conjugation

DD direct detection

DE dark energy

DI Davidson-Ibarra

DM dark matter

DMWG dark matter working group

dof degree of freedom

EFT effective field theory

EOM equation of motion

EW electroweak

FCNCs flavor changing neutral currents

GR general relativity

ID indirect detection

IO inverted ordering

LHC Large Hadron Collider

MET missing transverse energy

NFC natural flavor conservation

NLO next-to-leading order

NO normal ordering

PDF parton distribution function

PMNS Pontecorvo-Maki-Nakagawa-Sakata

pNGB pseudo-Nambu-Goldstone boson

QCD quantum chromo dynamics

QFT quantum field theory

RHN right-handed neutrino

SI spin independent

SM standard model of particle physics

UV ultraviolet

vev vacuum expectation value

WIMP weakly interacting massive particle

Acknowledgments

First and foremost I want to thank my supervisor Prof. Dr. Dr. Manfred Lindner, who made my PhD at the Max-Planck-Institut für Kernphysik possible in the first place. The scientific freedom he gave me to pursue a broad range of research topics, combined with discussions and insights into what might be worth investigating and which schools are worth attending, made my time at the institute a very enjoyable and also fruitful one.

Also a huge thank you goes out to my fellow PhD students with whom I had the pleasure of working closely together on the various projects: Gonzalo Alonso-Álvarez, Moritz Platscher, Thomas Rink and Valentin Tenorth. There are a lot of things that only started to become clear after long and enjoyable discussions with you.

My thanks of course also go to all the postdocs and professors that helped and supported me during and besides the projects of my PhD, be it through discussions, explanations or general tips and tricks. Without any claim to be complete, these include Tommi Alanne, Giorgio Arcadi, Giorgio Busoni, Rasmus S. L. Hansen, Jörg Jäckel, Farinaldo S. Queiroz, Kai Schmitz, Stefan Schoppmann and Stefan Vogl.

Furthermore I am grateful to the experimentalists in the analysis group of the CONUS collaboration Aurelie Bonhomme, Christian Buck, Janina Hakenmüller and Werner Maneschg for having the patience to explain some aspects of experimental physics to a phenomenologist / theorist like me.

As no thesis would be complete without an exam, my gratitude goes especially to my second referee Prof. Dr. Björn Malte Schäfer and also to my two further examiners Prof. Dr. Jörg Jäckel and Prof. Dr. Stephanie Hansmann-Menzemer.

Special thanks also go out to Anja Berneiser, Britta Schwarz and the HGSFP office, who made everything run smoothly from an administrative point of view and without whom doing a PhD would have definitely been much harder.

I am also indebted to Ingolf Bischer, Christian Döring, Thomas Rink and Valentin Tenorth for proofreading my thesis and valuable comments on the manuscript.

Moreover, I want to thank Hannes Bonet and Aurelie Bonhomme for being my walking buddies, probably contributing significantly to my fitness in the last year, and also to the tea crew Thomas Rink and Veronica Pizzella that always kept me hydrated.

A huge thank you of course belongs to all my "office mates" for all the funny and interesting conversations we had that made the PhD overall a great time. Trying to follow an alphabetical order, this includes Ingolf Bischer, Simone Blasi, Miguel Campos Vidal,

Christian Döring, Alexander Helmboldt, Carlos Jaramillo, Daniel Jiménez, Christiane Klein, Moritz Platscher, Thomas Rink, Tobias Schierhuber, Oliver Scholer, Valentin Tenorth and Susan van der Woude.

Special thanks also to Aisling and all my friends with whom one can spend both long enjoyable days as well as evenings, all of which I wouldn't want to have missed.

Last but not least, an infinite thank you to my parents Alfred and Sabine and my sister Manuela for being who they are.

Bibliography

[1] The Royal Society. *History of the Royal Society*. URL: https://royalsociety.org/about-us/history/ (visited on 02/05/2020).

[2] ATLAS Standard Model Working Group. *ATLAS Experiment - Public Results - Standard Model Results*. URL: https://twiki.cern.ch/twiki/bin/view/AtlasPublic/StandardModelPublicResults (visited on 04/18/2020).

[3] CMS Standard Model Working Group. *CMS Standard Model Physics Results*. URL: https://twiki.cern.ch/twiki/bin/view/CMSPublic/PhysicsResultsSMP (visited on 04/18/2020).

[4] N. Aghanim et al. "Planck 2018 results. VI. Cosmological parameters". In: (July 2018). arXiv: 1807.06209 [astro-ph.CO].

[5] Douglas Clowe et al. "A direct empirical proof of the existence of dark matter". In: *Astrophys. J.* 648 (2006), pp. L109–L113. DOI: 10.1086/508162. arXiv: astro-ph/0608407.

[6] S. Perlmutter et al. "Measurements of Ω and Λ from 42 high redshift supernovae". In: *Astrophys. J.* 517 (1999), pp. 565–586. DOI: 10.1086/307221. arXiv: astro-ph/9812133.

[7] Adam G. Riess et al. "Observational evidence from supernovae for an accelerating universe and a cosmological constant". In: *Astron. J.* 116 (1998), pp. 1009–1038. DOI: 10.1086/300499. arXiv: astro-ph/9805201.

[8] C. Patrignani et al. "Review of Particle Physics". In: *Chin. Phys.* C40.10 (2016), p. 100001. DOI: 10.1088/1674-1137/40/10/100001.

[9] P. A. R. Ade et al. "Planck 2015 results. XIII. Cosmological parameters". In: *Astron. Astrophys.* 594 (2016), A13. DOI: 10.1051/0004-6361/201525830. arXiv: 1502.01589 [astro-ph.CO].

[10] Richard H. Cyburt et al. "Big Bang Nucleosynthesis: 2015". In: *Rev. Mod. Phys.* 88 (2016), p. 015004. DOI: 10.1103/RevModPhys.88.015004. arXiv: 1505.01076 [astro-ph.CO].

[11] Laurent Canetti, Marco Drewes, and Mikhail Shaposhnikov. "Matter and Antimatter in the Universe". In: *New J. Phys.* 14 (2012), p. 095012. DOI: 10.1088/1367-2630/14/9/095012. arXiv: 1204.4186 [hep-ph].

[12] E. Aprile et al. "Dark Matter Results from 225 Live Days of XENON100 Data". In: *Phys. Rev. Lett.* 109 (2012), p. 181301. DOI: 10.1103/PhysRevLett.109.181301. arXiv: 1207.5988 [astro-ph.CO].

[13] E. Aprile et al. "Dark Matter Search Results from a One Ton-Year Exposure of XENON1T". In: *Phys. Rev. Lett.* 121.11 (2018), p. 111302. DOI: 10.1103/PhysRevLett.121.111302. arXiv: 1805.12562 [astro-ph.CO].

[14] Thomas Hugle, Moritz Platscher, and Kai Schmitz. "Low-Scale Leptogenesis in the Scotogenic Neutrino Mass Model". In: *Phys. Rev.* D98.2 (2018), p. 023020. DOI: 10.1103/PhysRevD.98.023020. arXiv: 1804.09660 [hep-ph].

[15] Edwin Hubble. "A relation between distance and radial velocity among extra-galactic nebulae". In: *Proc. Nat. Acad. Sci.* 15 (1929), pp. 168–173. DOI: 10.1073/pnas.15.3.168.

[16] Arno A. Penzias and Robert Woodrow Wilson. "A Measurement of excess antenna temperature at 4080-Mc/s". In: *Astrophys. J.* 142 (1965), pp. 419–421. DOI: 10.1086/148307.

[17] R. H. Dicke et al. "Cosmic Black-Body Radiation". In: *Astrophys. J.* 142 (1965), pp. 414–419. DOI: 10.1086/148306.

[18] A. Friedman. "On the Curvature of space". In: *Z. Phys.* 10 (1922). [Gen. Rel. Grav.31,1991(1999)], pp. 377–386. DOI: 10.1007/BF01332580.

[19] Georges Lemaitre. "A Homogeneous Universe of Constant Mass and Growing Radius Accounting for the Radial Velocity of Extragalactic Nebulae". In: *Annales Soc. Sci. Bruxelles A* 47 (1927). [Gen. Rel. Grav.45,no.8,1635(2013)], pp. 49–59. DOI: 10.1007/s10714-013-1548-3.

[20] R. A. Alpher, H. Bethe, and G. Gamow. "The origin of chemical elements". In: *Phys. Rev.* 73 (1948), pp. 803–804. DOI: 10.1103/PhysRev.73.803.

[21] G. Gamow. "Expanding universe and the origin of elements". In: *Phys. Rev.* 70 (1946), pp. 572–573. DOI: 10.1103/PhysRev7.0.572.

[22] C. S. Wu et al. "Experimental Test of Parity Conservation in Beta Decay". In: *Phys. Rev.* 105 (1957), pp. 1413–1414. DOI: 10.1103/PhysRev.105.1413.

[23] J. H. Christenson et al. "Evidence for the 2π Decay of the K_2^0 Meson". In: *Phys. Rev. Lett.* 13 (1964), pp. 138–140. DOI: 10.1103/PhysRevLett.13.138.

[24] A. D. Sakharov. "Violation of CP Invariance, C asymmetry, and baryon asymmetry of the universe". In: *Pisma Zh. Eksp. Teor. Fiz.* 5 (1967). [JETP Lett.5,24(1967); Sov. Phys. Usp.34,no.5,392(1991); Usp. Fiz. Nauk161,no.5,61(1991)], pp. 32–35. DOI: 10.1070/PU1991v034n05ABEH002497.

[25] M. Fukugita and T. Yanagida. "Baryogenesis Without Grand Unification". In: *Phys. Lett.* B174 (1986), pp. 45–47. DOI: 10.1016/0370-2693(86)91126-3.

[26] Peter Minkowski. "$\mu \to e\gamma$ at a Rate of One Out of 10^9 Muon Decays?" In: *Phys. Lett.* 67B (1977), pp. 421–428. DOI: 10.1016/0370-2693(77)90435-X.

[27] Tsutomu Yanagida. "Horizontal Symmetry and Masses of Neutrinos". In: *Conf. Proc.* C7902131 (1979), pp. 95–99.

[28] Tsutomu Yanagida. "Horizontal Symmetry and Masses of Neutrinos". In: *Prog. Theor. Phys.* 64 (1980), p. 1103. DOI: 10.1143/PTP.64.1103.

[29] Murray Gell-Mann, Pierre Ramond, and Richard Slansky. "Complex Spinors and Unified Theories". In: *Conf. Proc.* C790927 (1979), pp. 315–321. arXiv: 1306.4669 [hep-th].

[30] Rabindra N. Mohapatra and Goran Senjanovic. "Neutrino Mass and Spontaneous Parity Violation". In: *Phys. Rev. Lett.* 44 (1980). [,231(1979)], p. 912. DOI: 10.1103/PhysRevLett.44.912.

[31] Sacha Davidson and Alejandro Ibarra. "A Lower bound on the right-handed neutrino mass from leptogenesis". In: *Phys. Lett.* B535 (2002), pp. 25–32. DOI: 10.1016/S0370-2693(02)01735-5. arXiv: hep-ph/0202239 [hep-ph].

[32] W. Buchmuller, P. Di Bari, and M. Plumacher. "Cosmic microwave background, matter - antimatter asymmetry and neutrino masses". In: *Nucl. Phys.* B643 (2002). [Erratum: Nucl. Phys.B793,362(2008)], pp. 367–390. DOI: 10.1016/S0550-3213(02)00737-X,10.1016/j.nuclphysb.2007.11.030. arXiv: hep-ph/0205349 [hep-ph].

[33] G. F. Giudice et al. "Towards a complete theory of thermal leptogenesis in the SM and MSSM". In: *Nucl. Phys.* B685 (2004), pp. 89–149. DOI: 10.1016/j.nuclphysb.2004.02.019. arXiv: hep-ph/0310123 [hep-ph].

[34] W. Buchmuller, P. Di Bari, and M. Plumacher. "Leptogenesis for pedestrians". In: *Annals Phys.* 315 (2005), pp. 305–351. DOI: 10.1016/j.aop.2004.02.003. arXiv: hep-ph/0401240 [hep-ph].

[35] Thomas Hambye et al. "Constraints on neutrino masses from leptogenesis models". In: *Nucl. Phys.* B695 (2004), pp. 169–191. DOI: 10.1016/j.nuclphysb.2004.06.027. arXiv: hep-ph/0312203 [hep-ph].

[36] Steve Blanchet and Pasquale Di Bari. "New aspects of leptogenesis bounds". In: *Nucl. Phys.* B807 (2009), pp. 155–187. DOI: 10.1016/j.nuclphysb.2008.08.026. arXiv: 0807.0743 [hep-ph].

[37] Stefan Antusch et al. "Non-unitary Leptonic Mixing and Leptogenesis". In: *JHEP* 01 (2010), p. 017. DOI: 10.1007/JHEP01(2010)017. arXiv: 0910.5957 [hep-ph].

[38] K. Moffat et al. "Three-flavored nonresonant leptogenesis at intermediate scales". In: *Phys. Rev.* D98.1 (2018), p. 015036. DOI: 10.1103/PhysRevD.98.015036. arXiv: 1804.05066 [hep-ph].

[39] Eldad Gildener. "Gauge Symmetry Hierarchies". In: *Phys. Rev.* D14 (1976), p. 1667. DOI: 10.1103/PhysRevD.14.1667.

[40] Francesco Vissani. "Do experiments suggest a hierarchy problem?" In: *Phys. Rev.* D57 (1998), pp. 7027–7030. DOI: 10.1103/PhysRevD.57.7027. arXiv: hep-ph/9709409 [hep-ph].

[41] Frank F. Deppisch, Julia Harz, and Martin Hirsch. "Falsifying High-Scale Leptogenesis at the LHC". In: *Phys. Rev. Lett.* 112 (2014), p. 221601. DOI: 10.1103/PhysRevLett.112.221601. arXiv: 1312.4447 [hep-ph].

[42] Frank F. Deppisch et al. "Falsifying High-Scale Baryogenesis with Neutrinoless Double Beta Decay and Lepton Flavor Violation". In: *Phys. Rev.* D92.3 (2015), p. 036005. DOI: 10.1103/PhysRevD.92.036005. arXiv: 1503.04825 [hep-ph].

[43] Julia Harz, Wei-Chih Huang, and Heinrich Päs. "Lepton Number Violation and the Baryon Asymmetry of the Universe". In: *Int. J. Mod. Phys.* A30.17 (2015). [Adv. Ser. Direct. High Energy Phys.25,207(2015)], p. 1530045. DOI: 10.1142/S0217751X15300458,10.1142/9789814704779_0022. arXiv: 1505.07632 [hep-ph].

[44] Apostolos Pilaftsis. "CP violation and baryogenesis due to heavy Majorana neutrinos". In: *Phys. Rev.* D56 (1997), pp. 5431–5451. DOI: 10.1103/PhysRevD.56.5431. arXiv: hep-ph/9707235 [hep-ph].

[45] Apostolos Pilaftsis and Thomas E. J. Underwood. "Resonant leptogenesis". In: *Nucl. Phys.* B692 (2004), pp. 303–345. DOI: 10.1016/j.nuclphysb.2004.05.029. arXiv: hep-ph/0309342 [hep-ph].

[46] Evgeny K. Akhmedov, V. A. Rubakov, and A. Yu. Smirnov. "Baryogenesis via neutrino oscillations". In: *Phys. Rev. Lett.* 81 (1998), pp. 1359–1362. DOI: 10.1103/PhysRevLett.81.1359. arXiv: hep-ph/9803255 [hep-ph].

[47] Ernest Ma. "Verifiable radiative seesaw mechanism of neutrino mass and dark matter". In: *Phys. Rev.* D73 (2006), p. 077301. DOI: 10.1103/PhysRevD.73.077301. arXiv: hep-ph/0601225 [hep-ph].

[48] Jisuke Kubo, Ernest Ma, and Daijiro Suematsu. "Cold Dark Matter, Radiative Neutrino Mass, $\mu \to e\gamma$, and Neutrinoless Double Beta Decay". In: *Phys. Lett.* B642 (2006), pp. 18–23. DOI: 10.1016/j.physletb.2006.08.085. arXiv: hep-ph/0604114 [hep-ph].

[49] D. Aristizabal Sierra et al. "Radiative seesaw: Warm dark matter, collider and lepton flavour violating signals". In: *Phys. Rev.* D79 (2009), p. 013011. DOI: 10.1103/PhysRevD.79.013011. arXiv: 0808.3340 [hep-ph].

[50] Daijiro Suematsu, Takashi Toma, and Tetsuro Yoshida. "Reconciliation of CDM abundance and mu —> e gamma in a radiative seesaw model". In: *Phys. Rev.* D79 (2009), p. 093004. DOI: 10.1103/PhysRevD.79.093004. arXiv: 0903.0287 [hep-ph].

[51] Laura Lopez Honorez et al. "The Inert Doublet Model: An Archetype for Dark Matter". In: *JCAP* 0702 (2007), p. 028. DOI: 10.1088/1475-7516/2007/02/028. arXiv: hep-ph/0612275 [hep-ph].

[52] T. Hambye et al. "Scalar Multiplet Dark Matter". In: *JHEP* 07 (2009). [Erratum: JHEP05,066(2010)], p. 090. DOI: 10.1007/JHEP05(2010)066,10.1088/1126-6708/2009/07/090. arXiv: 0903.4010 [hep-ph].

[53] Ethan M. Dolle and Shufang Su. "The Inert Dark Matter". In: *Phys. Rev.* D80 (2009), p. 055012. DOI: 10.1103/PhysRevD.80.055012. arXiv: 0906.1609 [hep-ph].

[54] Laura Lopez Honorez and Carlos E. Yaguna. "The inert doublet model of dark matter revisited". In: *JHEP* 09 (2010), p. 046. DOI: 10.1007/JHEP09(2010)046. arXiv: 1003.3125 [hep-ph].

[55] A. Goudelis, B. Herrmann, and O. Stål. "Dark matter in the Inert Doublet Model after the discovery of a Higgs-like boson at the LHC". In: *JHEP* 09 (2013), p. 106. DOI: 10.1007/JHEP09(2013)106. arXiv: 1303.3010 [hep-ph].

[56] Maria Krawczyk et al. "Constraining Inert Dark Matter by $R_{\gamma\gamma}$ and WMAP data". In: *JHEP* 09 (2013), p. 055. DOI: 10.1007/JHEP09(2013)055. arXiv: 1305.6266 [hep-ph].

[57] Marco Aurelio Díaz, Benjamin Koch, and Sebastián Urrutia-Quiroga. "Constraints to Dark Matter from Inert Higgs Doublet Model". In: *Adv. High Energy Phys.* 2016 (2016), p. 8278375. DOI: 10.1155/2016/8278375. arXiv: 1511.04429 [hep-ph].

[58] Camilo Garcia-Cely, Michael Gustafsson, and Alejandro Ibarra. "Probing the Inert Doublet Dark Matter Model with Cherenkov Telescopes". In: *JCAP* 1602.02 (2016), p. 043. DOI: 10.1088/1475-7516/2016/02/043. arXiv: 1512.02801 [hep-ph].

[59] Debasish Borah and Aritra Gupta. "New viable region of an inert Higgs doublet dark matter model with scotogenic extension". In: *Phys. Rev.* D96.11 (2017), p. 115012. DOI: 10.1103/PhysRevD.96.115012. arXiv: 1706.05034 [hep-ph].

[60] Ernest Ma. "Common origin of neutrino mass, dark matter, and baryogenesis". In: *Mod. Phys. Lett.* A21 (2006), pp. 1777–1782. DOI: 10.1142/S0217732306021141. arXiv: hep-ph/0605180 [hep-ph].

[61] Adisorn Adulpravitchai, Manfred Lindner, and Alexander Merle. "Confronting Flavour Symmetries and extended Scalar Sectors with Lepton Flavour Violation Bounds". In: *Phys. Rev.* D80 (2009), p. 055031. DOI: 10.1103/PhysRevD.80.055031. arXiv: 0907.2147 [hep-ph].

[62] Takashi Toma and Avelino Vicente. "Lepton Flavor Violation in the Scotogenic Model". In: *JHEP* 01 (2014), p. 160. DOI: 10.1007/JHEP01(2014)160. arXiv: 1312.2840 [hep-ph].

[63] Avelino Vicente and Carlos E. Yaguna. "Probing the scotogenic model with lepton flavor violating processes". In: *JHEP* 02 (2015), p. 144. DOI: 10.1007/JHEP02(2015)144. arXiv: 1412.2545 [hep-ph].

[64] Alexander Merle and Moritz Platscher. "Running of radiative neutrino masses: the scotogenic model — revisited". In: *JHEP* 11 (2015), p. 148. DOI: 10.1007/JHEP11(2015)148. arXiv: 1507.06314 [hep-ph].

[65] Gerard 't Hooft. "Naturalness, chiral symmetry, and spontaneous chiral symmetry breaking". In: *NATO Sci. Ser. B* 59 (1980), pp. 135–157. DOI: 10.1007/978-1-4684-7571-5_9.

[66] J.A. Casas and A. Ibarra. "Oscillating neutrinos and $\mu \to e\gamma$". In: *Nucl.Phys.* B618 (2001), pp. 171–204. DOI: 10.1016/S0550-3213(01)00475-8. arXiv: hep-ph/0103065 [hep-ph].

[67] B. Pontecorvo. "Inverse beta processes and nonconservation of lepton charge". In: *Sov. Phys. JETP* 7 (1958). [Zh. Eksp. Teor. Fiz.34,247(1957)], pp. 172–173.

[68] Ziro Maki, Masami Nakagawa, and Shoichi Sakata. "Remarks on the unified model of elementary particles". In: *Prog. Theor. Phys.* 28 (1962), pp. 870–880. DOI: 10.1143/PTP.28.870.

[69] Daijiro Suematsu. "Thermal Leptogenesis in a TeV Scale Model for Neutrino Masses". In: *Eur. Phys. J.* C72 (2012), p. 1951. DOI: 10.1140/epjc/s10052-012-1951-z. arXiv: 1103.0857 [hep-ph].

[70] Shoichi Kashiwase and Daijiro Suematsu. "Baryon number asymmetry and dark matter in the neutrino mass model with an inert doublet". In: *Phys. Rev.* D86 (2012), p. 053001. DOI: 10.1103/PhysRevD.86.053001. arXiv: 1207.2594 [hep-ph].

[71] Shoichi Kashiwase and Daijiro Suematsu. "Leptogenesis and dark matter detection in a TeV scale neutrino mass model with inverted mass hierarchy". In: *Eur. Phys. J.* C73 (2013), p. 2484. DOI: 10.1140/epjc/s10052-013-2484-9. arXiv: 1301.2087 [hep-ph].

[72] J. Racker. "Mass bounds for baryogenesis from particle decays and the inert doublet model". In: *JCAP* 1403 (2014), p. 025. DOI: 10.1088/1475-7516/2014/03/025. arXiv: 1308.1840 [hep-ph].

[73] Jackson D. Clarke, Robert Foot, and Raymond R. Volkas. "Natural leptogenesis and neutrino masses with two Higgs doublets". In: *Phys. Rev.* D92.3 (2015), p. 033006. DOI: 10.1103/PhysRevD.92.033006. arXiv: 1505.05744 [hep-ph].

[74] Yi Cai et al. "From the trees to the forest: a review of radiative neutrino mass models". In: *Front.in Phys.* 5 (2017), p. 63. DOI: 10.3389/fphy.2017.00063. arXiv: 1706.08524 [hep-ph].

[75] Mark Trodden. "Baryogenesis and leptogenesis". In: *eConf* C040802 (2004), p. L018. arXiv: hep-ph/0411301.

[76] M. A. Luty. "Baryogenesis via leptogenesis". In: *Phys. Rev.* D45 (1992), pp. 455–465. DOI: 10.1103/PhysRevD.45.455.

[77] Michael Plumacher. "Baryogenesis and lepton number violation". In: *Z. Phys.* C74 (1997), pp. 549–559. DOI: 10.1007/s002880050418. arXiv: hep-ph/9604229 [hep-ph].

[78] Clemens P. Kiessig, Michael Plumacher, and Markus H. Thoma. "Decay of a Yukawa fermion at finite temperature and applications to leptogenesis". In: *Phys. Rev.* D82 (2010), p. 036007. DOI: 10.1103/PhysRevD.82.036007. arXiv: 1003.3016 [hep-ph].

[79] Steve Blanchet et al. "Leptogenesis with heavy neutrino flavours: from density matrix to Boltzmann equations". In: *JCAP* 1301 (2013), p. 041. DOI: 10.1088/1475-7516/2013/01/041. arXiv: 1112.4528 [hep-ph].

[80] Stefan Antusch et al. "A fuller flavour treatment of N_2-dominated leptogenesis". In: *Nucl. Phys.* B856 (2012), pp. 180–209. DOI: 10.1016/j.nuclphysb.2011.10.036. arXiv: 1003.5132 [hep-ph].

[81] Wilfried Buchmuller and Stefan Fredenhagen. "Quantum mechanics of baryogenesis". In: *Phys. Lett.* B483 (2000), pp. 217–224. DOI: 10.1016/S0370-2693(00)00573-6. arXiv: hep-ph/0004145 [hep-ph].

[82] Andrea De Simone and Antonio Riotto. "Quantum Boltzmann Equations and Leptogenesis". In: *JCAP* 0708 (2007), p. 002. DOI: 10.1088/1475-7516/2007/08/002. arXiv: hep-ph/0703175 [hep-ph].

[83] Laura Covi, Esteban Roulet, and Francesco Vissani. "CP violating decays in leptogenesis scenarios". In: *Phys. Lett.* B384 (1996), pp. 169–174. DOI: 10.1016/0370-2693(96)00817-9. arXiv: hep-ph/9605319 [hep-ph].

[84] A. Ibarra and Graham G. Ross. "Neutrino phenomenology: The Case of two right-handed neutrinos". In: *Phys. Lett.* B591 (2004), pp. 285–296. DOI: 10.1016/j.physletb.2004.04.037. arXiv: hep-ph/0312138 [hep-ph].

[85] Juan Racker and E. Roulet. "Leptogenesis, Z-prime bosons, and the reheating temperature of the Universe". In: *JHEP* 03 (2009), p. 065. DOI: 10.1088/1126-6708/2009/03/065. arXiv: 0812.4285 [hep-ph].

[86] J. Racker. "Mini-review on baryogenesis at the TeV scale and possible connections with dark matter". In: *Nucl. Part. Phys. Proc.* 273-275 (2016), pp. 334–339. DOI: 10.1016/j.nuclphysbps.2015.09.047. arXiv: 1410.5482 [hep-ph].

[87] E. Aprile et al. "Implications on Inelastic Dark Matter from 100 Live Days of XENON100 Data". In: *Phys. Rev.* D84 (2011), p. 061101. DOI: 10.1103/PhysRevD.84.061101. arXiv: 1104.3121 [astro-ph.CO].

[88] Michela D'Onofrio, Kari Rummukainen, and Anders Tranberg. "Sphaleron Rate in the Minimal Standard Model". In: *Phys. Rev. Lett.* 113.14 (2014), p. 141602. DOI: 10.1103/PhysRevLett.113.141602. arXiv: 1404.3565 [hep-ph].

[89] A. Osipowicz et al. "KATRIN: A Next generation tritium beta decay experiment with sub-eV sensitivity for the electron neutrino mass. Letter of intent". In: (2001). arXiv: hep-ex/0109033 [hep-ex].

[90] M. Aker et al. "Improved Upper Limit on the Neutrino Mass from a Direct Kinematic Method by KATRIN". In: *Phys. Rev. Lett.* 123.22 (2019), p. 221802. DOI: 10.1103/PhysRevLett.123.221802. arXiv: 1909.06048 [hep-ex].

[91] Antonio J. Cuesta, Viviana Niro, and Licia Verde. "Neutrino mass limits: robust information from the power spectrum of galaxy surveys". In: *Phys. Dark Univ.* 13 (2016), pp. 77–86. DOI: 10.1016/j.dark.2016.04.005. arXiv: 1511.05983 [astro-ph.CO].

[92] Tommi Alanne et al. "Low-scale leptogenesis assisted by a real scalar singlet". In: *JCAP* 1903.03 (2019), p. 037. DOI: 10.1088/1475-7516/2019/03/037. arXiv: 1812.04421 [hep-ph].

[93] Diego Aristizabal Sierra et al. "Leptogenesis with a dynamical seesaw scale". In: *JCAP* 1407 (2014), p. 052. DOI: 10.1088/1475-7516/2014/07/052. arXiv: 1405.4706 [hep-ph].

[94] Matthias Le Dall and Adam Ritz. "Leptogenesis and the Higgs Portal". In: *Phys. Rev.* D90.9 (2014), p. 096002. DOI: 10.1103/PhysRevD.90.096002. arXiv: 1408.2498 [hep-ph].

[95] Vanda Silveira and A. Zee. "Scalar phantoms". In: *Phys. Lett.* 161B (1985), pp. 136–140. DOI: 10.1016/0370-2693(85)90624-0.

[96] John McDonald. "Gauge singlet scalars as cold dark matter". In: *Phys. Rev.* D50 (1994), pp. 3637–3649. DOI: 10.1103/PhysRevD.50.3637. arXiv: hep-ph/0702143 [HEP-PH].

[97] C. P. Burgess, Maxim Pospelov, and Tonnis ter Veldhuis. "The Minimal model of nonbaryonic dark matter: A Singlet scalar". In: *Nucl. Phys.* B619 (2001), pp. 709–728. DOI: 10.1016/S0550-3213(01)00513-2. arXiv: hep-ph/0011335 [hep-ph].

[98] Peter Athron et al. "Status of the scalar singlet dark matter model". In: *Eur. Phys. J.* C77.8 (2017), p. 568. DOI: 10.1140/epjc/s10052-017-5113-1. arXiv: 1705.07931 [hep-ph].

[99] Rose Natalie Lerner and John McDonald. "Gauge singlet scalar as inflaton and thermal relic dark matter". In: *Phys. Rev.* D80 (2009), p. 123507. DOI: 10.1103/PhysRevD.80.123507. arXiv: 0909.0520 [hep-ph].

[100] Felix Kahlhoefer and John McDonald. "WIMP Dark Matter and Unitarity-Conserving Inflation via a Gauge Singlet Scalar". In: *JCAP* 1511.11 (2015), p. 015. DOI: 10.1088/1475-7516/2015/11/015. arXiv: 1507.03600 [astro-ph.CO].

[101] Tommi Tenkanen, Kimmo Tuominen, and Ville Vaskonen. "A Strong Electroweak Phase Transition from the Inflaton Field". In: *JCAP* 1609.09 (2016), p. 037. DOI: 10.1088/1475-7516/2016/09/037. arXiv: 1606.06063 [hep-ph].

[102] Yohei Ema et al. "Higgs-Inflaton Mixing and Vacuum Stability". In: (2017). arXiv: 1711.10554 [hep-ph].

[103] Kari Enqvist et al. "Standard Model with a real singlet scalar and inflation". In: *JCAP* 1408 (2014), p. 035. DOI: 10.1088/1475-7516/2014/08/035. arXiv: 1407.0659 [astro-ph.CO].

[104] John McDonald. "Electroweak baryogenesis and dark matter via a gauge singlet scalar". In: *Phys. Lett.* B323 (1994), pp. 339–346. DOI: 10.1016/0370-2693(94)91229-7.

[105] Stefano Profumo, Michael J. Ramsey-Musolf, and Gabe Shaughnessy. "Singlet Higgs phenomenology and the electroweak phase transition". In: *JHEP* 08 (2007), p. 010. DOI: 10.1088/1126-6708/2007/08/010. arXiv: 0705.2425 [hep-ph].

[106] Vernon Barger et al. "Complex Singlet Extension of the Standard Model". In: *Phys. Rev.* D79 (2009), p. 015018. DOI: 10.1103/PhysRevD.79.015018. arXiv: 0811.0393 [hep-ph].

[107] Jose R. Espinosa, Thomas Konstandin, and Francesco Riva. "Strong Electroweak Phase Transitions in the Standard Model with a Singlet". In: *Nucl. Phys.* B854 (2012), pp. 592–630. DOI: 10.1016/j.nuclphysb.2011.09.010. arXiv: 1107.5441 [hep-ph].

[108] James M. Cline and Kimmo Kainulainen. "Electroweak baryogenesis and dark matter from a singlet Higgs". In: *JCAP* 1301 (2013), p. 012. DOI: 10.1088/1475-7516/2013/01/012. arXiv: 1210.4196 [hep-ph].

[109] Tommi Alanne, Kimmo Tuominen, and Ville Vaskonen. "Strong phase transition, dark matter and vacuum stability from simple hidden sectors". In: *Nucl. Phys.* B889 (2014), pp. 692–711. DOI: 10.1016/j.nuclphysb.2014.11.001. arXiv: 1407.0688 [hep-ph].

[110] Tommi Alanne, Aurora Meroni, and Kimmo Tuominen. "Neutrino mass generation and leptogenesis via pseudo-Nambu-Goldstone Higgs portal". In: *Phys. Rev.* D96.9 (2017), p. 095015. DOI: 10.1103/PhysRevD.96.095015. arXiv: 1706.10128 [hep-ph].

[111] Oleg Lebedev. "On Stability of the Electroweak Vacuum and the Higgs Portal". In: *Eur. Phys. J.* C72 (2012), p. 2058. DOI: 10.1140/epjc/s10052-012-2058-2. arXiv: 1203.0156 [hep-ph].

[112] Joan Elias-Miro et al. "Stabilization of the Electroweak Vacuum by a Scalar Threshold Effect". In: *JHEP* 06 (2012), p. 031. DOI: 10.1007/JHEP06(2012)031. arXiv: 1203.0237 [hep-ph].

[113] Vernon Barger et al. "LHC Phenomenology of an Extended Standard Model with a Real Scalar Singlet". In: *Phys. Rev.* D77 (2008), p. 035005. DOI: 10.1103/PhysRevD.77.035005. arXiv: 0706.4311 [hep-ph].

[114] Tania Robens and Tim Stefaniak. "Status of the Higgs Singlet Extension of the Standard Model after LHC Run 1". In: *Eur. Phys. J.* C75 (2015), p. 104. DOI: 10.1140/epjc/s10052-015-3323-y. arXiv: 1501.02234 [hep-ph].

[115] Víctor Martín Lozano, Jesús M. Moreno, and Chan Beom Park. "Resonant Higgs boson pair production in the $hh \to b\bar{b}\, WW \to b\bar{b}\ell^+\nu\ell^-\overline{\nu}$ decay channel". In: *JHEP* 08 (2015), p. 004. DOI: 10.1007/JHEP08(2015)004. arXiv: 1501.03799 [hep-ph].

[116] Adam Falkowski, Christian Gross, and Oleg Lebedev. "A second Higgs from the Higgs portal". In: *JHEP* 05 (2015), p. 057. DOI: 10.1007/JHEP05(2015)057. arXiv: 1502.01361 [hep-ph].

[117] Dario Buttazzo, Filippo Sala, and Andrea Tesi. "Singlet-like Higgs bosons at present and future colliders". In: *JHEP* 11 (2015), p. 158. DOI: 10.1007/JHEP11(2015)158. arXiv: 1505.05488 [hep-ph].

[118] J. M. No and M. Spannowsky. "Signs of heavy Higgs bosons at CLIC: An e^+e^- road to the Electroweak Phase Transition". In: (2018). arXiv: 1807.04284 [hep-ph].

[119] Dario Buttazzo et al. "Fusing Vectors into Scalars at High Energy Lepton Colliders". In: *JHEP* 11 (2018), p. 144. DOI: 10.1007/JHEP11(2018)144. arXiv: 1807.04743 [hep-ph].

[120] Pasquale Di Bari. "Seesaw geometry and leptogenesis". In: *Nucl. Phys.* B727 (2005), pp. 318–354. DOI: 10.1016/j.nuclphysb.2005.08.032. arXiv: hep-ph/0502082 [hep-ph].

[121] Ivan Esteban et al. "Global analysis of three-flavour neutrino oscillations: synergies and tensions in the determination of $\theta_2 3$, $\delta_{\rm CP}$, and the mass ordering". In: (2018). arXiv: 1811.05487 [hep-ph].

[122] Michael E. Peskin and Daniel V. Schroeder. *An Introduction to quantum field theory*. Reading, USA: Addison-Wesley, 1995. ISBN: 9780201503975, 0201503972. URL: http://www.slac.stanford.edu/~mpeskin/QFT.html.

[123] Steve Blanchet and Pasquale Di Bari. "Leptogenesis beyond the limit of hierarchical heavy neutrino masses". In: *JCAP* 0606 (2006), p. 023. DOI: 10.1088/1475-7516/2006/06/023. arXiv: hep-ph/0603107 [hep-ph].

[124] Mark D. Goodsell and Florian Staub. "Unitarity constraints on general scalar couplings with SARAH". In: *Eur. Phys. J.* C78.8 (2018), p. 649. DOI: 10.1140/epjc/s10052-018-6127-z. arXiv: 1805.07306 [hep-ph].

[125] Agnieszka Ilnicka, Tania Robens, and Tim Stefaniak. "Constraining Extended Scalar Sectors at the LHC and beyond". In: *Mod. Phys. Lett.* A33.10n11 (2018), p. 1830007. DOI: 10.1142/S0217732318300070. arXiv: 1803.03594 [hep-ph].

[126] Albert M Sirunyan et al. "Search for a new scalar resonance decaying to a pair of Z bosons in proton-proton collisions at $\sqrt{s} = 13$ TeV". In: *JHEP* 06 (2018), p. 127. DOI: 10.1007/JHEP06(2018)127. arXiv: 1804.01939 [hep-ex].

[127] Georges Aad et al. "Constraints on new phenomena via Higgs boson couplings and invisible decays with the ATLAS detector". In: *JHEP* 11 (2015), p. 206. DOI: 10.1007/JHEP11(2015)206. arXiv: 1509.00672 [hep-ex].

[128] Vardan Khachatryan et al. "Searches for invisible decays of the Higgs boson in pp collisions at $\sqrt{s} = 7$, 8, and 13 TeV". In: *JHEP* 02 (2017), p. 135. DOI: 10.1007/JHEP02(2017)135. arXiv: 1610.09218 [hep-ex].

[129] S. Dittmaier et al. "Handbook of LHC Higgs Cross Sections: 1. Inclusive Observables". In: (2011). DOI: 10.5170/CERN-2011-002. arXiv: 1101.0593 [hep-ph].

[130] Georges Aad et al. "Observation of a new particle in the search for the Standard Model Higgs boson with the ATLAS detector at the LHC". In: *Phys. Lett.* B716 (2012), pp. 1–29. DOI: 10.1016/j.physletb.2012.08.020. arXiv: 1207.7214 [hep-ex].

[131] Serguei Chatrchyan et al. "Observation of a New Boson at a Mass of 125 GeV with the CMS Experiment at the LHC". In: *Phys. Lett.* B716 (2012), pp. 30–61. DOI: 10.1016/j.physletb.2012.08.021. arXiv: 1207.7235 [hep-ex].

[132] Felix Kahlhoefer. "Review of LHC Dark Matter Searches". In: *Int. J. Mod. Phys.* A32.13 (2017), p. 1730006. DOI: 10.1142/S0217751X1730006X. arXiv: 1702.02430 [hep-ph].

[133] Gianfranco Bertone, Dan Hooper, and Joseph Silk. "Particle dark matter: Evidence, candidates and constraints". In: *Phys. Rept.* 405 (2005), pp. 279–390. DOI: 10.1016/j.physrep.2004.08.031. arXiv: hep-ph/0404175 [hep-ph].

[134] Tomohiro Abe et al. "LHC Dark Matter Working Group: Next-generation spin-0 dark matter models". In: *Phys. Dark Univ.* 27 (2020), p. 100351. DOI: 10.1016/j.dark.2019.100351. arXiv: 1810.09420 [hep-ex].

[135] Georges Aad et al. "Summary of the ATLAS experiment's sensitivity to supersymmetry after LHC Run 1 — interpreted in the phenomenological MSSM". In: *JHEP* 10 (2015), p. 134. DOI: 10.1007/JHEP10(2015)134. arXiv: 1508.06608 [hep-ex].

[136] Qing-Hong Cao et al. "Effective Dark Matter Model: Relic density, CDMS II, Fermi LAT and LHC". In: *JHEP* 08 (2011), p. 018. DOI: 10.1007/JHEP08(2011)018. arXiv: 0912.4511 [hep-ph].

[137] Maria Beltran et al. "Maverick dark matter at colliders". In: *JHEP* 09 (2010), p. 037. DOI: 10.1007/JHEP09(2010)037. arXiv: 1002.4137 [hep-ph].

[138] Jessica Goodman et al. "Constraints on Light Majorana dark Matter from Colliders". In: *Phys. Lett.* B695 (2011), pp. 185–188. DOI: 10.1016/j.physletb.2010.11.009. arXiv: 1005.1286 [hep-ph].

[139] Yang Bai, Patrick J. Fox, and Roni Harnik. "The Tevatron at the Frontier of Dark Matter Direct Detection". In: *JHEP* 12 (2010), p. 048. DOI: 10.1007/JHEP12(2010)048. arXiv: 1005.3797 [hep-ph].

[140] Jessica Goodman et al. "Constraints on Dark Matter from Colliders". In: *Phys. Rev.* D82 (2010), p. 116010. DOI: 10.1103/PhysRevD.82.116010. arXiv: 1008.1783 [hep-ph].

[141] Patrick J. Fox et al. "Missing Energy Signatures of Dark Matter at the LHC". In: *Phys. Rev.* D85 (2012), p. 056011. DOI: 10.1103/PhysRevD.85.056011. arXiv: 1109.4398 [hep-ph].

[142] Nicole F. Bell, Giorgio Busoni, and Isaac W. Sanderson. "Two Higgs Doublet Dark Matter Portal". In: *JCAP* 1801 (2018), p. 015. DOI: 10.1088/1475-7516/2018/01/015. arXiv: 1710.10764 [hep-ph].

[143] Giorgio Busoni et al. "On the Validity of the Effective Field Theory for Dark Matter Searches at the LHC". In: *Phys. Lett.* B728 (2014), pp. 412–421. DOI: 10.1016/j.physletb.2013.11.069. arXiv: 1307.2253 [hep-ph].

[144] Giorgio Busoni et al. "On the Validity of the Effective Field Theory for Dark Matter Searches at the LHC, Part II: Complete Analysis for the s-channel". In: *JCAP* 1406 (2014), p. 060. DOI: 10.1088/1475-7516/2014/06/060. arXiv: 1402.1275 [hep-ph].

[145] Giorgio Busoni et al. "On the Validity of the Effective Field Theory for Dark Matter Searches at the LHC Part III: Analysis for the t-channel". In: *JCAP* 1409 (2014), p. 022. DOI: 10.1088/1475-7516/2014/09/022. arXiv: 1405.3101 [hep-ph].

[146] O. Buchmueller, Matthew J. Dolan, and Christopher McCabe. "Beyond Effective Field Theory for Dark Matter Searches at the LHC". In: *JHEP* 01 (2014), p. 025. DOI: 10.1007/JHEP01(2014)025. arXiv: 1308.6799 [hep-ph].

[147] Ian M. Shoemaker and Luca Vecchi. "Unitarity and Monojet Bounds on Models for DAMA, CoGeNT, and CRESST-II". In: *Phys. Rev.* D86 (2012), p. 015023. DOI: 10.1103/PhysRevD.86.015023. arXiv: 1112.5457 [hep-ph].

[148] Jalal Abdallah et al. "Simplified Models for Dark Matter and Missing Energy Searches at the LHC". In: (2014). arXiv: 1409.2893 [hep-ph].

[149] Jalal Abdallah et al. "Simplified Models for Dark Matter Searches at the LHC". In: *Phys. Dark Univ.* 9-10 (2015), pp. 8–23. DOI: 10.1016/j.dark.2015.08.001. arXiv: 1506.03116 [hep-ph].

[150] Giorgio Arcadi et al. "The waning of the WIMP? A review of models, searches, and constraints". In: *Eur. Phys. J.* C78.3 (2018), p. 203. DOI: 10.1140/epjc/s10052-018-5662-y. arXiv: 1703.07364 [hep-ph].

[151] Felix Kahlhoefer et al. "Implications of unitarity and gauge invariance for simplified dark matter models". In: *JHEP* 02 (2016), p. 016. DOI: 10.1007/JHEP02(2016)016. arXiv: 1510.02110 [hep-ph].

[152] Nicole F. Bell, Yi Cai, and Rebecca K. Leane. "Impact of Mass Generation for Simplified Dark Matter Models". In: (2016). arXiv: 1610.03063 [hep-ph].

[153] Nicole F. Bell, Giorgio Busoni, and Isaac W. Sanderson. "Self-consistent Dark Matter Simplified Models with an s-channel scalar mediator". In: *JCAP* 1703.03 (2017), p. 015. DOI: 10.1088/1475-7516/2017/03/015. arXiv: 1612.03475 [hep-ph].

[154] Christoph Englert, Matthew McCullough, and Michael Spannowsky. "S-Channel Dark Matter Simplified Models and Unitarity". In: (2016). arXiv: 1604.07975 [hep-ph].

[155] Dorival Goncalves, Pedro A. N. Machado, and Jose Miguel No. "Simplified Models for Dark Matter Face their Consistent Completions". In: *Phys. Rev.* D95.5 (2017), p. 055027. DOI: 10.1103/PhysRevD.95.055027. arXiv: 1611.04593 [hep-ph].

[156] Ulrich Haisch, Felix Kahlhoefer, and Tim M. P. Tait. "On Mono-W Signatures in Spin-1 Simplified Models". In: *Phys. Lett.* B760 (2016), pp. 207–213. DOI: 10.1016/j.physletb.2016.06.063. arXiv: 1603.01267 [hep-ph].

[157] P. Ko et al. "Simplified DM models with the full SM gauge symmetry : the case of t-channel colored scalar mediators". In: *JHEP* 01 (2017), p. 086. DOI: 10.1007/JHEP01(2017)086. arXiv: 1605.07058 [hep-ph].

[158] Jose Miguel No. "Looking through the pseudoscalar portal into dark matter: Novel mono-Higgs and mono-Z signatures at the LHC". In: *Phys. Rev.* D93.3 (2016), p. 031701. DOI: 10.1103/PhysRevD.93.031701. arXiv: 1509.01110 [hep-ph].

[159] Stefan von Buddenbrock et al. "Phenomenological signatures of additional scalar bosons at the LHC". In: *Eur. Phys. J.* C76.10 (2016), p. 580. DOI: 10.1140/epjc/s10052-016-4435-8. arXiv: 1606.01674 [hep-ph].

[160] Martin Bauer, Ulrich Haisch, and Felix Kahlhoefer. "Simplified dark matter models with two Higgs doublets: I. Pseudoscalar mediators". In: (2017). arXiv: 1701.07427 [hep-ph].

[161] Stefan von Buddenbrock et al. "Constraints on a 2HDM with a singlet scalar and implications in the search for heavy bosons at the LHC". In: *J. Phys.* G46.11 (2019), p. 115001. DOI: 10.1088/1361-6471/ab3cf6. arXiv: 1809.06344 [hep-ph].

[162] Giorgio Arcadi et al. "Comparing 2HDM + Scalar and Pseudoscalar Simplified Models at LHC". In: (2020). arXiv: 2001.10540 [hep-ph].

[163] Seyda Ipek, David McKeen, and Ann E. Nelson. "A Renormalizable Model for the Galactic Center Gamma Ray Excess from Dark Matter Annihilation". In: *Phys. Rev.* D90.5 (2014), p. 055021. DOI: 10.1103/PhysRevD.90.055021. arXiv: 1404.3716 [hep-ph].

[164] Nicole F. Bell, Giorgio Busoni, and Isaac W. Sanderson. "Loop Effects in Direct Detection". In: *JCAP* 1808.08 (2018). [Erratum: JCAP1901,no.01,E01(2019)], p. 017. DOI: 10.1088/1475-7516/2018/08/017, 10.1088/1475-7516/2019/01/E01. arXiv: 1803.01574 [hep-ph].

[165] Giorgio Arcadi et al. "Pseudoscalar Mediators: A WIMP model at the Neutrino Floor". In: (2017). arXiv: 1711.02110 [hep-ph].

[166] Giorgio Arcadi. "2HDM portal for Singlet-Doublet Dark Matter". In: *Eur. Phys. J.* C78.10 (2018), p. 864. DOI: 10.1140/epjc/s10052-018-6327-6. arXiv: 1804.04930 [hep-ph].

[167] Sacha Davidson and Howard E. Haber. "Basis-independent methods for the two-Higgs-doublet model". In: *Phys. Rev.* D72 (2005). [Erratum: Phys. Rev.D72,099902(2005)], p. 035004. DOI: 10.1103/PhysRevD.72.099902,10.1103/PhysRevD.72.035004. arXiv: hep-ph/0504050 [hep-ph].

[168] Andreas Trautner. "Systematic construction of basis invariants in the 2HDM". In: *JHEP* 05 (2019), p. 208. DOI: 10.1007/JHEP05(2019)208. arXiv: 1812.02614 [hep-ph].

[169] Igor P. Ivanov, Celso C. Nishi, and Andreas Trautner. "Beyond basis invariants". In: *Eur. Phys. J.* C79.4 (2019), p. 315. DOI: 10.1140/epjc/s10052-019-6845-x. arXiv: 1901.11472 [hep-ph].

[170] Margarete Muhlleitner et al. "The N2HDM under Theoretical and Experimental Scrutiny". In: *JHEP* 03 (2017), p. 094. DOI: 10.1007/JHEP03(2017)094. arXiv: 1612.01309 [hep-ph].

[171] John F. Gunion and Howard E. Haber. "The CP conserving two Higgs doublet model: The Approach to the decoupling limit". In: *Phys. Rev.* D67 (2003), p. 075019. DOI: 10.1103/PhysRevD.67.075019. arXiv: hep-ph/0207010 [hep-ph].

[172] Marcela Carena et al. "Impersonating the Standard Model Higgs Boson: Alignment without Decoupling". In: *JHEP* 04 (2014), p. 015. DOI: 10.1007/JHEP04(2014)015. arXiv: 1310.2248 [hep-ph].

[173] P. S. Bhupal Dev and Apostolos Pilaftsis. "Maximally Symmetric Two Higgs Doublet Model with Natural Standard Model Alignment". In: *JHEP* 12 (2014). [Erratum: JHEP11,147(2015)], p. 024. DOI: 10.1007/JHEP11(2015)147,10.1007/JHEP12(2014)024. arXiv: 1408.3405 [hep-ph].

[174] Antonio Pich and Paula Tuzon. "Yukawa Alignment in the Two-Higgs-Doublet Model". In: *Phys. Rev.* D80 (2009), p. 091702. DOI: 10.1103/PhysRevD.80.091702. arXiv: 0908.1554 [hep-ph].

[175] Paula Tuzon and Antonio Pich. "The Aligned two-Higgs Doublet model". In: *Acta Phys. Polon. Supp.* 3 (2010), pp. 215–220. arXiv: 1001.0293 [hep-ph].

[176] Antonio Pich. "Flavour constraints on multi-Higgs-doublet models: Yukawa alignment". In: *Nucl. Phys. Proc. Suppl.* 209 (2010), pp. 182–187. DOI: 10.1016/j.nuclphysbps.2010.12.030. arXiv: 1010.5217 [hep-ph].

[177] Ana Peñuelas and Antonio Pich. "Flavour alignment in multi-Higgs-doublet models". In: (2017). arXiv: 1710.02040 [hep-ph].

[178] Stefania Gori, Howard E. Haber, and Edward Santos. "High scale flavor alignment in two-Higgs doublet models and its phenomenology". In: *JHEP* 06 (2017), p. 110. DOI: 10.1007/JHEP06(2017)110. arXiv: 1703.05873 [hep-ph].

[179] Werner Rodejohann and Ulises Saldaña-Salazar. "Multi-Higgs-Doublet Models and Singular Alignment". In: *JHEP* 07 (2019), p. 036. DOI: 10.1007/JHEP07(2019)036. arXiv: 1903.00983 [hep-ph].

[180] S. Centelles Chuliá, W. Rodejohann, and U. J. Saldaña-Salazar. "Two-Higgs-Doublet Models with a Flavored $\mathbb{Z}_2$". In: (2019). arXiv: 1911.06824 [hep-ph].

[181] Tetsuya Enomoto and Ryoutaro Watanabe. "Flavor constraints on the Two Higgs Doublet Models of Z_2 symmetric and aligned types". In: *JHEP* 05 (2016), p. 002. DOI: 10.1007/JHEP05(2016)002. arXiv: 1511.05066 [hep-ph].

[182] Marco Cirelli, Eugenio Del Nobile, and Paolo Panci. "Tools for model-independent bounds in direct dark matter searches". In: *JCAP* 1310 (2013), p. 019. DOI: 10.1088/1475-7516/2013/10/019. arXiv: 1307.5955 [hep-ph].

[183] Matthew J. Dolan et al. "A taste of dark matter: Flavour constraints on pseudoscalar mediators". In: *JHEP* 03 (2015). [Erratum: JHEP07,103(2015)], p. 171. DOI: 10.1007/JHEP07(2015)103,10.1007/JHEP03(2015)171. arXiv: 1412.5174 [hep-ph].

[184] Chiara Arina, Eugenio Del Nobile, and Paolo Panci. "Dark Matter with Pseudoscalar-Mediated Interactions Explains the DAMA Signal and the Galactic Center Excess". In: *Phys. Rev. Lett.* 114 (2015), p. 011301. DOI: 10.1103/PhysRevLett.114.011301. arXiv: 1406.5542 [hep-ph].

[185] Tomohiro Abe, Motoko Fujiwara, and Junji Hisano. "Loop corrections to dark matter direct detection in a pseudoscalar mediator dark matter model". In: *JHEP* 02 (2019), p. 028. DOI: 10.1007/JHEP02(2019)028. arXiv: 1810.01039 [hep-ph].

[186] Fatih Ertas and Felix Kahlhoefer. "Loop-induced direct detection signatures from CP-violating scalar mediators". In: *JHEP* 06 (2019), p. 052. DOI: 10.1007/JHEP06(2019)052. arXiv: 1902.11070 [hep-ph].

[187] Tomohiro Abe et al. "Maximum value of the spin-independent cross section in the THDM+a". In: (2019). arXiv: 1910.09771 [hep-ph].

[188] Marat Freytsis and Zoltan Ligeti. "On dark matter models with uniquely spin-dependent detection possibilities". In: *Phys. Rev.* D83 (2011), p. 115009. DOI: 10.1103/PhysRevD.83.115009. arXiv: 1012.5317 [hep-ph].

[189] A. Albert et al. "Searching for Dark Matter Annihilation in Recently Discovered Milky Way Satellites with Fermi-LAT". In: *Astrophys. J.* 834.2 (2017), p. 110. DOI: 10.3847/1538-4357/834/2/110. arXiv: 1611.03184 [astro-ph.HE].

[190] Shinya Kanemura and Kei Yagyu. "Unitarity bound in the most general two Higgs doublet model". In: *Phys. Lett.* B751 (2015), pp. 289–296. DOI: 10.1016/j.physletb.2015.10.047. arXiv: 1509.06060 [hep-ph].

[191] K. G. Klimenko. "On Necessary and Sufficient Conditions for Some Higgs Potentials to Be Bounded From Below". In: *Theor. Math. Phys.* 62 (1985). [Teor. Mat. Fiz.62,87(1985)], pp. 58–65. DOI: 10.1007/BF01034825.

[192] Howard E. Haber and Alex Pomarol. "Constraints from global symmetries on radiative corrections to the Higgs sector". In: *Phys. Lett.* B302 (1993), pp. 435–441. DOI: 10.1016/0370-2693(93)90423-F. arXiv: hep-ph/9207267 [hep-ph].

[193] Alex Pomarol and Roberto Vega. "Constraints on CP violation in the Higgs sector from the rho parameter". In: *Nucl. Phys.* B413 (1994), pp. 3–15. DOI: 10.1016/0550-3213(94)90611-4. arXiv: hep-ph/9305272 [hep-ph].

[194] Riccardo Barbieri, Lawrence J. Hall, and Vyacheslav S. Rychkov. "Improved naturalness with a heavy Higgs: An Alternative road to LHC physics". In: *Phys. Rev.* D74 (2006), p. 015007. DOI: 10.1103/PhysRevD.74.015007. arXiv: hep-ph/0603188 [hep-ph].

[195] J. -M. Gerard and M. Herquet. "A Twisted custodial symmetry in the two-Higgs-doublet model". In: *Phys. Rev. Lett.* 98 (2007), p. 251802. DOI: 10.1103/PhysRevLett.98.251802. arXiv: hep-ph/0703051 [HEP-PH].

[196] B. Grzadkowski, M. Maniatis, and Jose Wudka. "The bilinear formalism and the custodial symmetry in the two-Higgs-doublet model". In: *JHEP* 11 (2011), p. 030. DOI: 10.1007/JHEP11(2011)030. arXiv: 1011.5228 [hep-ph].

[197] Howard E. Haber and Deva O'Neil. "Basis-independent methods for the two-Higgs-doublet model III: The CP-conserving limit, custodial symmetry, and the oblique parameters S, T, U". In: *Phys. Rev.* D83 (2011), p. 055017. DOI: 10.1103/PhysRevD.83.055017. arXiv: 1011.6188 [hep-ph].

[198] Morad Aaboud et al. "Search for dark matter produced in association with bottom or top quarks in $\sqrt{s} = 13$ TeV pp collisions with the ATLAS detector". In: *Eur. Phys. J.* C78.1 (2018), p. 18. DOI: 10.1140/epjc/s10052-017-5486-1. arXiv: 1710.11412 [hep-ex].

[199] Albert M Sirunyan et al. "Search for dark matter produced in association with a single top quark or a top quark pair in proton-proton collisions at $\sqrt{s} = 13$ TeV". In: *JHEP* 03 (2019), p. 141. DOI: 10.1007/JHEP03(2019)141. arXiv: 1901.01553 [hep-ex].

[200] Morad Aaboud et al. "Constraints on mediator-based dark matter and scalar dark energy models using $\sqrt{s} = 13$ TeV *pp* collision data collected by the ATLAS detector". In: *JHEP* 05 (2019), p. 142. DOI: 10.1007/JHEP05(2019)142. arXiv: 1903.01400 [hep-ex].

[201] Daniel Dercks et al. "CheckMATE 2: From the model to the limit". In: *Comput. Phys. Commun.* 221 (2017), pp. 383–418. DOI: 10.1016/j.cpc.2017.08.021. arXiv: 1611.09856 [hep-ph].

[202] Morad Aaboud et al. "Search for dark matter and other new phenomena in events with an energetic jet and large missing transverse momentum using the ATLAS detector". In: (2017). arXiv: 1711.03301 [hep-ex].

[203] Elias Bernreuther et al. "Actual Physics behind Mono-X". In: *SciPost Phys.* 5.4 (2018), p. 034. DOI: 10.21468/SciPostPhys.5.4.034. arXiv: 1805.11637 [hep-ph].

[204] Francesco D'Eramo, Jordy de Vries, and Paolo Panci. "A 750 GeV Portal: LHC Phenomenology and Dark Matter Candidates". In: *JHEP* 05 (2016), p. 089. DOI: 10.1007/JHEP05(2016)089. arXiv: 1601.01571 [hep-ph].

[205] John F. Gunion et al. "The Higgs Hunter's Guide". In: *Front. Phys.* 80 (2000), pp. 1–404.

[206] Giorgio Arcadi, Abdelhak Djouadi, and Martti Raidal. "Dark Matter through the Higgs portal". In: (2019). arXiv: 1903.03616 [hep-ph].

[207] J. Alwall et al. "The automated computation of tree-level and next-to-leading order differential cross sections, and their matching to parton shower simulations". In: *JHEP* 07 (2014), p. 079. DOI: 10.1007/JHEP07(2014)079. arXiv: 1405.0301 [hep-ph].

[208] Valentin Hirschi and Olivier Mattelaer. "Automated event generation for loop-induced processes". In: *JHEP* 10 (2015), p. 146. DOI: 10.1007/JHEP10(2015)146. arXiv: 1507.00020 [hep-ph].

[209] Giovanni Ossola, Costas G. Papadopoulos, and Roberto Pittau. "CutTools: A Program implementing the OPP reduction method to compute one-loop amplitudes". In: *JHEP* 03 (2008), p. 042. DOI: 10.1088/1126-6708/2008/03/042. arXiv: 0711.3596 [hep-ph].

[210] Tiziano Peraro. "Ninja: Automated Integrand Reduction via Laurent Expansion for One-Loop Amplitudes". In: *Comput. Phys. Commun.* 185 (2014), pp. 2771–2797. DOI: 10.1016/j.cpc.2014.06.017. arXiv: 1403.1229 [hep-ph].

[211] Ansgar Denner, Stefan Dittmaier, and Lars Hofer. "Collier: a fortran-based Complex One-Loop LIbrary in Extended Regularizations". In: *Comput. Phys. Commun.* 212 (2017), pp. 220–238. DOI: 10.1016/j.cpc.2016.10.013. arXiv: 1604.06792 [hep-ph].

[212] Jon Butterworth et al. "PDF4LHC recommendations for LHC Run II". In: *J. Phys.* G43 (2016), p. 023001. DOI: 10.1088/0954-3899/43/2/023001. arXiv: 1510.03865 [hep-ph].

[213] Andy Buckley et al. "LHAPDF6: parton density access in the LHC precision era". In: *Eur. Phys. J.* C75 (2015), p. 132. DOI: 10.1140/epjc/s10052-015-3318-8. arXiv: 1412.7420 [hep-ph].

[214] Torbjörn Sjöstrand et al. "An Introduction to PYTHIA 8.2". In: *Comput. Phys. Commun.* 191 (2015), pp. 159–177. DOI: 10.1016/j.cpc.2015.01.024. arXiv: 1410.3012 [hep-ph].

[215] J. de Favereau et al. "DELPHES 3, A modular framework for fast simulation of a generic collider experiment". In: *JHEP* 02 (2014), p. 057. DOI: 10.1007/JHEP02(2014)057. arXiv: 1307.6346 [hep-ex].

[216] Eric Conte et al. "Designing and recasting LHC analyses with MadAnalysis 5". In: *Eur. Phys. J.* C74.10 (2014), p. 3103. DOI: 10.1140/epjc/s10052-014-3103-0. arXiv: 1405.3982 [hep-ph].

[217] Eric Conte and Benjamin Fuks. "Confronting new physics theories to LHC data with MADANALYSIS 5". In: *Int. J. Mod. Phys.* A33.28 (2018), p. 1830027. DOI: 10.1142/S0217751X18300272. arXiv: 1808.00480 [hep-ph].

[218] Morad Aaboud et al. "Search for Heavy Higgs Bosons A/H Decaying to a Top Quark Pair in pp Collisions at $\sqrt{s} = 8$ TeV with the ATLAS Detector". In: *Phys. Rev. Lett.* 119.19 (2017), p. 191803. DOI: 10.1103/PhysRevLett.119.191803. arXiv: 1707.06025 [hep-ex].

[219] Albert M Sirunyan et al. "Search for heavy Higgs bosons decaying to a top quark pair in proton-proton collisions at $\sqrt{s} = 13$ TeV". In: (2019). arXiv: 1908.01115 [hep-ex].

[220] A. Djouadi, J. Kalinowski, and P. M. Zerwas. "Two and three-body decay modes of SUSY Higgs particles". In: *Z. Phys.* C70 (1996), pp. 435–448. DOI: 10.1007/s002880050121. arXiv: hep-ph/9511342 [hep-ph].

[221] T. Hahn et al. "SM and MSSM Higgs boson production cross-sections at the Tevatron and the LHC". In: *TEV4LHC Workshop: 3rd Meeting Geneva, Switzerland, April 28-30, 2005*. 2006. arXiv: hep-ph/0607308 [hep-ph].

[222] M. Aaboud et al. "Search for an invisibly decaying Higgs boson or dark matter candidates produced in association with a Z boson in pp collisions at $\sqrt{s} = 13$ TeV with the ATLAS detector". In: *Phys. Lett.* B776 (2018), pp. 318–337. DOI: 10.1016/j.physletb.2017.11.049. arXiv: 1708.09624 [hep-ex].

[223] A. M. Sirunyan et al. "Search for new physics in events with a leptonically decaying Z boson and a large transverse momentum imbalance in proton–proton collisions at $\sqrt{s} = 13$ TeV". In: *Eur. Phys. J.* C78.4 (2018), p. 291. DOI: 10.1140/epjc/s10052-018-5740-1. arXiv: 1711.00431 [hep-ex].

[224] Glen Cowan. "Discovery sensitivity for a counting experiment with background uncertainty". In: (2012). Available at https://www.pp.rhul.ac.uk/~cowan/stat/medsig/medsigNote.pdf.

[225] CMS Collaboration. "Projection of the Mono-Z search for dark matter to the HL-LHC". In: (2018).

[226] Morad Aaboud et al. "Search for Dark Matter Produced in Association with a Higgs Boson Decaying to $b\bar{b}$ using 36 fb^{-1} of pp collisions at $\sqrt{s} = 13$ TeV with the ATLAS Detector". In: (2017). arXiv: 1707.01302 [hep-ex].

[227] Albert M Sirunyan et al. "Search for dark matter produced in association with a Higgs boson decaying to a pair of bottom quarks in proton–proton collisions at $\sqrt{s} = 13$ TeV". In: *Eur. Phys. J.* C79.3 (2019), p. 280. DOI: 10.1140/epjc/s10052-019-6730-7. arXiv: 1811.06562 [hep-ex].

[228] Albert M Sirunyan et al. "Search for dark matter particles produced in association with a Higgs boson in proton-proton collisions at $\sqrt{s} = 13$ TeV". In: (2019). arXiv: 1908.01713 [hep-ex].

[229] Morad Aaboud et al. "Combination of searches for invisible Higgs boson decays with the ATLAS experiment". In: *Phys. Rev. Lett.* 122.23 (2019), p. 231801. DOI: 10.1103/PhysRevLett.122.231801. arXiv: 1904.05105 [hep-ex].

[230] John Preskill, Mark B. Wise, and Frank Wilczek. "Cosmology of the Invisible Axion". In: *Phys. Lett.* B120 (1983), pp. 127–132. DOI: 10.1016/0370-2693(83)90637-8.

[231] L. F. Abbott and P. Sikivie. "A Cosmological Bound on the Invisible Axion". In: *Phys. Lett.* B120 (1983), pp. 133–136. DOI: 10.1016/0370-2693(83)90638-X.

[232] Michael Dine and Willy Fischler. "The Not So Harmless Axion". In: *Phys. Lett.* B120 (1983), pp. 137–141. DOI: 10.1016/0370-2693(83)90639-1.

[233] Pierre Sikivie. "Axion Cosmology". In: *Lect. Notes Phys.* 741 (2008), pp. 19–50. DOI: 10.1007/978-3-540-73518-2_2. arXiv: astro-ph/0610440 [astro-ph].

[234] Ann E. Nelson and Jakub Scholtz. "Dark Light, Dark Matter and the Misalignment Mechanism". In: *Phys. Rev.* D84 (2011), p. 103501. DOI: 10.1103/PhysRevD.84.103501. arXiv: 1105.2812 [hep-ph].

[235] Paola Arias et al. "WISPy Cold Dark Matter". In: *JCAP* 1206 (2012), p. 013. DOI: 10.1088/1475-7516/2012/06/013. arXiv: 1201.5902 [hep-ph].

[236] Joerg Jaeckel. "A Family of WISPy Dark Matter Candidates". In: *Phys. Lett.* B732 (2014), pp. 1–7. DOI: 10.1016/j.physletb.2014.03.005. arXiv: 1311.0880 [hep-ph].

[237] David J. E. Marsh. "Axion Cosmology". In: *Phys. Rept.* 643 (2016), pp. 1–79. DOI: 10.1016/j.physrep.2016.06.005. arXiv: 1510.07633 [astro-ph.CO].

[238] Joerg Jaeckel and Andreas Ringwald. "The Low-Energy Frontier of Particle Physics". In: *Ann. Rev. Nucl. Part. Sci.* 60 (2010), pp. 405–437. DOI: 10.1146/annurev.nucl.012809.104433. arXiv: 1002.0329 [hep-ph].

[239] *Fundamental Physics at the Intensity Frontier*. 2012. DOI: 10.2172/1042577. arXiv: 1205.2671 [hep-ex]. URL: http://lss.fnal.gov/archive/preprint/fermilab-conf-12-879-ppd.shtml.

[240] Rouven Essig et al. "Working Group Report: New Light Weakly Coupled Particles". In: *Proceedings, 2013 Community Summer Study on the Future of U.S. Particle Physics: Snowmass on the Mississippi (CSS2013): Minneapolis, MN, USA, July 29-August 6, 2013*. 2013. arXiv: 1311.0029 [hep-ph]. URL: http://www.slac.stanford.edu/econf/C1307292/docs/IntensityFrontier/NewLight-17.pdf.

[241] Peter W. Graham et al. "Experimental Searches for the Axion and Axion-Like Particles". In: *Ann. Rev. Nucl. Part. Sci.* 65 (2015), pp. 485–514. DOI: 10.1146/annurev-nucl-102014-022120. arXiv: 1602.00039 [hep-ex].

[242] Igor G. Irastorza and Javier Redondo. "New experimental approaches in the search for axion-like particles". In: *Prog. Part. Nucl. Phys.* 102 (2018), pp. 89–159. DOI: 10.1016/j.ppnp.2018.05.003. arXiv: 1801.08127 [hep-ph].

[243] Alexei A. Starobinsky and Junichi Yokoyama. "Equilibrium state of a selfinteracting scalar field in the De Sitter background". In: *Phys. Rev.* D50 (1994), pp. 6357–6368. DOI: 10.1103/PhysRevD.50.6357. arXiv: astro-ph/9407016 [astro-ph].

[244] P. J. E. Peebles and A. Vilenkin. "Noninteracting dark matter". In: *Phys. Rev.* D60 (1999), p. 103506. DOI: 10.1103/PhysRevD.60.103506. arXiv: astro-ph/9904396 [astro-ph].

[245] Peter W. Graham and Adam Scherlis. "Stochastic axion scenario". In: *Phys. Rev.* D98.3 (2018), p. 035017. DOI: 10.1103/PhysRevD.98.035017. arXiv: 1805.07362 [hep-ph].

[246] Fuminobu Takahashi, Wen Yin, and Alan H. Guth. "QCD axion window and low-scale inflation". In: *Phys. Rev.* D98.1 (2018), p. 015042. DOI: 10.1103/PhysRevD.98.015042. arXiv: 1805.08763 [hep-ph].

[247] Shu-Yu Ho, Fuminobu Takahashi, and Wen Yin. "Relaxing the Cosmological Moduli Problem by Low-scale Inflation". In: *JHEP* 04 (2019), p. 149. DOI: 10.1007/JHEP04(2019)149. arXiv: 1901.01240 [hep-ph].

[248] Tommi Tenkanen. "Dark matter from scalar field fluctuations". In: (2019). arXiv: 1905.01214 [astro-ph.CO].

[249] Peter W. Graham, Jeremy Mardon, and Surjeet Rajendran. "Vector Dark Matter from Inflationary Fluctuations". In: *Phys. Rev.* D93.10 (2016), p. 103520. DOI: 10.1103/PhysRevD.93.103520. arXiv: 1504.02102 [hep-ph].

[250] Sami Nurmi, Tommi Tenkanen, and Kimmo Tuominen. "Inflationary Imprints on Dark Matter". In: *JCAP* 1511.11 (2015), p. 001. DOI: 10.1088/1475-7516/2015/11/001. arXiv: 1506.04048 [astro-ph.CO].

[251] Kimmo Kainulainen et al. "Isocurvature Constraints on Portal Couplings". In: *JCAP* 1606.06 (2016), p. 022. DOI: 10.1088/1475-7516/2016/06/022. arXiv: 1601.07733 [astro-ph.CO].

[252] Orfeu Bertolami, Catarina Cosme, and João G. Rosa. "Scalar field dark matter and the Higgs field". In: *Phys. Lett.* B759 (2016), pp. 1–8. DOI: 10.1016/j.physletb.2016.05.047. arXiv: 1603.06242 [hep-ph].

[253] Catarina Cosme, João G. Rosa, and O. Bertolami. "Scale-invariant scalar field dark matter through the Higgs portal". In: *JHEP* 05 (2018), p. 129. DOI: 10.1007/JHEP05(2018)129. arXiv: 1802.09434 [hep-ph].

[254] Gonzalo Alonso-Álvarez and Joerg Jaeckel. "Lightish but clumpy: scalar dark matter from inflationary fluctuations". In: *JCAP* 1810.10 (2018), p. 022. DOI: 10.1088/1475-7516/2018/10/022. arXiv: 1807.09785 [hep-ph].

[255] Prateek Agrawal et al. "Relic Abundance of Dark Photon Dark Matter". In: (2018). arXiv: 1810.07188 [hep-ph].

[256] Jeff A. Dror, Keisuke Harigaya, and Vijay Narayan. "Parametric Resonance Production of Ultralight Vector Dark Matter". In: *Phys. Rev.* D99.3 (2019), p. 035036. DOI: 10.1103/PhysRevD.99.035036. arXiv: 1810.07195 [hep-ph].

[257] Raymond T. Co et al. "Dark Photon Dark Matter Produced by Axion Oscillations". In: *Phys. Rev.* D99.7 (2019), p. 075002. DOI: 10.1103/PhysRevD.99.075002. arXiv: 1810.07196 [hep-ph].

[258] Mar Bastero-Gil et al. "Vector dark matter production at the end of inflation". In: *JCAP* 1904.04 (2019), p. 015. DOI: 10.1088/1475-7516/2019/04/015. arXiv: 1810.07208 [hep-ph].

[259] Andrew J. Long and Lian-Tao Wang. "Dark Photon Dark Matter from a Network of Cosmic Strings". In: *Phys. Rev.* D99.6 (2019), p. 063529. DOI: 10.1103/PhysRevD.99.063529. arXiv: 1901.03312 [hep-ph].

[260] Alexey Golovnev, Viatcheslav Mukhanov, and Vitaly Vanchurin. "Vector Inflation". In: *JCAP* 0806 (2008), p. 009. DOI: 10.1088/1475-7516/2008/06/009. arXiv: 0802.2068 [astro-ph].

[261] Gonzalo Alonso-Álvarez, Joerg Jaeckel, and Thomas Hugle. "Misalignment & Co.: (Pseudo-)scalar and vector dark matter with curvature couplings". In: *JCAP* 02.02 (2020), p. 014. DOI: 10.1088/1475-7516/2020/02/014. arXiv: 1905.09836 [hep-ph].

[262] Thomas Hugle. "Hidden Photons as Dark Matter Candidates". In: *ITP Master's Thesis* (2015).

[263] Konstantinos Dimopoulos et al. "Statistical anisotropy of the curvature perturbation from vector field perturbations". In: *JCAP* 0905 (2009), p. 013. DOI: 10.1088/1475-7516/2009/05/013. arXiv: 0809.1055 [astro-ph].

[264] Mindaugas Karciauskas and David H. Lyth. "On the health of a vector field with $(RA^2)/6$ coupling to gravity". In: *JCAP* 1011 (2010), p. 023. DOI: 10.1088/1475-7516/2010/11/023. arXiv: 1007.1426 [astro-ph.CO].

[265] John F. Donoghue. "General relativity as an effective field theory: The leading quantum corrections". In: *Phys. Rev.* D50 (1994), pp. 3874–3888. DOI: 10.1103/PhysRevD.50.3874. arXiv: gr-qc/9405057 [gr-qc].

[266] N. D. Birrell and P. C. W. Davies. *Quantum Fields in Curved Space*. Cambridge Monographs on Mathematical Physics. Cambridge, UK: Cambridge Univ. Press, 1984. ISBN: 0521278589, 9780521278584, 9780521278584. DOI: 10.1017/CBO9780511622632. URL: http://www.cambridge.org/mw/academic/subjects/physics/theoretical-physics-and-mathematical-physics/quantum-fields-curved-space?format=PB.

[267] Curtis G. Callan Jr., Sidney R. Coleman, and Roman Jackiw. "A New improved energy - momentum tensor". In: *Annals Phys.* 59 (1970), pp. 42–73. DOI: 10.1016/0003-4916(70)90394-5.

[268] Astrid Eichhorn. "Status of the asymptotic safety paradigm for quantum gravity and matter". In: *Found. Phys.* 48.10 (2018), pp. 1407–1429. DOI: 10.1007/s10701-018-0196-6. arXiv: 1709.03696 [gr-qc].

[269] Alfio Bonanno and Frank Saueressig. "Asymptotically safe cosmology – A status report". In: *Comptes Rendus Physique* 18 (2017), pp. 254–264. DOI: 10.1016/j.crhy.2017.02.002. arXiv: 1702.04137 [hep-th].

[270] Steven Weinberg. "Critical Phenomena for Field Theorists". In: *14th International School of Subnuclear Physics: Understanding the Fundamental Constitutents of Matter Erice, Italy, July 23-August 8, 1976*. 1976, p. 1. DOI: 10.1007/978-1-4684-0931-4_1. URL: https://www.quantamagazine.org/why-an-old-theory-of-everything-is-gaining-new-life-20180108.

[271] Gaurav Narain and Roberto Percacci. "Renormalization Group Flow in Scalar-Tensor Theories. I". In: *Class. Quant. Grav.* 27 (2010), p. 075001. DOI: 10.1088/0264-9381/27/7/075001. arXiv: 0911.0386 [hep-th].

[272] Gaurav Narain and Christoph Rahmede. "Renormalization Group Flow in Scalar-Tensor Theories. II". In: *Class. Quant. Grav.* 27 (2010), p. 075002. DOI: 10.1088/0264-9381/27/7/075002. arXiv: 0911.0394 [hep-th].

[273] Roberto Percacci and Gian Paolo Vacca. "Search of scaling solutions in scalar-tensor gravity". In: *Eur. Phys. J.* C75.5 (2015), p. 188. DOI: 10.1140/epjc/s10052-015-3410-0. arXiv: 1501.00888 [hep-th].

[274] Peter Labus, Roberto Percacci, and Gian Paolo Vacca. "Asymptotic safety in $O(N)$ scalar models coupled to gravity". In: *Phys. Lett.* B753 (2016), pp. 274–281. DOI: 10.1016/j.physletb.2015.12.022. arXiv: 1505.05393 [hep-th].

[275] Yuta Hamada and Masatoshi Yamada. "Asymptotic safety of higher derivative quantum gravity non-minimally coupled with a matter system". In: *JHEP* 08 (2017), p. 070. DOI: 10.1007/JHEP08(2017)070. arXiv: 1703.09033 [hep-th].

[276] Astrid Eichhorn, Stefan Lippoldt, and Vedran Skrinjar. "Nonminimal hints for asymptotic safety". In: *Phys. Rev.* D97.2 (2018), p. 026002. DOI: 10.1103/PhysRevD.97.026002. arXiv: 1710.03005 [hep-th].

[277] James M. Cline, Sangyong Jeon, and Guy D. Moore. "The Phantom menaced: Constraints on low-energy effective ghosts". In: *Phys. Rev.* D70 (2004), p. 043543. DOI: 10.1103/PhysRevD.70.043543. arXiv: hep-ph/0311312 [hep-ph].

[278] Fulvio Sbisà. "Classical and quantum ghosts". In: *Eur. J. Phys.* 36 (2015), p. 015009. DOI: 10.1088/0143-0807/36/1/015009. arXiv: 1406.4550 [hep-th].

[279] Burak Himmetoglu, Carlo R. Contaldi, and Marco Peloso. "Instability of anisotropic cosmological solutions supported by vector fields". In: *Phys. Rev. Lett.* 102 (2009), p. 111301. DOI: 10.1103/PhysRevLett.102.111301. arXiv: 0809.2779 [astro-ph].

[280] Burak Himmetoglu, Carlo R. Contaldi, and Marco Peloso. "Ghost instabilities of cosmological models with vector fields nonminimally coupled to the curvature". In: *Phys. Rev.* D80 (2009), p. 123530. DOI: 10.1103/PhysRevD.80.123530. arXiv: 0909.3524 [astro-ph.CO].

[281] D. S. Salopek, J. R. Bond, and James M. Bardeen. "Designing Density Fluctuation Spectra in Inflation". In: *Phys. Rev.* D40 (1989), p. 1753. DOI: 10.1103/PhysRevD.40.1753.

[282] Mark P. Hertzberg. "On Inflation with Non-minimal Coupling". In: *JHEP* 11 (2010), p. 023. DOI: 10.1007/JHEP11(2010)023. arXiv: 1002.2995 [hep-ph].

[283] Fedor L. Bezrukov and Mikhail Shaposhnikov. "The Standard Model Higgs boson as the inflaton". In: *Phys. Lett.* B659 (2008), pp. 703–706. DOI: 10.1016/j.physletb.2007.11.072. arXiv: 0710.3755 [hep-th].

[284] Javier Rubio. "Higgs inflation". In: *Front. Astron. Space Sci.* 5 (2019), p. 50. DOI: 10.3389/fspas.2018.00050. arXiv: 1807.02376 [hep-ph].

[285] L. H. Ford. "Gravitational Particle Creation and Inflation". In: *Phys. Rev.* D35 (1987), p. 2955. DOI: 10.1103/PhysRevD.35.2955.

[286] Daniel J. H. Chung, Edward W. Kolb, and Antonio Riotto. "Superheavy dark matter". In: *Phys. Rev.* D59 (1999), p. 023501. DOI: 10.1103/PhysRevD.59.023501. arXiv: hep-ph/9802238 [hep-ph].

[287] Daniel J. H. Chung et al. "On the Gravitational Production of Superheavy Dark Matter". In: *Phys. Rev.* D64 (2001), p. 043503. DOI: 10.1103/PhysRevD.64.043503. arXiv: hep-ph/0104100 [hep-ph].

[288] Yohei Ema et al. "Gravitational Effects on Inflaton Decay". In: *JCAP* 1505.05 (2015), p. 038. DOI: 10.1088/1475-7516/2015/05/038. arXiv: 1502.02475 [hep-ph].

[289] Tommi Markkanen and Sami Nurmi. "Dark matter from gravitational particle production at reheating". In: *JCAP* 1702 (2017), p. 008. DOI: 10.1088/1475-7516/2017/02/008. arXiv: 1512.07288 [astro-ph.CO].

[290] Malcolm Fairbairn et al. "Despicable Dark Relics: generated by gravity with unconstrained masses". In: *JCAP* 1904.04 (2019), p. 005. DOI: 10.1088/1475-7516/2019/04/005. arXiv: 1808.08236 [astro-ph.CO].

[291] Yohei Ema et al. "Gravitational particle production in oscillating backgrounds and its cosmological implications". In: *Phys. Rev.* D94.6 (2016), p. 063517. DOI: 10.1103/PhysRevD.94.063517. arXiv: 1604.08898 [hep-ph].

[292] Yohei Ema, Kazunori Nakayama, and Yong Tang. "Production of Purely Gravitational Dark Matter". In: *JHEP* 09 (2018), p. 135. DOI: 10.1007/JHEP09(2018)135. arXiv: 1804.07471 [hep-ph].

[293] Yohei Ema, Kazunori Nakayama, and Yong Tang. "Production of Purely Gravitational Dark Matter: The Case of Fermion and Vector Boson". In: (2019). arXiv: 1903.10973 [hep-ph].

[294] George R. Blumenthal et al. "Formation of Galaxies and Large Scale Structure with Cold Dark Matter". In: *Nature* 311 (1984), pp. 517–525. DOI: 10.1038/311517a0.

[295] Y. Akrami et al. "Planck 2018 results. X. Constraints on inflation". In: (2018). arXiv: 1807.06211 [astro-ph.CO].

[296] Andrew R Liddle and Samuel M Leach. "How long before the end of inflation were observable perturbations produced?" In: *Phys. Rev.* D68 (2003), p. 103503. DOI: 10.1103/PhysRevD.68.103503. arXiv: astro-ph/0305263 [astro-ph].

[297] Grant N. Remmen and Sean M. Carroll. "How Many e-Folds Should We Expect from High-Scale Inflation?" In: *Phys. Rev.* D90.6 (2014), p. 063517. DOI: 10.1103/PhysRevD.90.063517. arXiv: 1405.5538 [hep-th].

[298] Peter W. Graham, David E. Kaplan, and Surjeet Rajendran. "Cosmological Relaxation of the Electroweak Scale". In: *Phys. Rev. Lett.* 115.22 (2015), p. 221801. DOI: 10.1103/PhysRevLett.115.221801. arXiv: 1504.07551 [hep-ph].

[299] Wayne Hu, Rennan Barkana, and Andrei Gruzinov. "Cold and fuzzy dark matter". In: *Phys. Rev. Lett.* 85 (2000), pp. 1158–1161. DOI: 10.1103/PhysRevLett.85.1158. arXiv: astro-ph/0003365 [astro-ph].

[300] Simone Blasi, Vedran Brdar, and Kai Schmitz. "Fingerprint of Low-Scale Leptogenesis in the Primordial Gravitational-Wave Spectrum". In: (Apr. 2020). arXiv: 2004.02889 [hep-ph].

[301] Edward W. Kolb and Michael S. Turner. "The Early Universe". In: *Front. Phys.* 69 (1990), pp. 1–547.

[302] Kai Schmitz. "The B-L Phase Transition: Implications for Cosmology and Neutrinos". PhD thesis. Hamburg U., 2012. arXiv: 1307.3887 [hep-ph]. URL: http://www-library.desy.de/cgi-bin/showprep.pl?thesis12-039.

[303] Sacha Davidson, Enrico Nardi, and Yosef Nir. "Leptogenesis". In: *Phys. Rept.* 466 (2008), pp. 105–177. DOI: 10.1016/j.physrep.2008.06.002. arXiv: 0802.2962 [hep-ph].

[304] F. Hahn-Woernle, M. Plumacher, and Y. Y. Y. Wong. "Full Boltzmann equations for leptogenesis including scattering". In: *JCAP* 0908 (2009), p. 028. DOI: 10.1088/1475-7516/2009/08/028. arXiv: 0907.0205 [hep-ph].

[305] A. Anisimov et al. "Quantum Leptogenesis I". In: *Annals Phys.* 326 (2011). [Erratum: Annals Phys.338,376(2011)], pp. 1998–2038. DOI: 10.1016/j.aop.2011.02.002, 10.1016/j.aop.2013.05.00. arXiv: 1012.5821 [hep-ph].

[306] A. Hohenegger, A. Kartavtsev, and M. Lindner. "Deriving Boltzmann Equations from Kadanoff-Baym Equations in Curved Space-Time". In: *Phys. Rev.* D78 (2008), p. 085027. DOI: 10.1103/PhysRevD.78.085027. arXiv: 0807.4551 [hep-ph].

[307] Edward W. Kolb and Stephen Wolfram. "Baryon Number Generation in the Early Universe". In: *Nucl. Phys.* B172 (1980). [Erratum: Nucl. Phys.B195,542(1982)], p. 224. DOI: 10.1016/0550-3213(80)90167-4,10.1016/0550-3213(82)90012-8.